UNIVERSITÀ DEGLI STUDI DI MILANO

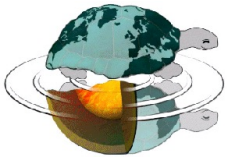

Dottorato di Ricerca in Scienze della Terra
Ciclo XXIX

Local disorder in the structure of $Ba(Ti, Ce)O_3$ perovskite by means of powder diffraction and total scattering. Effect of temperature, doping concentration and grain size

PhD Thesis

Giorgia Confalonieri

ID nr. R10690

Prof. Monica Dapiaggi
Tutor
Dr. Vincenzo Buscaglia
Prof. Alessandro Pavese
Co-Tutors

Academic Year
2015-2016

Prof. Elisabetta Erba
Coordinator

To those who love me,
to those who have supported me,
and to those I love

Contents

Research Aim

Ferroelectrics are materials characterized by a spontaneous electrical dipole moment even in the absence of an external electric field. The ferroelectric order appears when these systems are cooled through their ferroelectric Curie temperature passing from a non polar centrosymmetric to a polar non centrosymmetric structure. Among many types of ferroelectrics nowadays perovskites are extensively used in a wide range of applications thank to their particular properties. These materials present piezoelectric and pyroelectric response, switchable polarization, low losses and more important unusual high dielectric permittivity corresponding to the just mentioned paraelectric ferroelectric transition. Different devices take advantage of these effects as pyroelectric sensors, electromechanical transducers, non volatile memories, capacitors and multilayer capacitors. Moreover a long experience in the industrial mass production, reliability and low production cost make ferroelectric perovskites as base for the majority of electronic applications. Beyond their interesting characteristics the real key point, which make these materials unique, is their distinctive atomic structure named properly perovskite type structure. It presents chemical formula ABO_3 where, in a cubic cell belonging to Pm-3m space group, A cation (Na, K, Ca, Sr, Ba, Pb, Bi *etc.*) is at the origin in the dodecahedral site and B (Ti, Zr, Nb, Ta, Fe *etc.*) cation is placed at the center of the cell and thus of the oxygen octahedron BO_6. Lowering temperature this structure changes by transition to ferroelectric phases which are slight distorted variations of the cubic paraelectric structure. As described then perovskites present a very simple atomic arrangements, but their composition could be associated with a great variety of elements. The flexible chemistry allows to tune this material with a huge mixture of possible substitutions changing and improving properties. Doping by homovalent or heterovalent substitutions is possible at A, B or both sites. In $AB'^{IV}_{1-x}B''^{IV}_{x}O_3$ for example, depending on substitution type and amount, it is possible to obtain an almost continuous variation of the ferroelectric behaviour, from conventional ferroelectric, via diffuse ferroelectric transition (DPT) to a clear relaxor state. In relaxor materials the long range ferroelectric order is lost and only a short range polar order, corresponding to the so called polar nanoregions (PNRs), is maintained. Comparing to normal ferroelectrics, these materials present higher dielectric constants, great electromechanical coupling coefficients and frequency dependent properties. These characteristics make relaxors a very fascinating class among ferroelectrics, but unfortunately, despite many efforts, the determination of their exact structural nature still represents an experimental challenge. Currently lead free ferroelectrics and relaxors have attracted much attention. These have comparable good performances than those of the toxic lead based materials, but can be employed for environmental friendly applications. $BaTiO_3$ and its solid solutions $BaTi_{1-x}B^{IV}_{x}O_3$ have presently emerged as the most promising candidates to replace toxic Pb-ferroelectric and relaxor. The study of these compounds is then essential to improve their characteristics and make their suitable in more applications. Considering that their properties are deeply linked to the structure and especially to structural defects, average and local structural analyses are essential to better understand the origins of different polar behaviours and to have a real control on these materials. Despite this need, only $BaTi_{1-x}Zr_xO_3$ (BTZ) system, which is one of the most popular dielectrics used in multilayer ceramic capacitors, has been investigated in some detail. Although the similarity to BTZ suggests that $BaTi_{1-x}Ce_xO_3$ (BTC) may be promising

as lead free actuator materials, studies on this solid solution are almost limited. Especially those that deal with exhaustive explanations about the consequences of cerium introduction on polar behaviour are almost vague and no much works have examined accurately these polar variations with structural evolution. Thus in this research the BTC solid solution has been studied in order to provide knowledge lacks. Furthermore this material represents a limit and interesting case, in fact, in one hand Ce^{4+} (r = 0.87 Å) is much bigger than Ti^{4+} (r = 0.605 Å) and on the other this kind of substitution does not involve the creation of charge compensating lattice defects. Different ceramic samples with different doping amounts and different polar behaviours (from normal ferroelecric to relaxor via diffuse phase transition) have been investigated at different temperatures. In addition, taking into account the current tendency in miniaturized devices required in microelectronics, also chemical equivalent nano powders have been considered to explore not only doping effects, but also that of size. The aim is then furnish a detailed description of these materials exploring their structural characteristics and taking into account different effects (doping and size) in order to better exploit their capabilities. To do this, structural analyses on both average and local structure are indispensable, so total scattering experiments have been performed in order to collect both the Bragg scattering (used in traditional crystallography) and diffuse scattering, caused by anything that does not diffuse exactly following the Bragg law (such as defects, local distortions, *etc.*) This makes possible to have not only a picture of the average structure, but also a good representation of the local variations. The first step then is to use classical Rietveld method to interpreter the average structural transitions as a function of the temperature and compare them with the predicted polar behaviours of the different $BaTi_{1-x}Ce_xO_3$ understanding in one hand how cerium influences Curie temperatures and on the other which is the effect of the reducing size from micro to nano. The different size of the two B cations should be one of the causes at the basis of the particular behaviours of these materials, but at the same time it should create a certain degree of local disorder and variations. Thus local structures have been studied to explore the local arrangements by Pair Distribution Function (PDF). Indeed PDF describes the distribution of the atomic distances in the material where the correlations among the local variations are correctly represented. For ceramic samples different type of approaches (as carbox, biphasic and so on) have been employed to determine the local disorder. In order to defined the arrangements between cerium and titanium, lattice energy calculation has been used to compare different configurations, which present or a homogeneous distribution of cerium or cluster of $BaCeO_3$ in a $BaTiO_3$ matrix, while microprobe analysis has been performed to verify the homogeneous distribution of barium, titanium and cerium. In addition TEM investigations have furnished an extra exploration of the BTC local structure especially inspecting Ti and Ce structural relationship. Raman spectroscopy has been used as an addition technique to verify in one hand the right incorporation of cerium in Ti site and on the other to have a different point of view on the local structure. At the end also the contribution of size effect on the local structure has been taken into account and investigated by Pair Distribution Functions. In this dissertation then a complete description of $BaTi_{1-x}Ce_xO_3$ materials is proposed underlining links between polar behaviours, temperature, doping and size effects.

Chapter 1

Introduction

The term 'perovskite' is used to indicate a category of inorganic crystalline solids which include not only synthetic crystals, but also a huge variety of minerals. These materials are all characterized by a general formula ABO_3, where A and B are cations and X (oxides or halides) is an anion (Galasso 1969). Two different subgrups then occur: oxide and halide systems where X = O or X = F, Cl, Br, I, *etc.* (Li et al. 2008), however in this chapter only the first category will be considered in order to remain close to the topic of the present research. The chemical composition could be associated with a great variety of elements, but the atomic arrangement presents in all the cases the same framework. This type of structure, properly called perovskite structure, was firstly described for $CaTiO_3$: calcium ions were thought to be placed at the corners of a cubic cell with titanium at the body center and oxygen located at the center of each face (Galasso 1969). Here and in generic case A cation is coordinated with twelve anions and the B cation with six, so BO_6 octahedra are exclusively corner sharing (Davies et al. 2008). This configuration forms a cubic structure belonging to Pm-3m space group, which is besides frequently slightly distorted resulting in a lower symmetry such as orthorhombic, tetragonal, rhombohedric, trigonal systems and so on. These structural changes are governed by temperature, pressure, chemical composition, and in some cases, electric field. As an example: rising temperature usually induces a series of transitions to progressively higher symmetry, culminating in the cubic structure (Verma & Jindal 2010). The stability and distortions of this phase is mostly governed by Goldschmidt tolerance factor (Ravel 1957) (Shannon 1967) which is expressed as:

$$t = \frac{r_A + r_O}{\sqrt{2}(r_B + r_O)} \tag{1.1}$$

where r_A, r_B and r_O are respectively the atomic radii of A and B cation and oxygen. In Goldschmidt's formalism for the perovskite structure t range is from about 0.77 to about 1.05 with the 'ideal' cubic perovskite forming when t is about 1.00 (Tidrow 2014). By this definition the size of atoms involved could change a lot, therefore perovskite structure could be formed by a huge array of elements. Despite this, natural chemical compositions (or better the most abundant) are rather limited, but nonetheless extremely significant. Especially from the geological point of view these minerals and in particular $CaSiO_3$, $FeSiO_3$ and $MgSiO_3$ are really important. Indeed, since their discovery by synthetic preparation of $MgSiO_3$ at high pressures and high temperatures in 1975 (Liu 1975) (previously predicted by Ringwood (Ringwood 1962)), silicate perovskites have probably become the most studied minerals in the geophysical community during the past decade or so and it is nearly established that they should be the most abundant materials making up the bulk of the Earth (Liu 1989). As reported in figure 1.1 Mg perovskite is the major component of the lower mantle with a very high percentage, while $CaSiO_3$ reaches 7-8 vol.% (Irifune 1994).

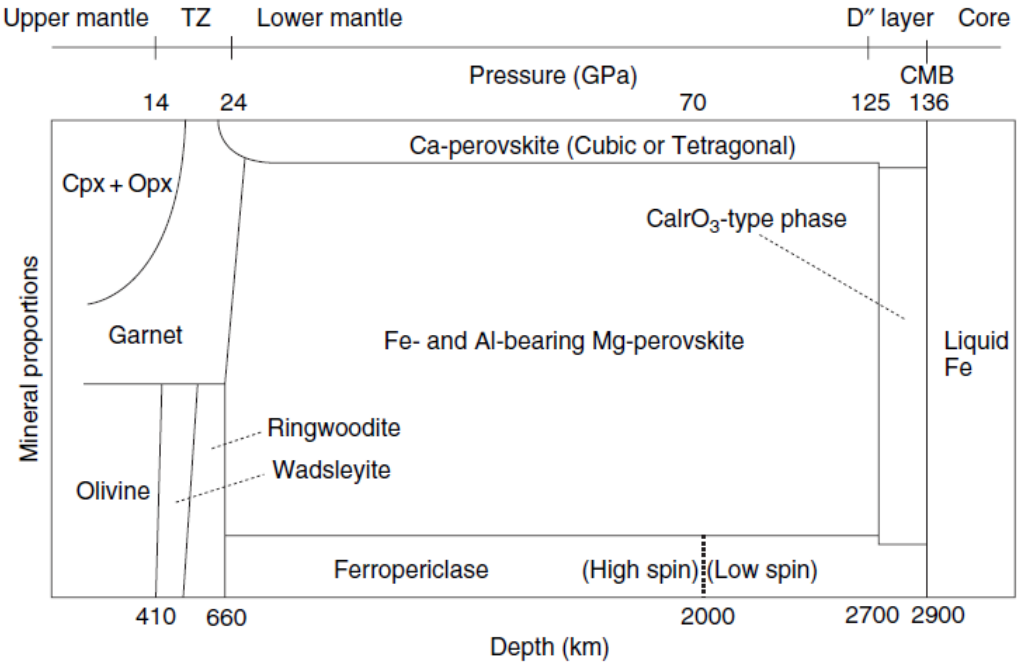

Figure 1.1: Phase relations of pyrolitic mantle composition as a function of depth (Ono & Oganov 2005).

$MgSiO_3$ perovskite and its appearance play a critical role in the so called transition zone at 660 km depth which is in fact one of the two larger discontinuities in the mantle. Here ringwoodite (highest pressure olivine polymorph) is dissolved in perovskite plus periclase phases according to the reaction (Liu 1976):

$$Mg_2SiO_4 \rightarrow MgSiO_3 + MgO \tag{1.2}$$

Similar effects have been described for the exsolution of calcium perovskite from garnet (Koito et al. 2000) which is considered one of the origin of the transition zone at 520 km. NB This discontinuity is only regionally observed, probably linked to chemical heterogeneity and possibly associated with subduction (Sinogeikin et al. 2003). However lower mantle is not formed by pure phases above reported, but rather by solid solutions. For example in peridotitic compositions Mg perovskite could incorporate 5-10 mol.% of $FeSiO_3$, whereas in pyrolite composition aluminium may be enter in perovskite structure (Irifune 1994). This point is to be underlined due to its influence on other elements incorporation: Ti, Zr, and Hf are incompatible in Al-free Mg perovskite, but become compatible as Al is added in the crystal structure. For example lantanium partition coefficient increases by an order of magnitude as Al_2O_3 increases from 0 to 6.5 wt.%. Moreover also $CaTiO_3$ could be affected by chemical substitutions: it indeed contains, in the lower mantle, more than 90 % of the heat-producing elements K, U, and Th together with most of the light rare earths (LRE) as Sr and Ba (Price 2009). The formation and stability of these phases are then very important, but also their transformations at very high pressure are deeply investigated. The mantle mineralogical model has been recently revised by the discovery of a postperovskite phase (Murakami et al. 2004), (Oganov & Ono 2000). This structural transition ($\sim$2500 km) seems to occur at the Earth mantle-core boundary given rise to the so called D" zone. Mg postperovskite has been predicted to assume a crystal structure identical to that of $CaIrO_3$ with a space group Cmcm (which is orthorhombic) and consisting in silica layers stacking along the $\vec{b}$ direction and intercalated Mg ions. However rates of accumulating data are so fast and the relevant research fields so vast that it is impossible at the moment to clearly evaluate available studies. (Price 2009). In any case understanding the evolution, structure, composition and physical behaviour of perovskites is

then extremely necessary to interpret the inner Earth structure and also to clarify their influence on complex Earth mechanisms. Recent advances in both experimental and computational techniques (as *ab initio* calculation) have enabled the quantitative study of these phase transitions and mineral physics properties under the lower mantle P-T conditions. Unfortunately these studies are in some way limited by the impossibility to investigate natural samples and compare their characteristics with their synthetic equivalents. In fact, despite the huge chemical assortment which is allowed by this structure, in nature (or better at the top of Earth crust) only a few perovskite type compounds, and not silicate, have been truly discovered. Some of these are reported in table 1.1 (Moure & Pena 2015). These minerals are rather rare and usually absent in most common rock types. The stability of not silicate

Name	Composition	Discovery sites
Latrappite	$Ca(Fe,Nb)O_3$	Oka, (Quebec, Canada)
Loparite	$(Na,Ce)TiO_3$	Khibiny and Kola Peninsula (Russia)
Lueshite	$NaNbO_3$	Lueshe (Democratic Republic of Congo
Macedonite	$PbTiO_3$	Crni and Kamen (Macedonia)
Perovskite	$CaTiO_3$	Zlatoust district (Ural Mountains, Russia)
Tausonite	$SrTiO_3$	Murun complex (Yakutia, Russia)

Table 1.1: Natural occurrence of non silicate perovskite by Moure et Pena (Moure & Pena 2015).

perovskite in silica saturated igneous rocks is in fact limited by its relation with sphene $CaTiSiO_5$ which replaces it by the reaction (Veksler & Teptelev 1990):

$$CaTiO_3 + SiO_2(melt) \rightarrow CaTiSiO_5 \tag{1.3}$$

Perovskites are then reachable, as typical accessories, only in silica undersaturated igneous rocks such as ultramafic alkaline rocks, agpaitic nepheline syenites and nonsilicate rocks as carbonatites. Only few types of deposits in which perovskite type minerals can form large accumulations are known. For example some ultra mafic-alkaline intrusive complexes olivinites and pyroxenites are enriched in perovskite with chemical compositions close to pure calcium titanate (Veksler & Teptelev 1990). Layered intrusions of agpaitic nepheline syenites are another case, here indeed some strata could contain high concentrations of perovskite type titanoniobates dominated by loparite (Chakhmouradian & Mitchell 1998). This compositional variation in the perovskites of the two ore types is justifiable taking into account the differentiation reaction which occurs between ultramafic and mafic alkaline melts and their agpaitic residual liquids. Peralkaline agpaitic magmas being a residual production could indeed accumulate the high concentrations of incompatible trace elements such as niobium, light rare earths, zirconium and thorium. Therefore perovskite type minerals crystallizing from agpaitic magmas are no longer pure calcium titanate, but a complex niobium and REE-bearing solid solutions, the main component of which is loparite (Veksler & Teptelev 1990). In light of this perovskite natural occurrences are of a great importance as indicators of geochemical evolution and of rare earths ores. These elements are indispensable in a huge variety of application as catalysts, glass making, lighting, metallurgy, permanent magnets, battery alloys and their demand is predicted to grow at 7-9 % per annum, increasing from $\sim$125,000 t in 2010 to $\sim$263,550 t in 2020, especially thank to the recent attention on energy efficient green products and an increased use of mobile electronics and electric vehicles (Amr-Mineral-Metal-Inc 2016). Considering that loparite is one of the principal bearing of the light rare earth elements (Feng et al. 2016), perovskites and related ores have a great importance in the world economy. Example of major deposits are: Powderhorn (Colorado, USA) where rocks contain 0.36 % rare earth oxide (REO) and Kola Peninsula (Russia), where a primary ore grades is of 2-3 % in loparite with 30-36 % of REO (Gupta & Krishnamurthy 1992). Beyond natural occurrence and their clear economical importance, perovskites, synthetically produced, are nowa-

days deeply investigated thank to their excellent physical properties (*i.e.*, dielectric, electronic, magnetic, *etc.*) which find application in the electronic industry. They can be used as insulators, ferroelectric compounds, semiconductors, superconductors, metallic conductors, ionic conductors, antiferro, ferro or ferrimagnetic compounds, multiferroics etc.; some examples are given in table 1.2 (Moure & Pena 2015).
In this work only ferroelectric phenomena will be treated and explained in order to introduce some basic concept related to the properties of the material on which this study is focused.

Property	Application	Material
Proton conductivity	SOFC electrolyte	$BaCeO_3$, $SrCeO_3$, $BaZrO_3$
Ionic conductivity	Solid electrolyte	$(La, Sr)(Ga, Mg)O_{3-\delta}$
	Hydrogen sensor	
	H_2 production/extraction	
Mixed conductivity	SOFC electrode	$La(Sr, Ca)MnO_{3-\delta}$, $LaCoO_3$, $(La, Sr)(Co, Fe)O_{3-\delta}$
	Gas separation	
	Membrane reactors	
Catalytic	Catalyst	$LaFeO_3$, $La(Ce, Co)O_3$
Electric/dielectric	Multilayer capacitor	$BaTiO_3$, $BaZrO_3$
	Dielectric resonator	$BaM_{1/3}Ta_{2/3}O_3$ ($M = Mg, Zn, Co$)
	Thin film resistor	
Ferroelectric/piezoelectric	Actuator, Transducer	$BaTiO_3$, $Pb(Zr, Ti)O_3$, $Pb(Mg, Nb)O_3$
		$Na_{0.5}K_{0.5}NbO_3$, $Bi_{0.5}Na_{0.5}TiO_3$
	Thin film resistor	
Magnetic	Magnetic memory	$GdFeO_3$, $LaMnO_3$
	Ferromagnetism	$SrRuO_3$
Magnetoelectric	Magnetic field detector	$BiFeO_3$
Optical	Electrooptical modulator	$(Pb.La)(Zr, Ti)O_3$
	Laser	$YAlO_3$, $KNbO_3$
Superconductivity	Superconductor	$Ba(Pb, Bi)O_3$, $BaKBiO_3$, $YBa_2Cu_3O_{7-\delta}$

Table 1.2: Some properties and applications of perovskites (most of them from Moure et Pena (Moure & Pena 2015)).

1.1 Ferroelectricity: a general introduction

The following explanation on the origin and nature of ferroelectricity takes inspiration and fundamental concepts from just few essential works (Jaffe & Cook 1971), (Yang 2005), (Heywang et al. 2008), (Damjanovic 1998). Piezoelectricity is the ability of certain crystalline materials to develop an electric charge proportional to a mechanical stress (or *vice versa* called anti-piezoelectricity), this phenomenon could express only if certain axes of the medium intrinsically possess a one-wayness, or polarity. Saying this, it is obvious that this polarity is deeply connected to the symmetry of the material and it can not onset in isotropic bodies. Therefore, if the crystal world is considered, only classes which lack a center of symmetry, and in specific 20 of these 21, show this effect. In these groups it is then possible to recognize a subgroup, consisting of 10 classes, characterized by a unique polar axis (electric dipole moment) in the unstrained condition. The polarization associated to this electrical dipoles is called spontaneous polarization, P_S (C/m^2). The variation of P_S with temperature determines a variation of the surface charge density and originates a pyroelectric current as:

$$I = \frac{dP_s}{dt} = (\frac{dP_s}{dT})(\frac{dT}{dt}) \tag{1.4}$$

This dipole effect is known as pyroelectricity. In some pyroelectric crystals the spontaneous electric moment can

assume two different orientations if exposed to an electric field. These materials are called ferroelectric and the linked phenomenon, just above described, is named ferroelectricity. In other words this is the property of some polar materials in which the spontaneous polarization P_S, that has at least two equilibrium orientations in the absence of an external electric field, may be switched between those orientations by an electric field. In order to clarify: all ferroelectrics materials are also pyroelectric and all of these are then piezoelectric too, but only some piezoelectric materials (those whose symmetry belongs to polar groups) are pyroelectric and only some of these are ferroelectrics. Differently to the other, these last have same typical and characteristic features. For example they present with temperature rise a structural transition between ferroelectric and paraelectric phase which corresponds to a variation from a polar to a non polar form and then to a spontaneous polarization disappearance. As deducible this phase transition is extremely important especially because associated to a high increase in the dielectric permittivity, which is for sure the most important characteristic of these materials. Indeed the anomalous values of this quantity (ϵ_r > 100, often > 1000) is usually expressed as a sharp peak around temperature transformation which is called Curie temperature (T_C). Above this crystal transition, the dielectric constant obeys to the Curie-Weiss law:

$$\epsilon_r = \frac{C}{T - T_0} \tag{1.5}$$

where ϵ_r is the dielectric permittivity, C is a constant called the Curie constant, and T_0 is the Curie-Weiss temperature. Depending of the order of this structural variation T_C could be identical or not to T_0 (which is actually a formula constant obtained by extrapolation). In the Landau theory transitions are characterized in terms of an order parameter which is a physical entity that is zero in the high symmetry phase and changes continuously to a finite value once the symmetry is lowered; in case of the paraelectric-ferroelectric transition this parameter is identified as the polarization P (Chandra & Littlewood 2007). Therefore in a ferroelectric presenting second order phase transition (in which then polarization changes continuously with temperature, but generally with a discontinuity of slope) the Curie and Curie-Weiss temperatures may be essentially identical, differently in first order (where P changes discontinuously) T_0 can be more than 10 °C lower than T_C.

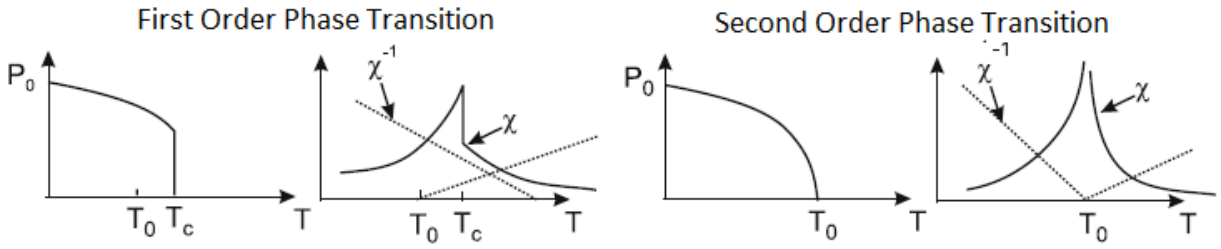

Figure 1.2: Variations of the spontaneous polarization, electric susceptibility and its inverse in first and second order ferroelectric transitions (Chandra & Littlewood 2007). The electric susceptibility is a dimensionless proportionality constant that indicates the degree of polarization of a dielectric material in response to an applied electric field. It is related to the dielectric constant as: $\chi_e = \varepsilon_r - 1$.

By figure 1.2 it is possible to notice the variation of the dielectric permittivity which shows high increase around T_C: in the second order phase transition, contrarily to the first , the peak is almost symmetric and affected by a discontinuity with a virtual infinity value corresponding to the Curie Point. Spontaneous polarization is also graphically presented as a function of the temperature. Above T_C, P_S is zero and only instantaneous randomly oriented dipoles exist. When a ferroelectric material is cooled through paraelectric-ferroelectric phase transition P_S appears and it is reoriented in some favourable directions imposed by the new structure. Usually polarization is not uniformly aligned throughout the whole crystal along the same direction, but rather the formation of domains

is favourite. These so called ferroelectric domains are zones separated by domain walls, characterized by different uniformly oriented P_S and formed to minimize the electrostatic energy of depolarizing fields and the elastic energy associated with mechanical constraints. Different directions of P_S in the neighboring domains form certain angles with each other (Sidorkin 2006), however, by applying an external electric field, it is possible to switch and reorient a large part of the polarization vectors in the direction of the field. Polarization switching, which is feasible only in ferroelectric materials, has a great application potential. The ferroelectric hysteresis loop, which can be obtained applying an electric field, is indeed an important phenomenon deeply exploited for example in memory devices. The described ferroelectric behaviour and the linked properties are found in a broad range of organic and inorganic materials with different natures as single crystals, bulk ceramics, thin films, polymer or liquid crystals presenting different structures which include for example perovskite type or tungsten-bronze-type (Xu 1991).

1.1.1 Ferroelectric and relaxor perovskites

In this section a briefly introduction to ferroelectric perovskites and especially a description of the link between structure and properties will be proposed. In these materials, considering only ferroelectric transition, a high symmetry cubic m3m prototype (paraelectric) could evolve to six different polar species by the classification of Shuvalov (Zheludev 1988) in table 1.3. Monoclinic and triclinic phases are then predicted to be feasible ferroelectric species from the perovskite m3m prototypic point symmetry. In ceramics however, even though permitted by symmetry and even if these states would be highly advantageous, no cases of transitions into monoclinic or triclinic symmetries have been reported (Cross 1993).

Phase	Symmetry	Polarization Components	Phase	Symmetry	Polarization Components
Cubic	m3m	$P_1 = P_2 = P_3 = 0$	Monoclinic	m	$P_1^2 \neq P_2^2 \neq 0\ P_3^2 = 0$
Tetragonal	4mm	$P_1^2 \neq 0\ P_2^2 = P_3^2 = 0$	Monoclinic	m	$P_1^2 = P_2^2 \neq 0\ P_3^2 \neq 0\ P_1^2 \neq P_3^2$
Orthorhombic	mm2	$P_1^2 = P_2^2 \neq 0\ P_3^2 = 0$	Triclinic	1	$P_1^2 \neq P_2^2 \neq P_3^2 \neq 0$
Rhombohedric	3m	$P_1^2 = P_2^2 = P_3^2 \neq 0$			

Table 1.3: Ferroelectric phase transitions possible from the cubic m3m prototype (Zheludev 1988).

As deducible the spontaneous polarization is then generated by a structural reorganization and then by displacements of certain ions (Zheludev 1971), indiscriminately for a first or second order phase transition. Specifically different mechanisms (here only the most commons are cited) are recognizable as causes of the P_S onset: for example an important role could be played by cation displacements within the BO_6 cage and or by oxygen octahedra distortions and tilts (Ortega SanMartin et al. 2004). These modifications are connected to the previously mentioned Goldshimdt factor t. When $t > 1$, the structure is imposed by the A-O distance and the B atom, which is too small for the oxygen octahedron, could be displaced developing a small polar distortion, as in $BaTiO_3$ (Chandra & Littlewood 2007). Conversely, when t is only slightly less than one, the A atom is small in comparison to the available space between the BO_6 polyhedra. Therefore at low temperature the net of orthogonal corner linked oxygen octahedra 'crumples' (Cross 1993). The octahedra remain corner linked, but adjacent octahedra must contra rotate relative to one another (as in $CaTiO_3$). Considering then the connection between the atomic arrangement and properties, it is clear how the control of the structure (transition, transition temperature, chemistry, size, defects *etc.*) leads to a control and improvements of the physical properties. Pure forms and, much more, tuned ferroelectric perovskite could be and are extremely functional in different technological fields. As an example they are largely used in many piezoelectric applications due to the high and efficient electromechanical transformation of energy and the relative signals which can be achieved. Another and probably the most important use exploits the high dielectric constant. This in fact supposes a high resistance to the passage of electric current under the action of the applied direct current voltage; thus ferroelectrics are then commonly inserted into capacitors allowing to

place conducting plates very close to one another without risk of contact. In addiction, considering that this kind of dielectrics are more resistant to ionization than air, a capacitor containing perovskites can be subjected to a higher voltage. In table 1.4 some examples of perovskite ferroelectrics are reported coupled with uses. Beyond their particular and attractive characteristics, decades of experience in the mass industrial production, reliability and low production cost make these materials as base for the majority of electronic applications (Heywang et al. 2008).

Material	Properties	Application
$BaTiO_3$	Dielectric	Capacitors, Sensors
$(Ba, Sr)TiO_3$	Pyroelectric	Pyroelectric sensors
$PbTiO_3$	Pyroelectric	Pyroelectric sensors
	Piezoelectric	Electromechanical transducers
$Pb(Zr, Ti)O_3$	Dielectric	Non volatile memories
	Pyroelectric	Pyroelectric sensors
	Piezoelectric	Electromechanical transducers
$(Pb, La)(Zr, Ti)O_3$	Pyroelectric	Pyroelectric sensors
	Electrooptic	Waveguides, optical displays
$LiNbO_3$	Piezoelectric	Surface acoustic waves
	Electrooptic	Optical modulators
$K(Ta, Nb)O_3$	Pyroelectric	Pyroelectric sensors
	Electrooptic	Waveguide devices
$Pb(Mg_{1/3}Nb_{2/3}Ti)O_3$	Dielectric	Capacitors, Memories

Table 1.4: Some compounds and their properties as ferroelectric materials by Moure et Pena (Moure & Pena 2015).

As shown in the table 1.4, doped perovskites are very popular and meet different technological requests. This is because chemical substitutions, according to the great flexibility of this structure (which allows to generate a lot of different compounds), are probably the simplest way to obtain tuned features and improved ferroelectric properties. For example in $AB^{'}B^{''}O_3$ the phase transition temperatures often change continuously with composition (Shvartsman & Lupascu 2012), then, by choosing the right doping type and amount it is possible to place transitions and the associated high permittivities at desired temperatures (Cross 1993). Incrementing more the substitution rate, also a variation from the conventional ferroelectric to a diffuse phase transition (DPT) behaviour could be achieved (Shvartsman & Lupascu 2012). This is characterized by an extending of the phase transition in a temperature interval around T_m (which is the temperature where ϵ assumes its maximum value) (Santos & Eiras 2001), then the related frequency independent permittivity peak becomes broader than that in classical ferroelectrics. This for instance guarantees to exploit high ϵ values in a wider range of temperatures, which is optimum for different applications which require flexibility in operating temperature. However when doping increases more a great compositional disorder is produced (*i.e.* in the arrangement of different ions on the crystallographically equivalent sites) and a deviation from diffuse phase transition to relaxor behaviour could occur (Bokov & Ye 2006). Relaxor ferroelectrics, also called relaxors, form a fascinating class among ferroelectrics, which has aroused a wide range of experimental and theoretical investigations (Laulhe et al. 2009). Macroscopically, the relaxor state is characterized by i) a strong frequency dependence of the permittivity below the maximum permittivity temperature T_m, ii) a shift of T_m towards higher values with increasing frequency and iii) deviations from the Curie-Weiss law in the paraelectric phase (Ye 2008). In other words the peak of the dielectric constant for relaxors is much broader in temperature than in conventional ferroelectrics and it is frequency dependent, moreover below the maximum of the permittivity most relaxors remain cubic and show no electric spontaneous polarization, so no structural transition takes place (Cowley et al. 2011). Differences between ferroelectric and relaxor state are reported schematically in

figure 1.3 by Samara *et al.* (Samara 2003).

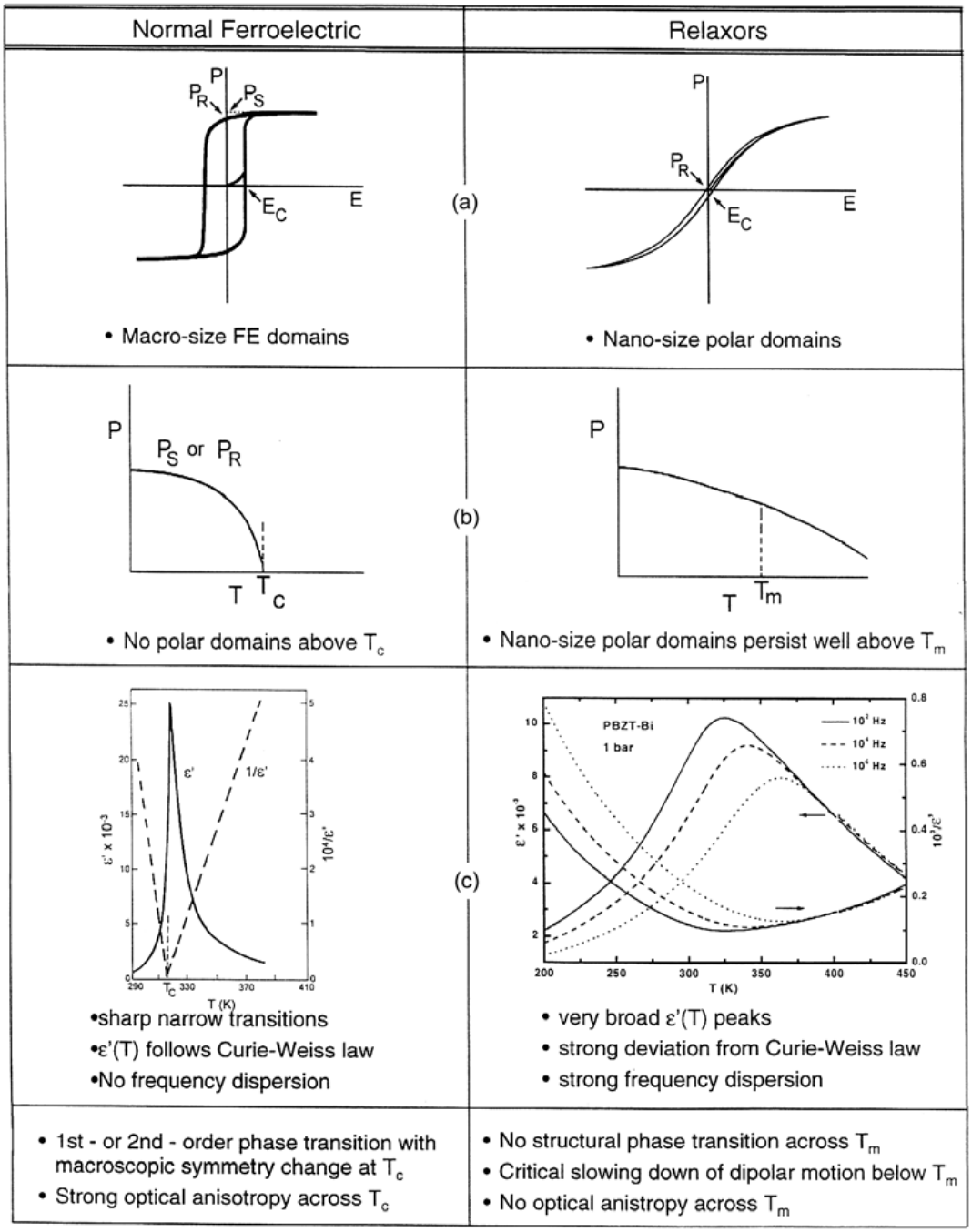

Figure 1.3: Comparison between the properties of normal ferroelectrics and relaxors (Samara 2003).

This kind of material was discovered in the 1950s, but many of their properties and their origin are not completely understood (Cowley et al. 2011). In the last two decades many efforts have been devoted to explore the physical nature of the ferroelectric-relaxor behavior (Xi et al. 1983), (Westphal et al. 1992), but the determination of their exact structural nature still represents an experimental challenge (Pasciak et al. 2007). In general, if present, the polarization arises from displacements of A and or B cations within their oxygen cages. In a classical ferroelectric, all the cation displacements share at least one common component, giving rise to a macroscopic polarization. Differently, in relaxors, the cation displacements are correlated or partially correlated on limited

length scales, typically 2-20 nm, leading to a null macroscopic polarization at all temperatures (Laulhe et al. 2009) and, structurally, to a retention of the higher symmetry of the parent paraelectric phase. These regions of locally correlated polarizations, randomly orientated, are named polar nanoregions (PNRs) and seem to be at basis of the relaxor behaviour. Despite no measurable residual polarization exists, the presence of PNRs is deducible by deviations of temperature dependences of the refractive index or by modification of thermal expansion coefficient from the behavior predicted for the paraelectric state (Shvartsman & Lupascu 2012). Different investigations have been carried out in order to understood the nature and development of PNRs. From the review of Shavartsma et Lupascu PNRs are predicted to appear at the Burns temperature (T_D), which is typically far above the maximum point of permittivity (T_m). Considering that the size of PNRs is related to diffuse scattering, experiments of total scattering on single crystals are useful to determine the evolution of these regions. For example investigating $PbMg_{1-x}Nb_xO_3$ these nanoregions have been studied and it was concluded that they grow from about 1.5 nm at T_D to $\sim$10 nm at 10 K (upon cooling). The most significant change of their size was observed around the freezing temperature T_f $\sim$210 K which coincides with those estimated from the analysis of the dynamic dielectric response of relaxors and corresponds to the slowing down of the relaxation related to the reorientation of PNRs. Practically their number shows a monotonic increase upon cooling, starting from T_D, and then an abrupt decrease at about T_f due to the merging of smaller PNRs into larger ones. This is associated to the freezing of the dipole dynamics and then to a large and wide peak in the temperature dependence of the dielectric constant with characteristic dispersion observed at all frequencies practically available for dielectric measurements (Bokov & Ye 2006). The microscopic origins of PNRs are closely related to the inherent structural inhomogeneities typical of relaxors. Classical examples are the solid solutions such as: $Bi_{2/3x}Sr_{1-x}TiO_3$ and $(Pb_{1x}La_{2/3x})(Zr_yTi_{1-y})O_3$ where A site substitutions occurs, $Pb(Sc_{1/2}Ta_{1/2})O_3$ and $Pb(B^{II}_{1/3}B^{V}_{2/3})O_3$ (where B^{II} = Mg, Co, Ni, Zn and B^{V} = Nb, Ta) (Dmowski et al. 2002) with B site doping (Heywang et al. 2008). In ferroelectric perovskites doped by homovalent B substitutions, as in $BaTi_{1-x}B^{IV}_xO_3$, larger substituent cations distort locally the lattice, but thank to their larger size they remain practically fixed and not displaced inside oxygen cage causing then a random breaking of the correlated displacement along B-O bond chains. If the doping amount is sufficiently high, these regions with an accumulated concentration of broken spatial correlation increase in size. Consequently, FE domains are less likely to nucleate, but due to the local distortions caused by cation substitutions, a redistribution of the charges and the formation of local charged centers results (DeLuca & Gajovic 2016). In these cases the relaxor behaviour is related to the size mismatch between the two B cations which then becomes the crucial structural element (Chen et al. 2000). For example, as in $BaTi_{1-x}Zr_xO_3$, it can be proposed that the large difference between different B ionic radii generates structural distortions, which then impede the long range ferroelectric arrangement of cations. However, the exact mechanism involved remains an open question (Farhi et al. 1999). Despite some uncertainties on the origin of the relaxor behaviour, their special properties make perovskite relaxors a material of choice for high-end industrial applications. For example they are widely utilized as actuator then to convert mechanical into electrical forms of energy and *vice versa* due to their high electrostrictive response or used in display or light valves for their large non linear optic effect (Uchino 1994). Furthermore thank to their very high permittivity and their temperature-insensitive characteristics (i.e., diffuse phase transition) relaxor are usually employed in compact chip capacitors (Uchino 2010). As previously discussed, ferroelectric perovskites are of a great practical importance because they have no substitutes for some key applications (pyroelectric devices and piezoelectric transducers/actuators). Unfortunately, most of the ceramics used in devices, such as $PbZr_xTi_{1-x}O_3$ (PZT), the most important commercial piezoelectric, contain lead. As well known Pb creates hazard during processing (lead volatilizes and is released into the atmosphere), limits applications (*e.g.* in vitro), and it is potentially environmentally toxic during disposal (Kumari et al. 2015). Lead materials are then dangerous and different regulations exist

to limit their use. By the 'Restriction of the Use of Certain Hazardous Substances in Electrical and Electronic Equipment (RoHS)' (2002/95/EC 2003), adopted by the European Parliament, the maximum allowed concentration of Pb is established to be 0.1 wt% in homogeneous materials for electrical and electronic equipment used in households as well as in industry. Currently it is not possible to adopt these rules in *toto* and some materials, as lead-containing ferroelectrics and relaxor, are for now exempt from the directive (Yasmin et al. 2011). However it becomes essential and necessary to discover, study, and use different compounds to provide for technological needs and at the same time to safeguard human health. $BaTiO_3$ and solid solution based on this perovskite have presently emerged as one the most promising candidates to replace toxic ferroelectric and relaxor lead containing materials.

1.2 $BaTiO_3$

$BaTiO_3$ is one of the most studied and famous perovskites since the 1940s when Wainer and Solomon in 1942 (Wainer & Salomon 1942) and then Wul and Goldman in 1945 (Wul & Goldman 1945) discovered its property of ferroelectricity. Thank to its simple crystal structure, high stability and extremely high dielectric constant, low leakage current and anisotropic optical behavior it finds large employment in many technological field (Yasmin et al. 2011). It is used in electro-optic, electromechanical and dielectric applications and it has become the basic capacitor material in semiconductor technology (Kingery et al. 1960) with a large commercial market as positive temperature coefficient resistors (PTCR) and multilayer capacitors (MLC) (Moulson & Herbert 2003). It is incorporated in actuators, sensors (Shrout & Zhang 2007) and in devices such as microphones, ultrasonic and underwater transducers, spark generators (Yasmin et al. 2011) and many others. This great interest in $BaTiO_3$ applications and consequent investigations on dielectric, ferroelectric and piezoelectric properties has furthermore generated extensive studies on structure and phase transitions (Jaffe & Cook 1971). Indeed the properties of this perovskite, as usual for all the materials, are linked to the atomic arrangement and its evolution.

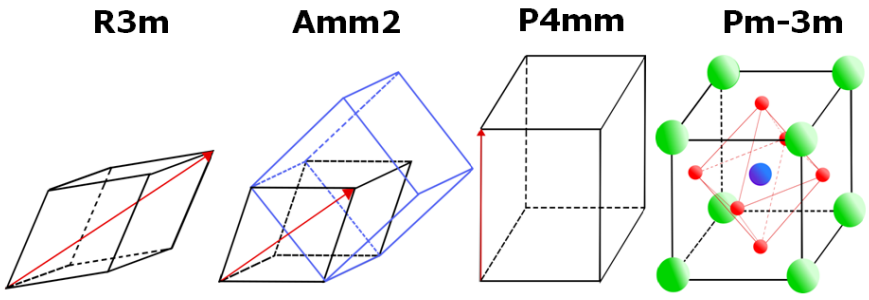

Figure 1.4: Schematic view of the structure of the different phases of $BaTiO_3$. The Ba ions are located at the corners, the Ti ions at the cell center, and the oxygen ions at the face centers. The arrows show the direction of the distortion which is equivalent to the direction of the polarization along the cubic [001] direction for the tetragonal phase, the [011] direction for the orthorhombic phase (the A-centered orthorhombic cell used to describe the structure is superimposed), and the [111] direction for the rhombohedric phase. The deformations in the ferroelectric structures are exaggerated for the sake of clarity (Kwei et al. 1993).

The paraelectric phase presents cubic structure (Pm-3m) whit a cell parameters around 4 Å and one formula unit per cell. Atoms are all in special positions. Assuming A atom as the origin 0,0,0, B cation is placed in 1/2, 1/2, 1/2, at the center of the cell, and oxygens occupy the center of each face with these fractional coordinates: 1/2, 1/2, 0; 1/2, 0, 1/2 and 0, 1/2, 1/2. In this configuration O ions form a regular octahedron in which Ti cation is placed perfectly in the middle. The octahedra are linked by their verticies and form a space structure in which large cavities are occupied by the A atoms. Each barium is surrounded by 12 equidistant oxygen atoms; so each O has two B type and four A type nearest neighbors. From this structure several successive ferroelectric phase transitions occur

with temperature decrease, schematically reported in figure1.4 underlining the distortion directions. At 393 K (Curie point) $BaTiO_3$ undergoes a transition from paraelectric to a tetragonal ferroelectric structure caused by the elongation of the cubic unit cell along the direction [001]. The new phase presents a non-centrosymmetric space group: P4mm with again one formula unit. B atom and oxygens acquire new freedom in movement and they are displaced by an amount of Δc along fourfold axis, which is the polar axis. The transition to the orthorhombic phase appears at 278 K. This structure can be interpreted as a slightly distorted cubic structure, obtained by stretching it along one face diagonal and compressing it along the other diagonal. Choosing the space group Amm2, the use of two formula units is mandatory. In this configuration cell is face centered and a twofold axis coincides with the c axis. Below 183 K barium titanate becomes rhombohedric, belonging to R3m space group, formed by stretching the original cube along one of its body diagonals [111]. This elongation causes atomic displacements along this direction which also coincides with the new spontaneous polarization orientation (Zheludev 1971). At this point it is clear that polarity is caused by ion displacements, in particular by the off-center displacement of Ti, which creates an electric dipole moments and then a spontaneous polarization. This results from the summation of the electric moments of all the charges. Therefore all atoms in a structure give their contribution and the ferroelectric state appears only when the long range forces due to the dipole-dipole interaction overcome the short range forces due to the Coulomb repulsions (Cochran 1986). In $BaTiO_3$ Cohen proposed as the origin of this phenomenon the hybridization between Ti 3d state and O 2p state (Ti 3d-O 2p), which weakens the short range force of the Coulomb repulsions between Ti and O ions (Cohen 1992) and determines the appearance of Ti ion displacement (Miura et al. 2011). Different authors agree on this last point recognizing Ti off-center as the dominant cause in ferroelectric onset. However some different interpretations exist depending on the nature of the phase transitions, which are still debated. Cochran (Cochran 1986) proposed a displacive phase transition model based on the soft-mode mechanism where the titanium atoms are displaced in the [111], [011], and [001] directions in the rhombohedric, orthorhombic, and tetragonal phases, respectively; in contrast, they sit in the middle of the TiO_6 octahedron in the cubic phase, leading to a centrosymmetric structure. Differently, other researches have introduced also an involvement of order-disorder component (Comes et al. 1970), (Muller & Berlinger 1986), (Muller et al. 1987). In this model titanium atoms are displaced along one of the eight [111] directions in all crystal phases and the correlation between these local displacements changes with temperature. These occur along one, two, four [111] directions in the rhombohedric, orthorhombic and tetragonal phases, respectively (Rabuffetti et al. 2014). Conversely in the cubic structure it was assumed that Ti atoms perform hopping between the eight equivalent [111] off-centered sites (Chaves et al. 1977). This order-disorder model has been supported by EXAFS results (Ravel et al. 1998) and also by theoretical calculations (Girshberg & Yacoby 2001). According to this view as the temperature increases the sequence of phase transitions is explained by a disordering of domains wherein the local structural environment remains approximately rhombohedrally distorted at all temperatures around both metal sites. As the temperature is raised, the long range correlations between these local distortions change, resulting in the observed sequence of phase transitions (Ravel et al. 1998). More in detail: the order-disorder component of phase transitions in $BaTiO_3$ consists of local displacements from cubic symmetry of constant magnitude that partially lose long range correlations, while the displacive component consists of reorientation of these displacements (Stern 2004) (Belushkin et al. 2006). In figure 1.5 (Fu & Itoh 2015) structural transitions (described by the simpler displacive model) are related to the evolution of the permittivity as a function of the temperature. As described above, $BaTiO_3$ could be a very useful material, but unfortunately its pure form does not have ideal properties for some industrial applications. For example the temperature dependence of permittivity is too large for capacitor applications (Li et al. 2005). In order to have similar performances as many Pb-based electroceramics, it is necessary to tune this material for example controlling microstructural characteristics (porosity level, grain size, secondary phases, core-shell

structures, *etc.*) and or changing its composition producing $BaTiO_3$ based solid solutions (Ciomaga et al. 2007).

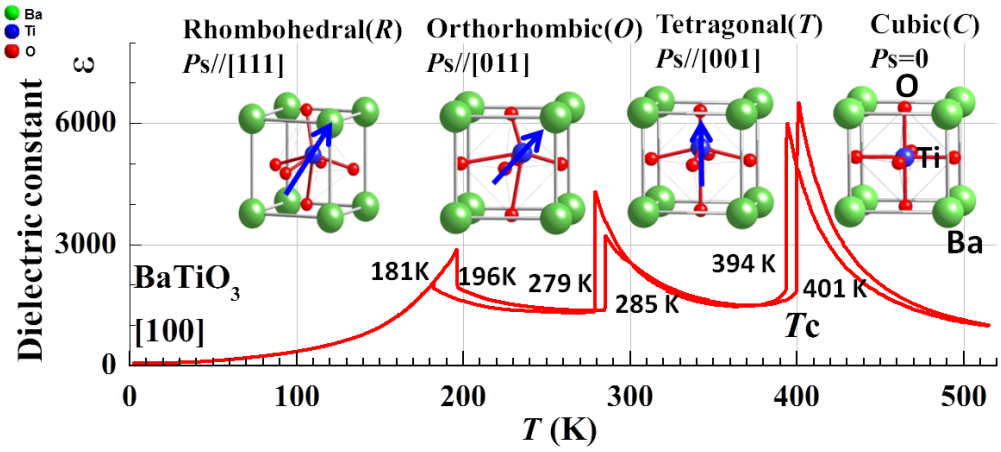

Figure 1.5: Change with temperature of the dielectric permittivity of a $BaTiO_3$ single crystal. The schematics of Ti displacement in the oxygen octahedron of the perovskite structure are also shown (Fu & Itoh 2015).

1.2.1 $BaTiO_3$: doping effect

In ABO_3 compounds chemical doping is commonly used to manipulate and control the electrical and electromechanical behavior (Caviglia et al. 2008) (Ohta et al. 2007), change physical properties such as the Curie temperature and domain switching (Jeon 2004) (Hagemann & Hennings 1981), tune the band gap of the host material (Upadhyay et al. 2011), enhance or suppress oxygen vacancies formation and conductivity (Metzmacher & Albertsen 2001) (Honda et al. 2011) and, more recently, to optimize the electrochemical or catalytic activity of the host material (Suntivich, May, Gasteiger, Goodenough & Shao-Horn 2011) (Suntivich, Gasteiger, Yabuuchi, Nakanishi, Goodenough & Shao-Horn 2011). In barium titanate chemical substitutions at the Ba^{2+} and Ti^{4+} sites are indeed usually made to tailor the properties and meet a variety of device and performance requirements (Maiti et al. 2008). The dielectric and semiconducting properties can be modified by additions of various ions, especially those which dissolve in the $BaTiO_3$ matrix (Makovec et al. 1996). In this way it is possible for example to shift ferroelectric-paraelectric transition below the room temperature as the concentration of additives is increased (Sen & Choudhary 2005). Considering that it is possible to replace A and or B cations by homovalent or heterovalent substitutions, the number of the possible solid solutions is very big. However in this work just homovalent substitution at Ti site will be taken into account. This kind of doping, depending on the nature of individual ions, could lead to changes in the lattice parameters and consequent changes in the Curie temperature, in elastic or electrical properties, *etc.* (Hong et al. 2016). Compositions modified by Sn, Hf, Ce, Y and Zr (Payne & Tennery 1965) (Jing et al. 1998) (Yu et al. 2007) have been extensively studied especially for their possible dielectric application. For example a slight substantial replacement of Ti^{4+} by any of the three ions Zr^{4+}, Sn^{4+} or Hf^{4+} causes a rise in the orthorhombic tetragonal transition temperature; differently higher amount generated a depression of the T_C below 300 K (Jaffe & Cook 1971). Increasing doping a crossover from typical ferroelectric to ferroelectric-relaxor behavior occurs (Zaghete et al. 2011). This is the case of $BaTi_{1-x}Zr_xO_3$ (BZT) system, which is for sure one of the first $BaTiO_3$ based solid solution studied for its temperature dependence of the dielectric permittivity and relaxor behaviour (Ravez & Simon 1997a) (Ravez & Simon 1997b) (Farhi et al. 1999). Different investigations have examined BZT polar behaviour as a function of doping amount (Neirman 1988) (Hennings et al. 1982) (Buscaglia et al. 2014). Between 0-15% of zirconium the material shows a normal ferroelectric behaviour, with doping increase (15% < Zr < 30%) BTZ presents a diffuse phase transition and at the end by substitution > 30% a crossover

to relaxor behaviour occurs. A summary of transitions which occur as a function of the doping in BTZ are reported in figure 1.6. As $BaTi_{1x}Zr_xO_3$ also rare earth doped $BaTiO_3$ shows a number of important features exploitable in dielectric devices: the incorporation of rare earth cations indeed allows to have a great control on conductivity and also on electrical degradation (Jonker 1964) (Kishi et al. 1999).

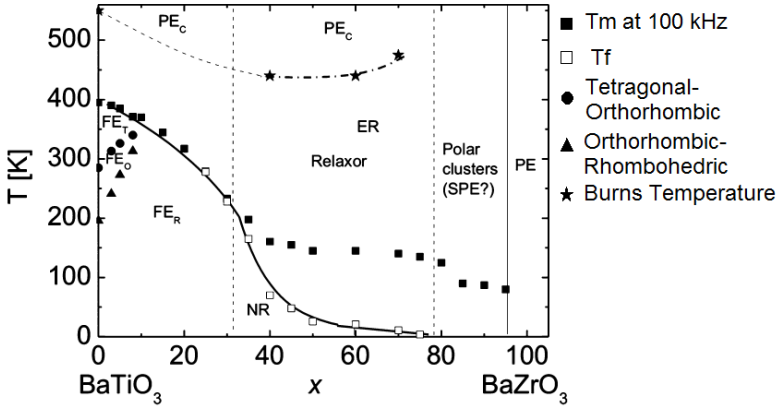

Figure 1.6: Phase diagram of the $(1-x)BaTiO_3$-$(x)BaZrO_3$ system, polar behaviours as a function of composition are specified. Transition temperatures were determined based on the dielectric permittivity measurements (Shvartsman & Lupascu 2012).

1.2.2 $BaTiO_3$: size effect

Nowadays nano material and then nanostructuring are required in microelectronics due to the current tendency in miniaturization which moreover imposes stringent conditions on processing and has a deep impact on functional properties (Alguero et al. 2016). Unfortunately, demanding advances in nano-science and technology have revealed a so called size effect in perovskite type oxides which consists in a disappearance of ferroelectricity under a critical grain size (Nuraje & Su 2013). In the previous section it has been reported that ferroelectricity appears as a collective phenomenon, arising from the competition between short range covalent repulsions and long range Coulomb interactions. As going down from the bulk to the nanoscale, these interactions will be modified and it is therefore expected that the physical properties of nano perovskite ferroelectric will be strongly affected by the electromechanical boundary conditions (*e.g.* surface charge, misfit epitaxial strain and inhomogeneous effects, particularly strain gradients) (Zhu & Liu 2011). The exact origin for this size effect is still not established. By a classical phenomenological thermodynamic theory (Landau Ginzburg Devonshire approach) this could be caused by an intrinsic nature of the nanoparticles smaller than a certain critical size, the effect could be then viewed as a phase transition from a ferroelectric to a paraelectric state taking place at a critical system size (Lin et al. 2006). A different interpretation considers, instead, the impurity surface ions, structural imperfections such as oxygen vacancies, dislocations, disorder *etc.*, as the causes of a local depolarization field which prevents the formation of the ferroelectric phases (Gerra et al. 2006). However this decrease of the ferroelectric response due to the reduced particles size provokes a suppression of the dielectric and piezoelectric coefficients, which could present changes up to 80 % if compared to their bulk counterparts. In figure 1.7 effects of reduced size is reported for different perovskites. Therefore a good compromise must be achieved between industrial requests, as miniaturization, and the decline of material properties due the size reduction. For example in $BaTiO_3$ ceramic the maximum permittivity at room temperature (5000-6000) is determined for a grain size around 1 μm, below this limit a progressive suppression of the spontaneous polarization and a reduction in the dielectric constant are observed (Petkov et al. 2008). This size is however too big for some new technological needs as multi layer capacitor with reduced dielectric layer thicknesses (even < 1 μm). Thus this demand and the obligation to provide good dielectric

and mechanical performances (reachable maintaining several grains, typically 5-6, spanning the thickness of the dielectric) lead to a grain perovskite size around 100 nm (Ihlefeld et al. 2016).

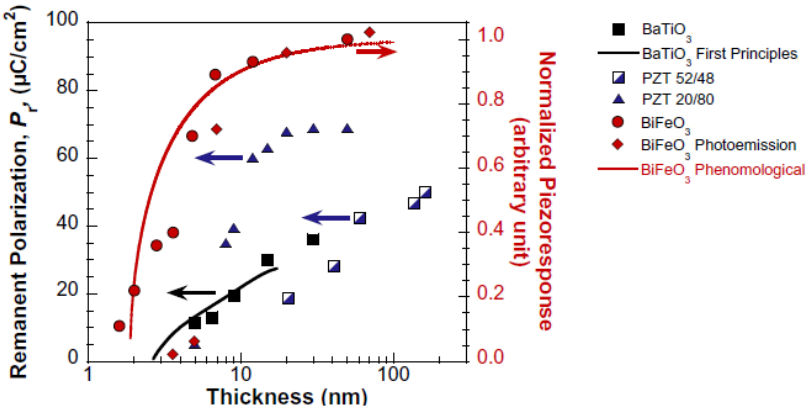

Figure 1.7: Remanant polarization (left axis) for $BaTiO_3$ and $PbZr1-xTi_xO_3$ (with two composition) and normalized piezoresponse and polarization measured using photoemission (right) for $BiFeO_3$ thin epitaxial films with decreasing film thickness. The lines are theoretical calculations of polarization for $BaTiO_3$ (from first principles) and $BiFeO_3$ (phenomological model). All systems show similar response saturation at large thicknesses (> 50 nm), with greatly reduced response at < 10 nm (Ihlefeld et al. 2016).

Neglecting a deep discussion on the implication of size reduction on the $BaTiO_3$ dielectric properties, the attention will be paid on ferroelectric response and structural evolution linked to the so called size effect. As well known and also reported in this section, the spontaneous polarization could not exist in centrosymmetric structures. This practically means that ferroelectricity in nano size $BaTiO_3$ is limited by the stability of the cubic phase, which is in turn dependent by temperature and grain size. In $BaTiO_3$ films, the lower limit for ferroelectricity at room temperature has been reported by various authors to range from 7 unit cells (2.8 nm) (Wen et al. 2013), (Soni et al. 2014) down to 4 unit cells (1.6 nm) (Tenne et al. 2009). Differently, for nanocrystals, ferroelectric phase stability is lost at dimensions that are comparatively larger than in semi-infinite thin films. Originally this limit was determined to be around 100 nm (Uchino et al. 1989), but recently, also thank to high resolution data and Raman experiments, a stability of the tetragonal phase has been proved in nano powders as small as 40 nm (Yashima & Ali 2009). However if even an average cubic structure is considered different authors agree about a local disorder nature of these nano powders. Indeed Yoneda *et al.* and also Page *et al.*, (Page et al. 2010), report that cubic nano $BaTiO_3$ presents local tetragonal distortions which are correlated only over distances of short range order (Yoneda et al. 2013). By EXAFS (Extended X ray Absorption Fine Structure) and XANES (X-ray Absorption Near Edge Structure) analysis Frenkel *et al.* find a local titanium displacements in contrast to the cubic macroscopic crystal structures (Frenkel et al. 1999). Results of Petkov *et al.* clearly show that TiO_6 octahedra are always distorted in submicron and nano sized samples and the material preserves its tetragonal type lattice atomic ordering within at least 3 unit cells. This distortion (*i.e.* the increased displacement in the centers of the positive and negative charges) should result in an enhancement of their local dipole moment, but this is not translated on average into an enhancement of the net spontaneous polarization (Petkov et al. 2008). Increased distortions have been detected with decreasing of particle size, albeit in conjunction with a tendency to a cubic average structure (Smith et al. 2008). At the end nano size provokes deep local distortions which though progressively lose their long-range order reducing the length of structural coherence and resulting in an average deterioration of the spontaneous polarization (Petkov et al. 2008). As evidenced in this section just few information are available on barium titanate nano powders, and even less are reachable about nano solid solutions with B type substitution.

1.3 $BaTi_{1-x}Ce_xO_3$ system

Recently, among BT based ferroelectric relaxors, Ce doped $BaTiO_3$ (BTC) has received much attention especially for its technological application (Makovec et al. 1996) (Ianculescu et al. 2016): for example as multilayer ceramic capacitors with high capacitance (Park & Kim 1995). This material compared with lead-based relaxor, has different advantages as: simple composition, high flexural strength, excellent DC bias characteristics resulting from grain size refinement; moreover the dielectric constant *versus* temperature ratio is easily controlled by the amount of cerium used and it presents an excellent sinterability, reproducibility and simple manufacturing process (Park & Kim 1997). In principle Ce can exist in two oxidation states, Ce^{4+} and Ce^{3+}, then when it is introduced in $BaTiO_3$ it should be incorporated into the Ba^{2+} or and in Ti^{4+} site (Hwang & Han 2000). This depends by the ionic radii of the ions involved, then Ce^{4+} should enter in $BaTiO_3$ at Ti site, while Ce^{3+} should exchange with Ba acting as donor dopant (Ianculescu et al. 2016). The oxidation state of the cerium ions and the resulting compound are linked to the synthesis and sintering parameters and the precursor starting formula (Curecheriu et al. 2013). If samples are sintered in a reducing atmosphere Ce is incorporated into the $BaTiO_3$ lattice as Ce^{3+} independent of the starting compositions, instead when sintered in air, Ce may be incorporated as Ce^{4+} at the Ti sites as well as Ce^{3+} at the Ba sites. Depending on the starting formula this substitution could be better control. Indeed in air, in order to obtain a product as $BaTi_{1-x}Ce_xO_3$, an excess of BaO (BaO > TiO_2) is required, if the two amount are comparable Ce could be enter in both Ba and Ti site, instead an excess of TiO_2 leads to an incorporation of Ce^{3+} in Ba site (Makovec et al. 1996). The two solid solutions $Ba_{1-x}Ce_xTiO_3$ and $BaTi_{1-x}Ce_xO_3$ are different not only in composition, but especially they present different tendencies of the dielectric constant as a function of doping type and amount.

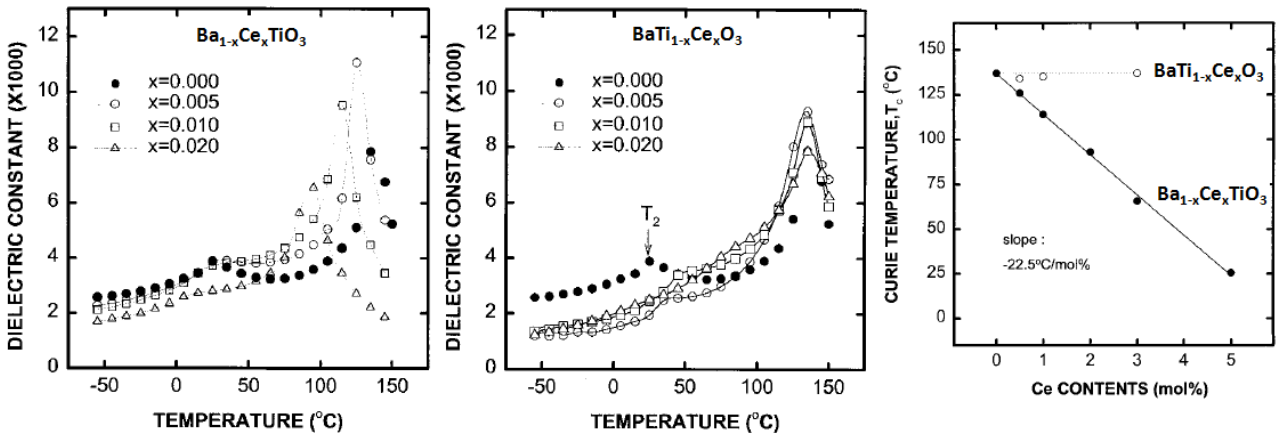

Figure 1.8: Temperature dependence of dielectric constant of $Ba_{1-x}Ce_xTiO_3$ (x = 0.005, 0.01, 0.02) compared with that of $BaTi_{1-x}Ce_xO_3$ (x= 0.005,0.01, 0.03). T_2 is the ferroelectric transition temperature from orthorhombic to tetragonal. Also Curie temperature variation versus amount of Ce added is shown on the right side (filled circles represent $Ba_{1-x}Ce_xTiO_3$ systems; open circles denote $BaTi_{1-x}Ce_xO_3$ systems (Hwang & Han 2001)

As reported in figure 1.8, by a slight doping between 0 and 2%, the Curie temperature in $Ba_{1-x}Ce_xTiO_3$ decreases of 22.5 °C/mol%, instead the composition $BaTi_{1-x}Ce_xO_3$ shows almost the same T_C as the pure $BaTiO_3$ and at the same time a shift to higher temperatures for the orthorhombic/tetragonal transition (Hwang & Han 2001). Taking into account the effect of larger doping amounts a systematic decrease of the Curie temperature is observable for $Ba_{1-x}Ce_xTiO_3$, instead $BaTi_{1-x}Ce_xO_3$ (BTC) shows an evolution of the ferroelectric behaviour (Curecheriu et al. 2016). Focusing on $BaTi_{1-x}Ce_xO_3$ a description of the changes relative to cerium abundance will be given starting to the small amounts up to reach 30%. Indeed the solid solution limit is de-

termined at 34% of cerium, over this point the system shows a biphasic feature (Lu et al. 2012). As mentioned in slightly doped BTCs transitions upon cooling occur similarly to those in pure barium titanate: cubic structure symmetry moves to tetragonal, orthorhombic and then rhombohedric (Ang et al. 2002b). If doping is between 0 and 2% cubic-tetragonal transition occurs at temperature similar to that in pure barium titanate, but if $BaCeO_3$ in $BaTiO_3$ reaches 5 mol % the Curie temperature starts to lower from 393.15 K to 385.15 K (Baxter et al. 1959). As cerium increases T_C shifts more to lower values (Issa et al. 1983), while the temperatures of tetragonal-orthorhombic and orthorhombic-tetragonal increase. In general T_C shifts slowly towards lower temperatures with a rate of about -7° C/at% (Jing et al. 2003) or of -3° C/at% (Ya-min et al. 2006) up to be even depressed to below room temperature for sufficiently higher Ce concentrations (Dughaish & Issa 2008). As an example at 300 K the tetragonal symmetry is stable for composition with x=0.02, while when cerium increases to x= 0.06 cubic phase is stabilized and an increment in unit cell is determined (Jing et al. 2003). With cerium > 10% paraelectric-ferroelectric and the tetragonal-orthorhombic and orthorhombic-tetragonal transitions merge in a so called pinched transition or diffuse phase transition (DPT) (Maiti et al. 2008). The system then directly transforms from the cubic paraelectric to the rhombohedric ferroelectric state. The corresponding peak of ϵ_r is usually much broader than in pure barium titanate, however, without the frequency shift of T_m typical of relaxors (Shvartsman & Lupascu 2012). The crossover to the relaxor behaviour occurs with 30% of cerium. An example of dielectric measurements performed by Ang *et al.* are summarized in figure 1.9, here a transition from classical to ferroelectric behaviour via DPT is linked to cerium amounts, but unfortunately results have been obtained at fixed frequency (Ang et al. 2002b). In order to better appraise the trend of the dielectric constant and its frequency dependence (which is the most important indicator of relaxation) figure 1.10 by Curecheriu *et al.* is also presented. They confirm a broad dependence of ϵ_r with the temperature for $0.1 \leq x \leq 0.3$ and a variation in frequency dependence up to a complete relaxor behaviour at $x \geq 0.3$. This is also confirmed by the polarisation-electric field loops which present a gradual reduction of the hysteretic nature of P(E) curves and a diminishing of the saturation polarization with increasing Ce addition.

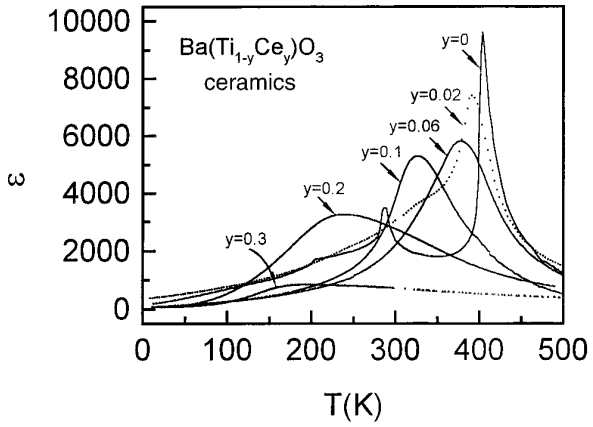

Figure 1.9: Temperature dependence of the dielectric constant ϵ of the $Ba(Ti_{1-x}Ce_x)O_3$ ceramics with x = 0, 0.02, 0.06, 0.1, 0.2, and 0.3 at 10 kHz (Ang et al. 2002b).

The described changes in polar behaviour, and especially the crossover to relaxor behaviour, seems to be related to the different size of the two B cations. Indeed high cerium introduction seems to provoke local distortions of the BO_6 octahedra disrupting the long range ferroelectric order (Curecheriu et al. 2013). However the exact connection of the evolution of the structure and properties as a function of temperature and cerium is rather vague. In fact in one hand this link is rather clear for the average structure, but on the other more studies are necessary to understand better the implications of the local structure, defects and local disorder, caused by cerium, on the

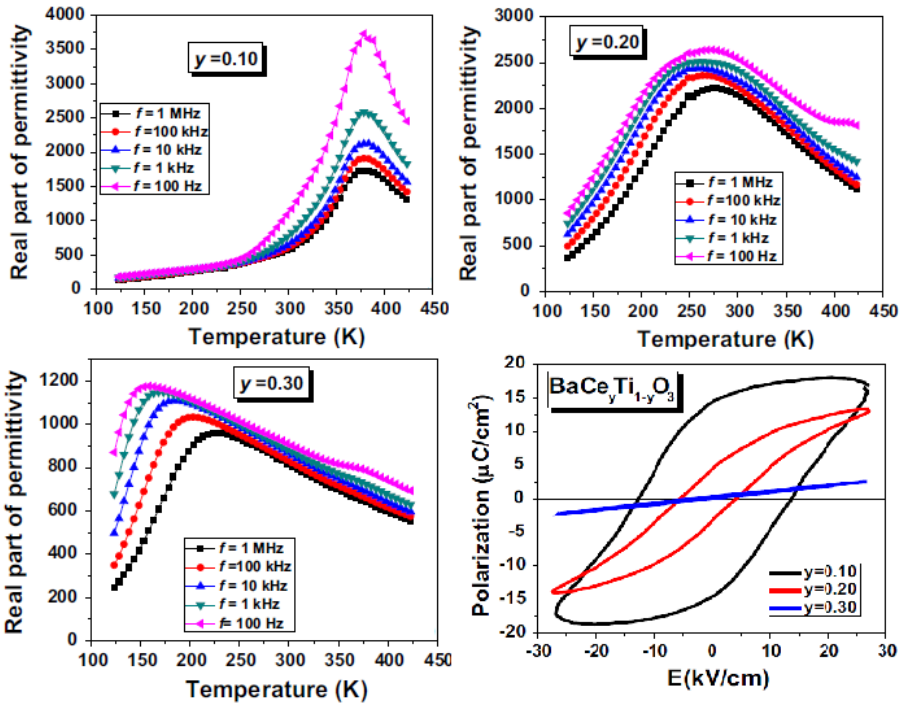

Figure 1.10: Temperature dependence of dielectric constant in $BaTi_{1-x}Ce_xO_3$ x=0.1, 0.2, 0.3, also polarisation-electric field hysteresis loops for the three ceramics at room temperature are reported (Curecheriu et al. 2016).

properties of this material. Moreover no information is available on the size effect then no indications on the structural and polar variations as a function of the grain size are available. The similarity to the BTO doped with Zr suggests that the Ce modified compositions may be promising as lead free actuator materials (Ang et al. 2002b), thus it becomes very important to increase knowledge on this material and investigate in details its polar and structural evolution as a function of doping and grain size.

Chapter 2

Total scattering and PDF

For few years new materials and complex compounds, required in many technological fields, have issued challenges not only in synthesis and in production, but also in structural characterization. Indeed many of these materials owe their interesting properties to defects (as compositional heterogeneity, vacancies, charge defect and so on) then most to the local structural order rather than to the long range lattice structure (Egami 2002). In this light it is necessary to acquire a knowledge of the 'true' local atomic arrangement in order to have a complete structural picture and to understand the linked properties (Proffen 2006). Powder diffraction technique is well known as a typical tool to study crystalline materials. Traditionally only Bragg scattering is collected and analysed (Billinge 2004), but unfortunately this gives only a spatially averaged description of the structure. The information regarding the correlation among the local variations is lost as soon as the assumption of perfect periodicity is made (Egami 2002), then this approach is completely blind to the local information as disorder. This is in fact contained in the so called diffuse scattering which is usually neglected in classical experiments. The name diffuse comes from the nature of this scattering which is not canalized at discrete and precise 2θ angles, but it is distributed around Bragg peaks and dispersed at the background level. Different to the traditional one, total scattering experiments consist in a voluntary collection of both diffuse and Bragg scattering and Pair Distribution Function (PDF) is an excellent way to analyse this kind of data. PDF allows to explore also local structure giving a correct representation of

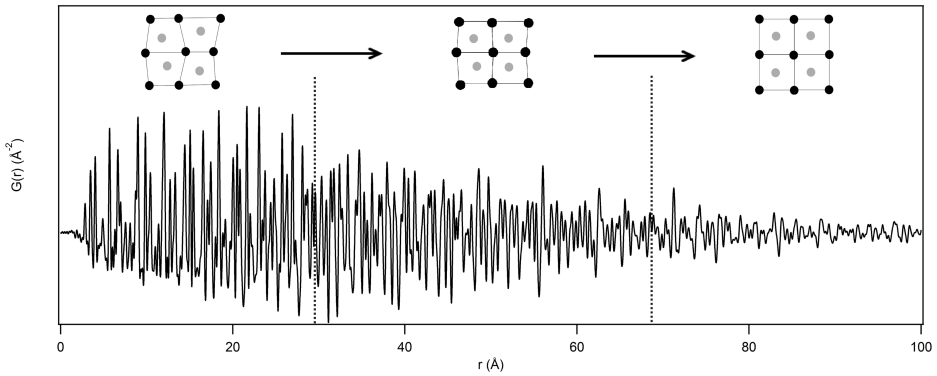

Figure 2.1: PDF analysis at different length scales in G(r) reveals disorder on the local structure which is gradually averaged as radius range increases up to give an average order cubic structure. These sketch shows the potential of the Pair Distribution Function investigation which allows to study structure at different length scales simply choosing adequate radius ranges (in figure delimited by dashed lines) in which perform refinements.

correlation among the local variations and then a description of the generated disorder. For many years it has been used to study very disordered materials as amorphouses and liquids, but more recently it has also been applied to the quantitative study of disorder in crystalline materials (Billinge 2004). PDF takes advantage of the Fourier

relationship between measurable diffraction intensities and the real space arrangement of pairs of atoms (Billinge & Kanatzidis 2004). This function gives the probability of finding an atom at a given distance r from another atom (Egami 2003), in other words the peak position in the function indicates the existence of a pair of atoms with that separation. Practically its analysis, by refinements, provides information about atomic arrangements. Furthermore, thank to the different length scales which could be investigated, characterization on both the average and local structure is obtainable giving a complete description of the material, as deducible by figure 2.1. PDF is then very flexibly, it could be employed to study a huge variety of materials as liquids, disorder and nano crystal and it is an amazing technique to reach structural knowledge at any length scale. In this chapter an overview on technique is presented. Note that in this dissertation just X ray has been considered as a radiation and the possible use of neutron or electron has been omitted.

2.1 Derivation of Pair Distribution Function

Treatise here presented is mostly a simplified summary of the mathematical description reachable in *'Underneath the Bragg peaks'* (Egami 2003). In order to introduce the mathematical derivation of PDF and then to explain its self, it is essential to start from the beginning. Specifically from a diffraction experiment where an X ray radiation (or neutron wave as well as an electron beam) hits a material. The answer to this interaction is an intensity scattered from the sample describable as:

$$I_T = I_C + I_{IC} + I_{MC} + I_{BG} \tag{2.1}$$

The total scattering intensity I_T is then a sum of different contributions: coherent I_C and incoherent I_{IC} scattering intensity, multiple scattering intensity I_{MC} and the background I_{BG} . The detection and then the quantification of the coherent intensity is the aim of any diffraction investigation because this variable is deeply linked to the sample atomic structure. In order to understand the importance of scattered intensity it is now useful to describe the interaction process defining first the incident radiation by a general wave equation:

$$\phi_{\vec{k}_{init}}(\vec{r}) = e^{i\vec{k}_{init}\vec{r}} \tag{2.2}$$

and in the same way the scattered one:

$$\chi_{\vec{k}_{final}}(\vec{r}) = Ae^{i\vec{k}_{final}\vec{r}} \tag{2.3}$$

where $\vec{k}_{init}$ and $\vec{k}_{final}$ are wavevectors (momenta) of the incident and scattered wave; notice that wave described in equation 2.3 has the wavevector with the same magnitude of incident one, but different direction and obviously different phase. When the incident wave reaches the sample and then the atom υ in a position described by $\vec{R}_\upsilon$, the amplitude is:

$$\phi_{\vec{k}_{init}}(\vec{R}_\upsilon) = e^{i\vec{k}_{init}\vec{R}_\upsilon} \tag{2.4}$$

After this interaction a scattered wave is generated. The ratio between the amplitudes of the incident and scattered waves is determined by the nature of the scatterer, and it is independent of the position of the scatterer so $\chi_{\vec{k}_{final}}(\vec{R}_\upsilon) = B\phi_{\vec{k}_{init}}(\vec{R}_\upsilon)$ and $Ae^{i\vec{k}_{final}\vec{R}_\upsilon} = Be^{i\vec{k}_{init}\vec{R}_\upsilon}$. Therefore:

$$A = Be^{i(\vec{k}_{init}-\vec{k}_{final})\vec{R}_\upsilon} \tag{2.5}$$

Expressing B by an absolute value B_0 and phase δ, as $A = Be^{i(\vec{k}_{init}-\vec{k}_{final})\vec{R}_\upsilon+i\delta}$, the scattered wave is now rewritten as:

$$\chi_{\vec{k}_{final}}(\vec{r}) = B_0 e^{i[(\vec{k}_{init}-\vec{k}_{final})\vec{R}_\upsilon+\delta+\vec{k}_{final}\vec{r}]} \tag{2.6}$$

Scattering vector is defined by the difference between initial and final momentum:

$$\vec{Q} = \vec{k}_{init} - \vec{k}_{final} \tag{2.7}$$

and in case of diffraction, being an elastic interaction, the equation 2.7 is also expressible as:

$$Q = \left|\vec{Q}\right| = (4\pi/\lambda)sin\theta \tag{2.8}$$

where 2θ is the scattering angle and λ is the wavelength. Considering the definition of Q just presented and the equation 2.6, scattered wave is represented dividing two different components:

$$\chi_{\vec{k}_{final}}(\vec{r}) = \Psi(\vec{Q})\chi_0(\vec{r}) \tag{2.9}$$

where $\Psi(\vec{Q}) = e^{i\vec{Q}\vec{R}_\upsilon}$ and $\chi_0(\vec{r}) = B_0 e^{i\delta} e^{i\vec{k}_{final}\vec{r}}$.
Now, taking in to account the amplitudes of all waves scattered by each atoms and summing over υ, we obtain the total scattering amplitude:

$$\Psi(\vec{Q}) = \frac{1}{\langle f\rangle}\sum_\upsilon f_\upsilon e^{i\vec{Q}\vec{R}_\upsilon} \tag{2.10}$$

f represents the scattering length of the atom υ, while $\langle f\rangle$ is the compositional average of the sample scattering length, in other words these terms hold the chemical information of the atoms. Differently to the coherent neutron scattering length b which replaces f if neutron scattering is considered, the scattering length of the atom f is Q dependent and related to the atomic number of the elements. The total scattering amplitude, which is a measure of the fraction of the incident wave scattered in a spatial angle element in a given direction, it is then a container of chemical information, but not only. In fact $\Psi(\vec{Q})$ is the Fourier transform of the electron density function, so this equation, in particular the phase of the exponential factor, contains also the information necessary to determine the atomic positions. It is then clear why the scattering amplitude is considered as the real heart of any diffraction investigation being the bearer of structural information. Therefore it would be sufficient to measure this quantity to define directly any crystal structure, but unfortunately this is not possible. The only quantifiable variable, detectable during an experiment, is in fact the intensity of the diffracted beam, which is regardless linked to the

scattering amplitude by the underlying relation:

$$\frac{d\sigma_C(\vec{Q})}{d\Omega} = \frac{\langle f \rangle^2}{N} \left| \Psi(\vec{Q}) \right|^2 \tag{2.11}$$

This equation shows the connection between the coherent scattering cross section $\frac{d\sigma_C(\vec{Q})}{d\Omega}$, or more simply the coherent diffracted intensity, and the square of the magnitude of $\Psi(\vec{Q})$. Despite the well known phase problem, whose explanation is here omitted, it is clear how the modulus of the scattering amplitude could be deduced from a collected intensity.
Using the definition of the total scattering amplitude (2.10), the cross section could be now defined making some terms explicit:

$$\frac{d\sigma_C(\vec{Q})}{d\Omega} = \frac{\langle f \rangle^2}{N} \left| \Psi(\vec{Q}) \right|^2 = \frac{1}{N} \sum_{\upsilon,\mu} f_\upsilon f_\mu e^{i\vec{Q}(\vec{R}_\upsilon - \vec{R}_\mu)} \tag{2.12}$$

The so called total scattering structure function, or often just structure function, which depends only on the arrangement of atoms is represented by:

$$S(\vec{Q}) = \sum_{\upsilon,\mu} e^{i\vec{Q}(\vec{R}_\upsilon - \vec{R}_\mu)} \tag{2.13}$$

Then:

$$S(\vec{Q}) \sim \frac{1}{\langle f \rangle^2} \frac{d\sigma_C(\vec{Q})}{d\Omega} \tag{2.14}$$

Considering that $I(\vec{Q}) = \frac{d\sigma_C(\vec{Q})}{d\Omega} + \langle f \rangle^2 - \langle f^2 \rangle$, equation 2.14 is redefined as:

$$S(\vec{Q}) \sim \frac{I(\vec{Q})}{N\langle f \rangle^2} - \frac{\langle f^2 \rangle - \langle f \rangle^2}{\langle f \rangle^2} \tag{2.15}$$

This means that in order to obtain the total scattering structure function the collected intensities must be normalized by the compositional average of the scattering length of the sample. In figure 2.2 a comparison between raw data and normalized reduced total scattering structure function is shown. The calculation of $S(Q)$ is extremely important due to its connection with scattering amplitude. Indeed by the equations 2.14 and 2.12:

$$S(\vec{Q}) \sim \frac{1}{\langle f \rangle^2} \frac{\langle f \rangle^2}{N} \left| \Psi(\vec{Q}) \right|^2 \sim \frac{1}{\langle f \rangle^2} \frac{1}{N} \sum_{\upsilon,\mu} f_\upsilon f_\mu e^{i\vec{Q}(\vec{R}_\upsilon - \vec{R}_\mu)} \tag{2.16}$$

At previous mentioned $\Psi(\vec{Q})$, defined in equation 2.10, is proportional to the Fourier transform of the electron density function $\rho(\vec{r})$:

$$FT\rho(\vec{r}) = \frac{1}{\langle f \rangle \sqrt{N}} \sum_{\upsilon} f_{\upsilon} e^{i\vec{Q}(\vec{r_{\upsilon}})} \tag{2.17}$$

At the end the total scattering structure function is rewritten as:

$$S(\vec{Q}) \sim \left|\Psi(\vec{Q})\right|^2 \sim |FT\rho(\vec{r})|^2 \tag{2.18}$$

Intuitively applying the inverse Fourier Transform is then possible to obtain information on the electron density function. Specifically FT S(Q) represents the electron density correlation function called the generalized Patterson function $P(\vec{r})$ which is defined as:

$$P(\vec{r}) = \rho_0 g_0(\vec{r}) = \frac{1}{4\pi r^2} \sum_{\upsilon} \sum_{\mu} \delta(r - r_{\upsilon\mu}) \tag{2.19}$$

where ρ_0 is the average number density of the material and $g_0(\vec{r})$ is the pair correlation function. Patterson function represents a pair electron density correlation function which gives the probability to finding any particle (as atom) at position $\vec{r}$ with respect to any particle taken as the origin. Exploiting this Fourier Transform relation between S(Q) and Patterson function it is possible to obtain the reduced Pair Distribution Function:

$$G(r) = \frac{2}{\pi} \int_0^{\infty} Q[S(Q) - 1] sinQrdQ \tag{2.20}$$

This function oscillates around zero and asymptotes to zero at high r. It also tends to zero at r = 0 with the slope $-4\pi\rho_0$, where ρ_0 is the average number density of the material (Billinge 2012). More detailed description and graphical example will be reported in following sections. Here only G(r) function and its definition is presented, but different functions exist to describe similar effects as the Atomic Pair Distribution Function or the Radial Distribution Function. However the use of G(r) presents different advantages: i) it is obtained directly from the Fourier transformation of the scattered data ii) the random uncertainties on the data (propagated from the measurement) are constant in r, then the fluctuations in the difference between a calculated and measured G(r) curve have the same significance at all values of r (Billinge 2012). NB The formalism and definitions of total scattering *formulae* are rather ambiguous, however for more details a full description and explanation of different functions are reported in *'A comparison of various commonly used correlation functions for describing total scattering'* by Keen (Keen 2001).

2.2 PDF in practice

2.2.1 How to perform X ray total scattering experiment

Total scattering experiments are performed in order to collect both Bragg and diffuse scattering. As in a classical diffraction experiment, scattering intensities are measured as a function of the momentum transfer, but here higher Q values must be explored in order to then obtain good PDFs. This need arises from:

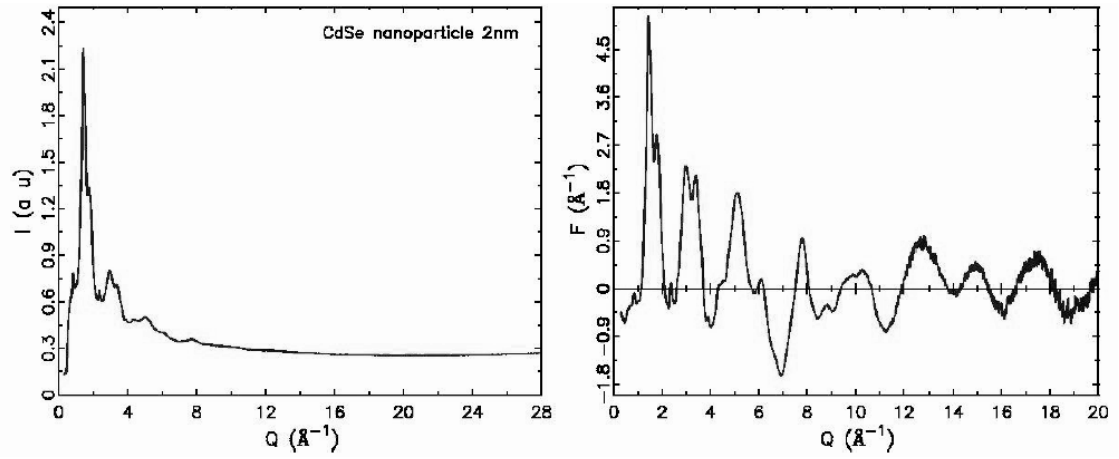

Figure 2.2: Comparison of raw data and normalized reduced total scattering structure function F(Q)=Q[S(Q)-1] of a $CdSe$ nanoparticles. The raw data are shown in the left panel. Data normalized and divided by the square of the atomic form-factor is reported on the right panel (Billinge 2012).

- diffuse scattering in powder diffraction data is almost Q independent, at low Q region diffuse scattering lies underneath the Bragg peaks. It becomes significant only at high Q where Bragg peaks are diminished due to the Debye-Waller factor which reflects the effect of atomic motion due to thermal or zero point quantum vibrations (Kim 2007).

- in equation 2.20 Q appears as the upper and lower limits of the integration which is taken over zero and infinity, practically these two terms are two real values named Qmin and Qmax. For most instruments Qmin is sufficiently small that the terms missing from the transform are of negligible importance, differently the omission of terms with Q > Qmax frequently results in spurious oscillations called termination ripples (Toby & Egami 1992). However it is important to notice that finite Qmin is the responsible of the missing small angle scattering (SAS) signal, this has important consequences especially for the study of nanoparticles (Farrow & Billinge 2009).

- by a reasonable approximation the resolution in G(r) is defined as $\pi/Qmax$ then points within a distance $\Delta r < \pi/Qmax$ of each other in G(r) will be statistically correlated (Egami 2003). In this way it is easy to understand that higher the Qmax higher the direct space resolution.

Considering equation 2.8 high Qmax is achievable lowering the wavelength value. Total scattering X ray experiments can be carried out using laboratory diffractometers with Mo (Confalonieri et al. 2015) or Ag sources which allow to use low λ and Qmax of 14 or 20 Å^{-1} respectively. This kind of instruments could be employed obtaining perfectly acceptable low resolution PDFs. For example molybdenum tubes give relatively good flux and are often used for laboratory liquid and amorphous measurements. However it is important to take into account the reduced intensity and then the long measurement times (Egami 2003). In order to obtain excellent PDFs with high resolution (then with higher Q up to $\sim$ 30 Å^{-1}), total scattering experiments performed by synchrotron radiation, which is very intense, well monochromatized, focused and collimated, are in fact more indicated (Billinge 2008). Recently different beamlines have been built for this purpose and present optimum setups for collecting total scattering as at ESRF (European Synchrotron Radiation Facility, Grenoble, France), at APS (Advanced Photon Source, Argonne National Laboratory, Illinois, USA), SPRING-8 (Japan) and many others. Instruments available in these facilities are not only optimise to achieve high Q values, but usually also to collect data with high reciprocal space resolution. This guarantees to define better Bragg peak positions decreasing the broadening of diffraction maxima

and on direct space to have a less dampening of the G(r) signal. Furthermore stable set-up and accurate incident intensity monitoring, usually furnished at synchrotron facility, are great advantages considering that data is normalized by incident intensity (Billinge 2008). Considering that signal at high Qmax is very weak, measurements on this region require long time to achieve good counting statistics. Comparing experiments involving point detector and performed by laboratory and synchrotron source this last shows again a great advantage lowering counting time of about 5 hours; see chapter 4 for a practical example. Counts of discrete events are subject to statistical fluctuations that are governed by the number of events recorded. The expected or estimated standard deviation for the observation N counts is $N^{1/2}$ (Toby & Egami 1992), then more counts less the ratio with relative errors. However good data collection must consider, beyond the need of high statistic at high Q, a good agreement between time and a real improvement of data quality. Last, but not least the obtaining of a good PDF demands not only accurate determination of the diffuse intensities, but also of the background. This includes scattering without the sample, then generated by sample holder, air, optical systems and so on. Their contributions, which must be collected separately from the sample, will be subtracted during data treatment. In this view low background is desirable to accurately measure weak diffuse scattering signals and later to obtain good Pair Distribution Functions.

2.2.2 How to generate PDF

Once total scattering data is collected some additional passages must be made in order to generate Pair Distribution Functions. First of all corrections for absorption, polarization, multiple scattering and either Placzek or inelastic scattering must be applied. Any inaccuracies in these corrections will introduce systematic errors to the computation of $\rho(r)$ then attention must be paid. However, these experimental effects are broad smoothly varying functions of Q. Thus any systematic errors due to these corrections (the deviations between the applied corrections and the true effects) can also be expected to be broad smoothly varying functions of Q (Toby & Egami 1992). A consequent step requires corrections for instrument background and scattering from the sample mounting or container (Billinge 2008). Practically this consist in a subtraction of every intensities which are not related to the sample scattering. Corrected data is then normalized and finally Fourier transformed (as explained in section 2.1). Fortunately several data correction programs are available for free download and these take care of the corrections and normalizations needed to obtain PDFs from raw data (Billinge 2008). For example a code that incorporates atomic scattering factors and Compton factors is PDFgetX, however more recent version PDFgetX3 is available (Juhas et al. 2013), which includes *ad hoc* data reduction algorithm. Thank to this the additive contributions (as incoherent Compton scattering and background scattering from the sample container) are corrected by fitting and subtracting low degree polynomial to produce the correct asymptotic behaviour in the F(Q) (where F(Q)=Q[S(Q)-1]). This still leaves some differences, but that signal is of a low frequency in Q and thus, after Fourier transformation, produces noise only in a very low-r region in the PDF. On the other hand the multiplicative differences (as sample self-absorption and polarization) are not corrected, but they tend to vary at a very low rate in Q then they are expected to just slightly change the shape of peak profiles in the PDF. Resulting functions are perfectly comparable with those obtainable by other programs which use physical corrections for data reduction. Another program is GudrunX which has been developed to perform the necessary data reduction steps to convert raw X ray data into a structure factor. It allows corrections to be made for effective density, absorption, multiple scattering, Compton scattering and bremsstralung (Soper 2011). These softwares not only perform all step necessary to PDF generation, but especially make this in a very automatized way requiring just few input information, little time and no particular user's experience.

2.2.3 How to interpret PDF

The function obtained (mathematically and physically) in previous sections will be now interpreted in a more practical way. As mentioned before Pair Distribution Function shows the probability of finding any two atoms at a given interatomic distance. Peaks then coincide with a higher probability, whereas function returns to its baseline if there is zero probability of finding atoms separated by that distance (Billinge 2008). In figure 2.3 a simple example is reported where a real structure, in which coordination spheres are evidenced, is linked to its G(r).

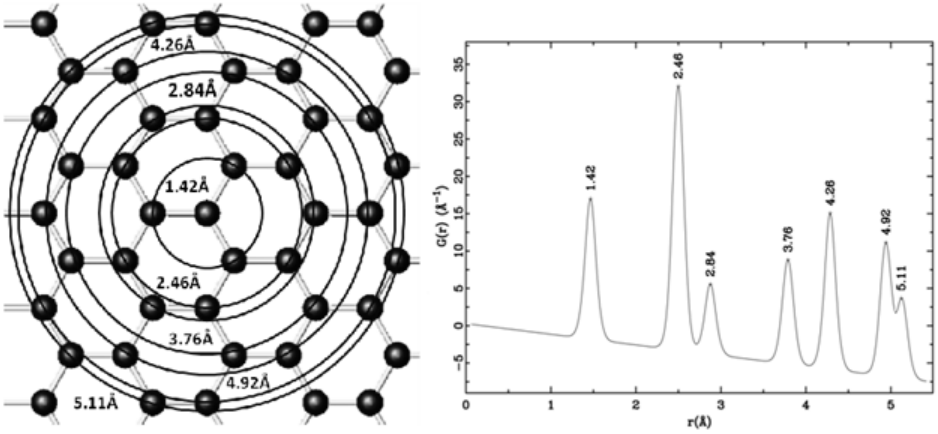

Figure 2.3: Relation between structure and G(r): interatomic distances cause maxima (peaks) in G(r) (Proffen 2007).

If the peak position is then mainly related to atomic bond lengths, different effects contribute to the intensity and shape (here just the most important and structurally connected will be cited). First of all more the structure is ordered more distances relative to a certain radius have similar values. This means that the distribution of distances will be narrow forming peak with high intensity and sharp shape. Differently atomic disorder, in the form of thermal and zero-point motion of atoms and any static displacements away from ideal lattice sites, gives rise to a broader, then less intense, distribution of atom-atom distances. Peak intensity is however also linked to the chemical species involved in the bond lengths. Indeed bonds of heavy elements will weigh more than those of lighter atoms due to the different atomic form factors, which in X ray raise as atomic numbers increase. Furthermore also the abundance of the chemical elements influence peak height. For example, in case of materials with different doping percentage, peaks related to substituent atoms will show different intensities as a function of doping amount. Another important point linked to the aspect of the Pair Distribution Function is related to the dampening of the signal. In the G(r) from a micro crystalline sample the peak-peak signal amplitude gradually falls off due to the finite Q resolution of the measurement, which is then the limitation on the spatial coherence of the measurement rather than the structural coherence itself. However in samples with a high degree of structural disorder, as nanosize crystals, the signal amplitude in G(r), and only in G(r), falls off faster than dictated by the Q resolution and this becomes a useful measure of the structural coherence of the sample. A visual investigation could be therefore very useful to evaluate the diameter of nanoparticles (Billinge 2012), as in the example in figure 2.4 (it is understood that this estimate should be then validated by appropriate calculations).

As just mentioned, sample chemical composition plays an important role deeply influencing PDF peaks. Moreover it is extremely important in structural investigation substantially allowing to describe atomic arrangements explaining how and which elements constitute a given material. This could be a simple consideration, but actually conceals one of the greatest limits of the PDF analysis. In the example reported in figure 2.3 only a single atom type is involved and the related peaks represent just the correlations between different atoms, but identical

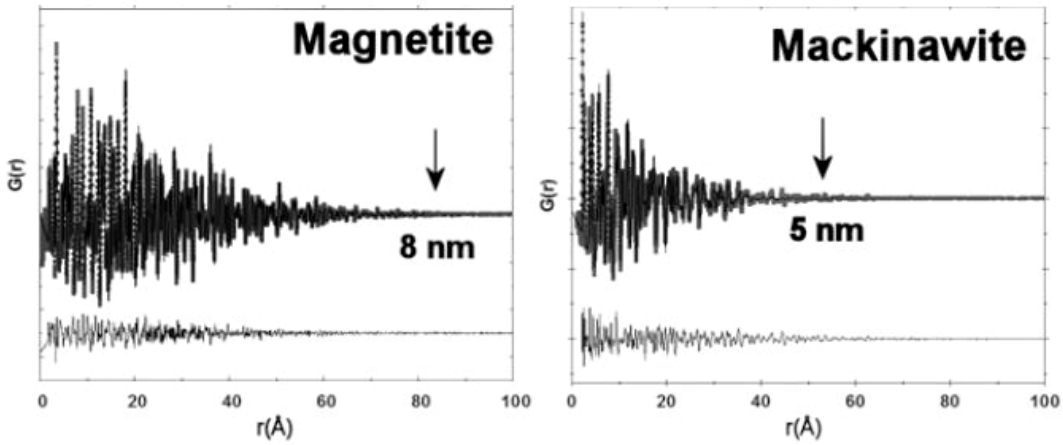

Figure 2.4: G(r) of two nanosize minerals: magnetite ($Fe^{II}Fe_2^{III}O_4$) and mackinawite (FeS). The dampening of two functions is related to the two different sizes of particles (Fernandez Martinez et al. 2008).

elements. Obviously this is a simple and almost rare case, usually investigated materials present a more complex composition. Unfortunately, differently to other techniques as EXAFS, Pair Distribution Function is not able to directly provide chemical information. This problem could be however partially overtaken calculating the so called partial Pair Distribution Functions. Partial PDF gives the distribution of atom pairs in the material coming only from atoms of type α around atoms of type β (Egami 2003). If the local environments of a particular chemical species is well defined this could be used to simplify the double-sum in equation 2.19, which is original taken over all atoms in the structure. If the sample is crystalline, the faster way to understand what kind of atoms is implicate in certain peaks is to choose a structure similar to that under the investigation, for example that obtained by Rietveld analysis, and then calculate all the theoretical partial PDFs related to each pair of chemical elements. The example in figure 2.5 demonstrates that this operation it is very useful to have a first idea about atomic bonds and related peaks, withal it is important to remember that this kind of knowledge is indirectly extrapolated. In

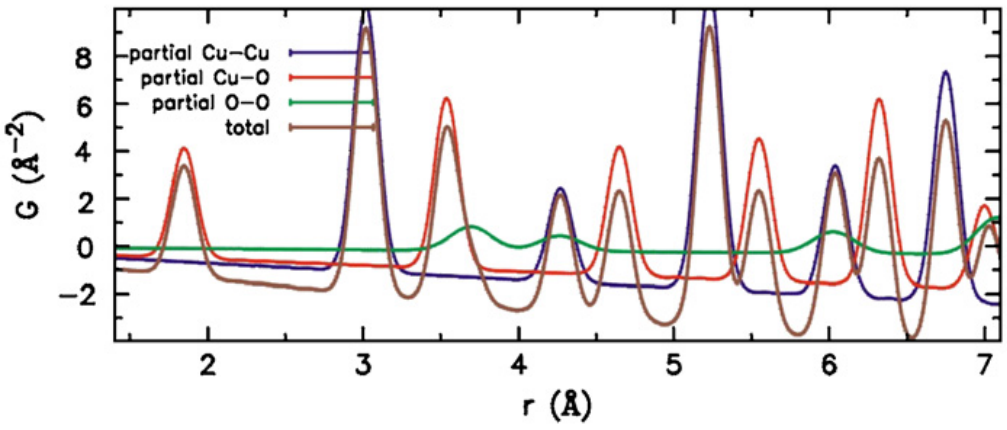

Figure 2.5: Partial PDFs for Cu-Cu, Cu-O and O-O bonds in the cuprite structure (Dapiaggi et al. 2008).

this section it has been reported how to interpret a PDF and to read its features considering peaks position, shape, even chemical composition (though predicted only) and so on; however, in order to obtain detailed information on atomic arrangement, structural analyses are necessary and must be performed accurately.

2.2.4 Structural analysis

The most popular approach for real space modeling is to use a full-profile fitting method analogous to the Rietveld method, but where the function being fit is the PDF. Structural and experiment dependent parameters are allowed to vary until achieve the best fit between PDF calculated from the model and the data using a least squares approach (Billinge 2008). Lattice parameters, atomic fractional coordinates, displacement, occupancies of the crystallographic sites and thermal vibrations parameters could be then refined in order to obtain a good agreement between calculated and observed functions. Suitable measure for the fit goodness is the so called Rw value. It is defined in equation 2.21 where sum goes over all data points i, G_{obs} is the observed PDF data, G_{calc} is calculated data and the weight of each data point is given by w (Proffen & Kim 2009).

$$Rw = \sqrt{\frac{\sum_{i=1}^{N} w(r_i)[G_{obs}(r_i) - G_{calc}(r_i)]^2}{\sum_{i=1}^{N} w(r_i)G_{obs}^2(r_i)}} \tag{2.21}$$

PDFs could be analysed at different length scales depending on the structural information which has to be obtained. Choosing the right radius range, it is indeed possible to deduce structural arrangements at local level, where local variations are well represented and inferable, or at intermediate or average length scale, where local disorder is averaged resulting in a long range ordered structure. Therefore PDF allows to study atomic structure, its coherent correlation length and its evolution using just a single function which is for sure one of stronger advantage of this technique. However, despite this great opportunity, local disorder investigation in general remains the main focus of any PDF analysis. Usual a starting model has been defined, good choice is represented by a bibliographic or average structure, and then analysis proceeds observing how it agrees with the local structural information contained in the experimental PDF (Bozin 2003). If the function is not well fitted then this means that the short and long range orders are structurally different. In order to increase the agreement and then to model the local atomic arrangement, the initial structure must be improved, as described above, refining parameters, changing structural constrains until even violating average symmetry. These operations are necessary to increase in some way the disorder in the model up to obtain a good fit. These types of analyses are performed taking into account just few atoms, they are indeed called small box modeling (Proffen & Kim 2009), resorting to crystallographic rules in order to simplify calculations. Under this philosophy different softwares have been written, but for sure the most used and famous is PDFgui (Farrow et al. 2007). Despite this, it is important to notice that other programs exist based on other approaches as Reverse Monte Carlo, which use a large box modeling where no crystallographic principles are involved in the refinements, two examples are RMCProfile (Tucker et al. 2007) and Discus (Proffen & Neder 1999) softwares.

Chapter 3

Experimental Procedure

3.1 Sample preparation

Samples have been prepared by Dr. Vincenzo Buscaglia, Dr. Giovanna Canu and Dr. Maria Teresa Buscaglia at Institute for Condensed Matter Chemistry and Technologies for Energy, National Research Council (ICMATE-CNR, Genoa, Italy). Two types of $BaTi_{1-x}Ce_xO_3$ (BCT) solid solutions have been synthesized: ceramic samples and nano powders. In table 3.1 all samples involved in present research have been reported specifying the short names used in the following discussion.

Ceramic Sample			Nano size Sample		
Chemical Formula	Ce (%)	Short name	Chemical Formula	Ce (%)	Short name
$BaTi_{0.98}Ce_{0.02}O_3$	2	BTC2	$BaTi_{0.98}Ce_{0.02}O_3$ Fine	2	BTC2 Nano Fine
$BaTi_{0.95}Ce_{0.05}O_3$	5	BTC5	$BaTi_{0.98}Ce_{0.02}O_3$ Coarse	2	BTC2 Nano Coarse
$BaTi_{0.9}Ce_{0.1}O_3$	10	BTC10	$BaTi_{0.95}Ce_{0.05}O_3$	5	BTC5 Nano
$BaTi_{0.8}Ce_{0.2}O_3$	20	BTC20	$BaTi_{0.9}Ce_{0.1}O_3$	10	BTC10 Nano
$BaTi_{0.7}Ce_{0.3}O_3$	30	BTC30	$BaTi_{0.8}Ce_{0.2}O_3$	20	BTC20 Nano

Table 3.1: All samples involved in present research have been reported specifying the short names used in the following discussion.

Ceramic BTC

$BaTi_{1-x}Ce_xO_3$ (BCT) ceramics with various compositions and different polar behaviours (reported in table 3.2) have been prepared according to the limit of the solid solubility of Ce^{4+} in $BaTiO_3$, which is about x = 0.3 as reported by Ang *et al.* (Ang et al. 2002a).

Ceramic Sample	
Chemical Formula	Expected Polar Behaviour
$BaTi_{0.98}Ce_{0.02}O_3$	Normal ferroelectric
$BaTi_{0.95}Ce_{0.05}O_3$	Normal ferroelectric
$BaTi_{0.9}Ce_{0.1}O_3$	Diffuse Phase Transition
$BaTi_{0.8}Ce_{0.2}O_3$	Relaxor
$BaTi_{0.7}Ce_{0.3}O_3$	Relaxor

Table 3.2: All ceramic samples involved in present research have been reported specifying the chemical composition and the expected polar behaviours.

High purity starting $BaCO_3$ (Solvay, 99.9% purity), TiO_2 (Degussa-P90, 99.9% purity) and CeO_2 (Degussa,

AdNano 50-99.95 % purity) nano powders have been weighted in stoichiometric proportions in order to obtain 30 g of $BaTi_{1-x}Ce_xO_3$ powders by a solid state reaction according to the formula:

$$BaCO_3 + (1-x)TiO_2 + xCeO_2 \rightarrow Ba(Ti_{1-x}Ce_x)O_3 + CO_2 \tag{3.1}$$

The obtained oxides were then wet-mixed with distilled water for 24 h. After freeze-drying, the powders have been calcined at 900 °C for 4 h to promote the solid-state reaction and consequently sieved and manually remilled. The resulted powders have been compacted in cylinders (length: 2-3 cm, diameter: 1 cm) by cold isostatic pressing at 1500 bar and the resulting greens have been sintered at 1450 °C for 6h with exception of BTC2 which was densified at 1550 °C (see table 3.1 for the used sample names). The density of the final ceramics has been measured by the Archimedes method. In figure 3.1 obtained samples are reported. Almost all the ceramics present a homogeneous color tending to orange nuances, which is a good indication of cerium substitution at B site. Differently $BaTi_{0.98}Ce_{0.02}O_3$ appears formed by two distinct zones. This separation is probably caused by different cerium oxidation states: Ce^{4+} gives orange color to the ceramic rim, whereas blue color in the core is due to some Ce^{3+}. As discussed later, the formation of Ce^{3+} in BTC2 is supported by the results of Raman investigation but in any case Ce^{3+} is minoritary in comparison to Ce^{4+}.

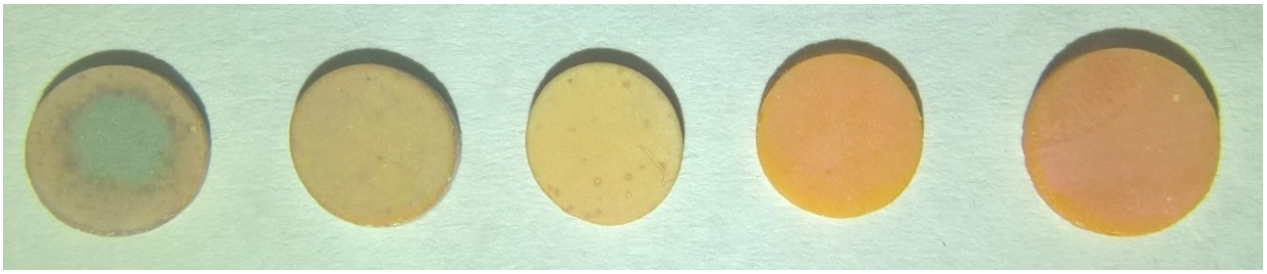

Figure 3.1: Ceramic samples from the left: BTC2, BTC5, BTC10, BTC20 and BTC30.

Before involving these samples in the present research, the suitability of preparation has been verified by different methods:

- X ray diffraction analysis using a laboratory diffractometer: no impurities have been detected. This should be a good indication about cerium incorporation at B site as Ce^{4+}, differently other reaction products would have formed especially in the samples containing a large amount of dopant.

- scanning electron microscopy has been employed to study ceramic morphology proving a uniform microstructure with faceted grains well interconnected without voids or pores, perfect triple junctions and a good densification of the materials.

- dielectric measurements have demonstrated the expected transition between normal ferroelectric to relaxor behaviour increasing cerium concentration. These results also prove the substitution of Ce^{4+} in Ti site.

None of these preliminary analyses are included in this dissertation, but detailed results have been reported in paper: *Diffuse phase transition and high electric field properties of $BaCe_yTi_{1-y}O_3$ relaxor ferroelectric ceramics* by Curecheriu *et al.* (Curecheriu et al. 2016). Nonetheless related conclusions have been included as a part of the state of the art in chapter 1.

Nano powders BTC

Nano powders $BaTi_{1-x}Ce_xO_3$ have been prepared in a similar way of ceramic samples, but avoiding powder compaction before high temperature treatment. Temperatures of thermal treatment, which influence the size of nano powders, are reported in table 3.3.

Nano Powders	
Chemical Formula	Thermal treatment ($^\circ C$)
$BaTi_{0.98}Ce_{0.02}O_3$ Fine	1000
$BaTi_{0.98}Ce_{0.02}O_3$ Coarse	1450
$BaTi_{0.95}Ce_{0.05}O_3$	1100
$BaTi_{0.9}Ce_{0.1}O_3$	1250
$BaTi_{0.8}Ce_{0.2}O_3$	1400

Table 3.3: Nano powders and relative temperatures of thermal treatment.

Powders obtained presents nanometric sizes around 100 nm, evaluated by scanning electron microscopy (SEM) images (in figure 3.2 some examples).

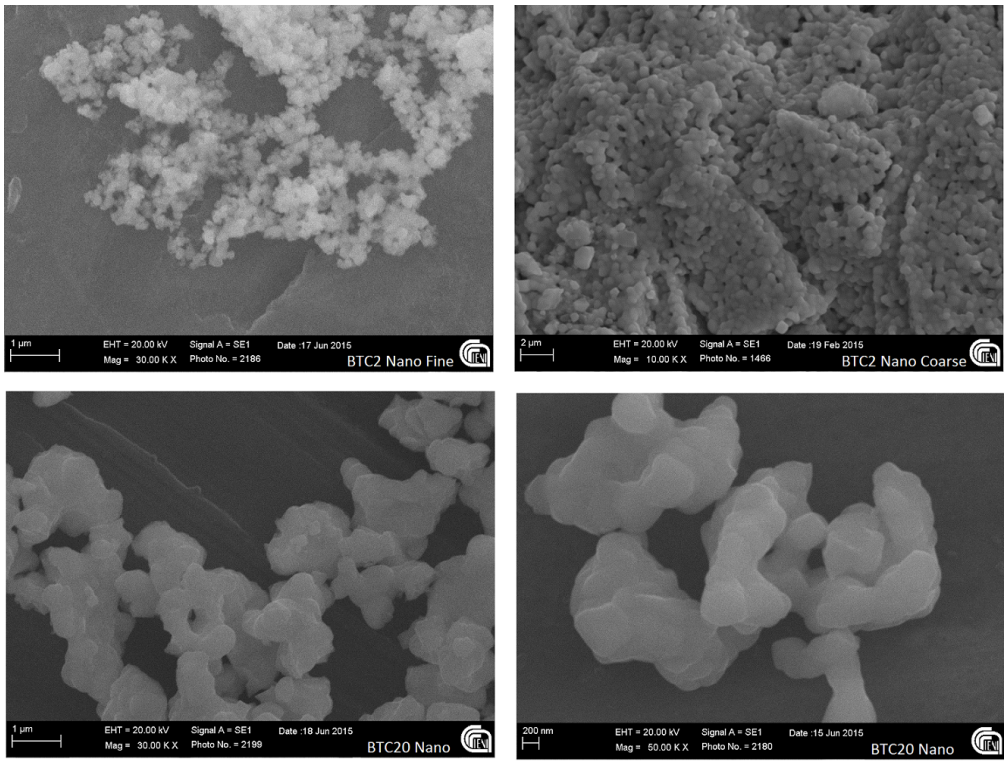

Figure 3.2: At the top comparison is reported between BTC2 Nano Fine and Coarse, which shows different sizes caused by the two different thermal treatments. At the bottom two images of BTC20 are shown.

3.2 Data collection

3.2.1 MA2315

ID22 is the high resolution powder diffraction beamline at ESRF (Grenoble, France) opened since May 2014 as a relocation of ID31. Its new position, at a 'high-β' section of the storage ring, leads to obtain an improvement of the

photon flux thank to a lower horizontal divergence and a better intrinsic angular resolution. Three undulators (U23 in-vacuum undulator and a revolver, which offers the choice of a U35 or a U19) are available to produce X ray from 60 keV to 80 keV covering a wide wavelength range. The monochromator, a channel cut Si 111 crystal, presents two diffracting surface separated by a distance of 4 mm. This arrangement allows to avoid problems caused by some changes in the Bragg angle generated by an overheating of the device. In fact in one hand the first block of monochromator is cooled through a liquid nitrogen flows and on the other the second surface could be tuned. The beam incident to the monochromator and that scattered are defined by water cooled slits, achieving a final size in the range of 0.5 - 1.6 mm (horizontal) by 0.1 - 1.5 mm (vertical). In order to canalize the monochromated beam to the sample a transport pipe is needed. It is delimited by two Be windows and includes: a beam-position monitor, anti-scatter slits, a fast radiation-damage shutter, Cu-foil attenuator and a beam-intensity monitor. The diffractometer is a two-circle machine accurate (nominally ± 1 arcsec) and precise (sensitive to displacements of $5\text{x}10^{-5^\circ}$). Diffracted intensity is detected, as a function of 2θ, by a bank of nine detectors, each preceded by a Si 111 analyser crystal. This configuration, in particular the limited acceptance of analyser crystals (a few arcsec, depending on energy) and a highly collimated beam, guarantees an high angular resolution rendering an accurate peak positions and a very narrow shapes. The combination of these features and the short achievable wavelengths makes ID22 a proper beamline to perform total scattering measurements. Technical information is mainly obtained in bibliography and personal documents (Fitch 2004), (Fitch 2012) (Fitch 2013) and by web site (*www.esrf.it*). Data collection on ceramic perovskite samples has been performed during the experiment MA2315. The experimental setup has been accurately chosen taking into account the transmission geometry and in order to obtain the best possible total scattering data. Samples for diffraction have been prepared grinding ceramics and filling borosilicate glass capillaries of 0.6 mm diameter with obtained powders; preferred orientation effects has been reduced by a spinning of the sample holder during collection. Wavelength value (lambda = 0.294932Å) has been selected to reach high Qmax value and to avoid samples absorption edge. The structural evolution of samples, depending on temperature, has been gained using an Oxford Cryosystems Cryostream cold-nitrogen-gas blower sample environment. The subtle phase transitions, occurred during heating, require a high resolution to be detected, therefore the line-detector, outline above, has been employed to record diffracted intensities. Data measured by each detector channel has been combined, taking into account the hoffsets and efficiencies, to return a single signal. Si standard material has been collected to complete this operation and to precisely calibrate the wavelength. Measurements have been performed at room temperature just for Si standard materials and the empty borosilicate glass capillary. The latter allows, during Pair Distribution Function analysis, to subtract the background caused by the scattering of everything that it is not sample. Total scattering analysis required a very good count statistics especially at high Q therefore each collection lasted 4 h for both samples (for each temperature) and empty capillary. In table 3.4 samples collected during the experiment are reported.

Sample	Type	Temperature (K)
BTC 2	Ceramic	150, 270, 350, 450
BTC 5	Ceramic	200, 300, 350, 380, 420
BTC 10	Ceramic	100, 200, 300, 400
BTC 20	Ceramic	100, 200, 300, 400
Empty Capillary		300
Si Standard		300

Table 3.4: MA2315: samples collected and related temperatures. NB BTC2 has been collected mixing whole sample, which is formed by to different slight compositions as reported in section 3.1.

3.2.2 MA2497

The experiment MA2497 has been performed at ID22 high resolution beamline at ESRF, Grenobe, France. The beamline setup is in the most part already described in the subsection 3.2.1. However some information has to be integrated due to the optical hutch renovation occurred between the two data collections. Indeed, after the monochromator, a new transfocator, using parabolic cylindrical Al lenses, has been installed in order to better focus beam. In other words this apparatus allows to avoid slits and the related beam cut down improving photon density. The focused beam (around 50μm) is indispensable for example in experiments involving mapping of residual strain in engineering components or to improve angular resolution when using the new available 2d detector. This flat panel is a Perkin Elmer XRD 1611CP3 which consists of a 41 x 41 cm^2 CsI scintillator bonded to an amorphous silicon substrate. The detector has a pixel size of 100 x 100 μm^2 and potentially a maximum readout speed of 3.75 frames per second (fps) at maximum resolution. In order to achieve the maximum transfer vector Q, the detector could be translate obtaining sample-detector distance between 2500 and 380 mm. This total scattering experiment proposes mostly a data collection of nano powders, then this detector has been rightly employed instead of the multianalyser considering a high direct-space resolution is preferable to the one in the reciprocal. Exactly for the MA2315, samples have been ground and placed in borosilicate glass capillaries of 0.7 mm diameter and then collected, using a spinning rotation, as a function of temperature using the Oxford Cryosystems Cryostream cold-nitrogen-gas blower. Energy of $\sim$80 keV and a lambda of 0.1549723 Å have been coupled with an appropriate sample-detector distance in order to obtain a high Q value indispensable to generate good PDFs. With the same intention, a standard material (LaB_6) loaded in borosilicate glass capillary has been collected at room temperature to calibrate the wavelength and dark-current images has been used to correct the heterogeneity in the pixel response. For all sample and related empty capillary, 60 images (exposure time 25 s) have been recorded and then averaged and integrated. The samples investigated during the experiments are listed in table 3.5.

Sample	Type	Temperature (K)
BTC 2 in	Ceramic	150, 270, 350, 450
BTC 2 out	Ceramic	150, 270, 350, 450
BTC 30	Ceramic	200, 300, 350, 380, 420
BTC 2 Nano Fine	Nano Powders	150, 270, 350, 450
BTC 2 Nano Coarse	Nano Powders	150, 270, 350, 450
BTC 5 Nano	Nano Powders	200, 300, 350, 380, 420
BTC 10 Nano	Nano Powders	100, 200, 300, 400
BTC 20 Nano	Nano Powders	100, 200, 300, 400
Empty Capillary		100, 150, 270, 350, 380, 400, 420, 450
LaB_6 Standard		300
Empty LaB_6 Capillary		300

Table 3.5: MA2497: samples collected and related temperatures. NB Two zones with slight different compositions of BTC2 ceramic sample have been accurately separated and separately collected. BTC2 in is related to the ceramic rim and BTC2 out to the core.

3.3 Lattice Energy

Lattice energy calculation has been performed as an additional and accessory method to describe $BaTi_{1-x}Ce_xO_3$ material, in any case a briefly introduction on the basic theory behind is necessary. Most the information here reported is taken by just few works (Gale 1996), (Gale & Rohl 2003). Lattice energy calculation is a simulation technique which is based on determination of internal energy of a given material. It represents a manybody quan-

tity depending by the positions and momenta of all electrons and nuclei and it could be represented as:

$$U = \sum_{i=1}^{N} U_i + \frac{1}{2}\sum_{i=1}^{N}\sum_{j=1}^{N} U_{ij} + \frac{1}{6}\sum_{i=1}^{N}\sum_{j=1}^{N}\sum_{k=1}^{N} U_{ijk} + ... \tag{3.2}$$

where N is the total number of atoms, first term represents the self energies of the atoms, the second the pairwise interaction (when *i* and *i* are equal it goes to zero), *etc.*. This definition is obviously a simplification: the energy has been decomposed into an expansion in terms of interactions between different subsets of the total number of atoms and the effect of the electrons is considered as subsumed into an effective atom. Assuming that the contributions of higher orders are practically negligible, an approximation including terms up to the to the four-body is reasonable (Hartree-Fock method). This could be also justified by a more practical concept: more the distance between two atoms weaker the interaction. Generally the calculation requires knowledge of the lattice constants and the coordinates of the ions (Glasser & Jenkins 2000), however also empirical models where these inputs are not needed, as the one of Kapustinskii, could be employed. In any case the interactions of atoms must be described in terms of interatomic potentials. Different forms exist, but in case of ionic bonded atoms repulsive type is suitable. Buckingham potentials, used in present calculations, are built taking into account an inverse variation with the distance and defined as:

$$U_{ij}^{Buckingham} = Aexp(-\frac{r_{ij}}{\rho}) - \frac{C_{ij}}{r_{ij}^6} \tag{3.3}$$

where A, B and C are constants, r_{ij} is the distance between the two atoms. This description allows to represent both the Pauli repulsion at short distances and the dispersive interaction at long range. In this work no dipolar shell model has been included considering only a core core interaction. In general lattice energy calculation is an amazing tool able to predict phase stability, crystal properties (as elastic constant, compressibility, piezoelectric stress and strain constants and many others) and even structural defects. The deep exploitation of this method is however beyond the scope of the present research. Here elementary energy calculation for given and simple phases is performed avoiding structural optimization. Furthermore no refined interatomic potential have been used favouring bibliographic values.

3.4 Electron Microprobe Analysis

JEOL 8200 Super Probe (Department of Earth Sciences, University of Milan, Italy) has been employed for electron microprobe analysis, machine time was obtained by courtesy of Dr. Pietro Vignola. $BaTi_{0.8}Ce_{0.2}O_3$ ceramic (sample size deducible by figure 3.3) has been prepared firstly embedding it in epoxy resin then polishing the surface, in order to avoid interferences between electron-sample and surface imperfection, and finally coating by a thin carbon film to achieve a homogeneous conductivity. Backscattered electron (BSE) image and element maps have been collected on the same area under operating conditions of 15 kV accelerating voltage and 5 nA beam current. Titanium and cerium distributions were obtained by WDS detector (Wavelength Dispersive Spectroscopy), differently EDS (energy dispersive spectroscopy) has been used for barium, no standard materials are required for these operations. Images of 714x714 pixels, where a pixel corresponds to 0.14 μm, have been acquired counting 50 ms for each pixel.

Figure 3.3: Polished $BaTi_{0.8}Ce_{0.2}O_3$ ceramic sample, not yet coated, prepared for electron microprobe analysis. Centimeter scale.

3.5 TEM

TEM analysis has been performed thank to the collaboration with Prof. Giancarlo Capitani (Department of Earth and Environmental Sciences, University of Milan Bicocca, Italy). In order to take advantage as best of the limited machine time assigned, only BTC20 ceramic sample has been explored. Two different kinds of preparation have been made on BTC20 resulting in two samples:

- the first was prepared from the same powders used for XRD analyses, which were dispersed in ethanol and ultrasonicated, then a 5 ml drop of the suspension was deposited on a carbon-coated Cu-grid (particulars in the left part of figure 3.4).

- the second was prepared by ion milling starting from the samples used for BSE observations. It was mechanically milled with silicon carbide, double polished with alumina, fixed on a Cu ring, and then gently ion-milled down to electron transparency (right part of figure 3.4). Ion milling was done at the Geology Dept. Sandro Botticelli of the University of Milan with a Gatan precision ion polishing system (PIPS). At the end sample was carbon coated to avoid electrostatic charging within the TEM.

Observations at room temperature on both samples were performed at the Dept. of Physical Sciences, Earth and Environment of the University of Siena with a Jeol JEM 2010 operating at 200 keV and equipped with an Oxford Link energy dispersive spectrometer for X ray microanalysis (EDS) and with an Olympus Tengra 2.3k x 2.3k x 14 bit slow scan CCD camera for image acquisition.

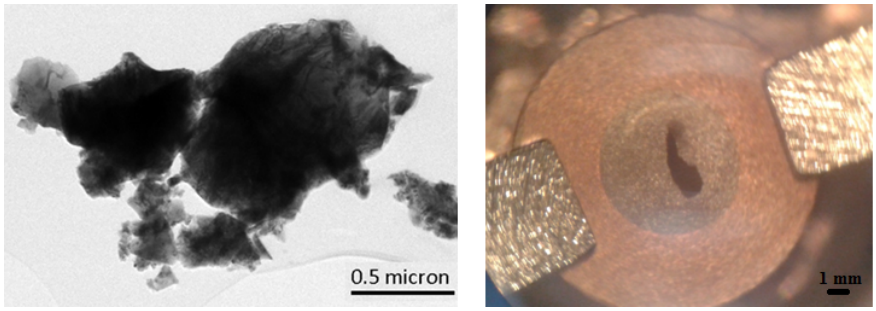

Figure 3.4: $BaTi_{0.8}Ce_{0.2}O_3$: two different preparations for TEM investigation. On the left powder material (image by TEM), on the right ion milled sample.

3.6 Raman spectroscopy

Temperature dependent Raman spectra were obtained by Dr. Marco DeLuca (Institut fur Struktur-und Funktionskeramik, Montanuniversitaet Leoben, Leoben, Austria) with a LabRAM microprobe system (Jobin-Yvon Horiba, Villeneuve d'Ascq, France) using a 532.02 nm Nd:YAG solid-state laser as the excitation source (effective power: 3 mW). The spectra were collected in a true backscattering geometry. In order to better appraise results which will be presented during discussion a briefly introduction on the technique and especially some details about $BaTiO_3$ spectrum are here proposed. All information can be found in chapter *'Raman Spectroscopy of Nanostructured Ferroelectric Materials'* of *'Ferroelectrics and Multiferroics Key processing and Characterization Issues and Nanoscale Effects*' (DeLuca & Gajovic 2016). Raman is a very powerful technique which allows for example to detect phase transition as a function of temperature, pressure, composition, and it is also possible to study bond strength and defects. Especially, being a vibrational spectroscopy, it is very sensitive to little structural differences which are peculiar of ferroelectric behaviour (such as para-ferroelectric transition, ferroelectric to relaxor crossover *etc.*). This spectroscopy exploits the inelastic scattering of visible light emitted by molecules or crystals. In few words incident photons interact with the electric dipole of molecules producing some effects. One of these is the inelastic scattering where the energy changes are related to the vibrational and rotational states of the system and to electronic transitions. If the radiation emitted is energetically low than the incident the so called Stokes bands can be observed in the spectrum, on the contrary anti-Stokes bands will be recognizable, as in example in figure 3.5. These two effects are deeply linked to the peculiarities of the system investigated and in particular to its modes of vibration, described by phonons. Their number, type, and symmetry depend on the number of atoms (N) in the primitive unit cell of the crystal and on the symmetry of the lattice. Not all phonons are detectable by Raman, only those defined as Raman active, which are those that produce changes in the polarizability of the lattice, are visible.

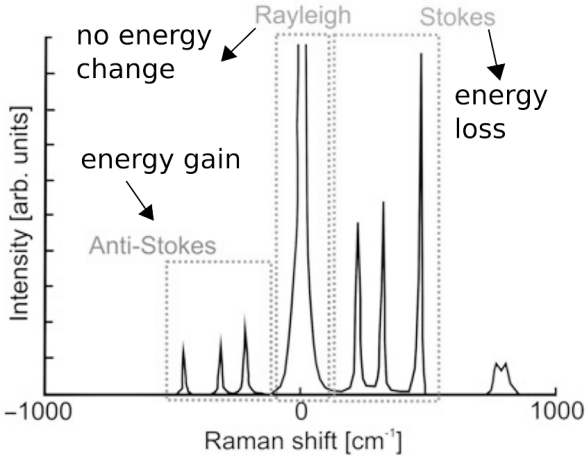

Figure 3.5: Example of room temperature Raman spectrum of CCl4. Inelastic scattering is related to an energy loss or energy gain mechanism between the incident radiation energy and the vibrational energy of the crystal giving the so called Stokes or anti-Stokes bands (DeLuca & Gajovic 2016).

3.6.1 Raman spectrum of pure $BaTiO_3$

As previously mentioned in $BaTiO_3$, as temperature lowers, a paraeletric-ferroelectric transition between cubic to tetragonal phase occurs. For cubic structure no first order vibrational bands are expected. Differently in the tetragonal phase, due to the titanium displacement, modes not detectable in cubic change (spitting) and become observable, as shown in figure 3.6. All Raman active modes in the tetragonal phase belong to A_1, B_1 and E type

and specifically: Γ_{OPtet} = 3[A_1(TO) + A_1(LO)] + B1+ 4[E(TO) + E(LO)], where TO and LO are generated by splitting in transversal and longitudinal components. In ceramic samples four dominant bands are well noticeable: at 250 cm^{-1} (A_1(TO)), at 370 cm^{-1} (B_1, E(TO+LO)), at 515 cm^{-1} (A_1, E(TO)) and at 715 cm^{-1} (A_1(LO), E(LO)). Two sharp peaks are presented at $\sim$305 cm^{-1} (which is related to B_1 silent mode) and $\sim$715 cm^{-1}; these two and dip at $\sim$180 cm^{-1} are an important fingerprint of ferroelectric phases being originated by the correlated displacements of Ti with respect to the oxygens. When orthorhombic phase is stable the spectrum slightly changes. A mode below 200 cm^{-1} starts to shyly appear as also a little shoulder around $\sim$490 cm^{-1}, whereas features at 250 to 270 cm^{-1} are shifted. Finally clear sharp peaks appear at below 200 cm^{-1} and $\sim$490 cm^{-1} signals of rhombhoedric transition. Despite description here presented, in figure 3.6 cubic structure presents two broad bands. In cubic centrosymmetric structure Raman activity should be forbidden, but as previously mentioned this technique is extremely sensitive to local variations. Indeed 'cubic' spectrum is deeply influenced by the presence of short-range disorder. This demonstrates how this spectroscopy could be very useful especially for disorder materials as doped $BaTiO_3$.

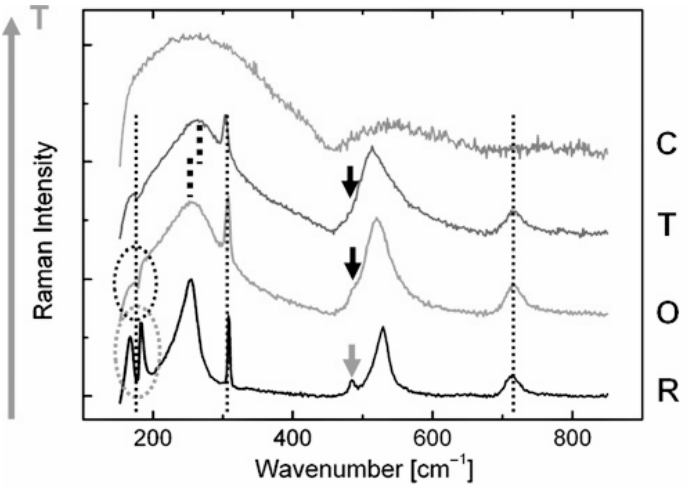

Figure 3.6: Raman spectra of pure, polycrystalline BT ceramics in the rhombohedric (R), orthorhombic (O), tetragonal (T), and cubic (C) phases. Thin, dashed vertical lines indicate modes present in FE phases. Circles indicate low-frequency modes that become damped in the O phase; arrows indicate the mode at 490 cm^{-1} that disappears in the tetragonal phase. The appearance of a spectrum in the C phase is a result of local spatial disorder. Temperature increases from the bottom to the top of the diagram (DeLuca & Gajovic 2016).

Starting from Raman interpretation of pure $BaTiO_3$ spectra, it should be more easy to solve those of doped perovskite. Usually in $BaTi_{1-x}B_x^{IV}O_3$ substitutions disrupts the long-range cooperative displacement of Ti atoms suppressing FE order. Consequently all peaks belonging to the FE phases (as dip at 180 cm^{-1}, the 'silent' mode at 305 cm^{-1} and the mode at 715 cm^{-1}) start to disappear. Furthermore if introduced element presents different size in comparison to Ti a shift of BO_6 polar phonons occurs (as at 270 cm^{-1}). Moreover when doping is sufficient a variation between normal ferroelectric to relaxor behaviour takes place, Raman is once again very helpful being able to detect the transition points between structural phases and the crossover to paraelectric phases.

Chapter 4

Method PDF generation setting: the case of gahnite nanocrystals

In this chapter the setup of the method to generate PDF is proposed by a particular case study, already reported in Confalonieri *et al.* (Confalonieri et al. 2015). This work is preparatory to that of $BaTi_{1-x}Ce_xO_3$ therefore materials, method, discussion and related conclusions will be presented here together to maintain a coherent tale. Extrapolation of Pair Distribution Functions is one of the most important points in local structure analysis. As reported in chapter 2 the passage between reciprocal and direct space data is rather complicated, fortunately different softwares are able to perform this operation quickly and requiring just few inputs. One of these is PDFgetX3 (Juhas et al. 2013) which has been designed for ease of use, speed and automated operation. Thank to the latter, a less user experience is demanded. Unfortunately this great advantage is coupled with a less control. Therefore it is important to deeply know the PDF processing operations and be able to evaluate the final results. In order to test this software and the generated PDFs, different total scattering data, collected on the same material (nanocrystalline gahnite) by three different instruments, has been used. Differently strategies have been applied in PDFs calculation and then evaluated by quick structural analyses. The chosen instruments are the most commonly used and present different peculiar characteristics: i) ID31 beamline at the European Synchrotron Radiation Facility (ESRF), with a very high reciprocal space resolution (and with a scanning detector setup) ii) ID11, is one of the high-energy experimental beamlines at the ESRF with a two-dimensional detector iii) a laboratory diffractometer with Mo anode (PANalytical Empyrean). Despite different configurations and peculiarities none of the latter should have a clear advantage thank to the nano size of the investigated sample which rise to a challenge for all the diffractometers involved.

4.1 Sample choice: gahnite nanocrystals

Gahnite is a zinc-aluminum spinel with stoichiometric formula $ZnAl_2O_4$ and face centered cubic structure (fcc), belonging to the space group Fd-3m. The zinc ion shows a tetrahedral coordination with four oxygens, while aluminum is placed in the octahedral site. Synthetic nano crystals (2-3 nm) have been prepared by hydrothermal method described by Chen *et al.* (Chen et al. 2008). Size has been evaluated by TEM observation (figure 4.1) carried out by Dr. Nicola Rotiroti at the Department of Earth Sciences, Section of Mineralogy, University of Milan. Nanometric dimension and then a possibly disordered structure allow to make a fair comparison between instruments, indeed none of the three should be favourite. This is guaranteed considering that high reciprocal space resolution is practically useless due to the peak broadening caused by nano size and too high direct space

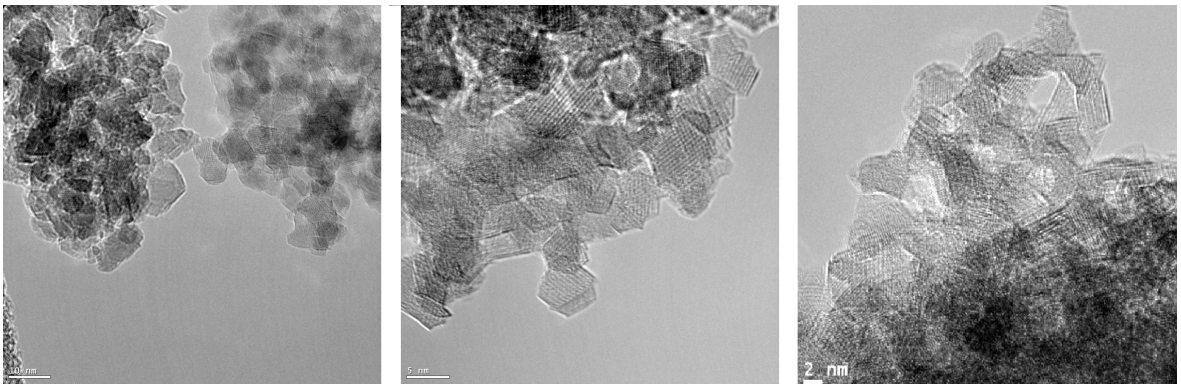

Figure 4.1: TEM investigation of gahnite nanocrystals. Images reveal, despite nanosize of particles, a perfect octahedron crystal shape, furthermore lattice planes are well visible inside nanocrystal.

resolution, unattainable by any X ray instrument, would be necessary to discriminate the first two atomic distances Zn-O and Al-O. Calculated partial PDFs of the gahnite structure, reported in figure 4.2 shows graphically Zn-O and Al-O bonds, presenting very slight difference in lengths, which form the first peaks. In theory, a Qmax $\geq$ 75 Å^{-1}, calculated by the well-known formula $\Delta r = \pi/Qmax$ (Egami 2003), would be indispensable to distinguish these two distances (Δr = 0.0418 Å).

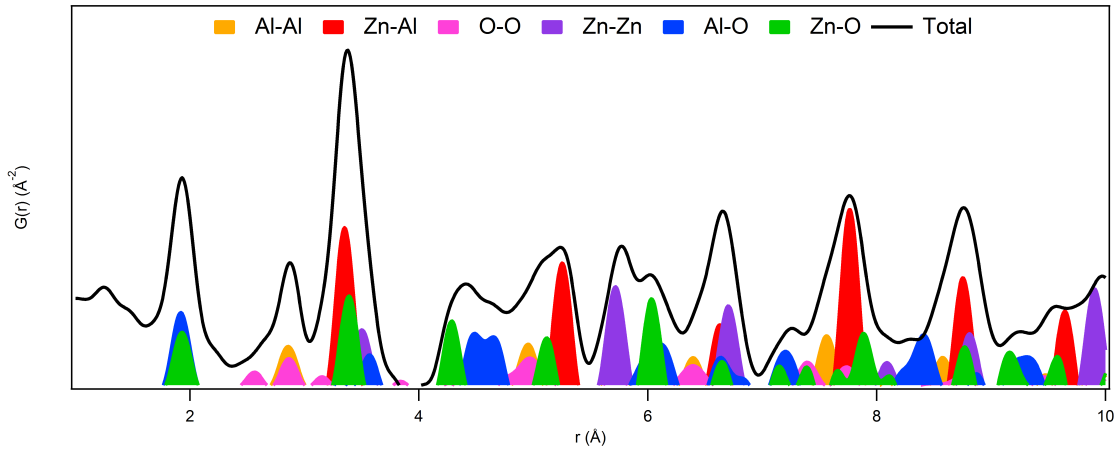

Figure 4.2: Gahnite partial PDFs from 1 to 10 Å radius. The partial PDFs are calculated from the structure used in refinements. It is evident that the first peak includes both Zn-O and Al-O bonds. The two bond lengths show a very small difference.

4.2 Instruments and data collection

ID31) The first data set has been collected at the beamline ID31 (ESRF, Grenoble, France), created for high resolution powder diffraction and optimized for capillary samples. A full instrument description and setting is already reported in subsection 3.2.1. In order to achieve high Q vector a short wavelength values has been choose (0.39996 Å) and calibrated against LaB_6 standard (NIST SRM 660b) at room temperature. Sample was hold in a boron glass capillary, and its contribution has been also individually collected and used for the background subtraction during PDFs generation. Data collection lasted 5 h for both sample and empty capillary.

Laboratory diffractometer) PANalytical Empyrean is a multipurpose diffraction system equipped with a sealed high resolution X ray tube with a Mo anode. The X ray tube was operated at 60 kV and 40 mA in order to achieve good yield of MoKα characteristic radiation (λ = 0.7107 Å). A special setup makes this instrument excellent for

home total scattering experiments. Beam is focused by X ray multilayer mirror and anti-scatter kit specifically developed for the PDF application has been used to achieve the needed featureless background (Nijenhuis et al. 2009), (Reiss et al. 2012), (Sommariva 2013). Considering the chemistry of investigated sample, discrimination levels of the solid state GaliPIX3D detector have been adjusted in order to suppress the fluorescence signal induced by the Mo radiation in the zinc atoms. The sample, loaded in a glass capillary with 0.5 mm external diameter, and the empty capillary have been separately measured between 5-145 $^\circ$ 2θ in 7.5 h. An optimized counting time strategy has been used in order to counteract the decrease of the scattered intensity at the highest angles because of the X ray form factor (Reiss et al. 2012), (Sommariva 2013).

ID11) ID11 is a multipurpose, high flux and high energy beamline (ESRF, Grenobe, France). The light source is provided by an in-vacuum undulator, U22 or CPM18 which differ in period and magnetic lattice. The coherence and source size of the beam has been measured as $\sim$18.5 micron FWHM vertically. A double bent crystal monochromator operating in horizontal Laue geometry allows to select the energy/ wavelength. The maximum energy range available is from 18-140 keV, though operationally, ID11 is optimized to work at energies above 35 keV. Thank to a in vacuum transfocator (which consists of 8 cylinders with 1, 2, 4, 8, 16, and 32 Be lenses, 32 and 64 Al lenses, and one with a pinhole) it is possible to focus beam up to $\sim$50x220 microns in the entire energy range and up to 7x45 microns above 70 keV. A full beamline description is available at *www.esrf.it*. Data collection has been performed with 0.20629 Å wavelength previously selected by a calibration with a silicon NIST SRM 640c standard. FReLoN camera has been employed for two dimensional diffraction pattern acquisition. This is optimized for very rapid readout, allowing full (2048 x 2048 pixels, 16 bit) frames to be read out in 240 ms (Labiche et al. 2007). The background correction has been carried out measuring and subtracting the scatter of empty silica glass capillary, with a diameter of 0.5 mm, used as holder. To achieve good counting statistics, 15 diffraction images have been collected and merged together (3 s for each collection).

4.3 Generation of PDFs and evaluation by visual comparison

Data have been treated (corrected and normalized) with PDFgetX3 (Juhas et al. 2013) which allows the obtainment of PDF by means of a low Q space polynomial correction. Five parameters are available to optimize the functions: *qmax* (the upper Q limit for the Fourier transformation of the F(Q) curve), *qmaxinst* (the Q cutoff for the meaningful input intensities), *qmin* (the lower Q limit for the Fourier transformation of the F(Q)), *bgscale* (scaling of the background intensities), and *rpoly* (r limit for the maximum frequency in the F(Q) correction polynomial). As explained in previous chapter Qmin, is in general so small and negligible that *qmin* parameter is usually fixed at value 0. PDFs, one for each data-set, have been initially calculated with default program parameters.

Then, in order to evaluate influences of the above cited parameters and especially the background subtraction, three different strategies (table 4.1) have been used to generated PDFs (therefore three for each data set):

- *bgscale* = 1: all the parameters available (described above) have been specifically chosen for each data-set to minimize the termination ripples and improve the PDF quality. Only *bgscale* has been fixed to 1 (the default value).

- *bgscale* = particular value: the functions calculated in the previous section (*bgscale* = 1) have been modified further by changing the *bgscale* parameter. The specific *bgscale* values have been chosen by comparing graphically each total scattering data-set with its background, and by minimizing the differences between them (see figure 4.3 for an example).

- Optimized: the *bgscale* values have been obtained as described in the previous section and kept fixed. Then,

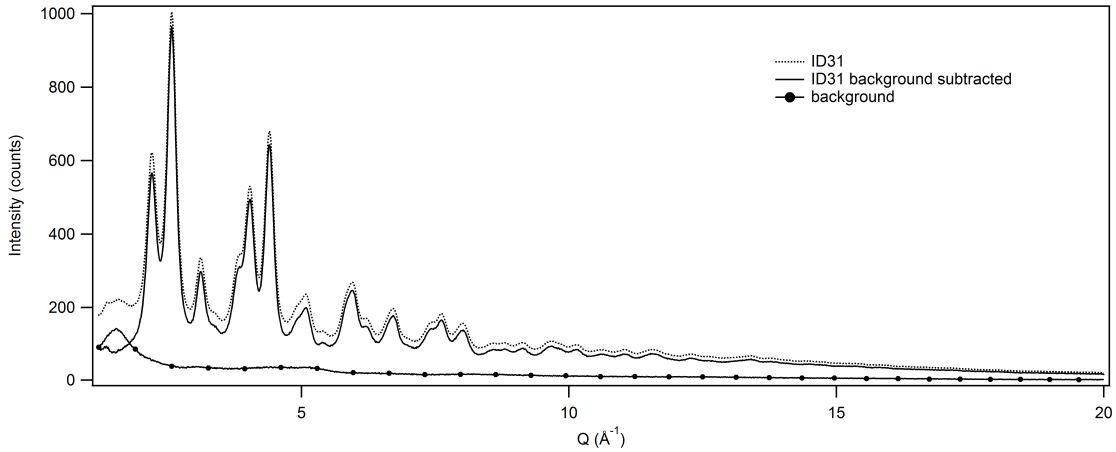

Figure 4.3: Example of background subtraction. PDFgetX3 allows the determination of the *bgscale* graphically in order to control and modify the background subtraction.

qmax, *rpoly* and *qmaxinst* have been modified individually for each data-set in order to get the best PDF with less noise because of termination effects, avoiding, at the same time, the loss of known structural features.

	ID31				Empyrean				ID11			
	Default	*bg*=1	*bg*=1.5	Optimized	Default	*bg*=1	*bg*=1.33	Optimized	Default	*bg*=1	*bg*=1.52	Optimized
bgscale	1	1	1.5	1.5	1	1	1.33	1.33	1	1	1.52	1.52
rpoly	0.9	2	2	1.77	0.9	1.78	1.78	1.35	0.9	1.48	1.48	1.5
qmaxinst	24	24	24	22.9	16.9	16.8	16.8	16.8	26.59	25.9	25.9	26
qmax	24	22	22	22	16.9	16.8	16.8	16.8	26.5	25.3	25.3	25.1

Table 4.1: PDFgetX3 parameters used in PDF calculation, *qmin* values are fixed at 0 for all PDFs. NB *bg* is short for bgscale.

Comparison between different strategies is reported in figure 4.4 for ID11. No important differences are to be underlined, then PDFs generated using different correction parameters, especially the *bgscale* values, are virtually identical. The same conclusion is valid for all instruments.

In figure 4.5 optimized PDFs and F(Q) for the three instruments are reported. Depending on the Qmax the three F(Q) show different truncation, but compared to the others a quite high noise is noticeable for ID31 data-set at high Q values. This effect is produced by an insufficient counting statistics. However, this does not affect significantly the PDF quality as demonstrated by the lower part of figure 4.5. The functions are indeed very similar and, as above mentioned, the first peak never presents any split or shoulder due to the not sufficient direct space resolution achievable by the three instruments. Despite these similarities, Empyrean PDF shows few features which are a bit less resolved, in particular at 4.3 and 6 Å, which are marked in figure by two arrows.

4.4 Evaluation by structural PDF analysis

Structural refinements have been performed by PDFgui software (Farrow et al. 2007). In order to proper analyse different PDFs *Qdamp* has been set using standard materials (investigated in the range from 1 to 50 Å of radial distances). LaB_6 NIST SRM 660b for ID31 and Empyrean data, and silicon NIST SRM 640c for ID11 have been employed as standards: the obtained *Qdamp* values were, respectively: 0.02, 0.01, and 0.059. Gahnite structural refinements have been done in the same way for all the functions. The simplest possible model of a totally direct $ZnAl_2O_4$ (Lucchesi et al. 1998) has been used and refined by the same parameters (only those allowed by the space group symmetry constraints). Firstly analyses between 1 to 55 Å have been executed in order to calculate the average spherical particle diameter, as defined in Howell *et al.* (Howell et al. 2006) and in Masadeh

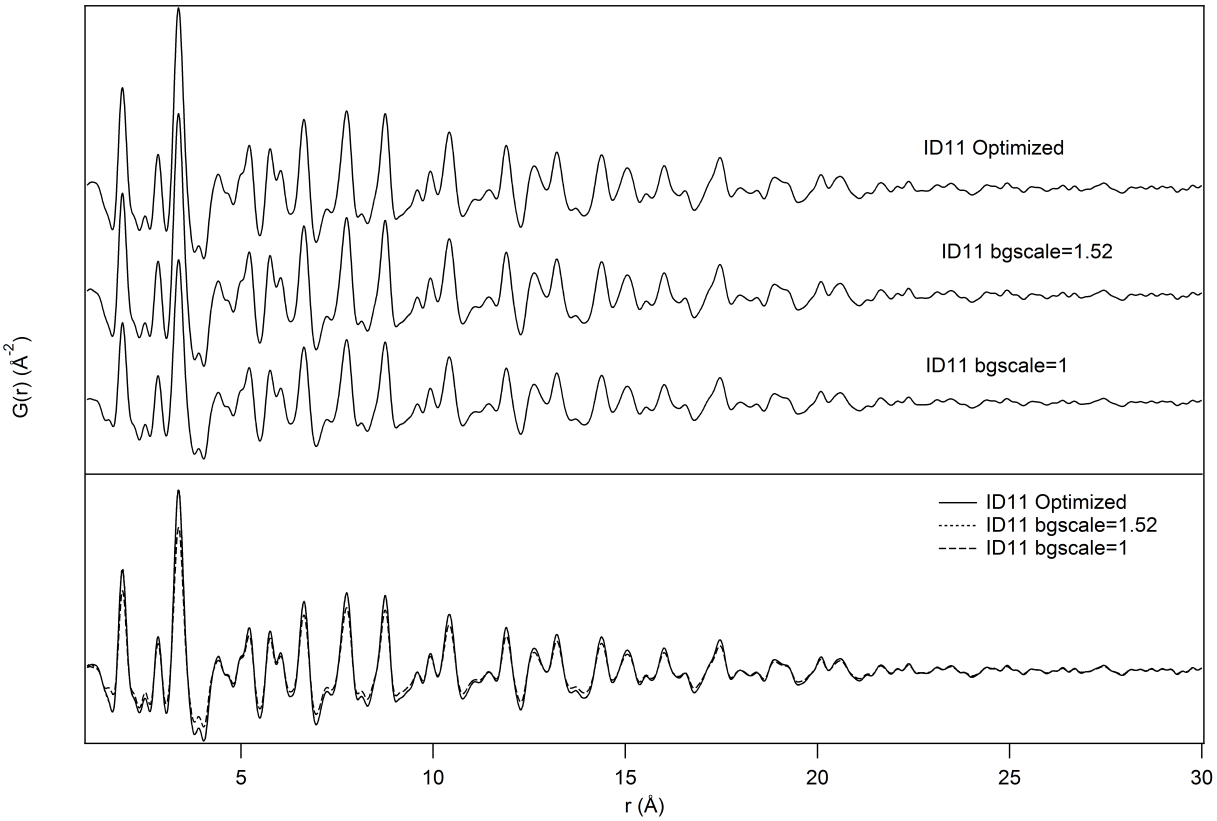

Figure 4.4: Visual comparison of G(r) from ID11 data-set. The PDFs are shown in a waterfall-like diagram (above) and superimposed (below).

et al. (Masadeh et al. 2007). A value around 30 Å has been obtained for all the PDFs, in good agreement with transmission electron microscopy (figure 4.1) and small angle X ray scattering measurements (Sommariva et al. 2013).

	ID31			Empyrean			ID11		
	bg=1	*bg*=1.5	Optimized	*bg*=1	*bg*=1.33	Optimized	*bg*=1	*bg*=1.52	Optimized
Cell (Å)	8.079(3)	8.080(2)	8.080(2)	8.089(4)	8.088(4)	8.088(4)	8.085(9)	8.085(6)	8.085(6)
Uiso Zn (Å^2)	0.0071(7)	0.0071(6)	0.0072(6)	0.012(1)	0.012(1)	0.012(1)	0.008(2)	0.008(1)	0.008(1)
Uiso Al (Å^2)	0.0050(9)	0.0049(8)	0.0049(8)	0.008(2)	0.008(1)	0.008(1)	0.005(2)	0.005(2)	0.005(2)
Uiso O (Å^2)	0.012(2)	0.012(2)	0.013(2)	0.018(3)	0.018(3)	0.017(3)	0.011(5)	0.012(4)	0.012(4)
Coordinate O	0.2617(8)	0.2617(7)	0.2617(7)	0.261(1)	0.261(1)	0.261(1)	0.262(2)	0.262(2)	0.262(2)
Delta 2	1.9(3)	2.0(3)	2.0(3)	1.9(4)	2.0(3)	2.1(3)	2.1(7)	2.2(4)	2.2(5)
Rw	0.209	0.216	0.215	0.225	0.23	0.207	0.2	0.206	0.207

Table 4.2: PDF refinements results obtained between 1 and 20 Å. Estimated standard deviations of the parameters are derived from the least squares minimization procedure in PDFgui and they are just indicative and not significant. In fact statistical variations of the measured intensities are not taken into account during the Fourier transformation of the data done by PDFgetX3. NB *bg* is short for bgscale.

Structural results obtained between 1 and 20 Å are shown in table 4.2. For the three data-sets similar values are reported. The small variations in lattice parameter could be caused by wavelength calibration, ambient temperature differences, or other possible experimental effects. The slightly broader peaks in the Empyrean PDFs seem to not affect the calculated lattice parameters and atomic positions, comparable with those obtained from the other instruments (figure 4.6). In addition the quality of the fits (measured by Rw values) is comparable for all data-sets and all analyses. However differences between the calculated and observed PDFs probably caused by structural defects and/or stoichiometrical effects. For example the misfit in peaks observed about 2.8 and 4.5 Å (figure 4.6), which represent mostly Al-Al bond (the O-O distance is clearly less significant with X rays), may be caused by

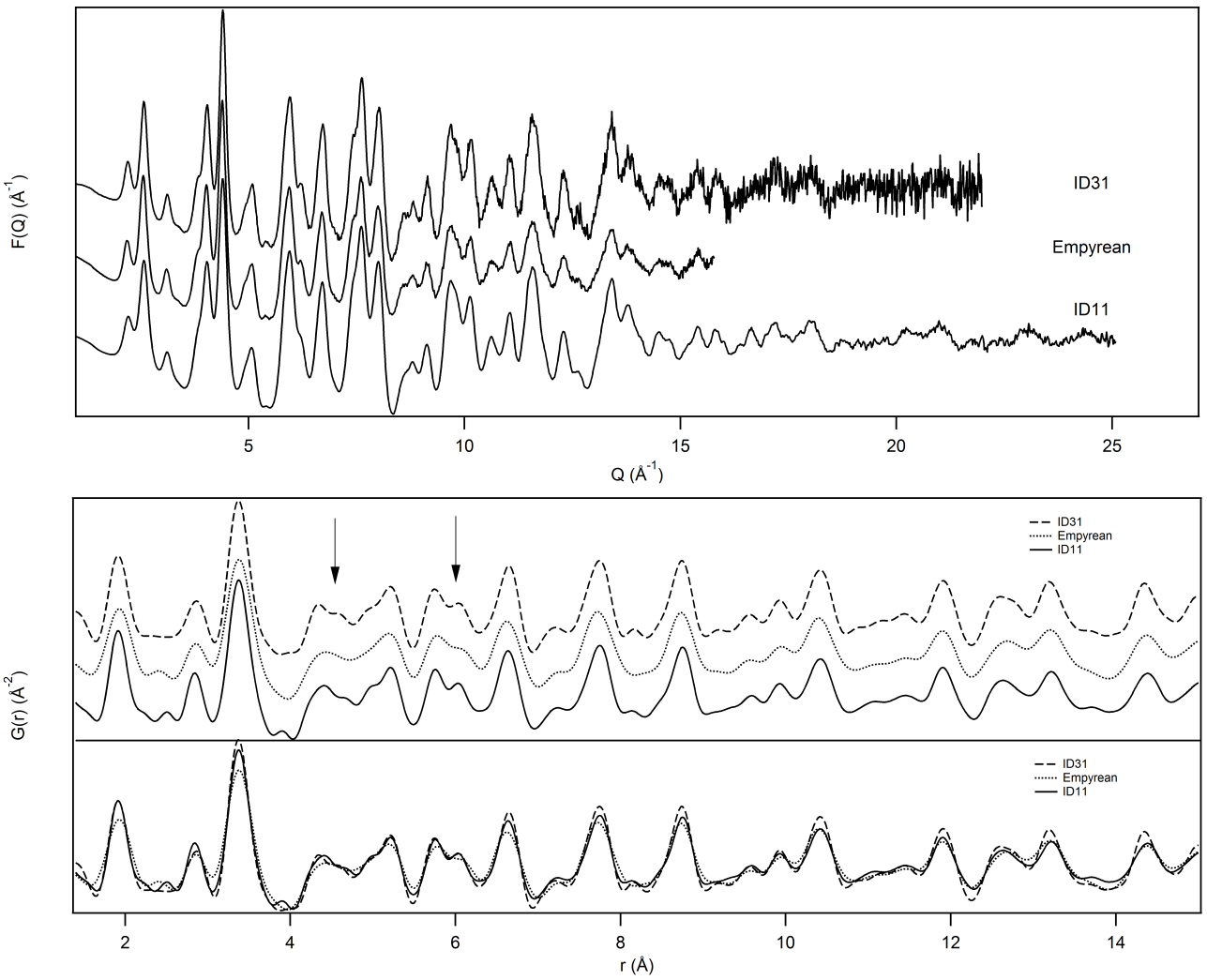

Figure 4.5: Higher part: visual comparison of optimized F(Q) from three data-sets. Visual comparison of optimized G(r) from three data sets. Lower part: PDFs are shown in a waterfall-like diagram (above) and superimposed (below). Arrows indicate the biggest differences in real space resolution.

a distortion within the octahedral site, which is not taken into account in the highly symmetric crystallographic structure (used in refinements). This interpretation could be extended also to the difference of the peak at 4.5 Å (Al-O and Zn-O distances). In fact, considering the gahnite compact cubic structure, the octahedral distortion described above would modify both Al-Al and Al-O bond lengths, but also Zn-O distances. Despite these consideration could be reasonable, a detailed discussions of the structural effects in this material are beyond the scope of this work. More important it is that all PDFs give acceptable results, despite the simple structural model used for the calculations (totally direct with space group symmetry respected). The slight higher values of oxygen Uiso in the Empyrean PDF may be because of the shorter Q range or effect of absorption of X rays in the sample material which has been not considered in the data processing.

4.5 PDFs generation: final consideration

The obtained PDFs from the different data-sets are substantially comparable. Small differences in the refined structural parameters could be caused by different instrumental characteristics, but also by the parameters used in

the PDF calculation, so attention should be paid to the procedure of PDF generation from total scattering data. The laboratory diffractometer with a Mo anode X ray tube can be used, with good results, in total scattering experiments in which high real space resolution is not required. Although accurate background subtraction is desirable, it does not seem to be decisive for the structural analysis.

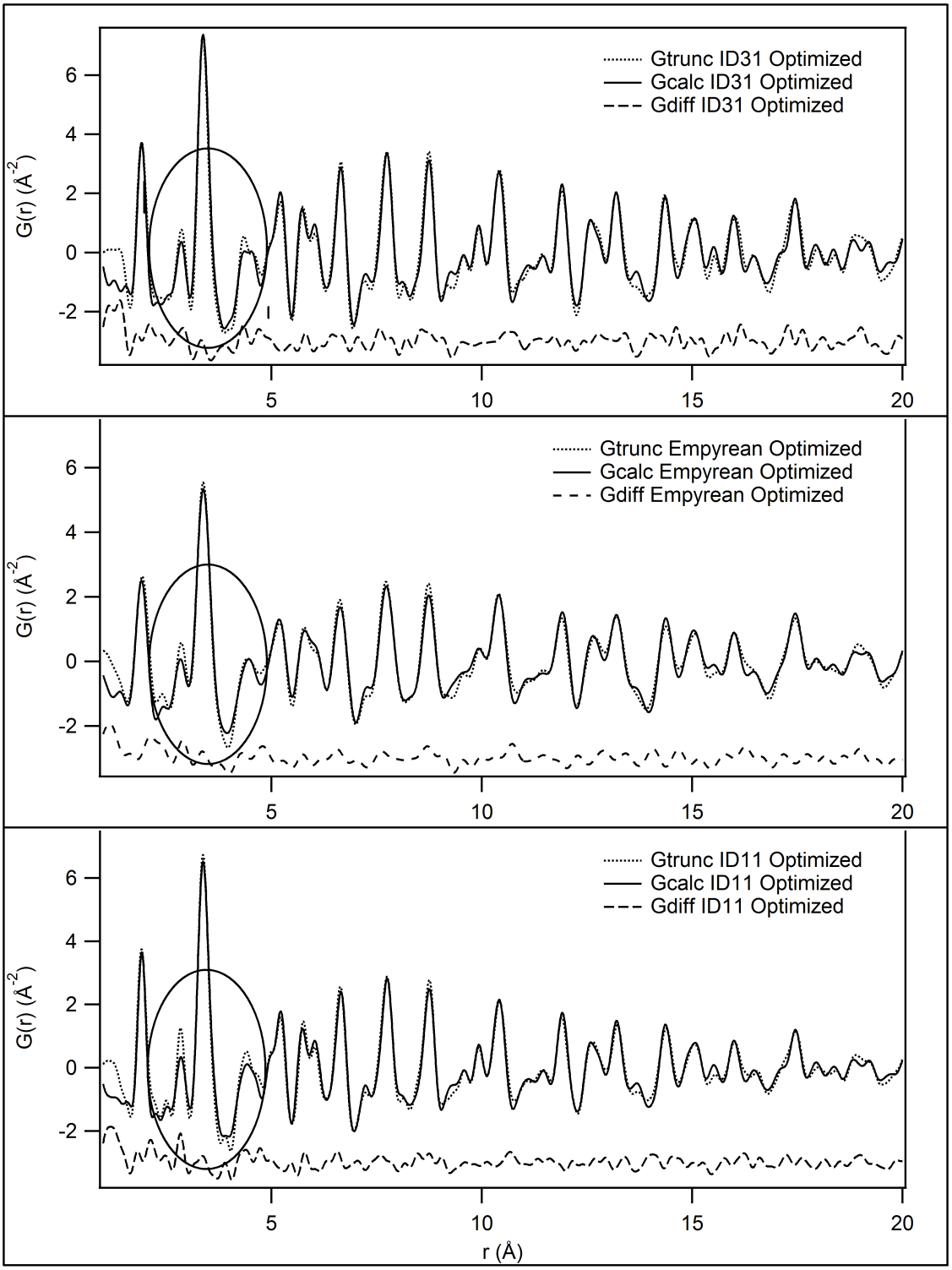

Figure 4.6: Fits of three optimized PDFs from r = 1 to 20 Å. Circles indicate the biggest differences in calculated and observed PDFs.

Chapter 5

Ceramics: results and discussion

As reported in chapter 1 the phase transitions and related temperatures in $BaTiO_3$ are very well known, but the eventual modifications due to the Ce introduction are not so clear particularly from the structural point of view. Then, in this chapter, results and interpretations on the average and local structure of ceramic BTC will be presented in order to clarify the role of cerium in the structure evolution.

5.1 Average Structure

The most part of this research is based on total scattering diffraction data. This allows to explore average structure from two different perspectives. Using raw diffraction data an average structure is definable thank to a reciprocal space analysis. Differently correcting, normalizing and Fourier transforming this data it is possible to study average structure in the direct space. In this section these two approaches will be used and compared.

5.1.1 Reciprocal Space

The first step in any crystallographic investigation is probably the structure determination and especially the choice of the right space group to describe properly the atomic arrangement. In barium titanate phase transitions are very subtle and it is quite difficult to correctly define them. The crystallographic symmetries of the explored models are: cubic (Pm-3m), tetragonal (P4mm), orthorhombic (Amm2), and rhombohedric (R3m). This because usually doped $BaTiO_3$ maintains the structures of pure perovskite, but with differences in stability field and sometimes with some omitted phases depending on doping type and amount. For example this is the case of $BaTi_{1-x}Zr_xO_3$ (Buscaglia et al. 2014), $BaTi_{1-x}Sn_xO_3$ (Veselinovic et al. 2014) and $BaTi_{1-x}Hf_xO_3$ (Anwar et al. 2006). Considering the high resolution data obtained for ceramic samples (BTC 2, 5, 10 and 20), the primary action to do is a visual comparison of diffractograms paying attention on peak evolutions. In order to better examine these, it is useful to underline the most significant differences between the structures which occur during $BaTiO_3$ transitions. In table 5.1 some typical peak splitting used to discriminate the different space groups are reported.

Cubic	Tetragonal	Orthorhombic	Rhombohedric
(111)	(111)	(002), (102), (120)	(111), (-111)
(200)	(002), (200)	(022), (200)	(020)
(211)	(112), (211)	(113), (131), (202), (220)	(121), (-2-11)
(220)	(202), (220)	(004), (040), (222)	(220), (-220)

Table 5.1: Miller indices related to similar *d* spacing values are reported for the four structures of $BaTiO_3$.

BTC2 diffraction data are shown in figure 5.1, and particular peaks as a function of the temperature are evidenced in figure 5.2. This sample has been collected in the first experiment grinding both inner and external ceramic which present slight different stoichiometry. In any case data of the two separated components are available, but collected with a very less resolution. Therefore high resolution data has been favourite both for visual comparison and successive Rietveld structural analysis. Comparing different temperatures, it is evident that all patterns are well analysable distinguishing easily the four temperatures. Taking into account the indications above reported in table 5.1 and in particular considering the (220) and its mutation, BTC2 150 K seems to be rhombohedric, orthorhombic and tetragonal respectively at 270 and 350 K and it is cubic at 450 K.

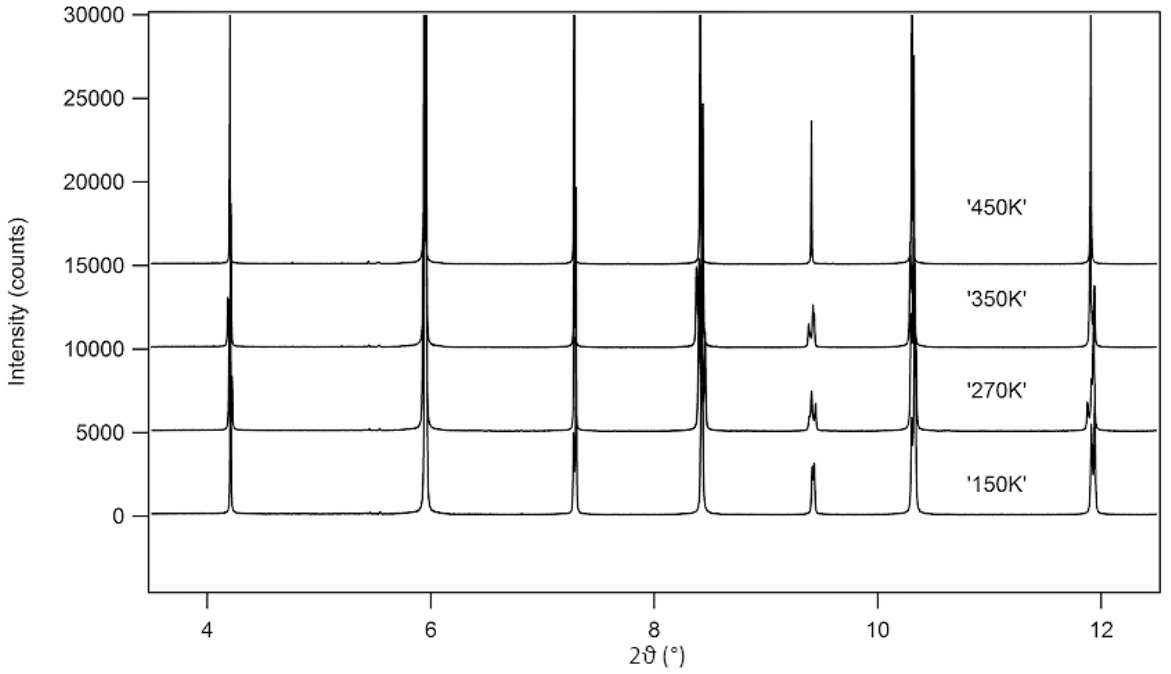

Figure 5.1: BTC2 diffractograms at different temperatures: data are shown in a waterfall-like diagram.

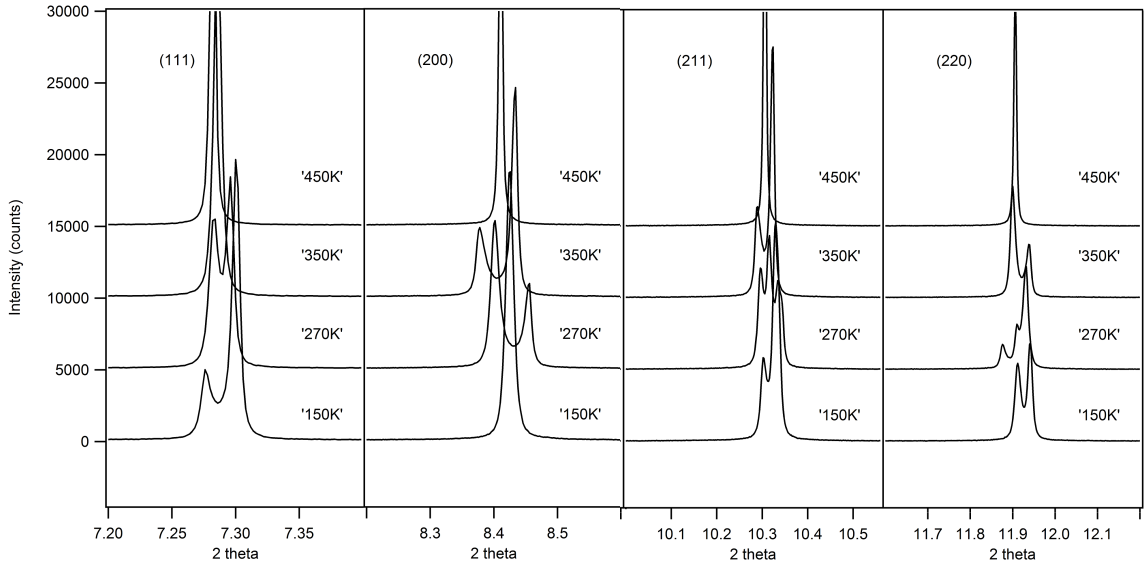

Figure 5.2: BTC2: the evolution of particular peaks is shown in order to better appraise phase transitions.

In the same way BTC5 diffractograms, in figure 5.3, are compared. Taking a look of figure 5.4 and in particular on the (220), structure seems to be cubic at 420 and 380 K. At 350 K a clear shoulder appears and, combining this to the evolution of the (200), it is possible to recognize a tetragonal phase. The nature of the room temperature structure is not obvious. In any case the total lack of any indication of an orthorhombic transition and the similarity to BTC5 200K, which is clearly rhombohehdric, entail the choice of R3m space group also for the 300 K.

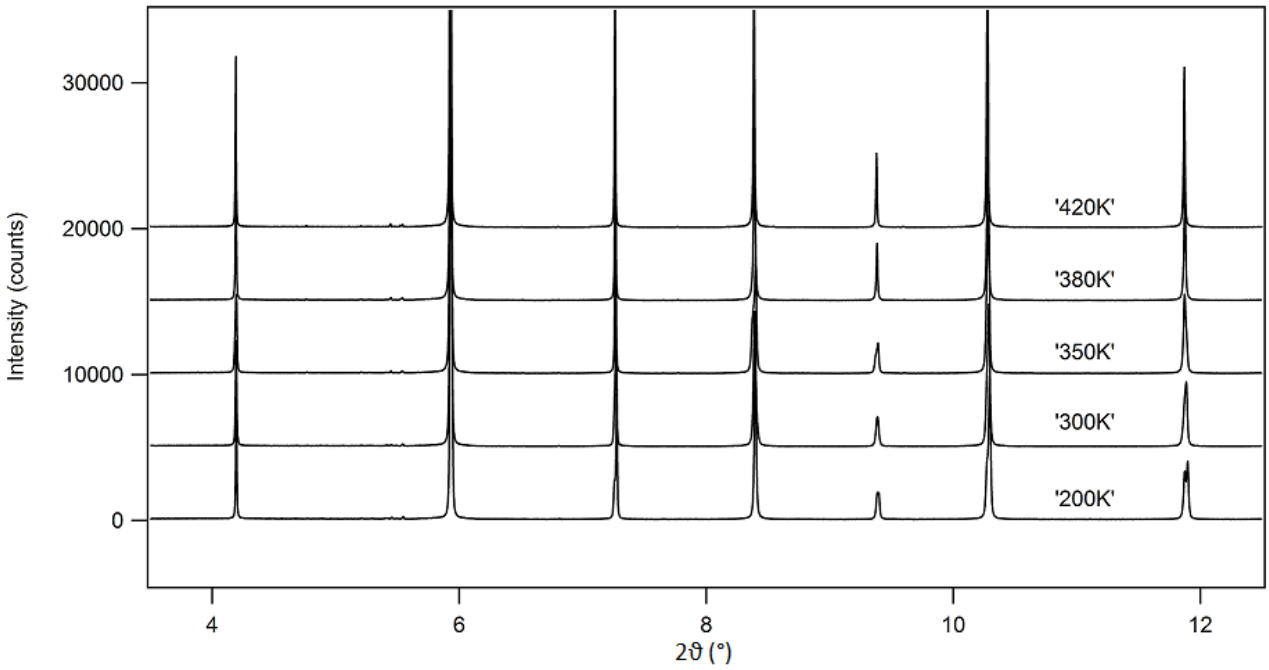

Figure 5.3: BTC5 diffractograms at different temperatures: data are shown in a waterfall-like diagram.

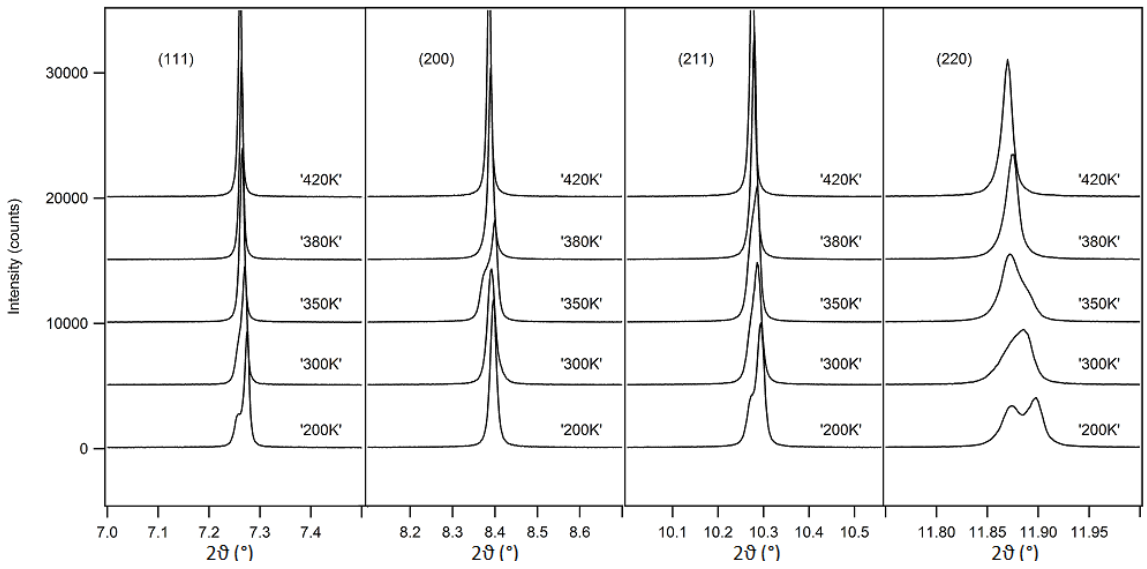

Figure 5.4: BTC5: the evolution of particular peaks is shown in order to better appraise phase transitions.

$BaTiO_3$ containing 10 % of cerium presents clear different structural transformations with a direct transition between cubic to rhombohedric, figure 5.5. Selected particulars of patterns in 5.6 demonstrate this, especially peak (220). This shows in fact a very sharp shape at 400 K (cubic) which becomes broader with cooling until a definitive splitting at 200 K and more evidently at 100 K. Despite this, it is not possible at this point to define certainly the nature of the BTC10 300K which could be cubic or slightly rhombohedric.

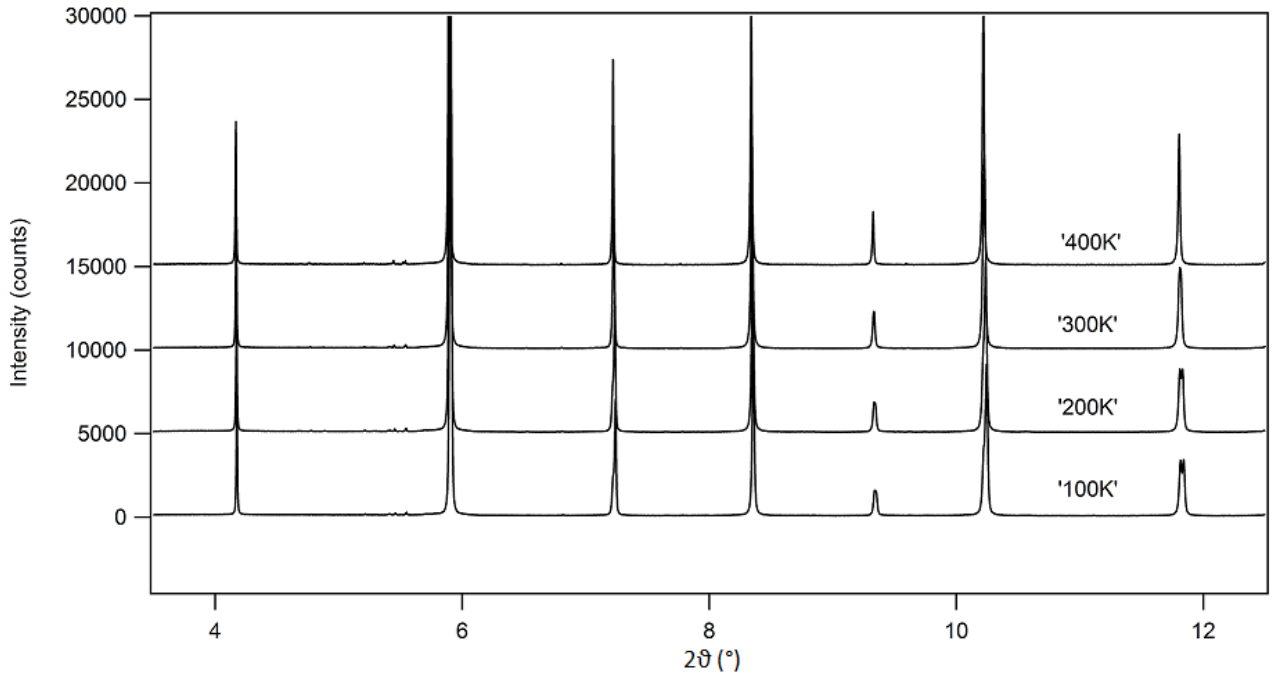

Figure 5.5: BTC10 diffractograms at different temperatures: data are shown in a waterfall-like diagram.

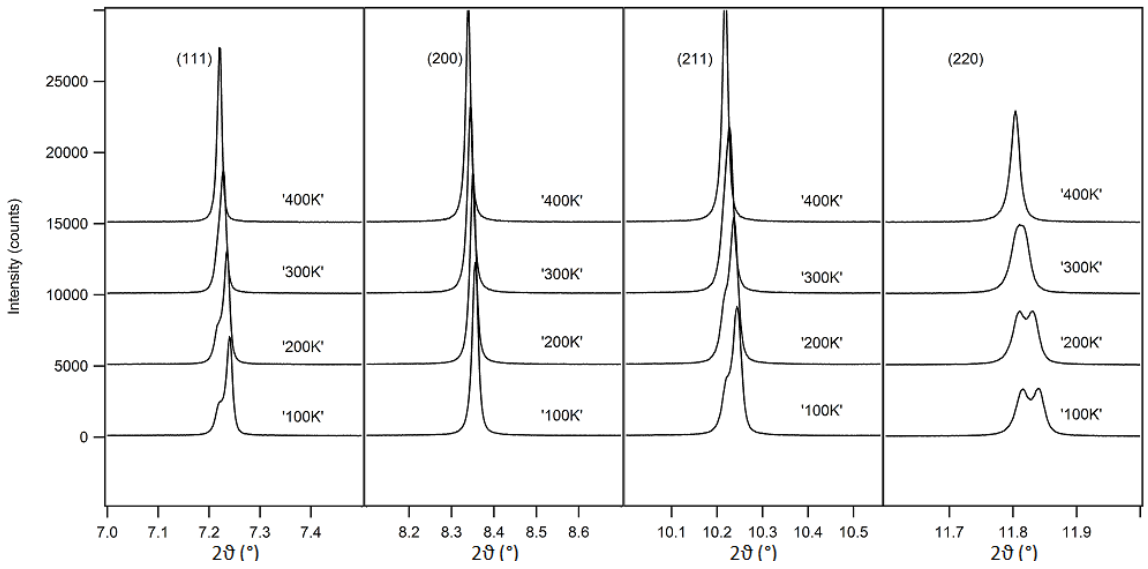

Figure 5.6: BTC10: the evolution of particular peaks is shown in order to better appraise phase transitions.

Figures 5.7 and 5.8 report diffrattograms of BTC doped with 20 % of cerium. In this comparison patterns do not show clear differences with temperature increase and in addition no peak split or shoulder appears demonstrating the stability of cubic phase for all data collected. In any case, especially for the lowest temperature, peaks are broader and for the (220) it is possible to notice a little asymmetry which could be a signal of an imminent rhombohedric transition.

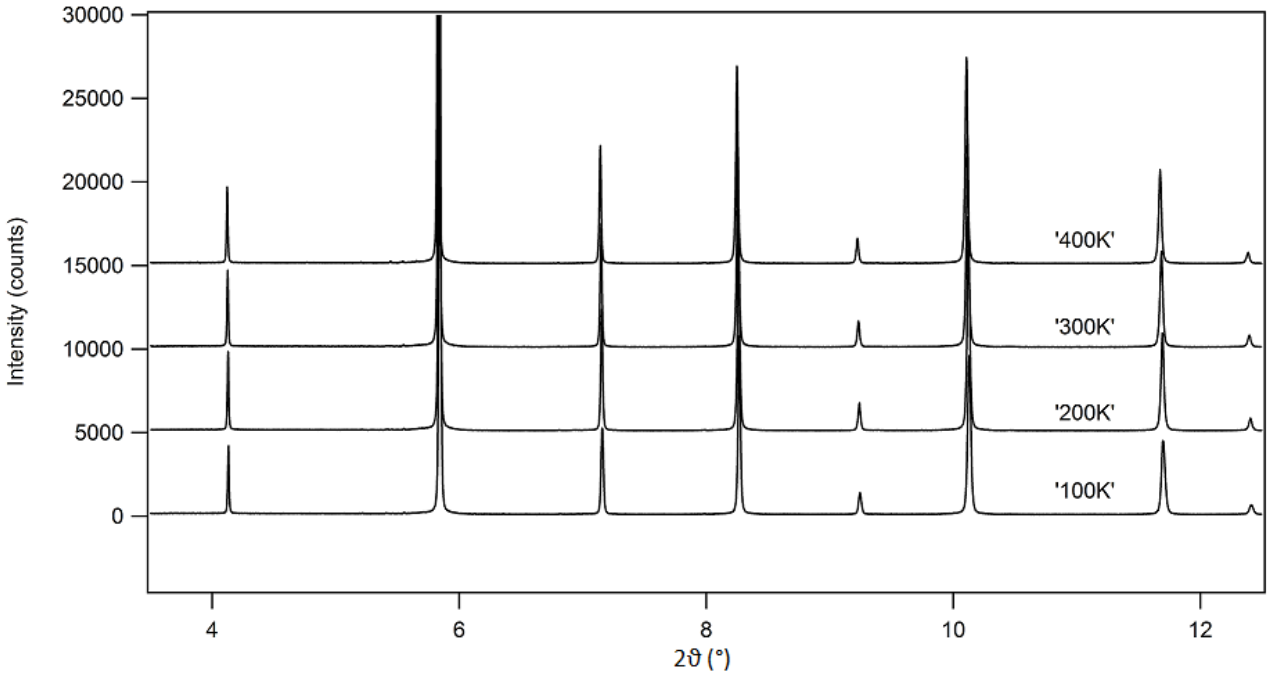

Figure 5.7: BTC20 diffractograms at different temperatures: data are shown in a waterfall-like diagram.

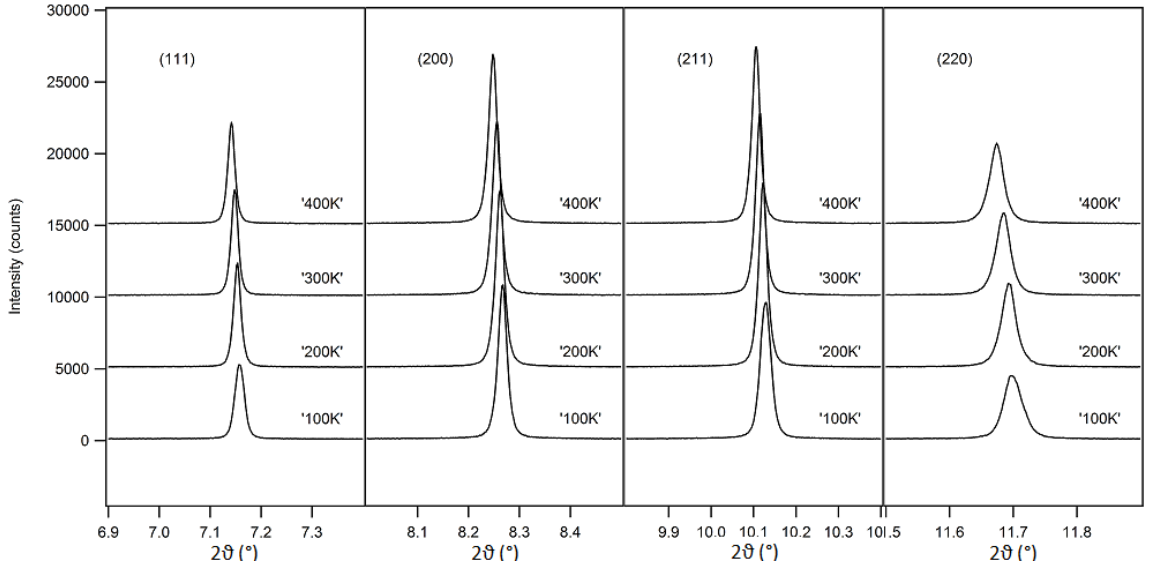

Figure 5.8: BTC20: the evolution of particular peaks is shown in order to better appraise phase transitions.

All diffractograms and peaks belonging to different structures have been opportunely yet presented then, in order to conclude the visual analysis of high resolution diffraction data, it is necessary to make a final and important consideration which is here described for the sake of convenience. Re-examining with attention all data, as in figure 5.9, it is possible to notice some additional peaks. These do not belong to space groups treated, but they are probably linked to some residual impurities. However the amount is very small and in the following dissertation it will be then omitted considering samples as pure.

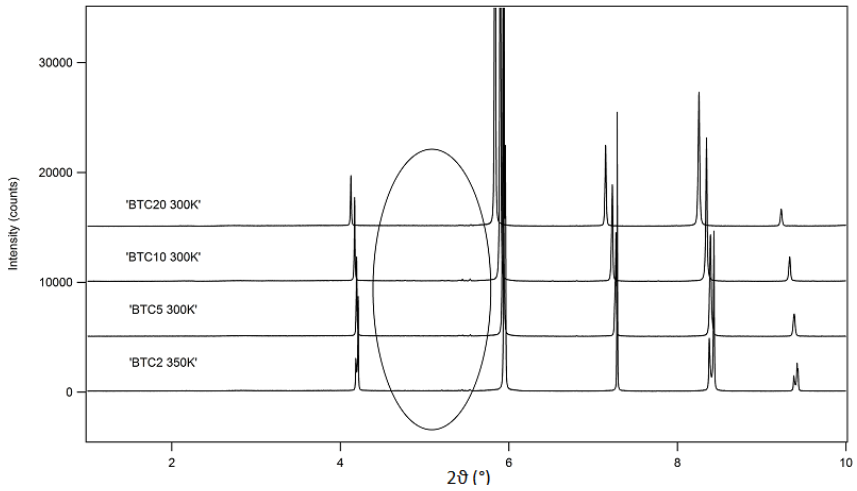

Figure 5.9: Comparison of few high resolution data by waterfall-like diagram. Impurities are evidenced by a circle.

BTC30 is a particular case. This sample compared with others has been indeed collected with a different strategy (experiment MA2497 described in subsection 3.2.2). 2D detector used for data obtaining does not allow to achieve the high resolution necessary to detect phase transition. In one hand this situation has been determined by sample preparation timing and machine time assignment, on the other dielectric measurements (Curecheriu et al. 2016) demonstrate a relaxor behaviour for this sample. In other words $BaTi_{0.7}Ce_{0.3}O_3$ should be cubic at all temperatures, then high resolution data should be not necessary. In figure 5.10 diffrattograms at various temperatures are reported: differently to the other samples peak broadening impedes any consideration. In any case it is clear that all diffractograms are similar, almost identical, with same shapes and aspect.

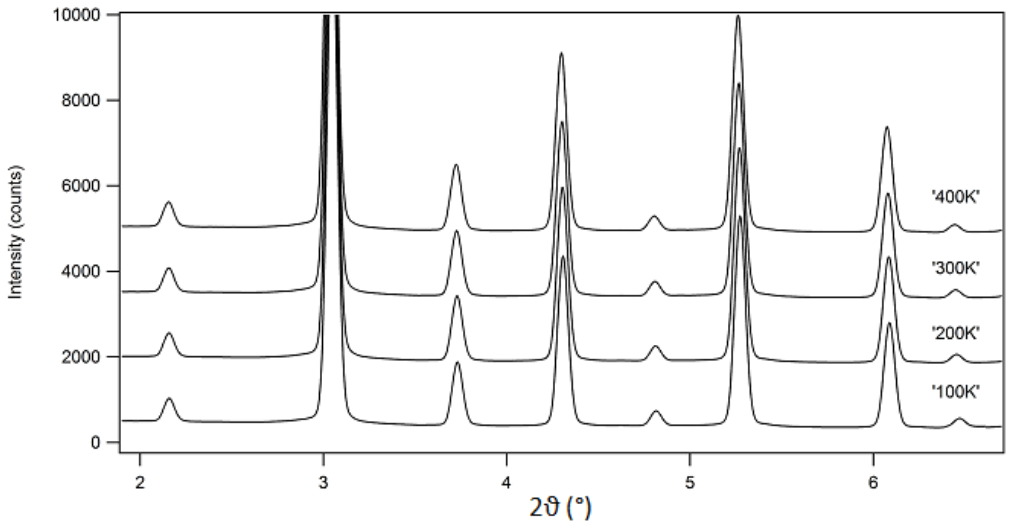

Figure 5.10: BTC30 diffractograms at different temperatures: data are shown in a waterfall-like diagram.

The visual comparison made for all diffraction data gives a first result on the phase stabilities of BTCs as function of temperatures and doping. Obviously this is not sufficient to a correct interpretation of the transitions and structural analyses are necessary to better recognize the right structural model. As reported in different papers (Buscaglia et al. 2014) (Petkov et al. 2008) the best way to do this is a comparison, in terms of the best fitting (Rw value), of different refinements where different single structures are used. Again the four structures, which occur in the transitions of pure $BaTiO_3$, have been taken into account. Maud software (Lutterotti & Wenk 1999) is employed to perform structural refinements and standard materials, Si for the first experiment and LaB_6 for the second, have been first analysed to create *ad hoc* instrumental functions. For all structures a common strategy has been chosen refining: cell parameters, microstrain, crystallite size, isotropic thermal parameters (in this dissertation they will be also named as Uiso) and all the coordinates allowed by the space group. Titanium and cerium has been kept as in the same position simply using a fractional occupancy imposed by the stoichiometry. In tables 5.2, 5.3 and 5.4 the resulting Rw values for the different structures have been reported. Considering the evaluation made by the visual comparison, just few models have been tested depending on the single case. As an example BTC20 does not present evidences of tetragonal and orthorhombic phase and then only refinements with cubic and rhombhoedric structures are performed. NB This analysis is not decisive for sample doped by 2% and 30% and it is not shown: the first does not present any doubt in structure identification, even by visual investigation, and BTC30 data does not allow any detailed structural comparison. In tables below the lowest Rw values, one for each temperature, are evidenced using bold style to underline the best fit and consequently the possible right structure.

BTC5	Rw: Cubic	Rw: Tetragonal	Rw: Orthorhombic	Rw: Rhombohedric
200 K	/	/	/	**0.0920**
300 K	/	/	0.1139	**0.1076**
350 K	/	**0.1017**	0.1484	0.1830
380 K	0.1220	**0.1158**	0.1294	/
420 K	**0.1110**	/	/	/

Table 5.2: Rw values for $BaTi_{0.95}Ce_{0.05}O_3$ fits using different structures. For each temperature lowest value is evidenced by bold style.

BTC10	Rw: Cubic	Rw: Tetragonal	Rw: Orthorhombic	Rw: Rhombohedric
100 K	0.0936	/	/	**0.0800**
200 K	0.1242	/	/	**0.0890**
300 K	0.0995	/	/	**0.0992**
400 K	**0.1127**	/	/	0.1130

Table 5.3: Rw values for $BaTi_{0.9}Ce_{0.1}O_3$ fits using different structures. For each temperature lowest value is evidenced by bold style.

BTC20	Rw: Cubic	Rw: Tetragonal	Rw: Orthorhombic	Rw: Rhombohedric
100 K	0.0795	/	/	**0.0786**
200 K	**0.0831**	/	/	0.0833
300 K	**0.0816**	/	/	0.0822
400 K	**0.0863**	/	/	0.0864

Table 5.4: Rw values for $BaTi_{0.8}Ce_{0.2}O_3$ fits using different structures. For each temperature lowest value is evidenced by bold style.

At the end, in order to define once and for all the structures of samples at each temperature, both visual analyses and refinements have been considered. This because the first approach is deeply subjective and the second often returns not statistically significant different Rw values (*e.g.* BTC10 300K). In table 5.5 definitive structures used

then for detailed analysis and derived by the double investigation above reported are presented. As discussed above, BTC30 has been described as cubic for all the temperatures.

Temperature	$BaTiO_3$	BTC2	BTC5	BTC10	BTC20	BTC30
100 K	Rhombohedric			Rhombohedric	Rhombohedric	Cubic
150 K	Rhombohedric	Rhombohedric				
200 K	Orthorhombic		Rhombohedric	Rhombohedric	Cubic	Cubic
270 K	Orthorhombic	Orthorhombic				
300 K	Tetragonal		Rhombohedric	Rhombohedric	Cubic	Cubic
350 K	Tetragonal	Tetragonal	Tetragonal			
380 K	Tetragonal		Tetragonal			
400 K	Cubic			Cubic	Cubic	Cubic
420 K	Cubic		Cubic			
450 K	Cubic	Cubic				

Table 5.5: Structures for $BaTi_{1-x}Ce_xO_3$ as a function of doping and temperatures. In first column transitions for pure $BaTiO_3$ (Kwei et al. 1993) are shown.

Using bibliographic reference for pure $BaTiO_3$ (Kwei et al. 1993) it is immediately possible to make some considerations about cerium introduction effect. The transition from paraelectric to ferroelectric phase is shifted at lower temperature with cerium increasing. This is clear for BTC10 and become more evident in BTC20. Moreover in pure barium titanate and in BTC2 a classical phase transition is recognized, but this sequence is altered in other cerium doped samples. Indeed, despite not all possible temperatures have been explored, a rhombohedric-cubic transition is observable in BTC10 while, for higher Ce concentration, the lack of evident phase transitions suggests the existence of a relaxor state. This kind of observation are demonstrated also by previous dielectric study performed on the same samples with 10, 20 and 30% of doping and reported by Curecheriu *et al.* (Curecheriu et al. 2016). These results are in good agreement with information reported in introduction. $BaTiO_3$ doped with 5 % of cerium shows a particular sequence. In this case orthorhombic phase is not detected, but this does not mean a complete disappearance of this phase. Furthermore some doubts on phase identification at some temperatures could hide a coexistence of two phases. Despite some attempts it has been impossible to analyse this data using together two structures which are in practice too similar to be correctly determined singularly, then just a single structure has been chosen for each temperature. After the determination of the right symmetry for each sample and temperature, it is then possible to explore in more details the results of structural analyses. In this discussion just few parameters will be considered, however complete tables reporting refinement results could be consulted in appendix. In the same place supplementary information can be found: for example results of Ti and Ce fractional occupancies refinements' performed in order to check the stoichiometry of samples. Refined cell parameters of BTC2 are shown in table 5.6. Angles at 270, 350 and 450 K are reported (figure 5.11) to make a direct comparison, but, as signaled by error lack, they have been kept fixed. Sample presents, as expected, an expansion in terms of volume as a function of the temperature. Cell parameters for BTC2 270K appears too high in comparison to the others. Actually this is just an effect of the S.G. choice: Amm2, which is the higher symmetry describer for this temperature, imposes indeed a different lattice vectors definition with Z=2 leading to over dimensioned *b* and *c* parameters. In order to produce a fair comparison between volumes, value obtained for the orthorhombic phase is rescaled for $Z = 1$. At 350 K tetragonal structure is stable, in this case a shortening on *a*, comparing to that at 150 K, is coupled whit a slight expansion on the c direction reaching a tetragonal distortion metric of 0.6 %, calculated as $100(c/a - 1)$ (Rabuffetti et al. 2014). In general, as said many time before, this material undergoes to very subtle transitions also demonstrated by the evolution of the angle which in rhombohedric phase shows a value really close to 90°.

BTC2	a (Å)	b (Å)	c (Å)	Angle (°)	Volume (Å^3)
150 K	4.01385(2)			89.8667 (2)	64.670(6)
270 K	4.00076(3)	5.68426(4)	5.69892(3)		64.801(2)
350 K	4.01067(2)		4.03505(3)		64.9057(7)
450 K	4.02114(6)				65.020(2)

Table 5.6: Diffraction data analisys: cell parameters at different temperatures of $BaTi_{0.98}Ce_{0.02}O_3$. Volume for 270 K is rescaled for 5 atoms to show a direct comparison with other temperatures.

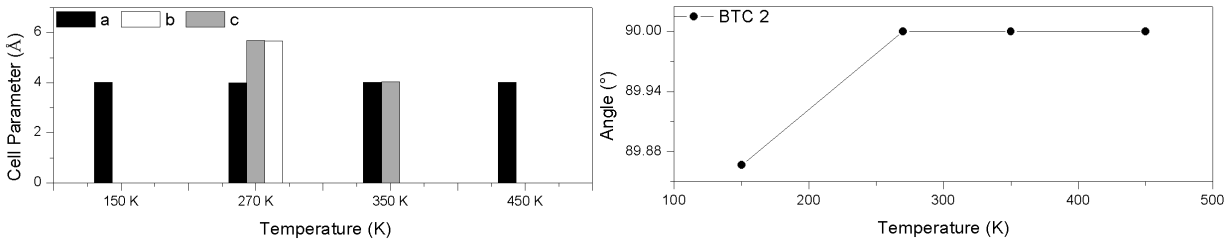

Figure 5.11: Diffraction data analisys of $BaTi_{0.98}Ce_{0.02}O_3$: cell parameters and angle evolution at different temperatures.

Results obtained by BTC5 refinements are shown in table 5.7 and in figure 5.12. As expected for the two temperatures, at which rhombohedric phase is stable, cell parameter *a* shows an expansion coupled with a progressive approach of the angle value to 90°. This is perfectly justifiable considering that temperature raising is ordinary associated to crystallographic symmetry increase. Having said this it is possible to also consider the tetragonal distortion metric, above explained for BTC2, which assumes the value of 0.28 % at 350 K decreasing to 0.1 % at 380 K.

BTC5	a (Å)	b (Å)	c (Å)	Angle (°)	Volume (Å^3)
200 K	4.02849(1)			89.8858(2)	65.380(2)
300 K	4.03104(2)			89.999(8)	65.500(4)
350 K	4.02826(1)		4.03952(2)		65.5488(4)
380 K	4.03123(1)		4.03544(2)		65.5792(4)
420 K	4.034492(7)				65.6698(2)

Table 5.7: Diffraction data analisys: cell parameters at different temperatures of $BaTi_{0.95}Ce_{0.05}O_3$.

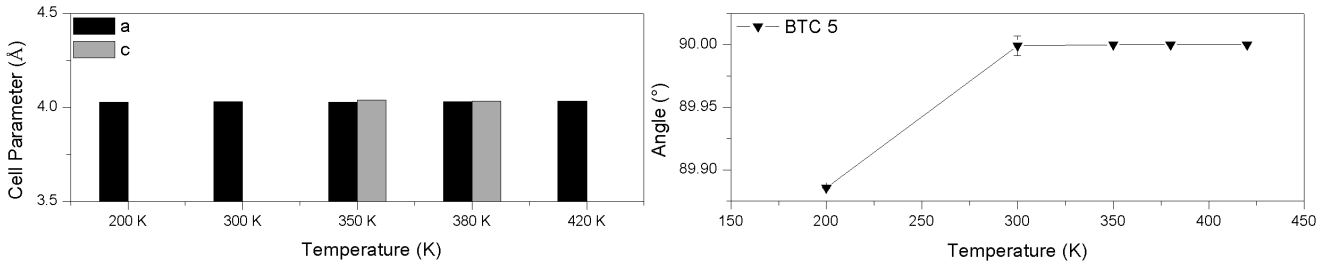

Figure 5.12: Diffraction data analisys of $BaTi_{0.95}Ce_{0.05}O_3$: cell parameters and angle evolution at different temperatures.

Differently from the previous sample, BTC10 presents just one direct transition from rhombohedric to cubic structure. It is then very easy to notice *a* parameter grows with temperature (table 5.8 and figure 5.13). As noticed for other BTC doped with smaller cerium amount, angle value, with temperature increase, approaches 90°. In picture 5.13 this trend seems be to not respect, but actually it is possible to describe rhombohedric cell using one of the two supplementary angles. BTC10 at 300K could be then defined not using 90.020(1)° for the angle, but with

a value of 89.980(1)° which is perfectly in line with other results. Moreover in this case rhombohedric structure is so close to the cubic which could be labeled as *"pseudocubic"*. In literature a clear definition is not presented, then in this dissertation rhombohedric structure presenting an angle ≥ 89.90 and close to a cubic transition will be defined as pseudocubic according to the author's opinion.

BTC10	a (Å)	b (Å)	c (Å)	Angle (°)	Volume (Å^3)
100 K	4.04856(1)			89.8740(2)	66.370(2)
200 K	4.05107(1)			89.8896(2)	66.480(3)
300 K	4.05397(1)			90.020(1)	66.630(3)
400 K	4.05672(1)				66.7614(3)

Table 5.8: Diffraction data analisys: cell parameters at different temperatures of $BaTi_{0.9}Ce_{0.1}O_3$.

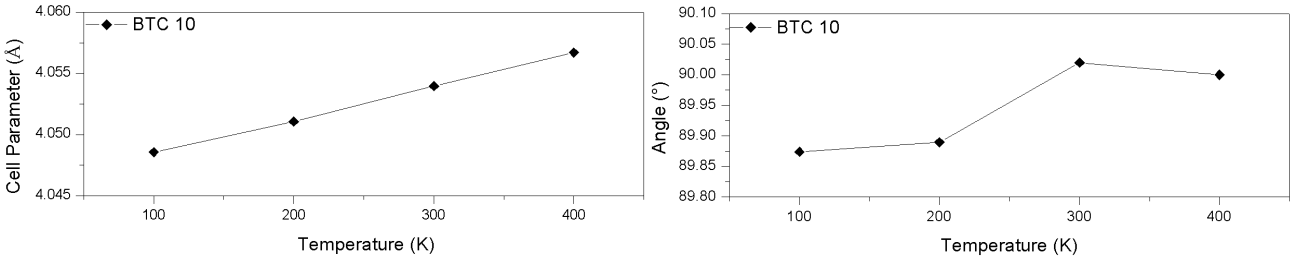

Figure 5.13: Diffraction data analisys of $BaTi_{0.9}Ce_{0.1}O_3$: cell parameters and angle evolution at different temperatures.

$BaTi_{0.8}Ce_{0.2}O_3$, as touched upon, shows very little modification in structure. As reported in table 5.9, only a little phase transition is noticed between 100 and 200 K from pseudocubic to cubic phase. This is also clear from figure 5.14 where the trend of angle is practically flat. In general, as expected, temperature increase causes cell expansion in terms of both *a* parameter and volume.

BTC20	a (Å)	b (Å)	c (Å)	Angle (°)	Volume (Å^3)
100 K	4.09255(1)			89.957(2)	68.5500(3)
200 K	4.0951(1)				68.6757(3)
300 K	4.09814(1)				68.8272(3)
400 K	4.10164(1)				69.0037(3)

Table 5.9: Diffraction data analisys: cell parameters at different temperatures of $BaTi_{0.8}Ce_{0.2}O_3$.

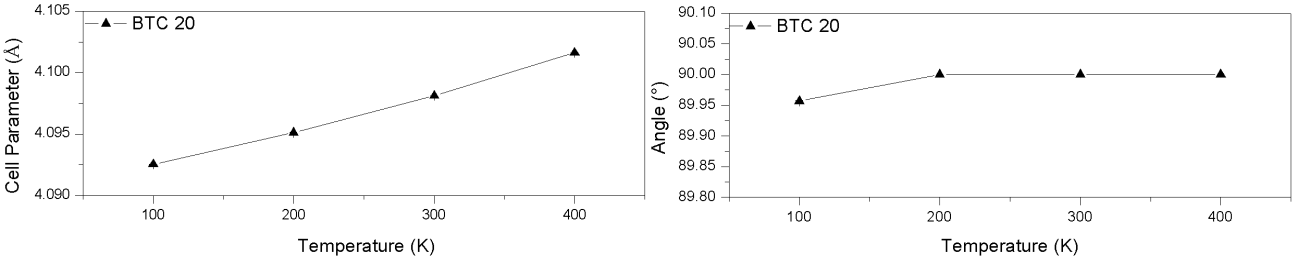

Figure 5.14: Diffraction data analisys of $BaTi_{0.8}Ce_{0.2}O_3$: cell parameters and angle evolution at different temperatures.

BTC30 presents no average structural variation, being cubic at all temperatures investigated. Despite this, refinements of this sample appear complicated. After many tests some problems were individuated on data collected during the second experiment, probably linked to the use of 2D detector. Thus in order to obtained the possible

best results, structural refinements have been performed up to $2\theta = 10°$. In figure 5.15 also angle values, despite they have not been refined, are reported as supplementary information in order to underline the stability of this parameter at different temperatures. Differently to this flat trend, cell edge shows a clear dilatation exactly as the volume.

BTC30	a (Å)	b (Å)	c (Å)	Angle (°)	Volume (Å^3)
100 K	4.1346(2)				70.681(6)
200 K	4.13711(6)				70.810(2)
300 K	4.14035(6)				70.976(2)
400 K	4.14385(6)				71.156(2)

Table 5.10: Diffraction data analisys: cell parameters at different temperatures of $BaTi_{0.7}Ce_{0.3}O_3$.

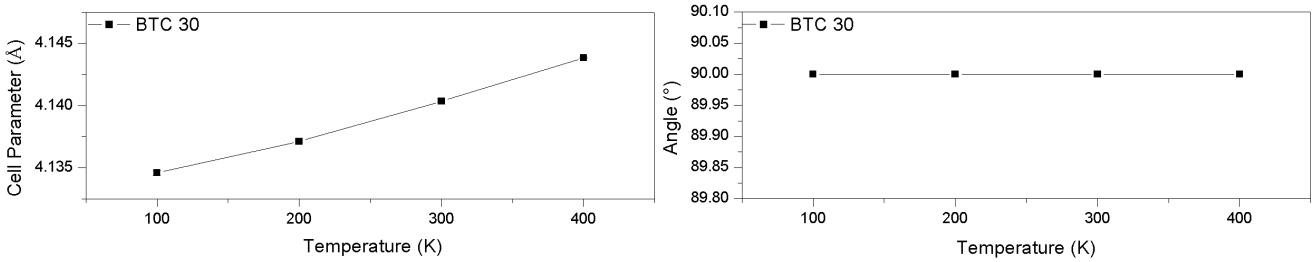

Figure 5.15: Diffraction data analisys of $BaTi_{0.7}Ce_{0.3}O_3$: cell parameters and angle evolution at different temperatures.

Summarizing information reported up to now figure 5.16 is presented. Here a direct comparison of cell volumes obtained for the different BTCs is shown. The right and expected cell expansion as a function of the temperature has been already discussed, but now the same effect is recognizable as a functional of doping increase. Furthermore this last aspect seems to mainly influenced volume spread than the temperature. In addition, in table 5.11, volumetric thermal expansion coefficients, calculated for each sample, are shown.

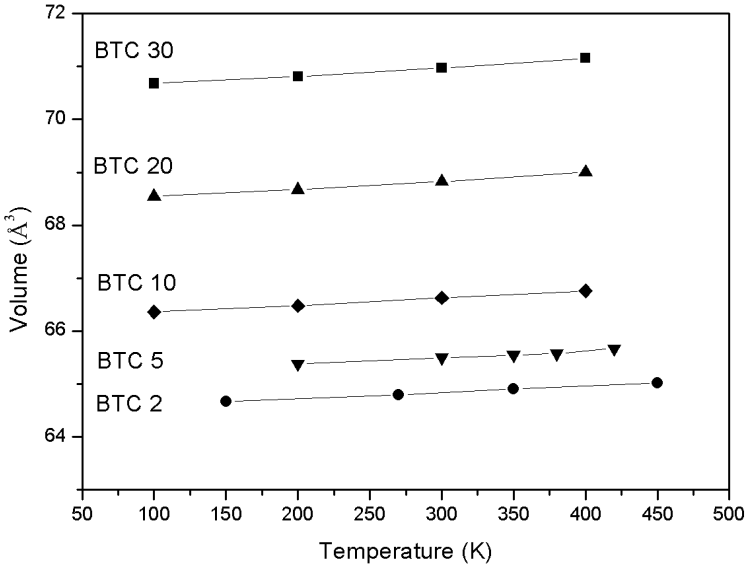

Figure 5.16: Cell volumes calculated by Rietveld analyses as a function of doping and temperatures.

Last considerations on volume evolution could be integrated by other observations made using bibliographic data. In figure 5.17 different types of doping and amount have been compared. In particular volumes at 300 K of

	BTC2	BTC5	BTC10	BTC20	BTC30
α_V	1.86E-05	1.84E-05	1.96E-05	2.19E-05	2.26E-05

Table 5.11: Volumetric thermal expansion coefficients α_V calculated for each sample are reported. Samples with more doping amount show higher values.

$BaTiO_3$ with Sn (Veselinovic et al. 2014) and Zr (Buscaglia et al. 2014) have been reported with results obtained in this research. These three atoms present very different ionic radii: Ce^{4+} is 0.87 Å, 0.72 Å for Zr^{4+} and 0.69 Å for Sn^{4+}. In view of this it is clear that bigger the atoms bigger the volume increase: cerium introduction entails a faster cell expansion with an increase of the regression line slope.

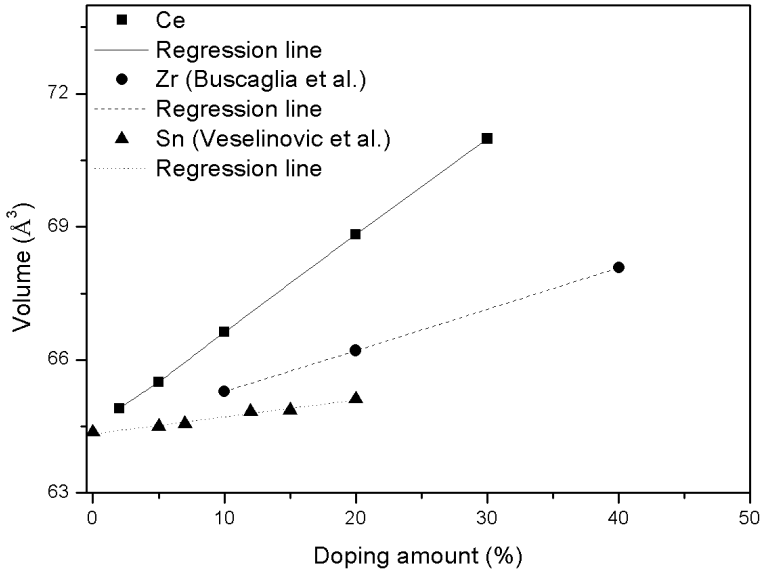

Figure 5.17: Cell volumes of $BaTi1-xM_xO_3$ as a function of different doping at 300K: the case of cerium, zirconium and tin.

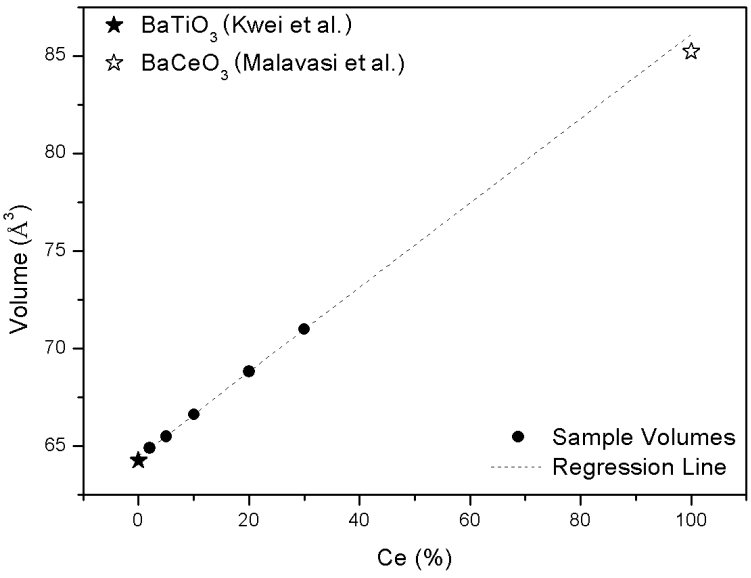

Figure 5.18: Volumes of samples at 300K. Regression line between them is in good agreement with bibliographic results of two end-members.

Using the above reported results for BTCs, it is also possible to make an empirical test to verify the composition of samples as ideal solid solutions using the so called Vegard's law. According to this, unit cell parameters should

vary linearly with composition for a continuous substitutional solid solution in which atoms or ions that substitute for each other are randomly distributed (Jacob et al. 2007). In figure 5.18 volumes at 300 K obtained by refinements are represented by black point, despite BTC2 volume is calculated at 350 K its value could be considered acceptable for this evaluation. In order to determine the trend between the two end-members a regression line between points has been calculated (dashed line) predicting volume at 0 and 100 % cerium amount. The volumes of two referenced structures have been also represented: $BaTiO_3$ (Kwei et al. 1993) by filled star and $BaCeO_3$ (Malavasi et al. 2009) by open star. The good agreement between prediction and real values of the two end-members indicates a random distribution of titanium and cerium in evaluated samples. One of the most important aspects of structural analysis is the possibility to compare cerium and titanium displacement as a function of doping and temperatures. Let remember that these two atoms are constrained in the same position, than at this point it is not possible to discriminate them. In any case the information about Ti displacement is truly relevant to understand the polar behaviour of these materials (as explained in section 1.2). In table 5.12 displacements of B cations (calculated from the center of the cell and using B refined coordinates reported in appendix) are presented for all ferroelectric phases. In order to have a direct comparison between doped and pure $BaTiO_3$, also bibliographic results obtained by Kwei *et al.* (Kwei et al. 1993) are presented. Not all temperatures are available for pure $BaTiO_3$, then results of the temperatures as close as possible to those of BTC have been used.

	B cations displacement (Å)				
Temperature	$BaTiO_3$	BTC2	BTC5	BTC10	BTC20
100 K	0.061(4)			0.039(1)	0.028(2)
150 K	0.077(6)	0.072(1)			
200 K	0.081(5)		0.050(1)	0.029(1)	
270 K	0.096(6)	0.057(1)			
300 K	0.090(3)		0.077(3)	0.042(3)	
350 K	0.079(1)	0.040(2)	0.008(4)		
380 K			0.036(2)		

Table 5.12: B cations displacements at different temperatures for doped and pure $BaTiO_3$ (Kwei et al. 1993).

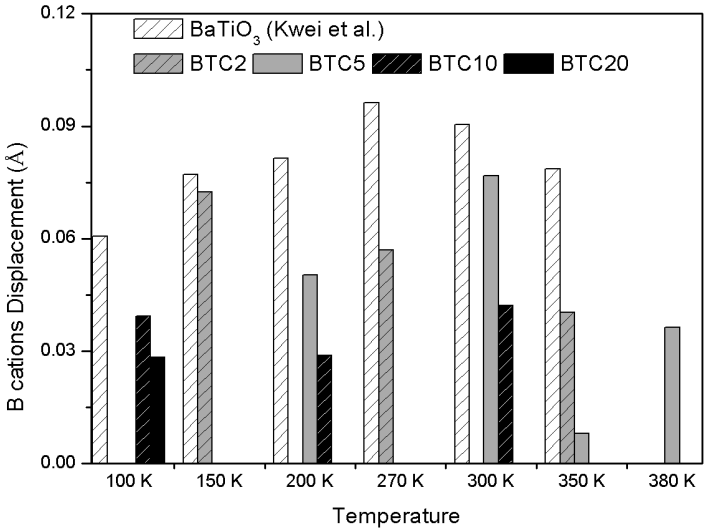

Figure 5.19: B cations displacement at different temperatures for doped and pure $BaTiO_3$ (Kwei et al. 1993). Titanium and cerium have been constrained in same position, then it is not possible to distinguish separately the two different displacements.

Results are also reported in figure 5.19. Despite Kwei *et al.* affirm that Ti displacements are consistently

slightly larger than in earlier reports, it is evident that those obtained in doped samples are certainly smaller. At all the temperatures indeed samples more doped present lower displacements. This graphic demonstrates how cerium introduction limits the total average B displacements. After this deep discussion on cell parameters and atomic positions, it is possible now to move to some particulars as thermal parameters. Results obtained have been reported in tables 5.13, 5.14, 5.15, 5.16 and 5.17. Refinements have been performed using isotropic U (actually recalculated from B values), as mentioned before Ti and Ce share the same parameter constrained to be identical.

BTC2	Uiso Ba (Å^2)	Uiso Ti-Ce (Å^2)	Uiso O (Å^2)
150 K	0.00241(8)	0.0028(3)	0.0118(8)
270 K	0.0033(1)	0.0061(4)	0.014(1)
350 K	0.0045(1)	0.0056(4)	0.014(1)
450 K	0.00637(8)	0.0105(1)	0.0134(5)

Table 5.13: Diffraction data analisys: Uiso of $BaTi_{0.98}Ce_{0.02}O_3$ at different temperatures.

BTC5	Uiso Ba (Å^2)	Uiso Ti-Ce (Å^2)	Uiso O (Å^2)
200 K	0.00355(4)	0.0061(1)	0.0103(1)
300 K	0.0063(1)	0.0024(6)	0.013(1)
350 K	0.00693(5)	0.0058(1)	0.0156(5)
380 K	0.00830(6)	0.0067(3)	0.0129(6)
420 K	0.00846(5)	0.0120(1)	0.0166(1)

Table 5.14: Diffraction data analisys: Uiso of $BaTi_{0.95}Ce_{0.05}O_3$ at different temperatures.

BTC10	Uiso Ba (Å^2)	Uiso Ti-Ce (Å^2)	Uiso O (Å^2)
100 K	0.00331(4)	0.0060(1)	0.0101(5)
200 K	0.00548(5)	0.0080(1)	0.0124(1)
300 K	0.00733(8)	0.0090(4)	0.009(1)
400 K	0.00980(5)	0.0125(1)	0.0196(4)

Table 5.15: Diffraction data analisys: Uiso of $BaTi_{0.9}Ce_{0.1}O_3$ at different temperatures.

BTC20	Uiso Ba (Å^2)	Uiso Ti-Ce (Å^2)	Uiso O (Å^2)
100 K	0.0056(3)	0.0070(3)	0.007(1)
200 K	0.00800(9)	0.00964(9)	0.0201(4)
300 K	0.00987(9)	0.01092(9)	0.0220(4)
400 K	0.01199(9)	0.01250(9)	0.0250(4)

Table 5.16: Diffraction data analisys: Uiso of $BaTi_{0.8}Ce_{0.2}O_3$ at different temperatures.

BTC30	Uiso Ba (Å^2)	Uiso Ti-Ce (Å^2)	Uiso O (Å^2)
100 K	0.00067(3)	0.0105(4)	0.042(1)
200 K	0.0024(3)	0.0115(4)	0.044(1)
300 K	0.0041(3)	0.0127(4)	0.0474(1)
400 K	0.0061(3)	0.012(4)	0.051(1)

Table 5.17: Diffraction data analisys: Uiso of $BaTi_{0.7}Ce_{0.3}O_3$ at different temperatures.

In figure 5.20 Uiso values for BTC 2, 5, 10 and 20 have been shown as a function of temperature. These four graphics are reported together because these samples were collected with the same conditions. Nonetheless

Uiso results seem to be coherent with the temperatures. Differently BTC30 presents too high values (table 5.17), obviously determined by problems in data collection, then related graphic is presented separately.

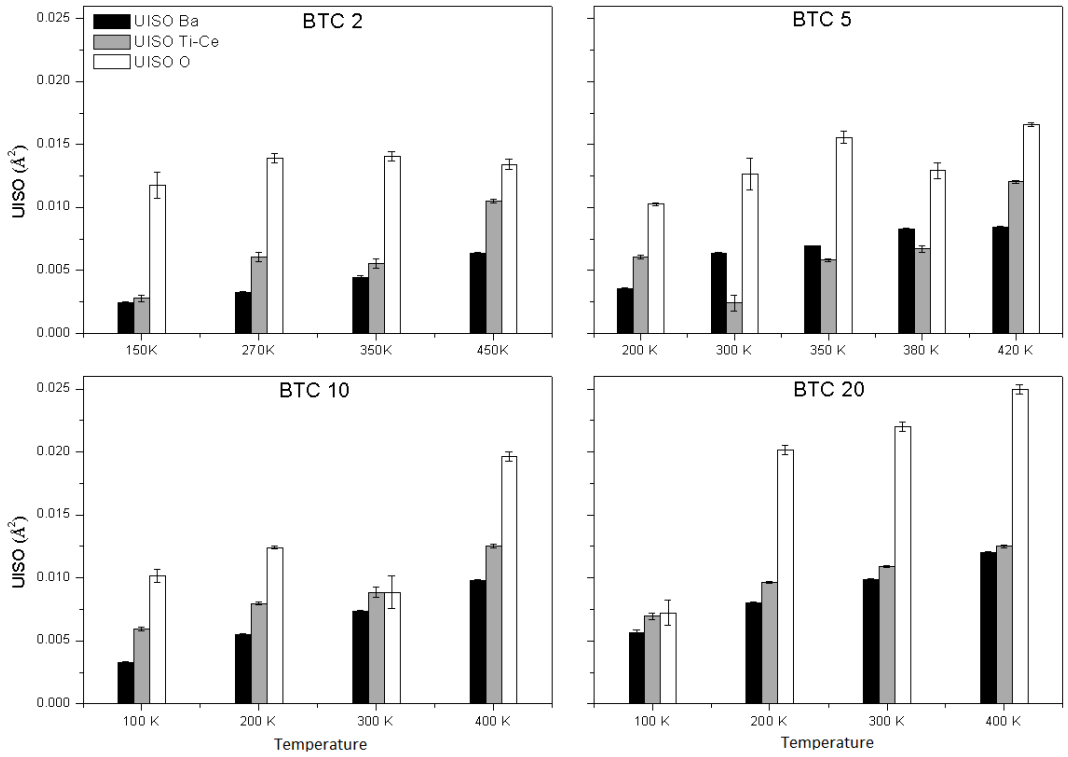

Figure 5.20: Uiso for BTC 2, 5, 10 and 20 are shown as a function of the temperatures.

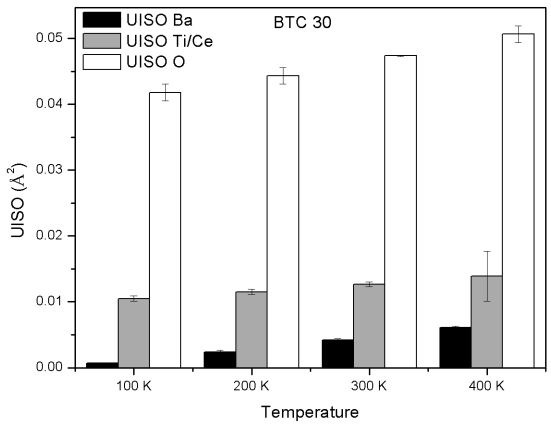

Figure 5.21: Uiso for BTC30 are shown as a function of the temperatures.

In general, at the most of the temperatures, parameters present a clear trend (figure 5.20): barium is the biggest atom then it is the most motionless, titanium and cerium have a little more high Uiso, but oxygen shows very variable and almost very high values. This result is a clear signal of disorder. Indeed, as previous mentioned, in this kind of analysis the information regarding the correlation among the local variations is lost as soon as the assumption of perfect periodicity is made. Thus if there are local atomic displacements away from the crystallographic sites, they are reflected in the average crystal structure only in terms of the large thermal, or Debye-Waller, factor (especially for light atoms as oxygen) and cannot be easily separated from the lattice vibration (Egami 2002). Therefore BTC 2, 5, 10 and 20 are probably affected by a disorder which is not possible to model using classical

structural analysis. Furthermore not all temperatures present coherent Uiso values, in some cases (for example BTC5 at 300, 350 and 380 K) titanium and cerium present thermal motions smaller than barium. BTC30, despite problems on data mentioned before, presents similar trend (figure 5.21), but with values higher than those obtained for the other samples. In any case also for this perovskite it is possible to suppose a great structural disorder. Another parameter which is related to structural disorder and should be evaluated is the microstrain. The shape of diffraction peaks depends on the size of coherent domains and by strain caused by any lattice imperfection (dislocations and different point defects). Evaluate the latter is then important to determine defects in BTC. In Maud software this is performed by the approach proposed by Nandi (Nandi et al. 1984) based on the Stokes' method of Fourier-transform deconvolution. Here the estimation of crystallite size and microstrain is executed unfolding the physically broadened line profile from the observed profile using a previously determined instrumental function (Balzar 2000). Obtained isotropic r.m.s. (root mean square) microstrain values of different samples are reported in table 5.18. Only high resolution data has been employed in this analysis.

BTC2	Microstrain	BTC5	Microstrain	BTC10	Microstrain	BTC20	Microstrain
150 K	0.0004883(2)	200 K	0.000640(2)	100 K	0.000753(1)	100 K	0.001083(3)
270 K	0.0005190(2)	300 K	0.001066(3)	200 K	0.000737(2)	200 K	0.000947(2)
350 K	0.000469(2)	350 K	0.000650(2)	300 K	0.0009055(4)	300 K	0.000915(2)
450 K	0.000219(1)	380 K	0.000373(2)	400 K	0.000548(2)	400 K	0.000907(2)
		420 K	0.000359(1)				

Table 5.18: R.m.s microstrains calculated by Maud software for BTC2, 5, 10 and 20 at different temperatures.

Figure 5.22 shows, despite some exceptions, a general increase of r.m.s microstrain as a function of doping amount. Only BTC5 at 300 K presents an unusual big microstrain, but, remarking some previous hypotheses, this could be an effect originated by a supposed coexistence of two different polymorphs. However results do not show a clear tendency as a function of temperature, but the trend related to the doping is rather evident.

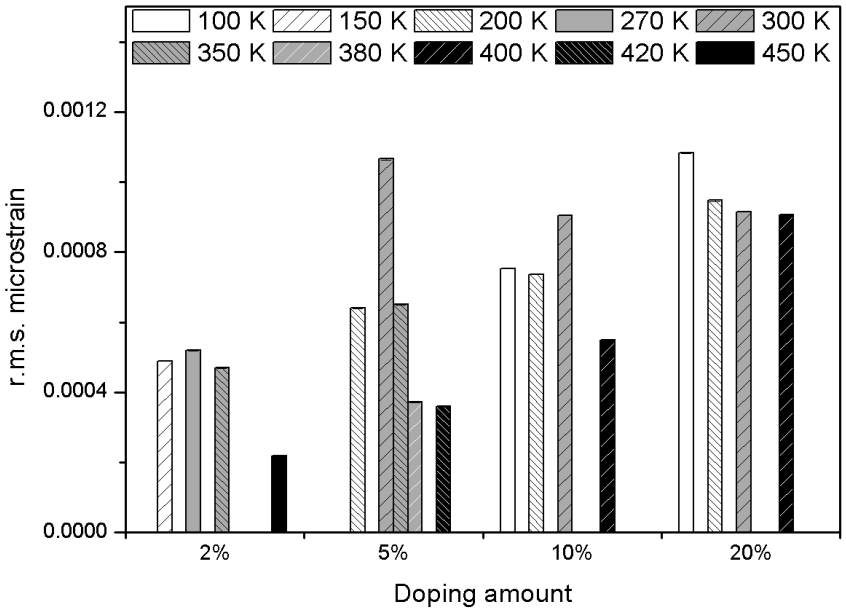

Figure 5.22: Comparison of r.m.s microstrain values of BTC2, 5, 10 and 20 as a function of temperature.

This discussion underlines and proves how high cerium amount leads to the creation of structural defects which are then created in order to reduce the stress induced by the big size of the dopant element. However it

is impossible to determine in this simple way the type of involved defects, in fact microstrain parameter could incorporate different contributions from, as an example, dislocation or stacking faults. Moreover the approach used to determine the effects of microstrain is rather basic and it has led to a not perfect peak fit especially on tails, as showed in figure 5.23.

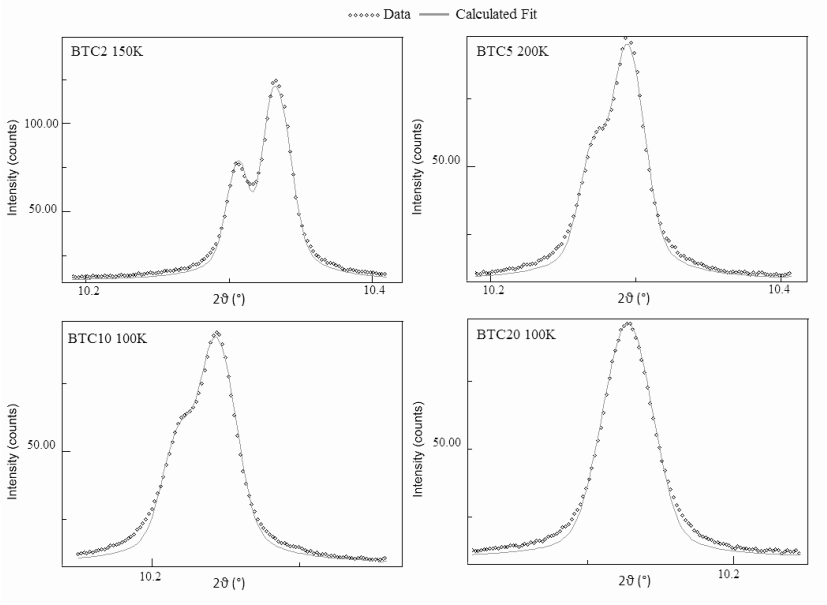

Figure 5.23: Example of peak profile fit for different samples, peak tails seem to be not correctly fitted.

5.1.2 PDF Average Structure

In this subsection results and discussion on average structure obtained by Pair Distribution Function are presented. This kind of analysis allows to explore average structure in direct space.

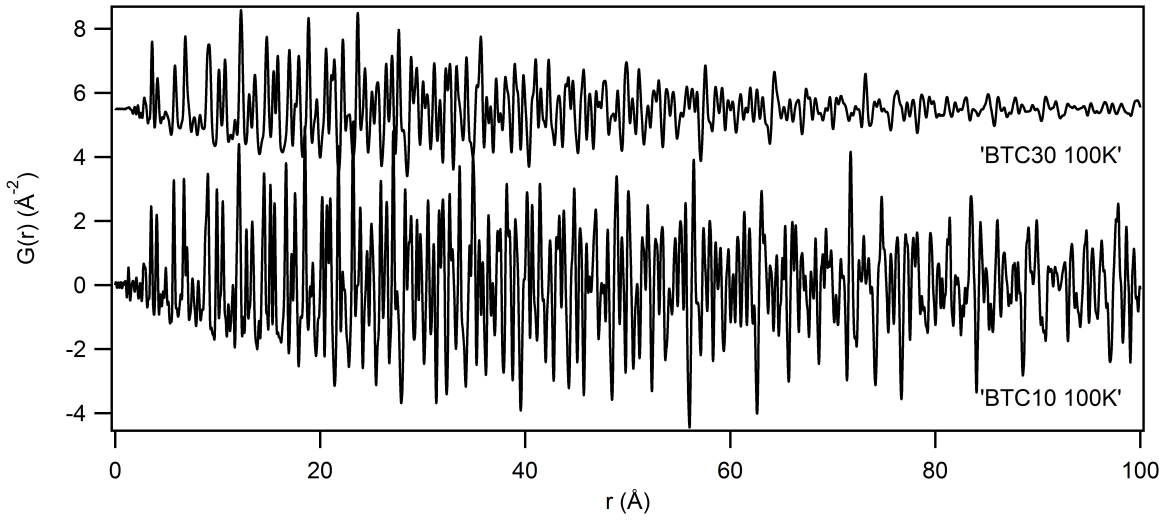

Figure 5.24: Pair Distribution Functions calculated for BTC30 and BTC10 at 100 K are presented in waterfall diagrams in order to compare signal damping.

Just three samples (BTC 5, 10 and 20) have been taken into account. High resolution data for BTC2 is not suitable for a direct space transformation being a sum of two different, although similar, materials. On the other

hand data of separated parts and of BTC30 present a high signal damping which does not allow to explore high *r* values (figure 5.24). Pair Distribution Functions have been obtained using PDFgetX3 software (Juhas et al. 2013). PDFs were calculated exactly in the same way for all samples of the first experiment to make then a fair comparison. In order to obtain good functions: *qmaxinst* was fixed at 27 and *qmax* at 26, *rpoly* was 1.4. Empty capillary, collected at room temperature, has been used to the background subtraction and *bgscale* was fixed at 1. This allows to eliminate not only the capillary, but also instruments and air contributions. Refinements were performed by PDFgui (Farrow et al. 2007). Standard material has been used to set *Qdamp*, which have been then kept fixed at 0.03. Analysis of the average structure has been performed between 50 and 100 Å using different single structures, again Rw values have been compared to understand the phase stability. Likewise in Rietveld refinement, Ti and Ce are in the same position with fractional occupancy based on the stoichiometry and all parameters allowed by S.G rules have been refined. In table 5.19, 5.20 and 5.21 Rw values are presented, the lowest are evidenced by bold style.

BTC5	Rw: Cubic	Rw: Tetragonal	Rw: Orthorhombic	Rw: Rhombohedric
200 K	0.1603	0.1446	0.1413	**0.1234**
300 K	0.1424	0.1327	0.1388	**0.1316**
350 K	0.1475	**0.1350**	0.1439	0.1475
380 K	0.1320	**0.1278**	0.1289	0.1296
420 K	**0.1515**	0.1528	0.2598	0.2827

Table 5.19: Rw vules for $BaTi_{0.95}Ce_{0.05}O_3$ fits using different phases: *r* range 50-100 (Å). For each temperature lowest Rw value is evidenced in bold style.

BTC10	Rw: Cubic	Rw: Tetragonal	Rw: Orthorhombic	Rw: Rhombohedric
100 K	0.1840	0.1699	0.1431	**0.1365**
200 K	0.1325	0.1260	0.1224	**0.1138**
300 K	0.1204	0.1169	0.1447	**0.1159**
400 K	**0.1327**	0.1306	0.1407	0.1444

Table 5.20: Rw vules for $BaTi_{0.9}Ce_{0.1}O_3$ fits using different phases: *r* range 50-100 (Å).For each temperature lowest Rw value is evidenced in bold style.

BTC20	Rw: Cubic	Rw: Tetragonal	Rw: Orthorhombic	Rw: Rhombohedric
100 K	0.1268	0.1218	0.1296	**0.1108**
200 K	**0.1029**	0.1103	0.1114	0.1190
300 K	**0.1113**	0.1091	0.1876	0.1164
400 K	**0.1658**	0.1673	0.3822	0.1704

Table 5.21: Rw vules for $BaTi_{0.8}Ce_{0.2}O_3$ fits using different phases : *r* range 50-100 (Å). For each temperature lowest Rw value is evidenced in bold style.

Structural results of the phases presenting the best fit are reported entirely in appendix and shortly in tables: 5.22, 5.23 and 5.24. Considering that Pair Distribution Functions extrapolated by PDFgetX3 do not include estimated standard deviations (ESDs) of the data points, errors calculated during refinements may be meaningless. In the light of that deviations reported, here and then, are guesstimated considering values bigger of one order of magnitude than those obtained by Rietveld analysis. Discussion on cell parameters and Uiso is postponed to the following subsection where the comparison between Pair Distribution Function and Rietveld analysis will be shown.

BTC5	a (Å)	b (Å)	c (Å)	Angle (°)	Uiso Ba (Å^2)	Uiso Ti-Ce (Å^2)	Uiso O (Å^2)
200 K	4.0288(5)			89.880(5)	0.006(5)	0.009(5)	0.022(5)
300 K	4.0311(5)			89.946(5)	0.010(5)	0.011(5)	0.027(5)
350 K	4.0283(5)		4.0395(5)	90	0.009(5)	0.014(5)	0.018(5)
380 K	4.0328(5)		4.0360(2)	90	0.010(5)	0.011(5)	0.015(5)
420 K	4.0346(5)			90	0.009(5)	0.014(5)	0.030(5)

Table 5.22: PDF average structure: Uiso and cell parameters of $BaTi_{0.95}Ce_{0.05}O_3$ at different temperatures.

BTC10	a (Å)	b (Å)	c (Å)	Angle (°)	Uiso Ba (Å^2)	Uiso Ti-Ce (Å^2)	Uiso O (Å^2)
100 K	4.0487(5)			89.866(5)	0.006(5)	0.009(5)	0.023(5)
200 K	4.0512(5)			89.892(5)	0.009(5)	0.011(5)	0.027(5)
300 K	4.0541(5)			89.974(5)	0.011(5)	0.011(5)	0.032(5)
400 K	4.0569(5)			90	0.011(5)	0.015(5)	0.035(5)

Table 5.23: PDF average structure: Uiso and cell parameters of $BaTi_{0.9}Ce_{0.1}O_3$ at different temperatures.

BTC20	a (Å)	b (Å)	c (Å)	Angle (°)	Uiso Ba (Å^2)	Uiso Ti-Ce (Å^2)	Uiso O (Å^2)
100 K	4.0925(5)			89.921(5)	0.009(5)	0.012(5)	0.029(5)
200 K	4.0950(5)			90	0.011(5)	0.015(5)	0.038(5)
300 K	4.0980(5)			90	0.013(5)	0.016(5)	0.040(5)
400 K	4.1015(5)			90	0.014(5)	0.017(5)	0.043(5)

Table 5.24: PDF average structure: Uiso and cell parameters of $BaTi_{0.8}Ce_{0.2}O_3$ at different temperatures.

5.1.3 Average Structure: Reciprocal vs Direct Space

A comparison between Rietveld and Pair Distribution Function analysis is here performed comparing structural results above presented. In general reciprocal space investigation is more adequate and efficient, but this subsection could be useful to test PDF average analysis and to obtain confirmations. For example structures which give the best fits for the two methods are practically the same as evidenced in tables 5.25, 5.26 and 5.27.

	BTC5	
Temperature	Rietveld	PDF
200 K	Rhombohedric	Rhombohedric
300 K	Rhombohedric	Rhombohedric
350 K	Tetragonal	Tetragonal
380 K	Tetragonal	Tetragonal
420 K	Cubic	Cubic

Table 5.25: BTC5: average structure symmetries deduced by Rietveld and PDF analyses.

	BTC10	
Temperature	Rietveld	PDF
100 K	Rhombohedric	Rhombohedric
200 K	Rhombohedric	Rhombohedric
300 K	Pseudocubic	Pseudocubic
400 K	Cubic	Cubic

Table 5.26: BTC10: average structure symmetries deduced by Rietveld and PDF analyses.

Agreement between PDF and Rietveld is then very good and this is also demonstrated by figures 5.25, 5.26

	BTC20	
Temperature	Rietveld	PDF
100 K	Pseudocubic	Rhombohedric
200 K	Cubic	Cubic
300 K	Cubic	Cubic
400 K	Cubic	Cubic

Table 5.27: BTC20: average structure symmetries deduced by Rietveld and PDF analyses.

and 5.27 which report cell parameter results.

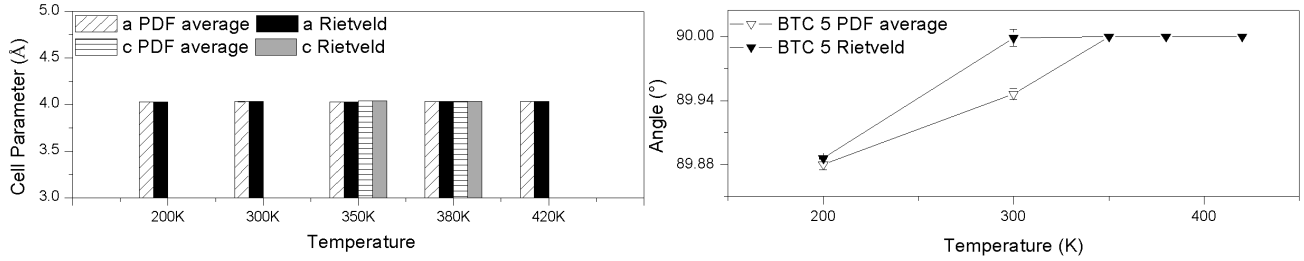

Figure 5.25: BTC5 average structure at different temperatures: comparison between Rietveld and PDF analyses.

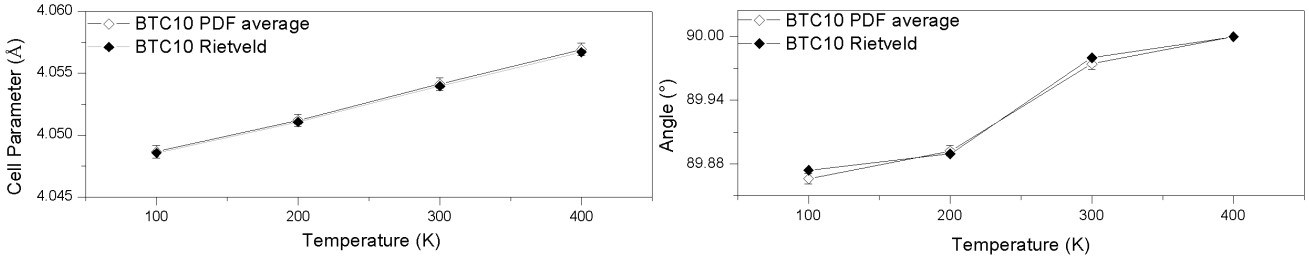

Figure 5.26: BTC10 average structure at different temperatures: comparison between Rietveld and PDF analyses.

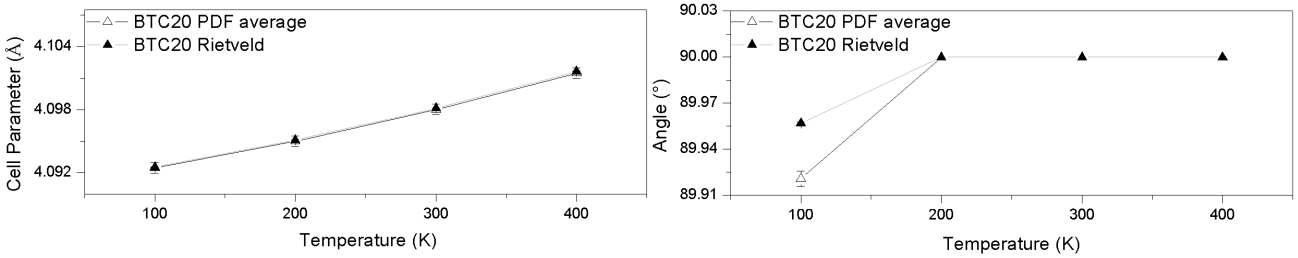

Figure 5.27: BTC20 average structure at different temperatures: comparison between Rietveld and PDF analyses.

The evolution of cells and angles has been yet before discussed in detail then at this point the purpose is to examine the differences between the two set of results (excluding errors cause those of PDF are just guesstimated). The comparison on cell parameters reveals a good agreement; differently some very little variations are shown on the angle transformation, but in any case results remain comparable. Moving from this, it could be also interesting to take a look at figures 5.28, 5.29 and 5.30 which represent Uiso parameters. Thermal parameters seem generally grow as temperature increases, but vibrations calculated by PDF appear higher than those obtained by Rietveld at all the temperatures and for all the samples. This difference is not so accentuated for barium and titanium, but

becomes more evident for the oxygen. Higher values for this atom are expected, as explained in subsection 5.1.1, but here they could be read as a great and clear disorder signal. In order to clarify this point and to understand the origin of some oddities on the average structure only local structure analysis could be helpful.

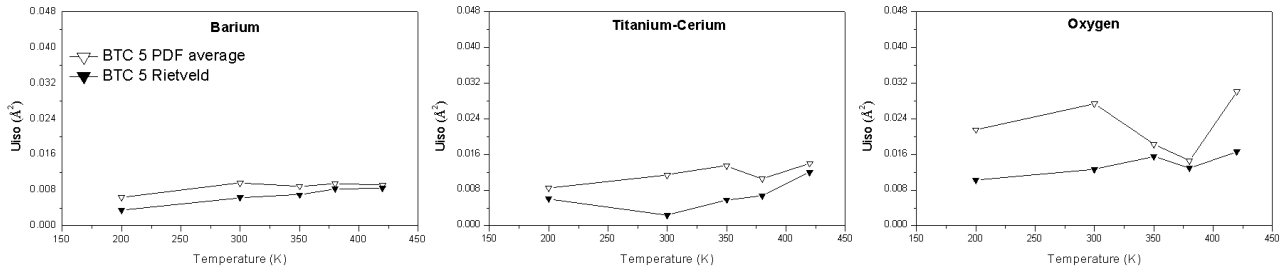

Figure 5.28: BTC5 Uiso of the average structure at different temperatures: comparison between Rietveld and PDF analyses (errors are not reported).

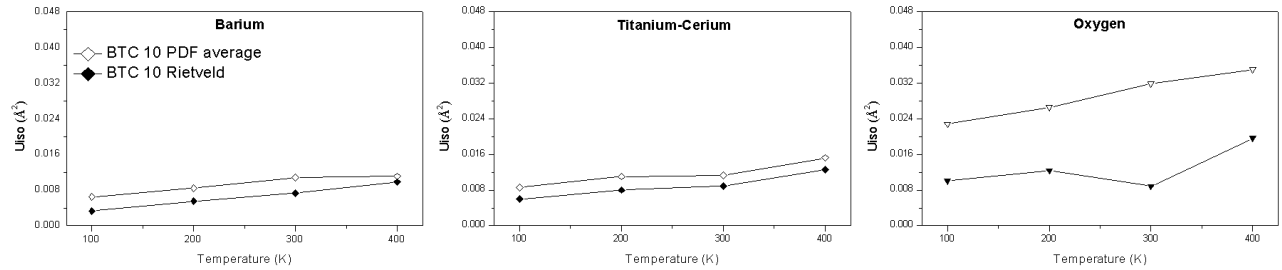

Figure 5.29: BTC10 Uiso of the average structure at different temperatures: comparison between Rietveld and PDF analyses (errors are not reported).

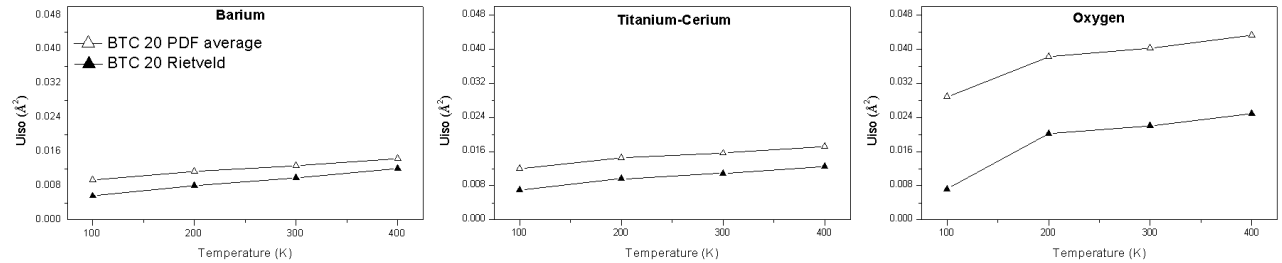

Figure 5.30: BTC20 Uiso of the average structure at different temperatures: comparison between Rietveld and PDF analyses (errors are not reported).

5.2 Local Structure

In previous section the average structural analyses have been discussed. Beyond good results and outcomes, also some problems and doubts have been highlighted. For example Rietveld refinements return a little bit high Rw values, Uiso parameters are slightly large and sometimes phase stability is in contrast with that expected (as the case of BTC5 where orthorhombic structure has been not detected). In addition due to the different sizes of B cations possible structural distortions at local level are foreseeable. The first step is then understand if all of these indications are expressions of a true local disorder. Pair Distribution Functions for BTC 2 and 30 have been extrapolated in the same way of the other samples: *qmax* has been kept at 26, *qmaxinst* at 27 and *rpoly* at 1.4. In this section data used for BTC 2 transformation has been collected during second experiments; the outer rim

and the inner zone of the ceramic diks, characterized by a different color (see section 3.1), have been collected separately. The difference between the two compositions is paltry, however considering that the outer part should present the right stoichiometry, the BTC2out will be used for the following discussion and will be labeled from here on out simply BTC2. Before making any analysis, a visual comparison of different PDFs has been performed and here proposed. This operation should allow to pay attention on peak evolution as a function of temperature and cerium amount. Furthermore some important information could be extrapolated observing differences between samples.

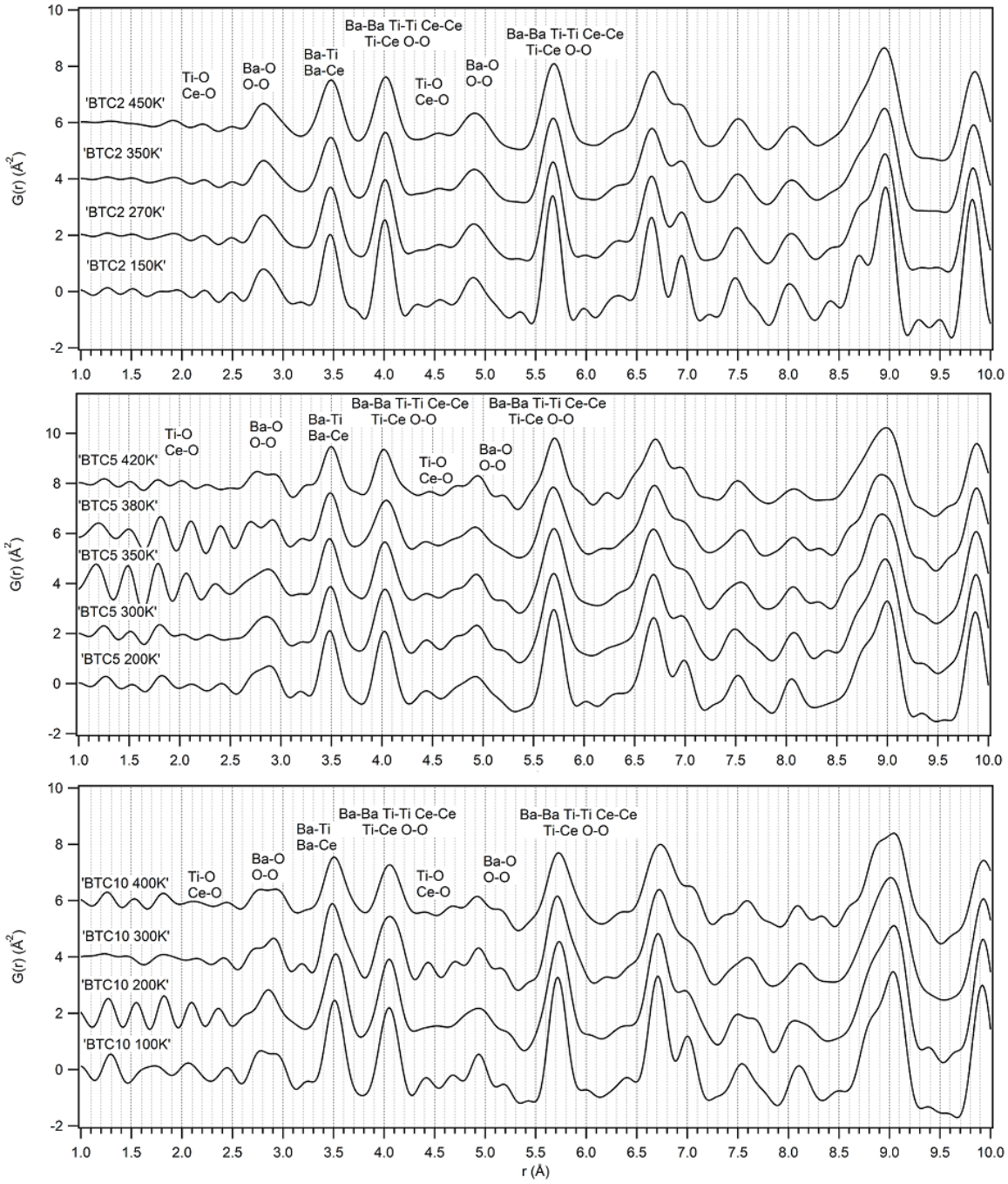

Figure 5.31: Pair Distribution Functions of BTC 2, 5 and 10 are reported at different temperatures between 1 and 10 Å. PDFs at different temperatures for each sample are shown in a waterfall-like diagram.

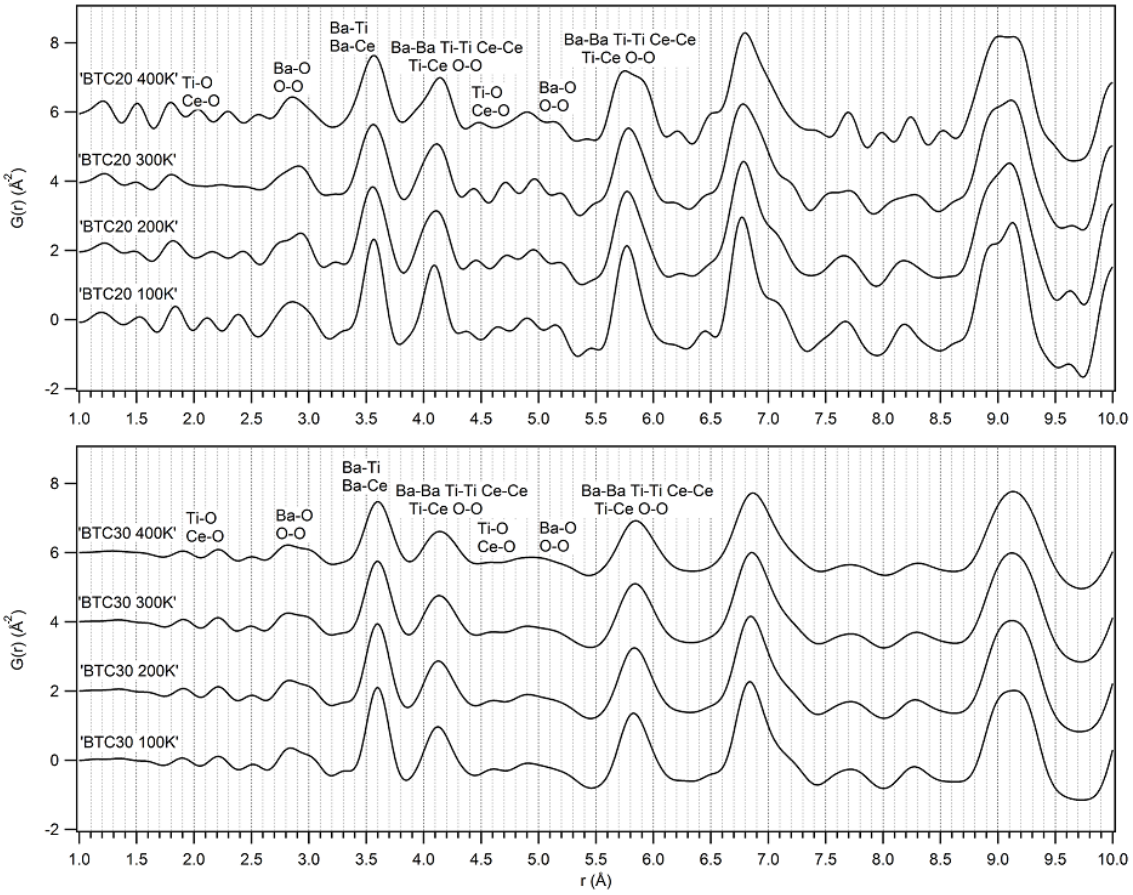

Figure 5.32: Pair Distribution Functions of BTC 20 and 30 are reported at different temperatures between 1 and 10 Å. PDFs at different temperatures for each sample are shown in a waterfall-like diagram.

In figures 5.31 and 5.32 only a low r range is considered, but at any rate this should be the most interesting for the purpose of this investigation. Some features are noticeable for all the BTCs:

- PDFs appearance, especially at very low r, seems very similar for all samples and temperatures in particular for peaks related to heavier atoms (*e.g.* around 3.5 and 4 Å).
- Unusual termination ripples belonging to the same data set, and even for the same samples, are not comparable in frequency (*e.g.* BTC5 sample). Furthermore some temperatures present them with a too high intensity, compromising even the shape of first Ba-O peak (*e.g.* BTC5 at 380 K).
- Unfortunately the first peak Ti-O and Ce-O is completely hidden by the background for all the temperatures and samples. This is not only a problem caused by high noise, but also by a big spread of these bond lengths.
- Differently for peaks linked to atom-O bonds, Ba-Ti and Ba-Ba peaks show practically the same shape (excepted for the broadening due to the thermal motion) for all the temperatures.
- If only the lowest r values are taken into account, peaks position seems to be not affected by temperature increase.

Another important point is the comparison between different doping amount. As reported above, samples seem to not present a great difference with temperatures, or otherwise in r range treated here, then just observations at lowest temperatures will be presented. This also allows to have peaks influenced by lower atomic thermal

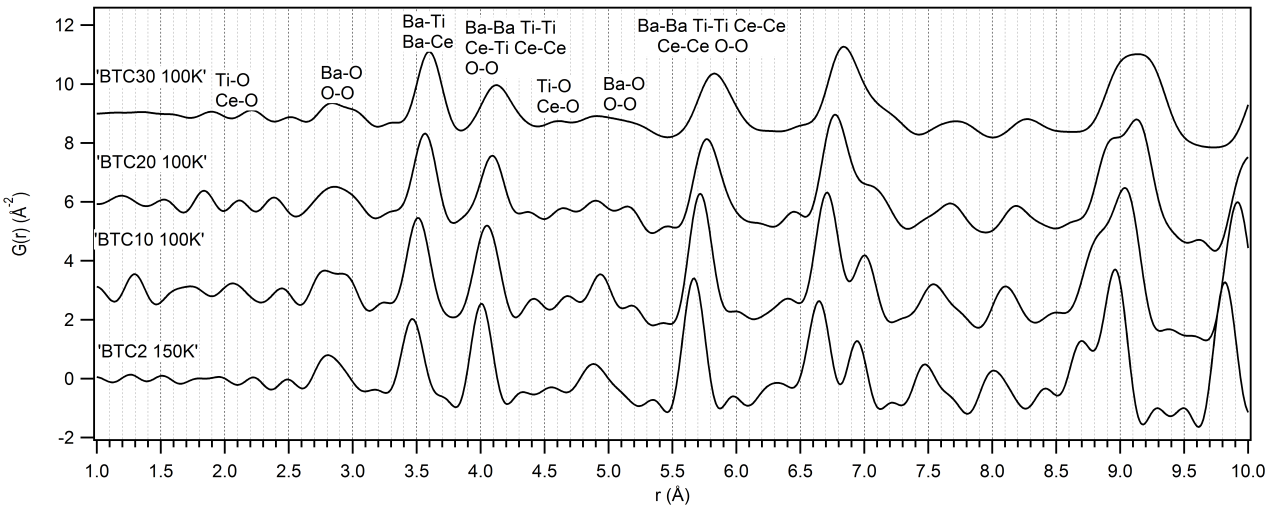

Figure 5.33: PDFs comparison between 1 and 10 Å of different samples around 100 K is presented in a waterfall-like diagram.

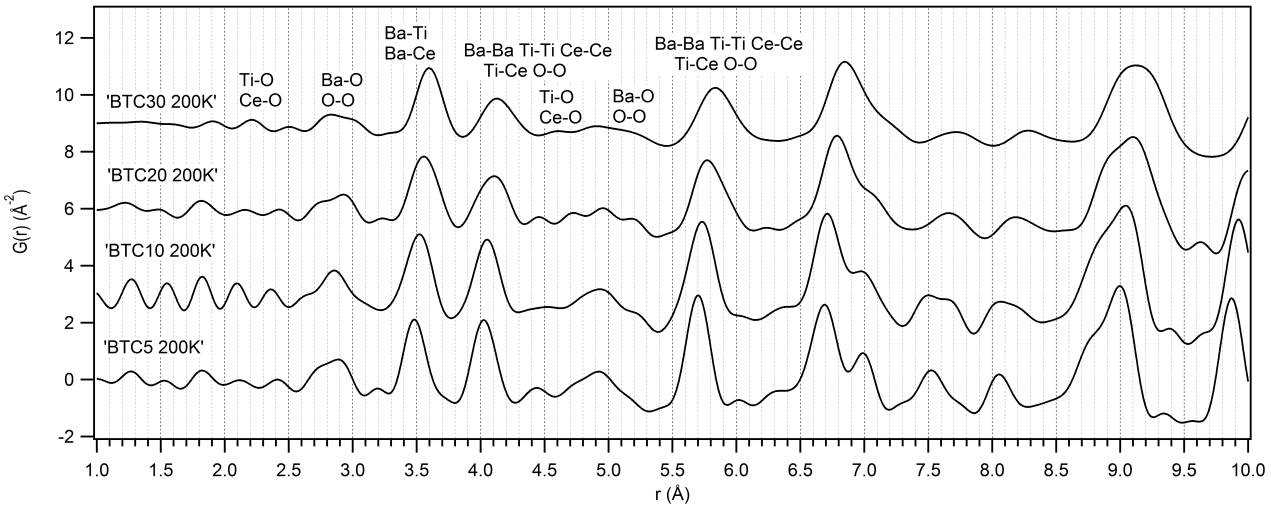

Figure 5.34: PDFs comparison between 1 and 10 Å of different samples around 200 K is presented in a waterfall-like diagrams.

vibrations. In figure 5.33 and 5.34 PDFs around respectively 100 and 200 K are shown. Making some general considerations:

- Increment in cell parameters is promoted by doping increase rather than the temperature (evident especially for Ba-Ti and Ba-Ba peaks).
- Considering thermal vibrations as comparable for all samples, an evolution from an ordered to a disordered structure seems to proceed as a function of doping increase. Peaks appear sharp in BTC2 and become broader and broader moving toward BTC30.
- This degree of disorder is also proved by a possible comparison with bibliographic PDF of pure $BaTiO_3$ (Yoneda et al. 2013) reported in figure 5.35.
- Ba-Ti/Ba-Ce and Ba-Ba/Ti-Ti/Ce-Ce/Ti-Ce peaks change their intensity ratio and the second becomes broader as a function of cerium amount, another signals of disorder.

All information gathered will be useful during the local structure analysis and they will be then examined in detail. Despite some problems linked to curious termination ripples intensity, all samples will be considered in this dissertation.

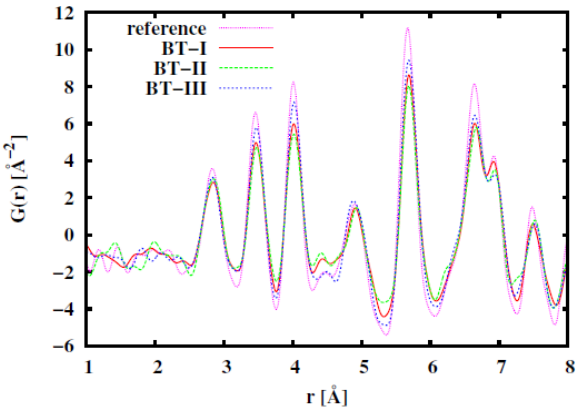

Figure 5.35: PDFs of pure $BaTiO_3$ which presents four different particle sizes: micro size, defined in graphic as reference, and three nano powders, defined as BT-I, BT-II and BT-III (Yoneda et al. 2013).

Local structure refinements have been performed by DiffPy-CMI (Juhas et al. 2015) and PDFgui software: *Qdamp* used on the average analysis for BTC 5, 10 and 20 have been maintained. Differently, for 30 and 2, it has been recalculated by LaB_6 refinement and fixed at 0.08. The choice of the local structure range when a material is locally disorder is a tricky matter. The author interprets the true local structure as the representation just of the first coordination shells, in other words the relation between at maximum two unit cells. Unfortunately it is often impossible to model them adequately and with the hindsight especially in this case particularly because the first coordination peak is not visible. Considering that the average sum of these components is observable at bigger and different length scales, it is usually necessary to take advantage by this situation and examine a wider radius range which includes the true and the average local structure. Moreover every single sample could have a different extension of these and it could be difficult to understand the right length scale to perform local analysis. Having said this firstly average structures have been used to fit data between 1 and 100 Å refining just the scale. This allows to define approximately where the local structure starts, which should coincide with a clear worsening of the fit. Performing this preliminary operation the radius range of the local structure analysis has been fixed between 1 and 20 Å. Obviously this is a good compromise between different samples and seems to be a suitable length scale to extract local structural information. The fact to be able to recognize different ranges in which average structure seems to fit better or worse it is a first proof of a local disorder. In order to confirm this, refinements using different space groups have been performed to identify the local symmetry using the lowest Rw principle. The same structures as in the average have been used refining: cell parameters, Uiso and all the coordinates allowed by S.G. rules. Titanium and cerium are kept as equal both for position and thermal vibration. In tables 5.28, 5.29, 5.30, 5.31 and 5.32 Rw values obtained for different analyses are shown.

BTC2	Rw: Cubic	Rw: Tetragonal	Rw: Orthorhombic	Rw: Rhombohedric
150 K	0.1730	0.1389	0.1387	**0.1370**
270 K	0.1854	0.1481	0.1328	**0.1323**
350 K	0.1863	0.1520	**0.1506**	0.1514
450 K	0.1698	0.1578	0.6989	**0.1481**

Table 5.28: Local structure: Rw values for $BaTi_{0.98}Ce_{0.02}O_3$ fits using different space groups. The lowest Rw value for each temperature is evidenced in bold style.

BTC5	Rw: Cubic	Rw: Tetragonal	Rw: Orthorhombic	Rw: Rhombohedric
200 K	0.1530	0.1445	0.1438	**0.1418**
300 K	0.1622	0.1558	0.1804	**0.1521**
350 K	0.1930	0.1858	0.1866	**0.1848**
380 K	0.1957	0.1854	**0.1841**	0.1845
420 K	0.1716	0.1601	**0.1521**	0.1599

Table 5.29: Local structure: Rw values for $BaTi_{0.95}Ce_{0.05}O_3$ fits using different space groups. The lowest Rw value for each temperature is evidenced in bold style.

BTC10	Rw: Cubic	Rw: Tetragonal	Rw: Orthorhombic	Rw: Rhombohedric
100 K	0.1660	0.1562	0.1566	**0.1556**
200 K	0.1551	0.1453	**0.1347**	0.1449
300 K	0.1533	0.1445	0.1514	**0.1432**
400 K	0.1618	0.1515	**0.1458**	0.1506

Table 5.30: Local structure: Rw values for $BaTi_{0.9}Ce_{0.1}O_3$ fits using different space groups. The lowest Rw value for each temperature is evidenced in bold style.

BTC20	Rw: Cubic	Rw: Tetragonal	Rw: Orthorhombic	Rw: Rhombohedric
100 K	0.1456	0.172	0.1716	**0.1371**
200 K	0.1391	0.1371	0.1817	**0.1321**
300 K	0.143	0.1377	0.1674	**0.1369**
400 k	0.1723	0.1693	0.2217	**0.1689**

Table 5.31: Local structure: Rw values for $BaTi_{0.8}Ce_{0.2}O_3$ fits using different space groups. The lowest Rw value for each temperature is evidenced in bold style.

BTC30	Rw: Cubic	Rw: Tetragonal	Rw: Orthorhombic	Rw: Rhombohedric
100 K	0.1456	0.1720	0.1716	**0.1371**
200 K	0.1391	0.1371	0.1817	**0.1321**
300 K	0.1430	0.1379	0.1674	**0.1367**
400 K	0.1723	0.1693	0.2217	**0.1689**

Table 5.32: Local structure: Rw values for $BaTi_{0.7}Ce_{0.3}O_3$ fits using different space groups. The lowest Rw value for each temperature is evidenced in bold style.

As evidenced in previous tables, Rw values for different structures are often very similar and sometimes it is difficult to identify the right structure. This is perfectly understandable considering the figure 5.36. Here the $BaTiO_3$ calculated partial PDFs for each space group are represented. Using diffraction data the differences between these four space groups are indisputable, so it was easy to discriminate them, but by PDF this procedure is problematic because comparison of different calculated partials does not reveal any particular distinction. The only diversities are the peak broadening linked to a different symmetry degree and peak split (around 2 and 4.5 Å) related to Ti-O bonds.

As a result of these considerations and of refinements performed the rhombohedric phase has been chosen to represent the starting structural model for all the samples. This allows to play with a low symmetry gaining freedom degree in refinement. Considering that rhombohedric Rw values are the lowest, but they remain not satisfying, new analyses have been performed using a 2x2x2 supercell with titanium and cerium as independent in position and Uiso, but linked by fractional occupancies. Related fits are reported in figure 5.37, as evidenced by the vertical line the fitted G(r) is actually a very good match to the observed data although not as excellent as at distances above 10 Å (zoom in figure 5.38).

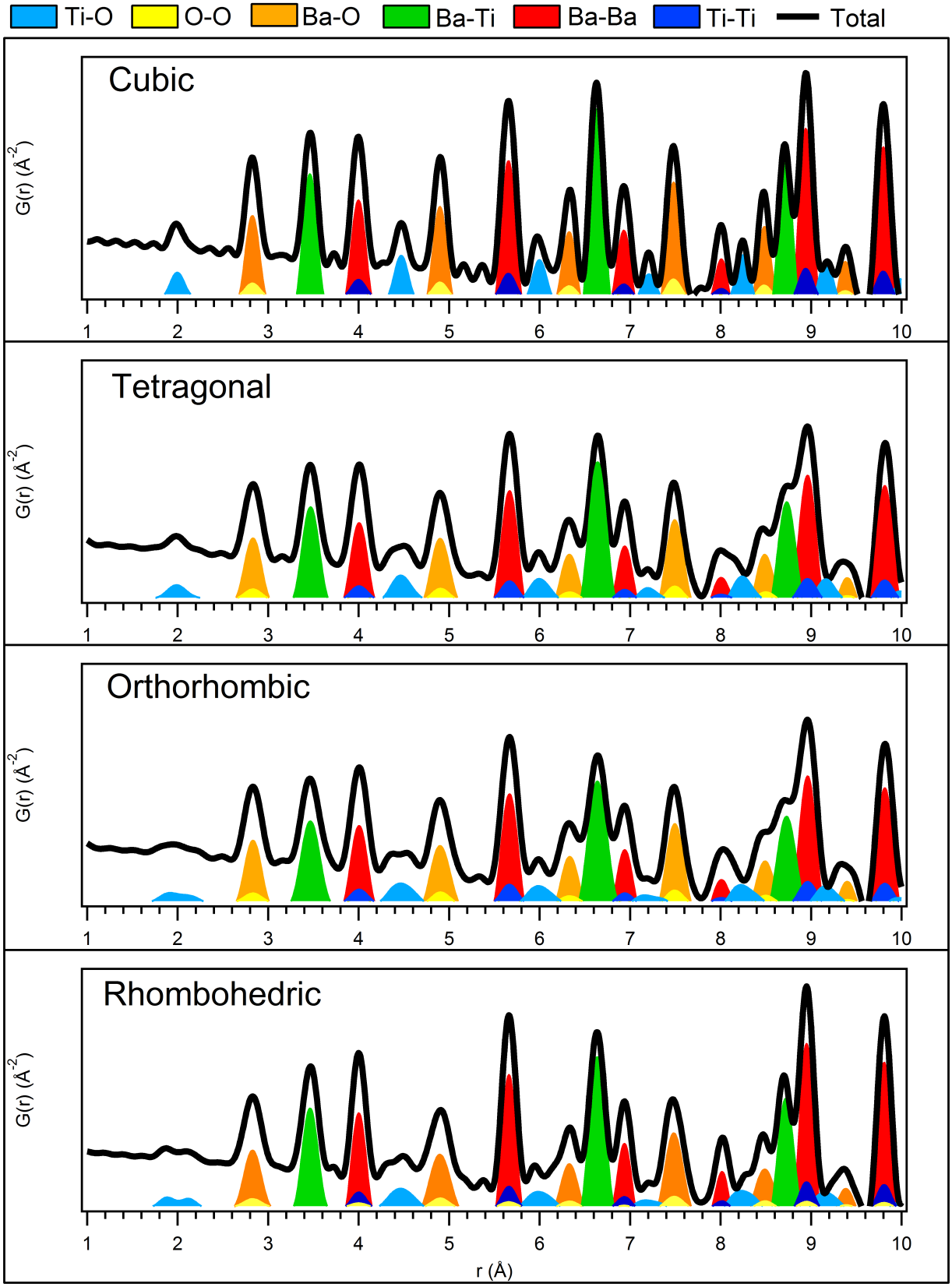

Figure 5.36: Calculated partial PDFs for the different space groups taken into account in this treatise.

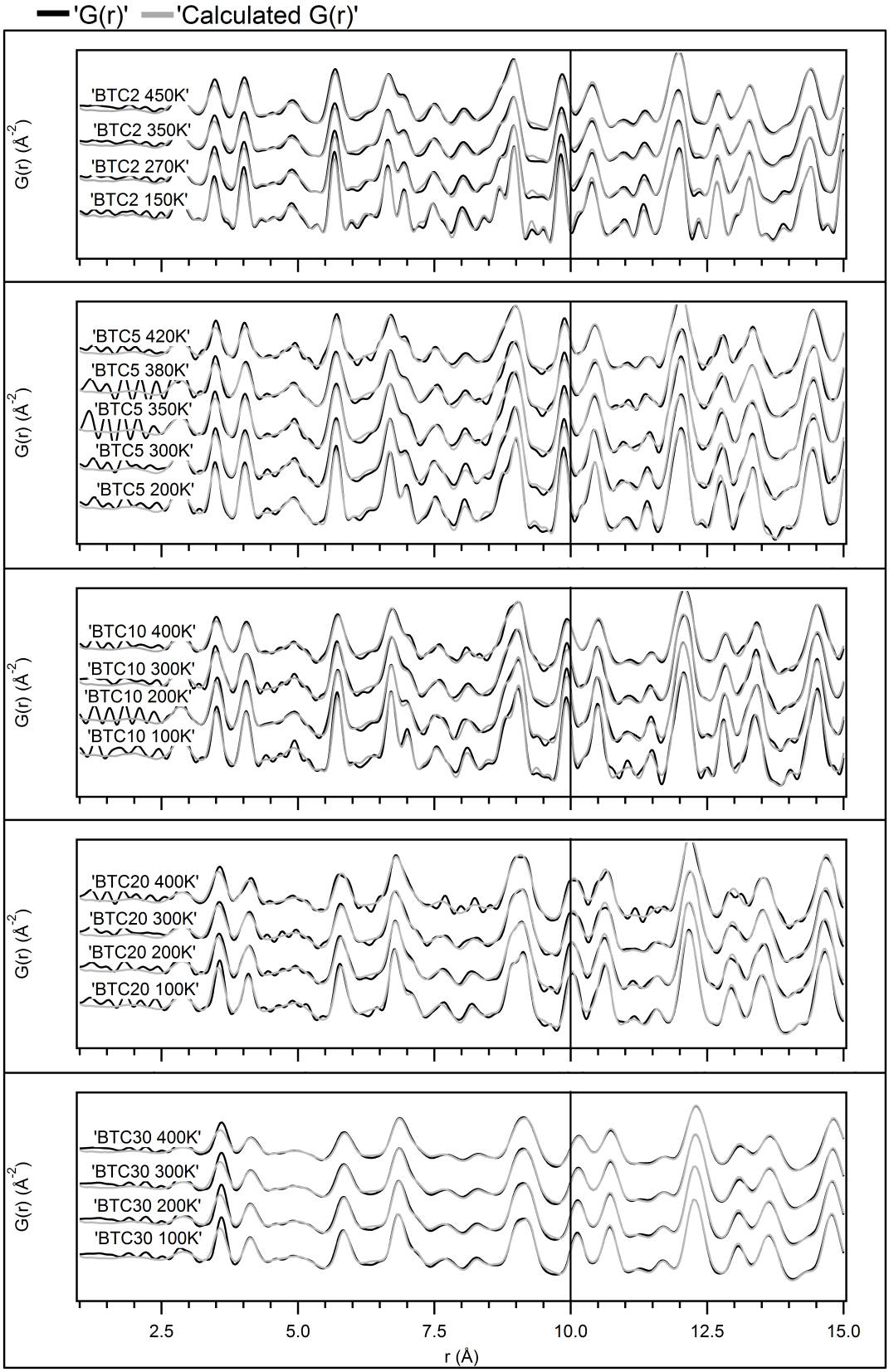

Figure 5.37: Fits performed between 1 and 20 Å using classical rhombohedric structure are presented in waterfall-like diagrams for each sample. Ti/Ce position and Uiso have been refined independently. In figure zoom from 1 to 15 Å is presented, vertical line signals where fits start to be good.

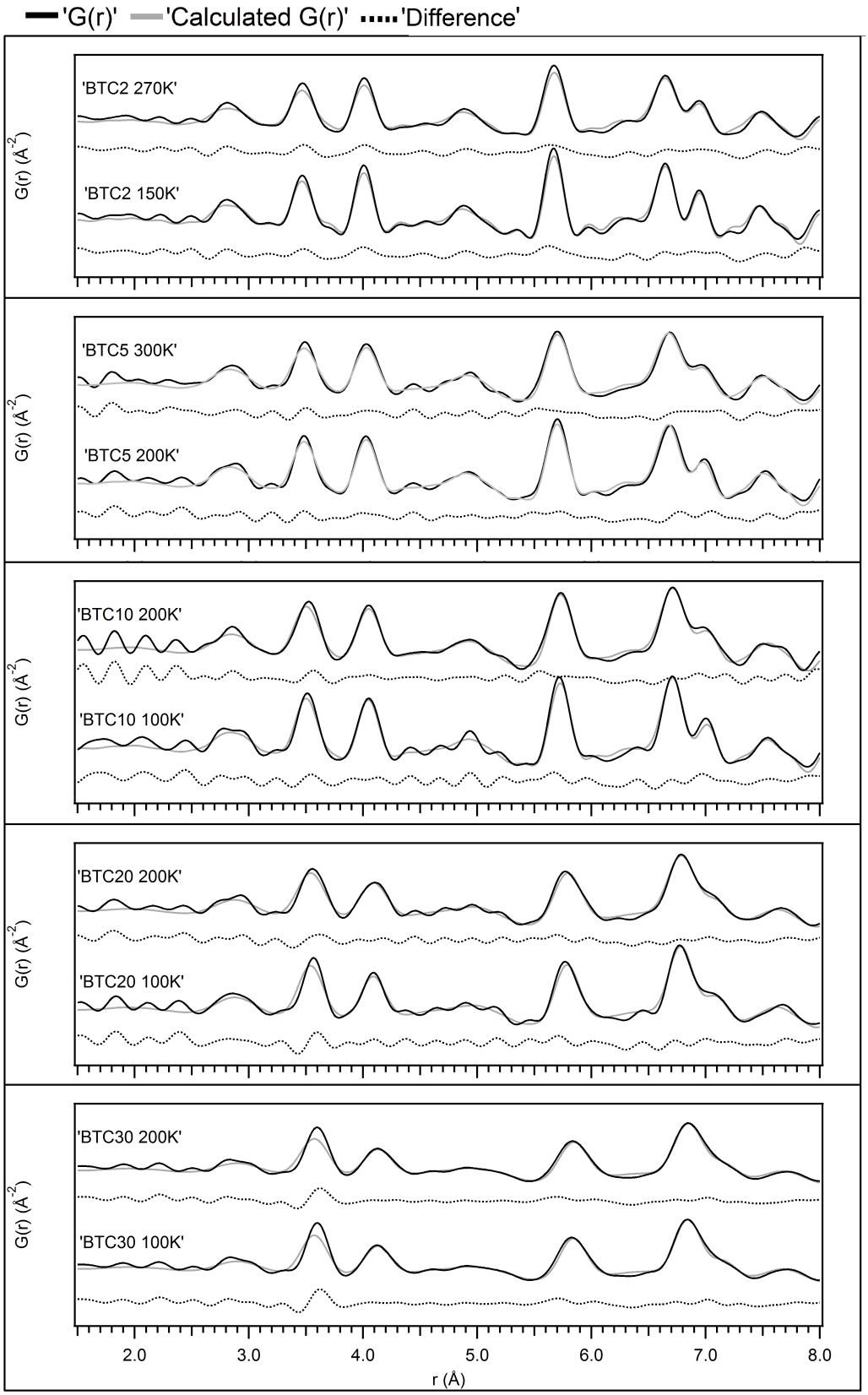

Figure 5.38: Some fits, reported as examples, performed between 1 and 20 Å using classical rhombohedric structure are presented in waterfall-like diagrams for each sample. Ti/Ce positions and Uiso have been refined independently. In figure zoom from 1 to 8 Å is shown.

These fits give a strong indication about the great disorder in these samples. However to have some first and tangible results new refinements have been performed using similar strategy. Uiso values have been fixed (with different values for different temperatures) in order to make a fair comparisons. Two different ranges have been selected: from 1 to 10 Å and from 10 to 20 Å. As expected the first gives again not good fits, but it is possible to deduce some information by the second. This range represents actually an average of the first, therefore it is obviously that results are not exactly representative of the first bond lengths, but however could be useful to have a first idea about bonds and to become familiar with the local structure.

BTC2	Cell Parameter (Å)	Angle (°)	Octahedra Volume (Å^3)	Ti displacement (Å)
150 K	4.0090	89.959	10.739	0.105
270 K	4.0111	89.988	10.756	0.108
350 K	4.0129	89.842	10.770	0.107
450 K	4.0173	89.773	10.806	0.095

Table 5.33: BTC2 local PDF analysis performed from 10 to 20 Å refining the most basic rhombohedric model. Ti displacement has been calculated from the center of the cell and considering Ti refined coordinates reported in appendix.

BTC5	Cell Parameter (Å)	Angle (°)	Octahedra Volume (Å^3)	Ti displacement (Å)
200 K	4.0297	89.734	10.905	0.100
300 K	4.0322	89.762	10.926	0.097
350 K	4.0338	89.621	10.939	0.101
380 K	4.0338	89.721	10.939	0.095
420 K	4.0362	89.597	10.958	0.097

Table 5.34: BTC5 local PDF analysis performed from 10 to 20 Å refining the most basic rhombohedric model. Ti displacement has been calculated from the center of the cell and considering Ti refined coordinates reported in appendix.

BTC10	Cell Parameter (Å)	Angle (°)	Octahedra Volume (Å^3)	Ti displacement (Å)
100 K	4.0496	89.722	11.068	0.048
200 K	4.0522	89.682	11.089	0.059
300 K	4.0555	89.561	11.116	0.050
400 K	4.0584	89.505	11.140	0.040

Table 5.35: BTC10 local PDF analysis performed from 10 to 20 Å refining the most basic rhombohedric model. Ti displacement has been calculated from the center of the cell and considering Ti refined coordinates reported in appendix.

BTC20	Cell Parameter (Å)	Angle (°)	Octahedra Volume (Å^3)	Ti displacement (Å)
100 K	4.0903	89.471	11.404	0.031
200 K	4.0931	89.429	11.428	0.019
300 K	4.0960	89.409	11.451	0.028
400 K	4.1000	89.402	11.485	0.000

Table 5.36: BTC20 local PDF analysis performed from 10 to 20 Å refining the most basic rhombohedric model. Ti displacement has been calculated from the center of the cell and considering Ti refined coordinates reported in appendix.

Refined parameters helpful in this first discussion are reported in tables 5.33,5.34, 5.35, 5.36, 5.37, errors (here and then) are not given because non significant in their calculation. In figure 5.39 cell parameters and related angles are presented. Increase of cell parameter, even in the local structure, is more influenced by cerium amount than by the temperature. For all the samples the volume variation as a function of temperature is around 0.2 % (calculated

BTC30	Cell Parameter (Å)	Angle (°)	Octahedra Volume (Å^3)	Ti displacement (Å)
100 K	4.1271	89.388	11.715	0.045
200 K	4.1300	89.359	11.739	0.054
300 K	4.1334	89.333	11.767	0.062
400 K	4.1370	89.308	11.798	0.064

Table 5.37: BTC30 local PDF analysis performed from 10 to 20 Å refining the most basic rhombohedric model. Ti displacement has been calculated from the center of the cell and considering Ti refined coordinates reported in appendix.

for each BTC using volumes at lowest and highest temperatures), differently, taking in to account the two end-member of BTC series (then volumes of BTC2 at 150 K and that of BTC30 at 100 K) the volume variation is around 2 %. Angle evolution shows a very interesting trend. BTC with lower cerium amount present angle nearer to 90° and in general values seem to decrease as a function of temperature in total contrast with results found for the average structure. A deep discussion on this difference will be treated at the end of the chapter in section 5.4.

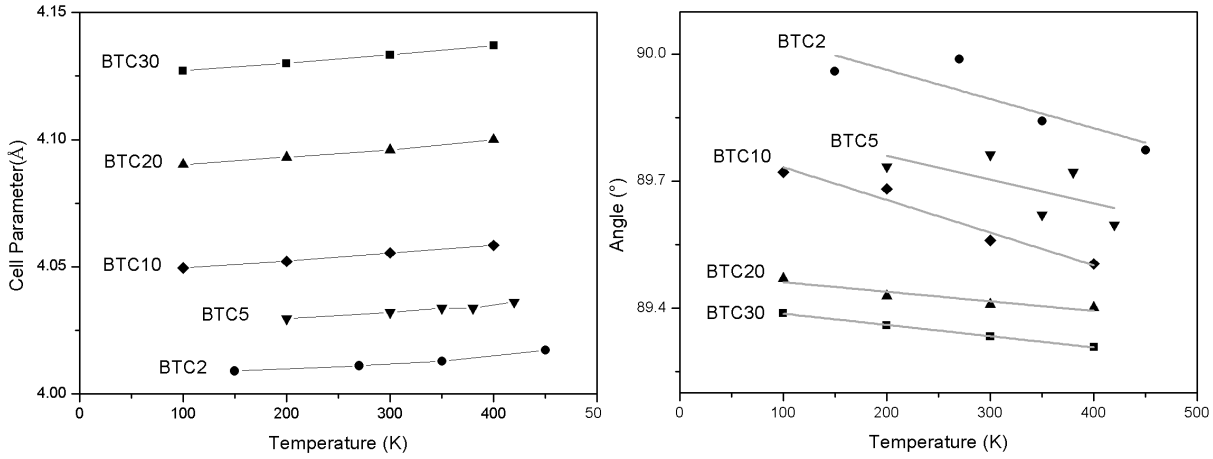

Figure 5.39: Local structure: cell parameters and angle evolution for all samples and temperatures. Analysis is performed from 10 to 20 Å refining the most basic rhombohedric model. In order to evidence angle trend also regression lines between point are reported as eye guide.

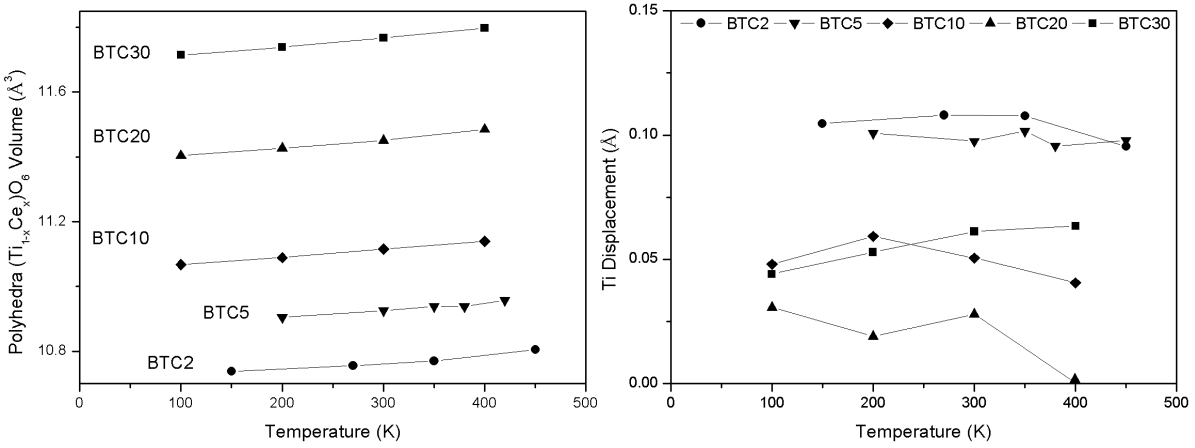

Figure 5.40: Local structure: octahedra volumes and titanium displacements for all samples and temperatures. Analysis is performed from 10 to 20 Å refining the most basic rhombhoedric model.

In figure 5.40 the octahedra volumes and titanium displacements are presented. Polyhedra show the same trend of cell volume. This is an obvious result considering that only classical parameters have been refined, practically the degree of disorder taken into account is very little consisting just in a different position between

cerium and titanium. Anyway some interesting information could be deduced: despite polyhedra volumes increase as a function of doping Ti displacement is reduced. This consideration is in very good agreement with that deduced in the average structure analyses. Cerium, depending of its abundance, then limits off-center movements of Ti cations. However this is rather curious considering that, as substitution increases, also the volume of BO_6 cage increases and from the logical point of view, more space you have more you can move. Thus, despite good agreement with dielectric measurements, other analyses and model are necessary to understand the origin of this tendency. Moreover Ti displacement deduced by refinements are not completely satisfactory, trends as a function of temperature are not linear. This problematic is for sure linked to a used model which is too simple. Having said that and considering fits below 10 Å it is obvious that model applied is inappropriate confirming a deep structural disorder. Once understood that a simple structure is not able to describe the local atomic arrangement, it is time to leave the classical approach and move to a complex view. In general, indeed, local structures present variations which are not included in the classical crystallographic structures available in bibliographic. These must be modified lowering symmetries as a function of disorder degree. The best way is to start from a structure consisting of a little crystallographic deviation and then eventually complicate it. One of the simpler initial solution is a symmetry reduction of the atomic position.

Atom	Multiplicity	Wyckoff letter	Site symmetry	Coordinates
/	6	c	1	1) x,y,z 2) z,x,y 3) y,z,x 4) z,y,x 5) y,x,z 6) x,z,y
O	3	b	.m	x,x,z z,x,x x,z,x
Ba, Ti	1	a	3m	x,x,x

Table 5.38: Atomic positions in $BaTiO_3$ rhombohedric structure belonging to R3m space group.

In table 5.38 atomic positions related to rhombohedric $BaTiO3$ are reported. In order to increase disorder it is possible to use a structure belonging to the same space group, but moving atoms in less special positions. This permits to have more refineble coordinates and more flexible system. Playing with these positions a great number of opportunities are available: it is possible to change one atoms at a time or use different combinations. Considering that more generic is the position greater is the multiplicity, the only important things is reduce the total occupancies to maintain the stoichiometry. In tables 5.39 all possible combinations obtained lowering the symmetry of the initial position of one atom or lowering together the symmetry positions of two atoms are shown, differently in table 5.40 a three components solutions are reported.

	Ba xxz	Ba xyz	Ti xxz	Ti xyz	O xyz
Ba xxz	Ba xxz	/	/	/	/
Ba xyz	/	Ba xyz	/	/	/
Ti xxz	Ti xxz Ba xxz	Ti xxz Ba xyz	Ti xxz	/	/
Ti xyz	Ti xyz Ba xxz	Ti xyz Ba xyz	/	Ti xyz	/
O xyz	O xyz Ba xxz	O xyz Ba xyz	O xyz Ti xxz	O xyz Ti xyz	O xyz

Table 5.39: $BaTiO3$ R3m: combination of possible coordinate constrains reducing the symmetry position of one or two atoms.

Refinements were executed with an increase disorder starting by a single atom variation until to a lowest possible symmetry. Furthermore titanium and cerium have been kept in the same symmetry position (in tables 5.39 and 5.40 just Ti is mentioned), but coordinates and Uiso were refined independently. Fits linked to these attempts will be presented with the example of BTC20 at 100 K. This because the author believes in a single structural solution which could work for all the samples (established by the PDFs visual comparison) and besides BTC20 is probably the most representative sample. In fact BTC2 presents too low cerium and on the contrary BTC30, even by the visual observation, seems to be too disordered, instead BTC5 and BTC10 are discarded

	Ba xxz	Ba xyz	Ti xxz	Ti xyz	O xyz
Ti xxz Ba xxz	/	/	/	/	/
Ti xxz Ba xyz	/	/	/	/	/
Ti xyz Ba xxz	/	/	/	/	/
Ti xyz Ba xyz	/	/	/	/	/
O xyz Ba xxz	/	/	/	/	/
O xyz Ba xyz	/	/	/	/	/
O xyz Ti xxz	Ba xxz Ti xxz O xyz	Ba xyz Ti xxz O xyz	/	/	/
O xyz Ti xyz	Ba xxz O xyz Ti xyz	**Ba xyz O xyz Ti xyz**	/	/	/

Table 5.40: $BaTiO3$ R3m: combination of possible coordinate constrains reducing the symmetry position of all atoms. In bold style the lowest possible symmetry allowed in R3m is underlined.

causing problems in termination ripples. NB BTC20 at 100 K will be taken as example also for almost all future analyses. In figure 5.41 the lowest possible symmetry of atomic positions has been used to fit data (reported in bold style in table 5.40). In this model Ba, Ti, Ce and O are placed in a generic position x,y,z. Despite a high freedom degree, fit appears good just above 10 Å. Under this radius some discrepancies are observable (figure 5.42) and must be examined to understand problems and to then solve them.

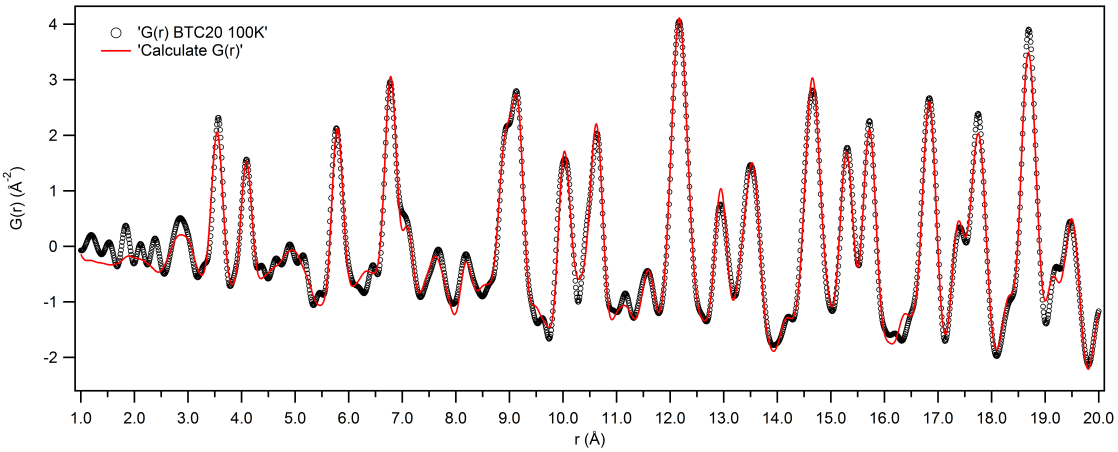

Figure 5.41: Fit performed between 1 and 20 Å using rhombohedric structure. Ba, Ti, Ce and O are placed in general positions.

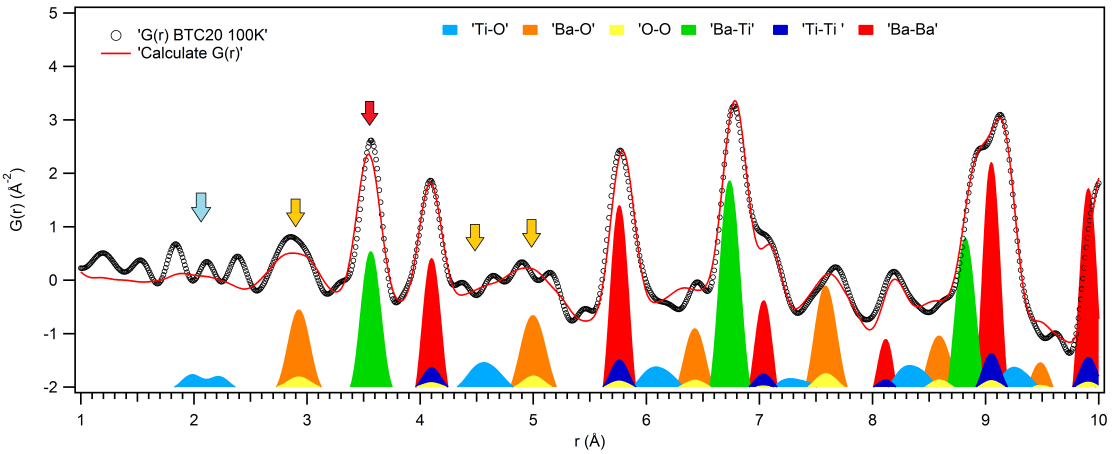

Figure 5.42: Zoom of fit performed between 1 and 20 Å using rhombohedric structure with Ba, Ti, Ce and O placed in general positions. Arrows indicate the most evident differences between calculated and observed G(r). Bonds related to different peaks are also reported.

The first and more evident problem is indicated in figure 5.42 by the blue arrow. In theory the different size of

Ti and Ce and then the different atomic scattering potential were supposed to guarantee a good visibility and even a splitting, thank to the high direct space resolution, of the first peak or peaks related to the bonds with oxygens. Unfortunately this supposition has proved to be unrealistic and, as mentioned before, termination ripples dominate the lower part of PDF hiding Ti-O and Ce-O peaks. From another point of view these ripples have not a regular frequency, then they could be alternated with true peaks, but however it is impossible to discriminate them. Orange arrows evidence peaks in which shape and position are inaccurate and they coincide with Ba-O bond lengths and obviously second distance Ti/Ce-O. Considering that:

- beyond higher intensity of ripples, probably a big disorder plays an important role making Ti-O/Ce-O peaks broad and flattened and then easily concealable.
- cation-cation peaks seems to be better fitted, than cation positions should be more correct than those of oxygens.
- Ba disorder is not probable. In one hand because barium is a heavy atoms and on the other Ba-Ba peaks is well fitted even using model with higher symmetry position.

problems above described could be caused by some kind of disorder on the oxygen positions. Differently, problems about cations could be at the base of peak shift around 3.5 Å (indicated by red arrow). This peak seems to be in wrong position as a function of cerium amount and no models up to now used are able to fit it adequately. In order to solve this, some considerations are necessary. Peak is slightly asymmetric (figure 5.43) then it could be necessary to consider at least two different bond lengths: Ba-Ti and Ba-Ce longer than first due to the atomic radius. Despite Ce atomic scattering potential is around three time than that of Ti, in order to obtain a second gaussian curve intense as in figure 5.43, also a probability to find Ba-Ce distances must be higher than 0.2 fixed by stoichiometry. The only way to achieve this is to consider cluster of $BaCeO_3$ in a $BaTiO_3$ matrix. This configuration provide a Ba-Ce probability of $0.2\bar{2}$ against $0.7\bar{8}$ for Ba-Ti. Furthermore this interpretation allows to explain also the reduction of Ba-Ba peak as a function of cerium amount (figure 5.44). It is true that cerium clusters should increase the Ce-Ce probability, but on the other hand a Ba-Ce bond bigger than Ba-Ti could cause a big disorder on the Ba-Ba lengths.

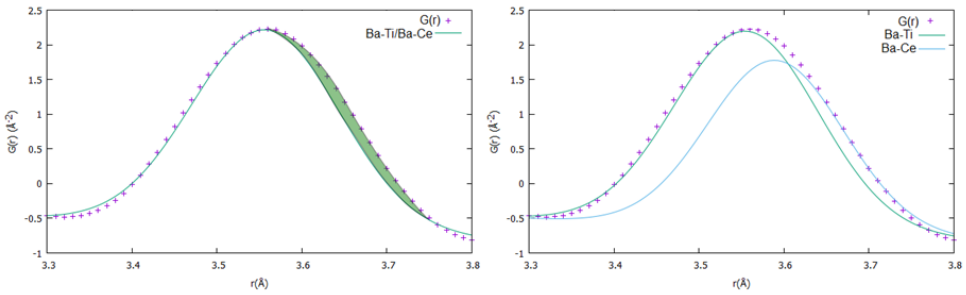

Figure 5.43: Left: manual fits of Ba-Ti/Ba-Ce peak by single Gaussian curve, a slightly asymmetry is evident. Right: manual fits of Ba-Ti/Ba-Ce peak by two Gaussian curves. The heights take into account Ti and Ce scattering potential and a Ba-Ce probability of $0.2\bar{2}$ against $0.7\bar{8}$ for Ba-Ti. These probability are calculated considering a possible cluster configuration.

According to the hypotheses above reported two different disorder causes are possible. Unfortunately using X ray data it could be difficult to deal with the oxygen disorder. Then, before to do this, it is better to be sure about the B cation order. In an ideal solid solution cerium should be distributed homogeneously; this is already demonstrated in the average analysis, but locally the situation could be different.

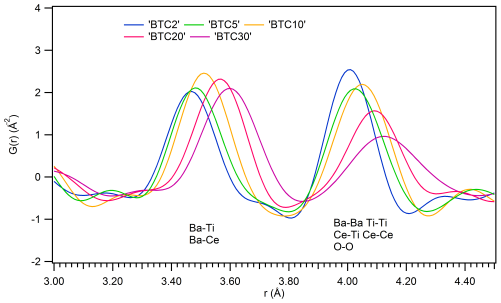

Figure 5.44: Comparison PDFs of different samples are reported at 300 K. Ba-Ti/Ba-Ce and then Ba-Ba/Ti-Ti/Ti-Ce/Ce-Ce/O-O peaks are shown.

5.2.1 B Cation Disorder

The purpose of this subsection is to understand if $BaCeO_3$ clusters in a $BaTiO_3$ matrix could be effectively present in BTC samples. Different works have been made on similar perovskites for example Laulhé *et al.* (Laulhe et al. 2006) show that Zr atoms tend to segregate in $BaTi_{1-x}Zr_xO_3$ relaxor. This hypothesis is then refuted by Levin *et al.* (Levin et al. 2011) excluding any significant short range ordering or clustering of Ti and Zr for samples with $x \geq 0.04$. Other example is $CaTi_{1-x}Zr_xO_3$ where B cation random distribution has been proved by EXAFS analysis (Levin et al. 2006), but a weak discernible local order has been then found using Reverse Monte Carlo method (Krayzman & Levin 2008). These investigations demonstrate how the B cation order or disorder is important and crucial to describe complex perovskites and their properties. In order to do this different methods will be employed.

Biphasic model

A biphasic model could be applied using the two end-members structures of the solid solution similarly as in Rietveld quantitative analysis. In general the author does not believe in this approach considering that the interaction of the two phases is not taken into account and then all the bonds between. However this strategy has been successfully employed in different works (Scavini et al. 2012) (Coduri et al. 2012a) (Coduri et al. 2012b) then there is no harm in trying. $BaCeO_3$ (Malavasi et al. 2009) and $BaTiO_3$ (Kwei et al. 1993) structures at room temperature has been used. Firstly a comparison between the theoretical PDFs of the two end-members and data is performed (figure 5.45), once again BTC20 is the reference sample.

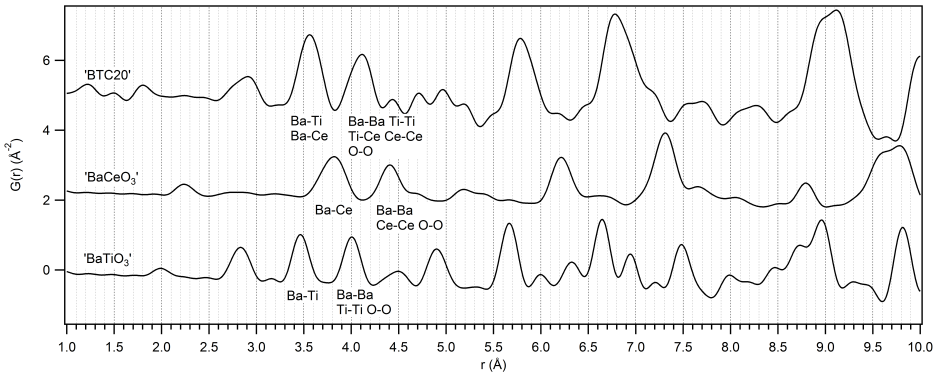

Figure 5.45: Comparison between theoretical PDFs of the two end-members at room temperature and BTC20 300 K. NB $BaCeO_3$ and $BaTiO_3$ functions have the same scale to ease the comparison. Functions are reported in a waterfall-like diagram.

As shown in figure, none of the two structures seems to represent data adequately. Observed peaks are indeed

in the middle, exactly between the two end-members. Furthermore it is not possible to recognize some particular features which could be assigned to one or to the other phase. Notwithstanding refinements have been then performed to apply the method scientifically and impartially. Indeed as reported in Coduri *et al.* end-members used in this kind of analysis could be different from their exact structure then they should be refined (Coduri et al. 2012b). First of all in order to respect the stoichiometry the two structural scales were fixed checking the ratio between atoms, unit cells and mass. Then cell parameters have been refined step by step, fixing one and then the other until reaching a good agreement with observed data, results in table 5.41.

	Cell parameter a (Å)	Cell parameter b (Å)	Cell parameter c (Å)
$BaTiO_3$ (Kwei *et al.* 1993)	3.9988(2)		4.0222(4)
$BaTiO_3$ refined	4.11(5)		4.10(1)
$BaCeO_3$ (Malavasi *et al.* 2009)	6.1861(5)	8.8039(8)	6.2525(5)
$BaCeO_3$ refined	5.80(2)	8.17(1)	5.81(2)

Table 5.41: Biphasic model applied for BTC20 100 K. Initial (referenced) and refined cell parameters are reported for pure $BaTiO_3$ and $BaCeO_3$.

Differently to other tables, here errors related to the PDF refinements, which are big, have been reported to underline how could be difficult to refine these two phases as independent entities. Practically it is quite impossible to distinguish clearly them. Furthermore the fit, reported in the lower part of figure 5.46, is not satisfying.

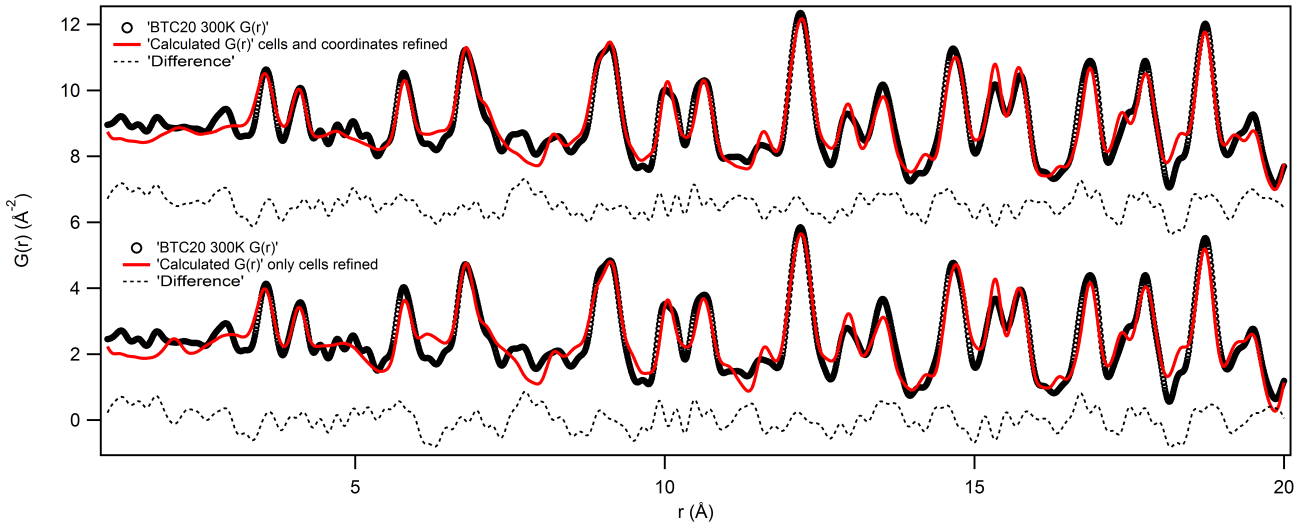

Figure 5.46: Biphasic model applied for BTC20 100 K. In the upper part fit with only cell refined parameters is shown, in the lower fit performed refining also atomic coordinates is documented.

In order to improve fit the two structures have been then refined in agreement to the S.G. rules keeping cell parameters fixed as in table 5.41 to do not complicate the calculation. Despite results (not reported being useless) present reasonable values, both for cell parameters and coordinates, final fit, reported in the upper part of figure 5.46, is not satisfying. At the end the biphasic model is not the right approach to explain the local disorder especially considering a fit worsening even in the range over 10 Å.

Cluster model

A new approach, philosophically different with that above employed, consists in a structural model composed by $BaCeO_3$ clusters in a $BaTiO_3$ matrix. A supercell is built allowing Ti and Ce with an integer occupancy, then the

interaction of the two phases are taken into account. In order to validate this model a kind of simulation has been performed. Supercell 5x5x5 made by 125 cells has been created (left part of figure 5.47), again BTC20 at 100 K is taken as example. Even though this model is simplified and not realistic, its outcome could be useful to get a better understanding of the type of disorder in the sample. In order to maintain the simulation as simple as possible cells and supercell present $a = b = c$, $\alpha = \beta = \gamma = 90°$, atoms in a single cell are placed as in a normal cubic structure. As mentioned before a good way to fit Ba-Ti and Ba-Ce peak is i) increase the Ba-Ce probability ii) consider Ba-Ce bigger than Ba-Ti. The first purpose is achieved positioning cerium in a single plane to reproduce a sort of cluster and the second moving barium atoms related to Ce.

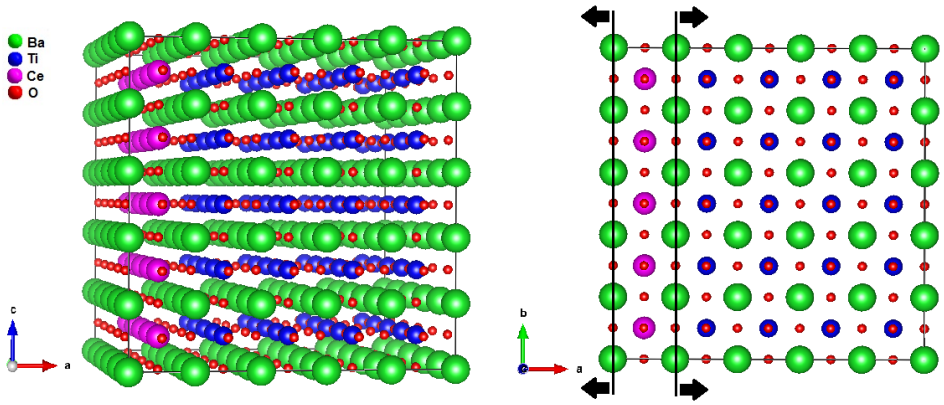

Figure 5.47: Starting model composed by a single planar $BaCeO_3$ cluster in a $BaTiO_3$ matrix. On the right side Ba movements, manually imposed, are evidenced by arrows.

In other words cerium cells have been made bigger moving manually barium along positive and negative x direction (as evidenced in the right part of figure 5.47). Obviously considering a S.G. P1 for the supercell this procedure is absolutely licit. Usually Ba displacement is not considered as a possible disorder due to its position, which in R3m is chosen as the origin of the cell, and due to its size. However in some cases a little Ba displacement is detected as in $BaTi_{1-x}Zr_xO_3$ (Laulhe et al. 2010). This kind of test has been performed, always respecting the stoichiometry, in a similar way for three samples: BTC5, 10 and 20. Ba atoms are moved in different steps, in figure 5.48 a comparison between PDF calculations of the initial configuration and the one with a displacement of ± 0.005 is presented.

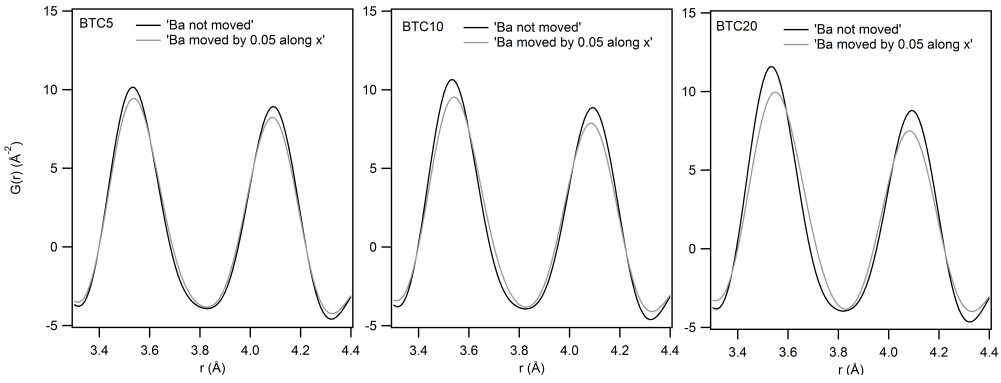

Figure 5.48: Comparison between calculated PDFs of initial configurations and those obtained by a Ba displacement equal to ± 0.005 is shown for BTC5 , 10 and 20. Only peaks related to Ba-Ti/Ba-Ce and Ba-Ba/Ti-Ti/Ti-Ce/Ce-Ce/O-O are presented.

The created barium displacements generate a peak shift (the first peak in each window of figure 5.48) to the right side as desired. As expected this shift is greater the larger the cerium amount. Furthermore the little induced

movements do not lead to a complete upset in Ba-Ba distance, related peak (the second in each window of figure 5.48) remains close to initial position, but a sufficient disorder is created reducing the intensity. All of these indications are very promising, but obviously to be verified refinements are necessary. In order to manage easily the analysis, performed just for lowest temperatures, a new supercell, built as a 5x6x1 to simplify the constrains respecting the right stoichiometry, has been used with a cluster of $BaCeO_3$ positioned in the middle. Different parameters are refined supposing a P1 S.G., but using some constrains derived by R3m:

- supercell parameters are constrained imposing i) $a = 5c$ and $b = 6c$ and ii) $\alpha = \beta = \gamma \neq 90°$.
- Ti in a single cell is refined constraining x=y=z, and then tied by translation with other Ti atoms. Same procedure for cerium.
- Ba atoms near to Ce in a single cell is refined constraining x=y=z, and then tied by translation. Same procedure for remaining Ba.
- O atoms near to Ce in a single cell is refined constraining x=y and different z, and then tied by translation. Same procedure for remaining O.

This approach comes from the idea of treating $BaCeO_3$ cells differently to those with titanium. The use of constrains above reported and the fixed Uiso allow to limit the number of parameters making the refinement easy, but at the same time ensuring a certain freedom degree. Resulting fit, shown in figure 5.49, appears good.

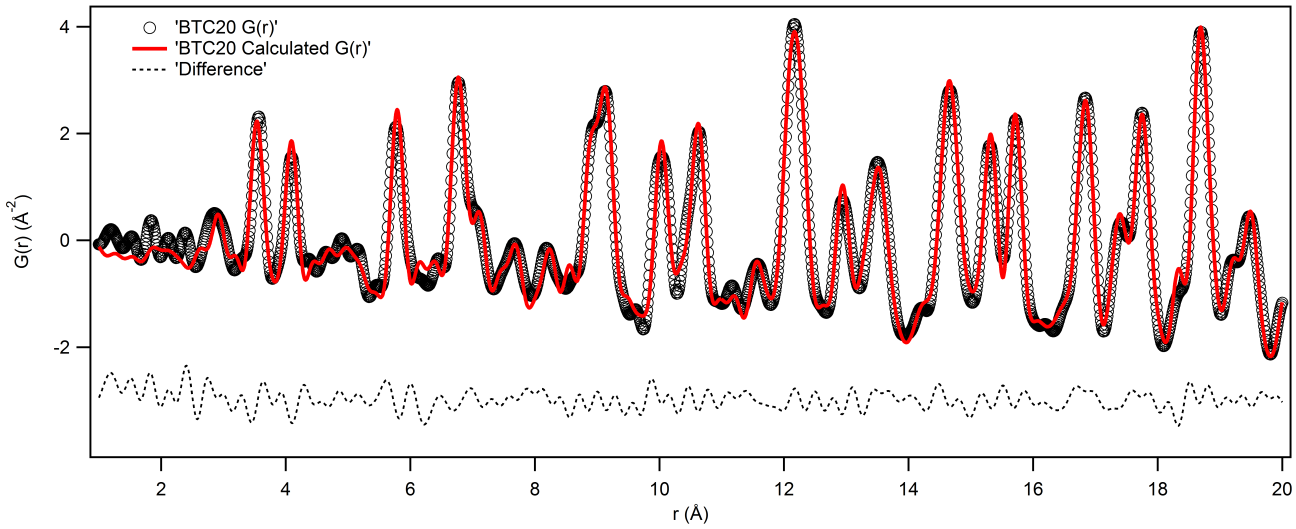

Figure 5.49: Fit of BTC20 100 K using, as a starting model, a simple supercell by 5x6x1 with a $BaCeO_3$ cluster. $BaCeO_3$ cells are treated differently to those with titanium.

Fortunately or unfortunately, results overturn the starting idea of Ba-Ce bonds longer than those of Ba-Ti. Indeed distribution of Ba-Ce lengths is between ~ 3.466 and ~ 3.613, whereas that of Ba-Ti is from ~ 3.263 to ~ 3.816. However the fact of obtain two different distributions suggests that it should be reasonable to treat Ce and Ti as different using not fractional occupancies, but resorting to a configuration as supercell. This analysis is then an indication, but not a final result. It is in fact not possible to consider truthful a cluster of this dimension which is not statistically representative.

Lattice Energy Calculation

The problem of statistical representation of clusters is overtaken thank to a home made software (written and developed by Professor Alessandro Pavese) which is able to produce big supercells and then big clusters or big cluster distributions. For every single sample (BTC 5, 10 and 20) the software allows to create different supercells (10x10x10 with 5000 atoms), respecting different stoichiometries, with different number of cluster. Obviously if cerium content is kept fixed, and it is, different number of cluster means different sizes of these $BaCeO_3$ 'islands'. It is sufficient to input a supercell, in this case, of pure $BaTiO_3$ with cell parameters equal to those found in the average structure and then specify the type of dopant element, the amount and time by time the number of desired clusters. At this point for every single supercell 3000 random configurations are generated changing casually cluster positions. Only this final operation allows to reach a statistical representation. In figure 5.50 an example of five configurations of supercell with ten clusters generated for BTC20 is shown. In order to understand if the $BaCeO_3$ clusters could be or not probable, an energetic lattice calculation has been then performed. To execute this operation GULP software (Gale 1997) has been used with atomic potentials found in bibliography (Freeman et al. 2011) (Woodley et al. 1999).

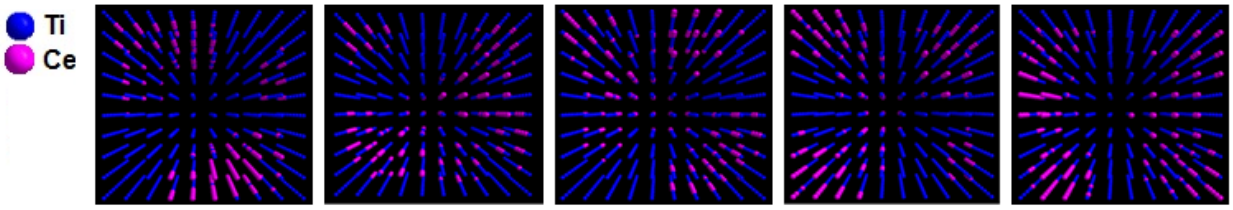

Figure 5.50: BTC20: five possible configurations for 10 clusters supercell. Only Ti and Ce are made visible.

It is important to point that the purpose of this work is not a calculation of absolute values, but a comparison between samples and configurations. Then eventual errors or simplifications in input potentials do not influence and condition the final result. For every configuration related to a single supercell lattice energy has been calculated and then the average value and the estimated standard deviation have been taken into account. In tables 5.42, 5.43 and 5.44 results calculated for structures at 100 K are reported. In detail for each sample and each supercell it is shown: i) the ratio between the average energy of all the related configurations and the average energy of all the supercells ii) the corresponding relative standard deviation (RSD), which is negative because related to a negative the average energy of the supercell.

BTC5	Number of clusters	Average E_C/Average E_{Ss}	RSD	Ce in each cluster
	1	1.00006	-0.00026	50
	2	1.00002	-0.00023	25
	5	1.00000	-0.00019	10
	10	0.99998	-0.00016	5
	20	0.99996	-0.00014	2.5
	35	0.99999	-0.00012	1.43
	50	0.99999	-0.00011	1

Table 5.42: BTC5 100 K: supercells with different number of clusters are reported linked to the ratio between the average energy of all the related 3000 random configurations E_C (which corresponds to the average energy of the supercell) and the average energy of all the supercells E_{Ss} and RSD. The number of cerium in each cluster in table reported is mathematically recalculated to give an idea of the possible cluster dimensions, in supercell each cluster must present an integer number of cerium atoms.

In figure 5.51 results reported in tables are shown. Comparison of different chemical materials is not very appropriate if the lattice energy is considered, so only differences between supercells related to each single sample will be discussed. Considering the calculated ratios, values greater than one mean a value of E_C bigger (in

BTC10	Number of clusters	Average E_C/Average E_{Ss}	RSD	Ce in each cluster
	1	1.00010	-0.00039	100
	5	1.00004	-0.00024	20
	10	1.00006	-0.00021	10
	20	0.99997	-0.00020	5
	50	0.99996	-0.00017	2
	70	0.99995	-0.00013	1.43
	100	0.99993	-0.00013	1

Table 5.43: BTC10 100 K: supercells with different number of clusters are reported linked to the ratio between the average energy of all the related 3000 random configurations E_C (which corresponds to the average energy of the supercell) and the average energy of all the supercells E_{Ss} and RSD. The number of cerium in each cluster in table reported is mathematically recalculated to give an idea of the possible cluster dimensions, in supercell each cluster must present an integer number of cerium atoms.

BTC20	Number of clusters	Average E_C/Average E_{Ss}	RSD	Ce in each cluster
	1	1.00020	-0.00066	200
	10	1.00007	-0.00034	20
	20	1.00011	-0.00031	10
	50	0.99995	-0.00026	4
	100	0.99990	-0.00022	2
	150	0.99987	-0.00018	1.333
	200	0.99989	-0.00017	1

Table 5.44: BTC20 100 K: supercells with different number of clusters are reported linked to the ratio between the average energy of all the related 3000 random configurations E_C (which corresponds to the average energy of the supercell) and the average energy of all the supercells E_{Ss} and RSD. The number of cerium in each cluster in table reported is mathematically recalculated to give an idea of the possible cluster dimensions, in supercell each cluster must present an integer number of cerium atoms.

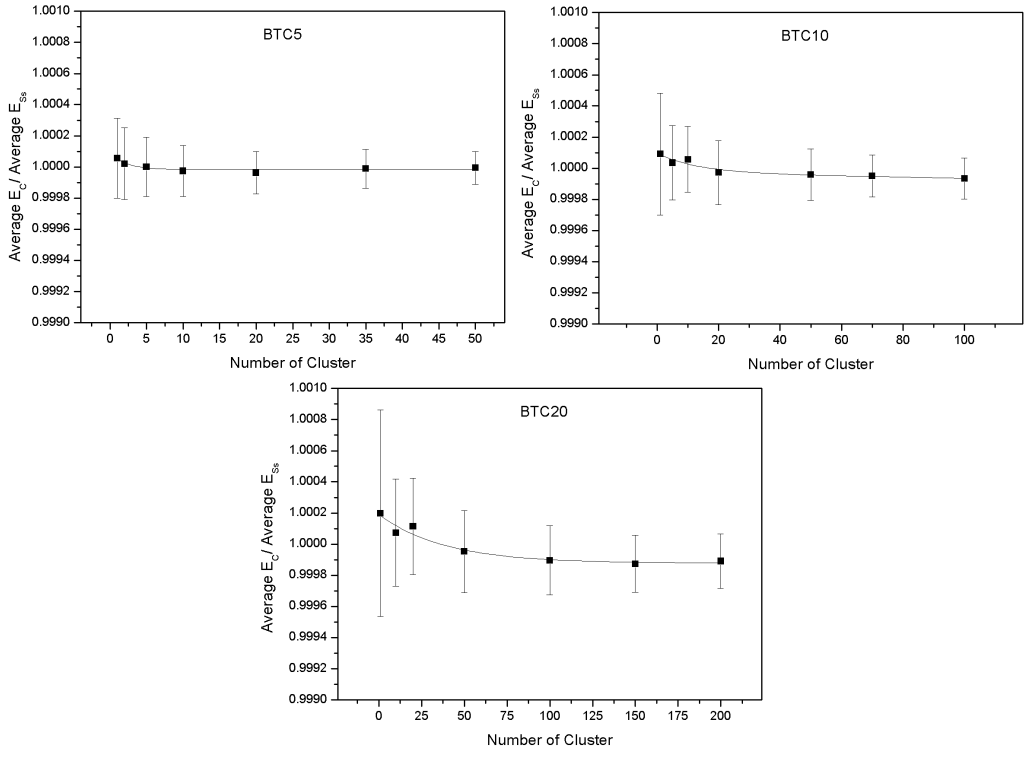

Figure 5.51: Comparison between lattice energy calculated for BTC 5, 10 and 20 at 100 K presenting different number of clusters is shown. Differently to the lower, in the upper part three windows present the same scale. Also fit curve is shown as a eye-guide.

modulus) than the average one. Then these supercells should represent the most stable structures. In the light of this, in all samples the lowest energies are calculated for configurations presenting just few clusters, but on the

other hand they are associated to bigger deviations. Considering also that the difference in values of supercells with some or few clusters is too slight, it is impossible to tend for the second model. By this analysis a more or less homogeneous distribution of cerium is then the most probable condition in $BaTi_{1-x}Ce_xO_3$, but, despite these results, the method applied is not sufficient to define a certain solution of the proposed problem.

Analysis by electron microprobe

$BaTi_{0.8}Ce_{0.2}O_3$ is studied by electron microbe in order to investigate elements distribution. Firstly backscattered electron (BSE) image has been collected to examine composition at microscopic scale. Picture 5.52 (bottom left square) proves a good sample preparation showing a low porosity, but on the other hand some zones exhibit a different gray nuance signal of heterogeneity.

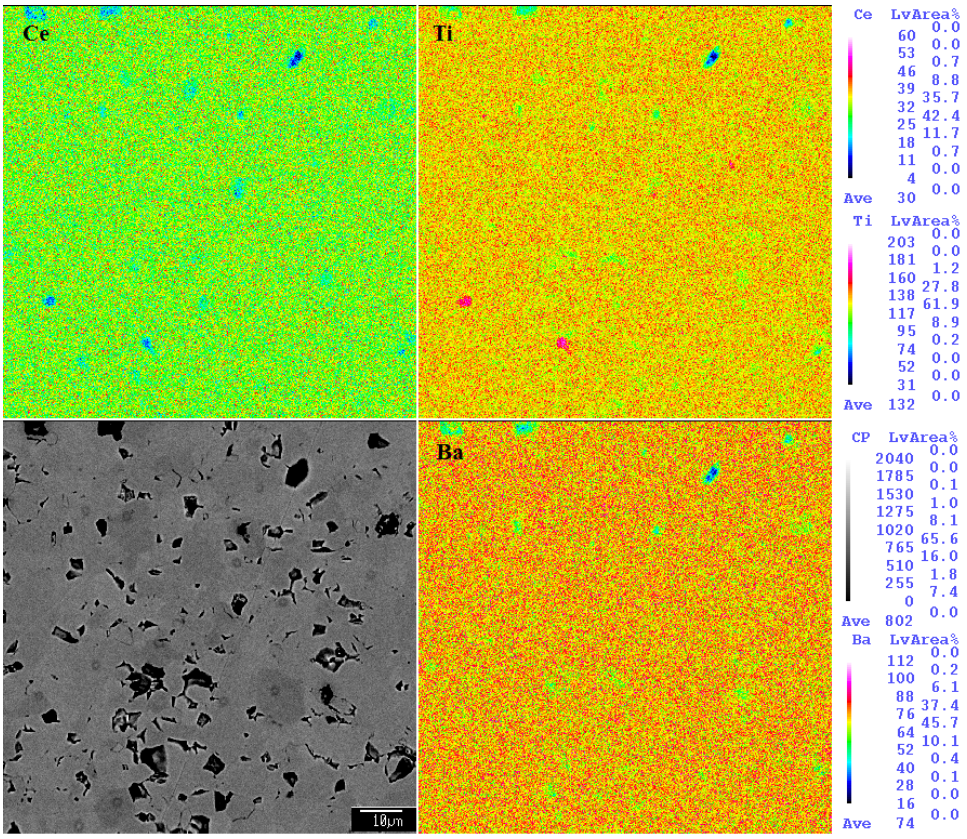

Figure 5.52: Electron microprobe analyses on BTC20. Clockwise: maps of cerium, titanium barium and related backscattered image collected on the same area.

Using BSE image as reference, element maps have been acquired on the same area by WDS detector for titanium and cerium and EDS for barium. Measurements are reported in picture 5.52. The four images could be perfectly superimposed demonstrated that the only diversities noticeable are actually linked to the sample porosity (*i.e.* in every map pores obviously present a lower content of the element). At the end no chemical heterogeneity has been detected proving an homogeneous element distribution at microscopic scale. Differences in BSE image could be then related not to diversities in the chemical composition, but rather to a not perfect polished surface. Despite results are in contrast with a sample composition consisting in different chemical domains, the scale of the reported analyses is bigger, four order of magnitude, than those observed using Pair Distribution Function. This highlights again the need of different and more decisive tests to describe the B cation disorder.

TEM investigation

In different works TEM has been used to characterize ceramic perovskite in terms of lattice parameter and particles size (example: investigation on $Ba_{1-x}Zr_xTiO_3$ (Zou et al. 2012)) or to prove a second phase existence (as in Y doped $BaTiO_3$ (Zheng et al. 2007)). Then, after a deep study using indirect methods to prove or not the supposed $BaCeO_3$ clusters in a $BaTiO_3$ matrix, TEM observations could give the last and definitive answer. At this point the reader could wonder why this analysis has not been performed before. First of all this investigation is certainly expensive and secondly there was the hope to model easily the local disorder or to have at any rate a clear expression of B cation order, but desperate times call for drastic measures. As reported in subsection 3.5 only BTC20 has been prepared in two different way. Considering that the discussion will follow a logic sequence from maximum to a minimum observation scale the analyses on the two samples will be mixed. In any case, for the sake of clarity, in figure captions sample preparation will be specified. In figure 5.53 it is possible to recognize a perfect equilibrium texture with grain boundaries at a triple junction (120°). In the same image also some diffraction patterns are reported demonstrating the single crystal nature of grains. Furthermore it is clear that substitution of titanium by cerium does not bring to a creation of superlattice reflections even at this scale demonstrating a not short range chemical order between the two B cations.

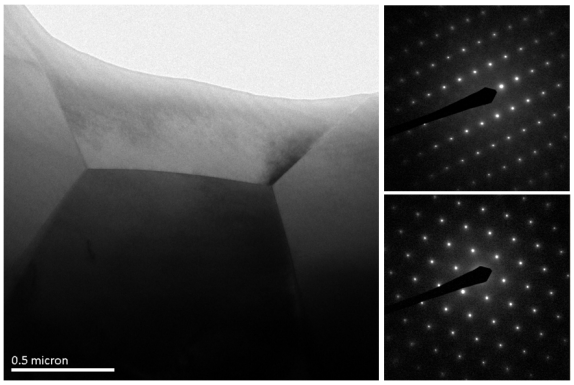

Figure 5.53: TEM image obtained investigating BTC20 prepared by PIPS. Equilibrium texture with grain boundaries at a triple junction ($120°$) is recognizable. Furthermore two diffraction patterns are reported demonstrating the existence of perfect single crystals.

In figure 5.54 a great dislocation density is clearly noticeable. Unfortunately despite this big presence of defects it is not possible to consider them as the prevalent cause of the disorder in the low PDF region. In fact the correlation length of these dislocations is too large to be responsible of the disorder up to here treated. However this is a considerable indication of the consequence in terms of strain generated by the cerium introduction.

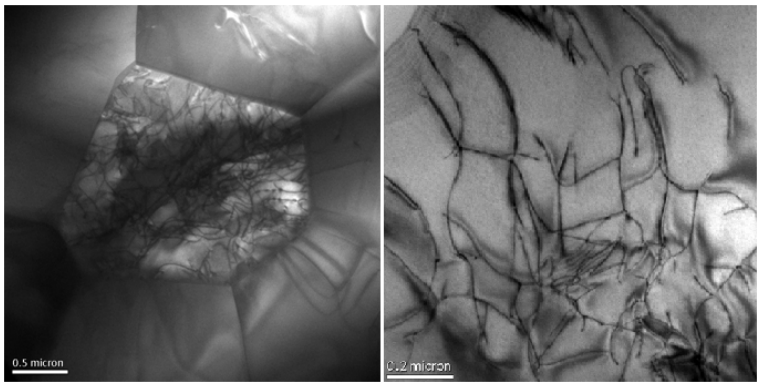

Figure 5.54: TEM image obtained investigating BTC20 prepared by PIPS. A great dislocation density is noticeable.

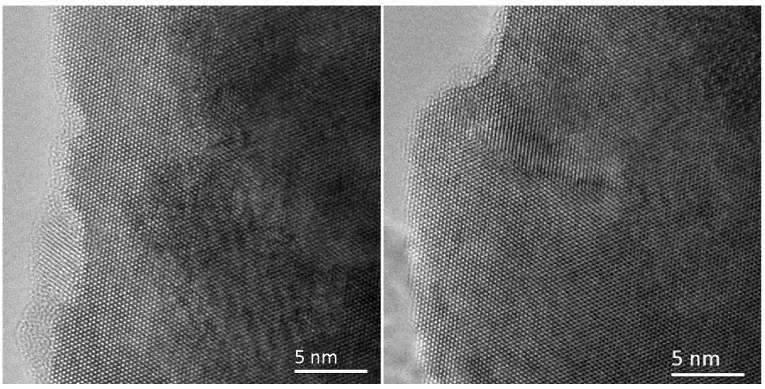

Figure 5.55: HR-TEM images obtained investigating BTC20 powders. In both figures a very regular atomic lattice is recognizable, no cluster or zones different to the matrix are observable. The only defects clearly noticeable are dislocations.

High resolution images are presented (figure 5.55). Making an accurate analysis on cell parameters and on the distance between barium rows, no different zones are detectable. This means that despite dislocations (example in the right side of figure 5.55), no other type of disorder seems to be present or better visible. Observations then subvert the hypothesis of cerium rich clusters. In order to have another evidence, EDS analyses has been performed on different points. An example of results is reported in table 5.45 and related point in figure 5.56; values demonstrate a homogeneous distribution of cerium.

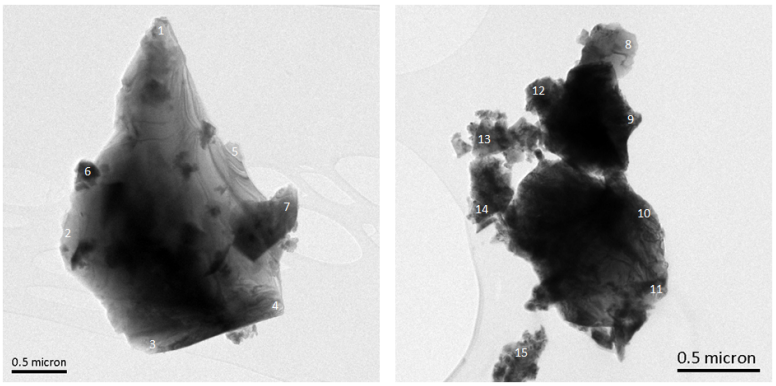

Figure 5.56: In this image points investigated by EDS analysis are reported. Result are shown in table 5.45.

		1	2	3	4	5	6	7		Mean	Min.	Max.
Element	Ti (%)	16.9	15.2	15.8	12	15	14	14.8		14.8	12	16.9
	Ba (%)	68.5	73.4	72.7	76	70.8	73.1	70.3		72.1	68.5	76
	Ce (%)	14.6	11.4	11.6	12	14.2	12.8	14.9		13.1	11.4	14.9
Atom	Ti (%)	36.9	34	35	28.2	33.6	32	33.4		33.3	28.2	36.9
	Ba (%)	52.2	57.3	56.3	62.3	55.5	58.1	55.2		56.7	52.2	62.3
	Ce (%)	10.9	8.8	8.8	9.6	10.9	10	11.5		10.1	8.8	11.5
		8	9	10	11	12	13	14	15	Mean	Min.	Max.
Element	Ti (%)	12.1	12.5	12	11.9	12.6	12.7	11.9	12.7	12.3	11.9	12.7
	Ba (%)	76.8	74.6	78.5	76	76.1	75.5	76.2	76.3	76.3	74.6	78.5
	Ce (%)	11.1	12.9	9.5	12.1	11.2	11.8	11.9	11.1	11.4	9.5	12.9
Atom	Ti (%)	28.4	29.2	28.2	27.9	29.4	29.5	27.9	29.4	28.7	27.9	29.5
	Ba (%)	62.8	60.6	64.2	62.4	61.7	61.1	62.5	61.8	62.1	60.6	64.2
	Ce (%)	8.9	10.3	7.6	9.7	8.9	9.4	9.6	8.8	9.1	7.6	10.3

Table 5.45: Values obtained by EDS analysis, performed on points reported in figure 5.56, are shown.

Definitively TEM and EDS observations exclude a B cation disorder in terms of $BaCeO_3$ clusters in a $BaTiO_3$ matrix and also preclude evident Ba displacements. Furthermore the absence of superlattice reflections demonstrates a not chemical order of titanium and cerium. In conclusion only a homogeneous distribution of the two B cations is recognizable in BTC.

5.2.2 Octahedra Tilt

Considering that the supposed particular arrangements between Ti and Ce is actually not the principle cause of the failure of the structural models used, the most probable solution to model local structure could be concealed in the oxygens positions. In this section some refinements which involve models with a certain oxygen disorder have been already proposed, but now in order to better understand where and how the local disorder is generated an approach as carbox is used. This consists in to perform refinements in different and increasing radius ranges allowing to explore the evolution of the structure at different length scales (as explained in chapter 2). Considering that increasing the radius ranges a more averaged structure is represented, this approach is useful to understand the coherent correlation length of the true local structure and then the correlation length of the disorder. All samples have been taken into account, but to reduce the contribution of dynamic disorder, only lowest temperatures have been inspected (specifically BTC2 at 150 K, BTC5 at 200 K and BTC 10, 20 and 30 at 100 K). Refinements have been performed in four steps changing time by time the radius range: from 1 to 5.5 Å, 5.5 to 10, 10 to 14.5 and at then end from 1 to 14.5 to have a reference. Four different strategies were used and all adopted range by range. Supercell has been built by 2x2x2 rhombohedric cells; Ti and Ce has been considered independent, but linked by fractional occupancy. For all the inspections cell parameters and scale have been refined just with:

- A strategy: Uiso for Ba, Ti, Ce and O
- B strategy: Ti and Ce coordinates, constrained as xxx
- C strategy: O coordinates: constrained as xxz
- D strategy: Ti, Ce and O coordinates as above

Here just the most promising results are reported. In tables 5.46, 5.47, 5.48, 5.49 and 5.50 Uiso values calculated by the A strategy refinements are shown.

BTC2 Range (Å)	Uiso Ba ($Å^2$)	Uiso Ti ($Å^2$)	Uiso Ce ($Å^2$)	Uiso O ($Å^2$)
1-14.5	0.00026	0.00447	0.03025	0.0095
1-5.5	0.00518	0.00312	0.00311	0.01492
5.5-10	0.00184	0.00758	1.62E-04	0.02777
10-14.5	0.00165	0.00755	0.03814	0.02353

Table 5.46: BTC2 local structure refinements by carbox approach. A strategy has been applied refining: cell, scale and Uiso.

BTC5 Range (Å)	Uiso Ba ($Å^2$)	Uiso Ti ($Å^2$)	Uiso Ce ($Å^2$)	Uiso O ($Å^2$)
1-14.5	0.00294	0.00673	0.00771	0.02657
1-5.5	0.00211	0.0051	0.00053	0.01699
5.5-10	0.00325	0.00654	0.03626	0.03624
10-14.5	0.00128	0.0061	0.02536	0.01499

Table 5.47: BTC5 local structure refinements by carbox approach. A strategy has been applied refining: cell, scale and Uiso.

In picture 5.57 Uiso for different atoms, samples and radius range are graphically expressed. As expected oxygen atoms present very high Uiso values for any cerium amount. Moreover, comparing different step analyses, oxygen Uiso results obtained for the range 5.5-10 Å appear very intense.

Proceeding in the discussion it is also useful to consider the C and the D approach, whereas B is not considered because it does not involve Uiso and positions of oxygens. Again the purpose is to investigate oxygen disorder,

BTC10 Range (Å)	Uiso Ba ($Å^2$)	Uiso Ti ($Å^2$)	Uiso Ce ($Å^2$)	Uiso O ($Å^2$)
1-14	0.00268	0.00665	0.00711	0.02853
1-5.5	0.00234	0.00305	0.00344	0.01612
5.5-10	0.00308	0.00448	0.04052	0.04242
10-14.5	0.00297	0.00746	0.0074	0.02765

Table 5.48: BTC10 local structure refinements by carbox approach. A strategy has been applied refining: cell, scale and Uiso.

BTC20 Range (Å)	Uiso Ba ($Å^2$)	Uiso Ti ($Å^2$)	Uiso Ce ($Å^2$)	Uiso O ($Å^2$)
1-14.5	0.00485	0.00589	0.00611	0.03434
1-5.5	0.00337	0.0033	0.00339	0.02227
5.5-10	0.00503	0.00546	0.00955	0.04378
10-14.5	0.00584	0.00669	0.00748	0.03333

Table 5.49: BTC20 local structure refinements by carbox approach. A strategy has been applied refining: cell, scale and Uiso.

BTC30 Range (Å)	Uiso Ba ($Å^2$)	Uiso Ti ($Å^2$)	Uiso Ce ($Å^2$)	Uiso O ($Å^2$)
1-14.5	0.00658	0.00565	0.00568	0.03942
1-5.5	0.00602	0.00327	0.00327	0.02798
5.5-10	0.00737	0.00742	0.00721	0.0505
10-14.5	0.00657	0.00759	0.00738	0.0355

Table 5.50: BTC30 local structure refinements by carbox approach. A strategy has been applied refining: cell, scale and Uiso.

thus in tables 5.51 and 5.52 and in figure 5.58 the displacements of this atom will be presented. As noticeable by comparison, the second range (5.5-10 Å) requires bigger movements to fit data adequately. Moreover bigger oxygen displacements correspond to BTC with high doping amount.

C Strategy: Oxygen displacements (Å)					
range (Å)	BTC2	BTC5	BTC10	BTC20	BTC30
1-14.5	0.180	0.194	0.233	0.215	0.258
1-5.5	0.173	0.188	0.172	0.207	0.235
5.5-10	0.208	0.223	0.324	0.280	0.304
10-14.5	0.160	0.186	0.196	0.210	0.208

Table 5.51: Carbox approach C strategy: oxygen displacements obtained for different radius ranges. Displacements have been calculated considering the center of each cell face and the refined oxygen coordinates.

D Strategy: Oxygen displacements (Å)					
range (Å)	BTC2	BTC5	BTC10	BTC20	BTC30
1-14.5	0.180	0.196	0.233	0.213	0.235
1-5.5	0.157	0.169	0.174	0.203	0.212
5.5-10	0.208	0.293	0.337	0.305	0.323
10-14.5	0.200	0.219	0.212	0.215	0.227

Table 5.52: Carbox approach D strategy: oxygen displacements obtained for different radius ranges. Displacements have been calculated considering the center of each cell face and the refined oxygen coordinates.

High Uiso and displacements detected from 5.5 to 10 Å suggest a disorder not only in first bond lengths, but also in the relationship between different octahedra. Carbox has been then useful to understand which is the range presenting more disorder and the deduced information could be a great help to built a new model which take it into account. By this type of analysis indeed seems that the interaction between different cells could be one of the

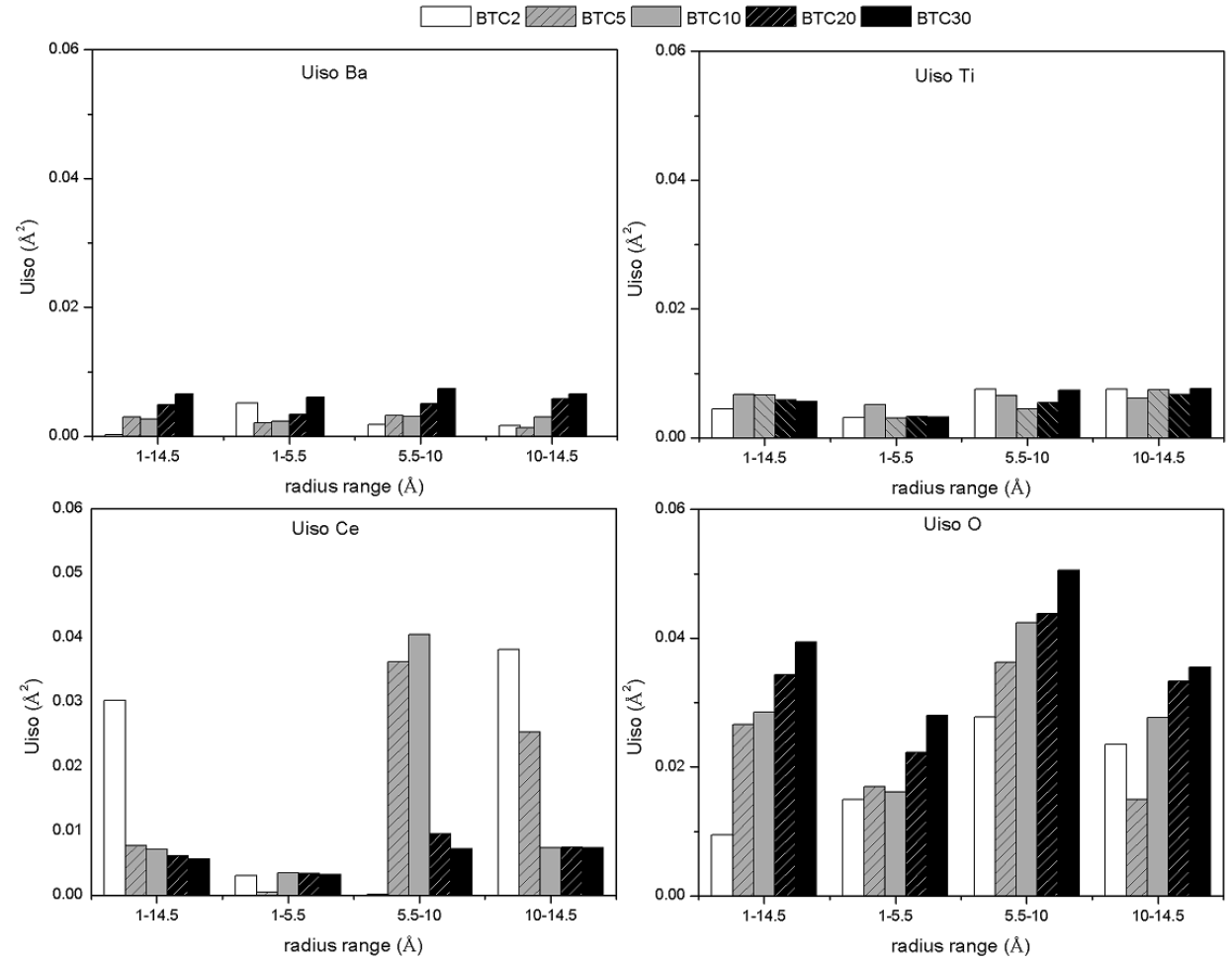

Figure 5.57: Carbox approach A strategy: Uiso values obtained for different radius ranges.

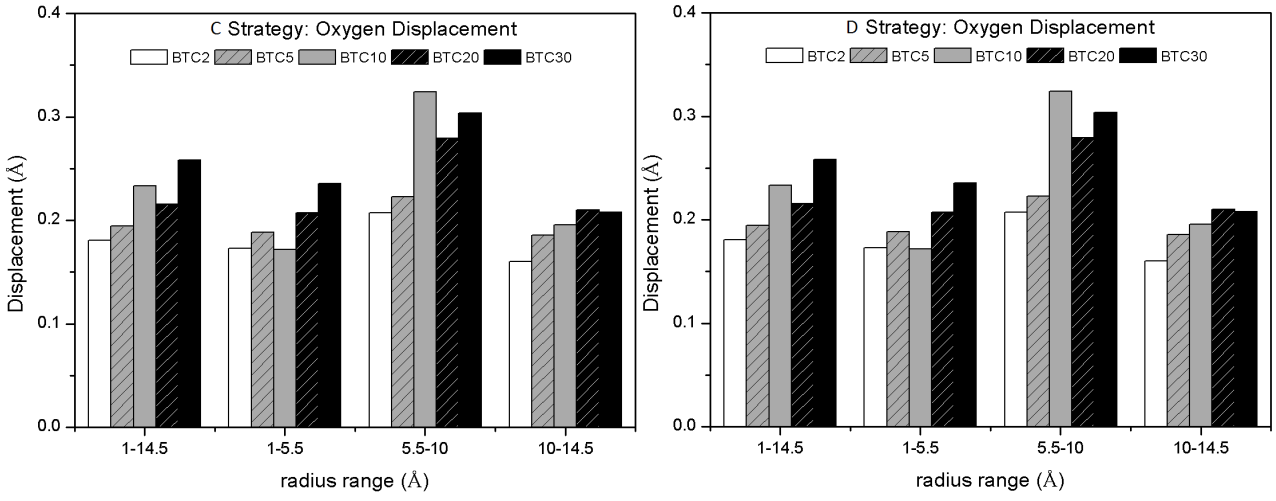

Figure 5.58: Comparison between oxygen displacements obtained for different radius ranges applying carbox approach with C and D strategy.

causes of the great local disorder. In figure 5.59 an example of distance where two atoms are related to different cells and to two different polyhedra is reported, this bond length belongs to the second radius range.

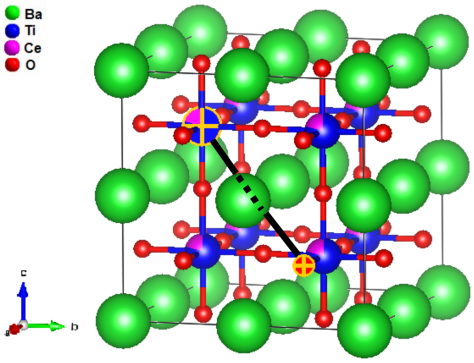

Figure 5.59: Example of bond length of Ti and O (6.1188 Å), then in the second second radius range previously treated.

Producing different tilts in different octahedra could be a good way to induce disorder especially on the third coordination shell. In general this type of distortion is not peculiar of pure $BaTiO_3$ where properties of ferroelectric phases are related only to the B cation displacement, as explained in introduction. However other perovskites, in which A cation is too small for the corner-sharing octahedral network, show a kind of distortion mechanism that can be realized by tilting, essentially rigid, BO_6 octahedra while maintaining their corner-sharing connectivity (Woodward 1997). Cooperative tilting of the undistorted octahedra occurs then to shorten A-O and thereby improve the coordination environment and bonding of the A site cation. This is exactly the case of $BaCeO_3$ (Camilo de Souza & Muccillo 2010). The disorder in BTC samples could be then thought as related to tilted Ce-O octahedra which caused consequent and different tilts of next Ti-O polyhedra. Furthermore a superposition of perfectly rigid B-O octahedra with different volumes, due to the inner B cations sizes, is not compatible with a construction of an ideal perovskite structure: indeed octahedra must be slightly distorted to be put together (Laulhe et al. 2009). This is in agreement with BTC PDFs where disorder in the lower r region is governed by the clear nonexistence of the first Ti-O/Ce-O peaks meaning a wide spread of the related bond lengths. In conclusion it is not possible to maintain rigid Ti-O tilts and only a complex model which includes tilts and different polyhedra volumes is admissible. The idea of different coordination polyhedra for cerium and titanium is generated not only by data considerations, which is any case the most important point, but also by bibliographic indications. For example in $BaTi_{1-x}Zr_xO_3$ Zr-O and Ti-O distances seem to remain distinct and close to their values in the respective end-compounds and same results have been found for $Ca(Ti,Zr)O_3$ (Levin et al. 2006). Most recent work (Levin et al. 2011) reports the same conclusion, but specifying Zr-O length could be slightly shorten than in the end-member for diluted concentrations of Zr in $BaTiO_3$. However Zr octahedra remain bigger than those with Ti due to the two different cation sizes (Laulhe et al. 2010). In order to apply the new possible solution a multiple cell has been created to avoid Ti and Ce fractional occupancies. The choice of symmetry is in this case a delicate topic. Indeed different and very famous works about perovskite has been written on the relation between space group and octahedra tilting. The first and most important is by Glazer (Glazer 1972) in which description and classification of octahedral tilting in perovskites linked to the unit cell geometries is given, then reviewed by Howard and Stokes (Howard & Stokes 1998). Other papers have been proposed dealing with same subject for example specifying parametrization for octahedra tilting description in orthorhombic and tetragonal ABO_3 (Thomas 1996) or even developing software for space group prediction in $A_2B'M''O_6$ perovskite and in different tilt systems (Woodward 1997). Summarizing the tilting distortion is unequivocally related just to certain space groups and for sure not allowed for R3m. However these considerations are inconsistent if local disorder structure is treated (A.M. Glazer, personal communication, Rimini, 2016). In case of BTC it is then unproductive to play by the classical crystallographic rules, and more creative approach is needed. According to this, final model has been

built in P1 space group, but to reduce refinable values some constrains are imposed on cell parameters: $a = b = c$ and $\alpha = \beta = \gamma$. In order to approach the right stoichiometry different supercells were involved in this analysis: 4x4x4 for BTC5 (with 4.68% of cerium) and 10 (9.38% of cerium), 2x2x2 for 20 (25% of cerium) and 30 (37.5% of cerium). The slight differences in cerium amounts between models and reality are, in the author's opinion, not significant on the final results and indispensable to use manageable cells. BTC2 is not included in this experiment, the low cerium amount is considered to small to induce a complex tilting as in the other samples. Ba, Ti and Ce are placed respectively in the corner and in the middle of every single cell, in any case are kept fixed focusing only on the oxygen positions. In every cell O atoms are initially placed in (1/2, 1/2, 0); (1/2, 0, 1/2) and (0, 1/2, 1/2) where the only constrain is x = y exactly as in R3m. Then in order to create a different rotation of the octahedron the other three oxygen atoms, practically belonging to other cells, are linked to the relative opposite moving in the reverse way and so on cell by cell. Better explaining: oxygen can move in $(1/2 + \Delta x, 1/2 + \Delta x, 0 + \Delta z)$ and then the opposite in $(1/2 - \Delta x, 1/2 - \Delta x, 0 - \Delta z)$. Considering the Glazer's notation (Glazer 1972) this kind of conditions creates a tilt $a^-a^-a^-$ type. This is not allowed in R3m (Thomas & Beitoliahi 1994), however the model is in SG P1 where octahedral tilting is permitted, even though come of the constraints of the rhombohedric SG. Indeed these have been kept active in order to reduce the number of refinable parameters, which, in such a large unit cell, may become easily unmanageable. Furthermore, in order to induce a difference in Ti-O and Ce-O bond lengths oxygens related to different octahedra are constrained to move of different $\pm\Delta x$ and $\pm\Delta z$. In figure 5.60 a simplified sketch of different oxygen groups is reported. The idea is to create different groups of octahedra depending of cerium vicinity. Ce atoms, due to their size, has been kept fixed in the refinements then related octahedra could rotate and expand, but, differently to those of Ti, the six distances are constrained to be equal. Three groups have been appointed for TiO_6: octahedra near to those of cerium, octahedra far from cerium and those between these two groups. It is important to notice that cerium amount influences the existence of these different Ti octahedra categories. For example in BTC20 and BTC30 TiO_6 cages far from cerium can not occur, furthermore in BTC30 only Ti octahedra near to cerium can exist. Analyses have been performed (between 1-20 Å) refining cell parameters and oxygen positions, Uiso are fixed with different acceptable values for different temperatures. In order to make reasonable and simpler refinements oxygens between two titanium atoms (for BTC5 only where one is near to those with cerium and the other not) are fixed in z=0, this because Ti atoms are fixed and then oxygen between, in theory, should be stay in the middle of the two. However the first step is to analyse results of cell parameters reported in table 5.53 and in figure 5.61.

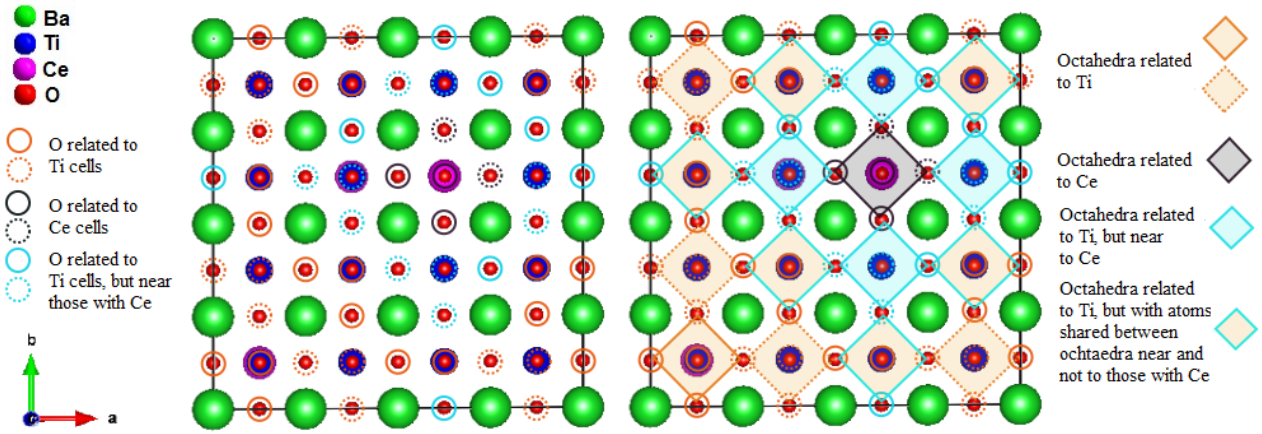

Figure 5.60: Complex octahedra tilts refinements: simplified sketch which represents strategy for oxygen positions for sample BTC5. On the right side oxygen groups are represented (full and dashed circle indicate oxygen and related opposite which moves in the reverse way). The right part describes different types of originated octahedra.

	Temperature	Cell Parameter (Å)	Angle (°)		Temperature	Cell Parameter (Å)	Angle (°)
BTC5	200 K	4.0299	89.602	BTC10	100 K	4.0494	89.587
	300 K	4.0322	89.691		200 K	4.0522	89.543
	350 K	4.0333	89.607		300 K	4.0551	89.502
	380 K	4.0340	89.608		400 K	4.0580	89.450
	420 K	4.0355	89.583				
BTC20	100 K	4.0945	89.450	BTC30	100 K	4.1317	89.403
	200 K	4.0970	89.413		200 K	4.1336	89.393
	300 K	4.1002	89.392		300 K	4.1368	89.375
	400 K	4.1037	89.369		400 K	4.1410	89.331

Table 5.53: Complex octahedra tilt refinements: cell parameters obtained for BTC5, 10, 20 and 30.

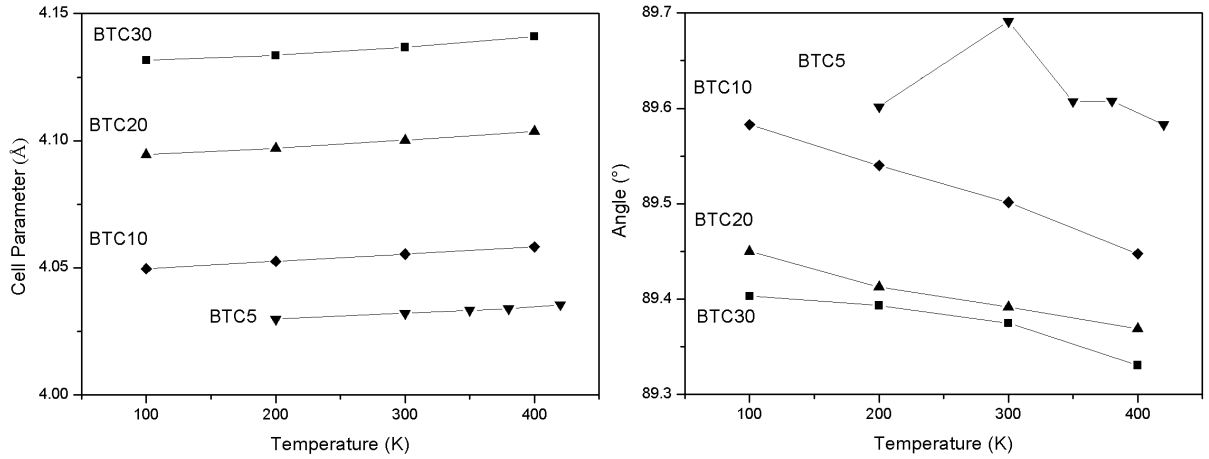

Figure 5.61: Complex octahedra tilt refinements: results of cell parameters and angles are compared.

Exactly as for other and before described attempts, cell parameter and angle evolution show opposite trends. The first in fact increases as a function of temperature and more for cerium amount, differently, angle moves further and further away from 90°. These results, being comparable with previous, are very promising and indicate how the complex model used does not affect this primarily information. A better discussion about the consequences and the effect of these results will be proposed in the next section 5.4. More interesting at this point is to explore the disorder induced by the oxygen positions described in terms of polyhedra volumes and shown in tables 5.54, 5.55, 5.56 and 5.57.

	Polyhedra Volume ($Å^3$) related to:			
BTC5	Ce	Ti, but near Ce	Ti in between	Ti
200 K	13.13	7.26	13.72	10.87
300 K	13.27	6.72	14.26	10.90
350 K	13.08	7.35	13.51	10.93
380 K	13.18	7.22	13.69	10.94
420 K	13.04	7.59	13.27	10.95

Table 5.54: Complex octahedra tilt refinements: Ti and Ce coordination polyhedra volumes are reported for BTC5. 'Ti in between' means titanium octahedra between the two other Ti octahedra types. Different labels of octahedra are described in text and in figure 5.60.

Before passing to the discussions, it is important to underline that these results could be misunderstood. Indeed the complexity of conceived constrains has a great influence on them and furthermore refinements are very driven, but ever legitimately, to achieve physical values (*e.g.* parameters refined step by step). In conclusion it is possible that these analyses lead to a not perfectly representation of reality, but it is also true that they are a product of

	Polyhedra Volume (Å^3) related to:			
BTC10	Ce	Ti, but near Ce	Ti in between	Ti
100 K	13.06	10.62	10.86	
200 K	13.60	10.58	10.90	
300 K	13.54	10.61	10.91	
400 K	13.88	10.62	10.97	

Table 5.55: Complex octahedra tilt refinements: Ti and Ce coordination polyhedra volumes are reported for BTC10. 'Ti in between' means titanium octahedra between the two other Ti octahedra types. Different labels of octahedra are described in text and in figure 5.60.

	Polyhedra Volume (Å^3) related to:			
BTC20	Ce	Ti, but near Ce	Ti in between	Ti
100 K	13.27	10.86		
200 K	13.32	10.87		
300 K	13.53	10.84		
400 K	13.73	10.82		

Table 5.56: Complex octahedra tilt refinements: Ti and Ce coordination polyhedra volumes are reported for BTC20. 'Ti in between' means titanium octahedra between the two other Ti octahedra types. Different labels of octahedra are described in text and in figure 5.60.

	Polyhedra Volume (Å^3) related to:			
BTC30	Ce	Ti, but near Ce	Ti in between	Ti
100 K	14.89	9.04		
200 K	14.41	9.37		
300 K	12.35	10.98		
400 K	12.32	11.05		

Table 5.57: Complex octahedra tilt refinements: Ti and Ce coordination polyhedra volumes are reported for BTC30. 'Ti in between' means titanium octahedra between the two other Ti octahedra types. Different labels of octahedra are described in text and in figure 5.60.

intense investigation based on a long try and error work. The model here presented is then the best result based on previous and less complex attempts and it should not be evaluated as perfectly accurate, but rather as a general trend. In figure 5.62 comparison between samples is shown, for each BTC octahedra volumes are reported as a function of temperature. Focusing on octahedra related to cerium and considering just an average view, volumes seem to remain approximately constant ($\sim$ 13 Å^3) in BTC5 ,10, 20 and also with temperature increase. Interpreting results related to Ti polyhedra is certainly more difficult. In $BaTi_{0.9}Ce_{0.1}O_3$ and $BaTi_{0.8}Ce_{0.2}O_3$ volumes are around $\sim$ 11 Å^3 without any evolution. The case of 5% of doping is different: in particular octahedra related to Ti, but near to cerium and those with some atoms shared whit these last present unusual values: the first is too small and the second too big (especially if it is compared with those of cerium). The two kind of polyhedra are strictly linked by (figure 5.60) a set of refined oxygens then the two volumes are complementary and problems are caused by just one refined O position (xxz). Unfortunately, despite various repetitions of the analysis, these parameters do not change. Anyway if a weighted average is calculated the average volume of the two is around $\sim$ 11 Å^3 which is similar to polyhedra related only to Ti and those of the other samples described. $BaTi_{0.7}Ce_{0.3}O_3$ is the only case in which volumes change with temperature. The two have very different starting points with trends which then become more and more convergent up to be practically parallel between 300 and 400 K. Here the two volumes, sharing all the oxygens, are completely dependent and then also the related errors. However, differently to BTC5, volumes reported are decisively more plausible. Rotation angle for each group of octahedra has been calculated also with distortion index, but the two parameters are not here presented because too dependent on the constrains used in data modeling. Furthermore in BTZ no relation between tilt angles and local chemical distribution has been found (Laulhe et al. 2010). Taking into account all the BTCs treated (expect for the problem of first sample) octahedra of titanium are smaller than those with cerium at all the temperatures. In this case B cation size clearly

determines the different bond lengths with oxygens resulting in a Ce-O distance bigger than Ti-O, as reported in bibliography above cited, and causing then structural disorder.

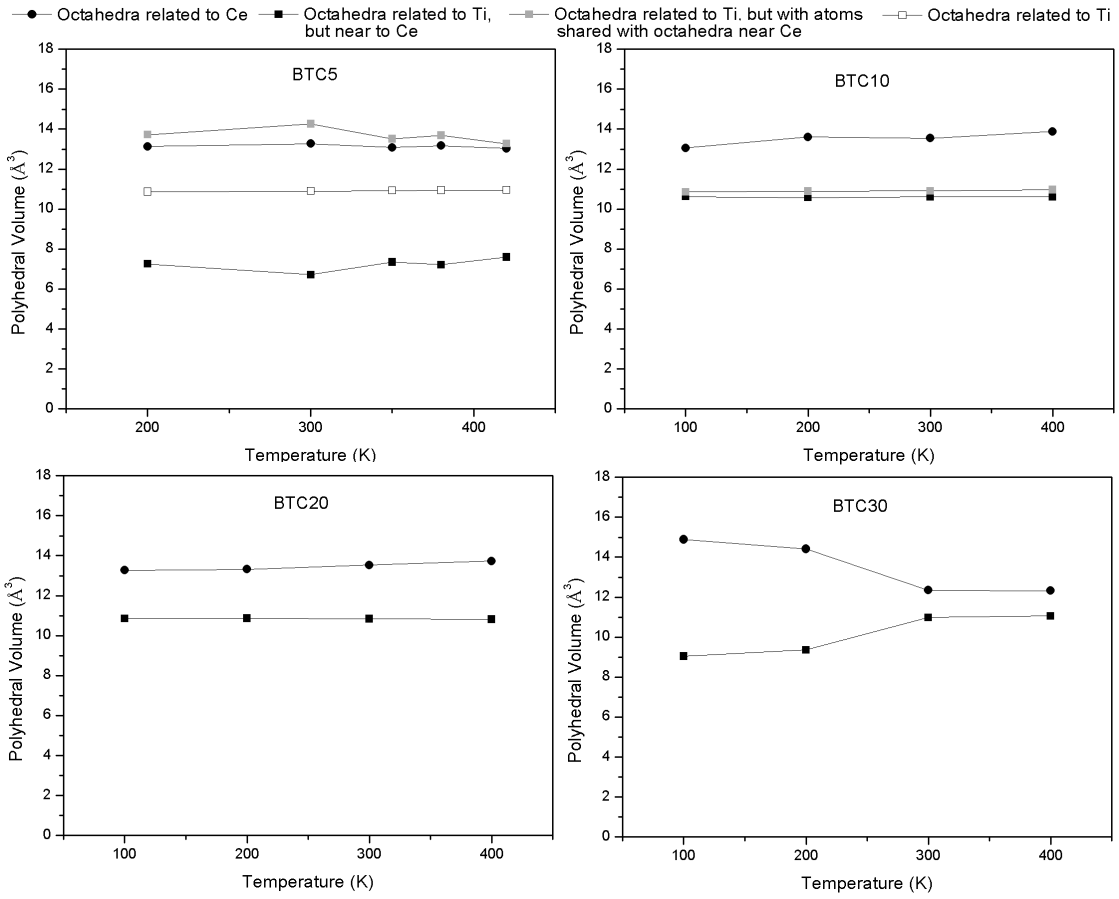

Figure 5.62: Complex octahedra tilt refinements: Ti and Ce coordination polyhedra volumes are compared for different doping amount and different temperatures. Labels of octahedra are described in text and in figure 5.60.

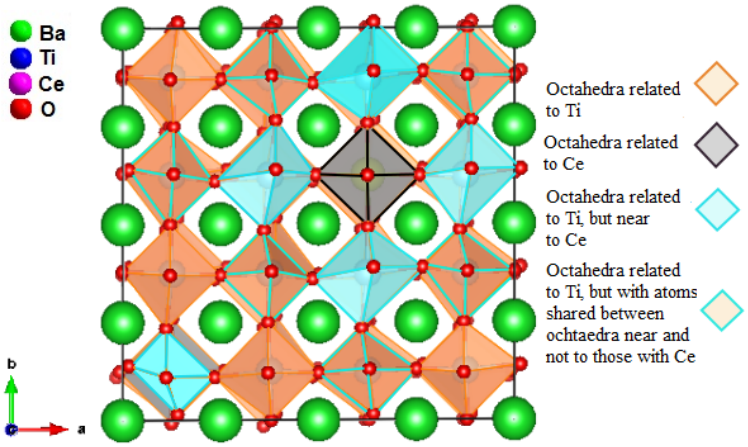

Figure 5.63: Example of refined supercell: BTC5 200 K.

Results presented are in very good agreement with those of $BaTi_{1-x}Zr_xO_3$ where Ti-O and Zr-O (first smaller than the second) are recognized as the most important deviation with respect to the crystallographic structure (Laulhe et al. 2009). This mentioned work, exactly as in this case (figure 5.63), also prove that oxygen environ-

ments of Ti and Zr atoms are not equivalent, which result also from a different shapes of O_6 cages around the two B cations. The differentiation in Ti octahedra shape fluctuates from on site to the other linked to dopant atom vicinity: oxygen cage are compressed in the direction of Zr and expanded in direction of Ti neighbors (Laulhe et al. 2010). Furthermore, as observed in BTC (maybe except the greater Ce content), B-O average lengths are practically rigid and almost not sensitive to the amount of Ti substitute (Laulhe et al. 2009) (Laulhe et al. 2010). In order to validate results obtained volumes calculated for the samples at room temperature are compared with those obtained for referenced end-members.

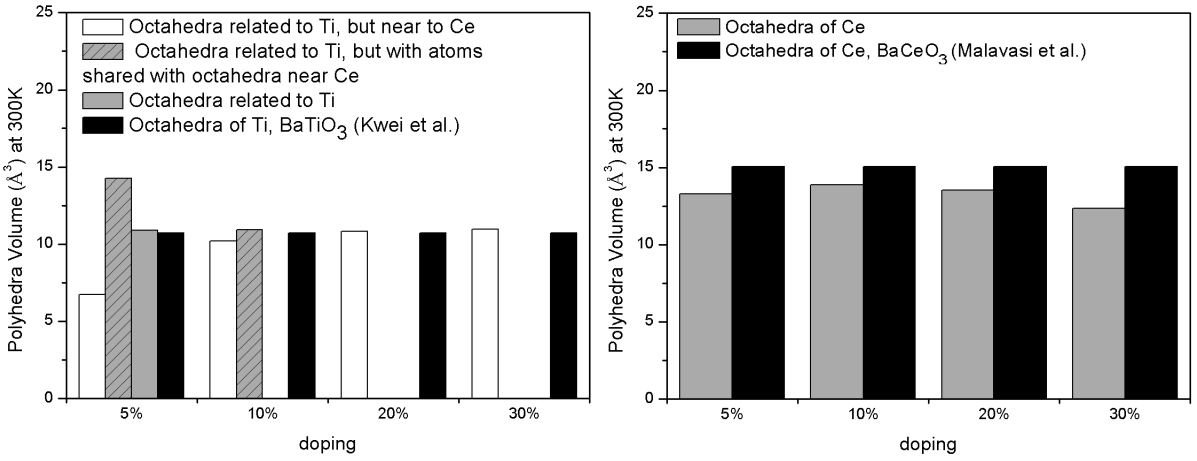

Figure 5.64: Comparison between Ti and Ce octahedra volumes of BTC and those of the end-members at room temperature.

In figure 5.64 volumes of cerium and titanium polyhedra in BTC are reported case by case with those of pure phases. Focusing on those related to cerium it is evident that values are lower in comparison of $BaCeO_3$ although almost constant. In most of the cited works bonds in perovskite solid solutions should be identical or very similar to those found in pure sample, only in Levin *et al.* (Levin et al. 2011) a reduction of Zr-O is reported to be around 0.5% in case of doping amount between 0.5 and 50%. In case of BTC, taking average values, Ce-O compared with pure phase is 11% smaller than the end-member. This difference between $BaTi_{1-x}Zr_xO_3$ and $BaTi_{1-x}Ce_xO_3$ could be explained in terms of different ionic radii of dopant elements. All results reported are then supported also by bibliographic evidences. However an easy and additional test could be performed using, as a term of comparison, the results calculated by carbox A strategy reported at the beginning of this subsection. New refinements, with the refined 'tilted' structures have been performed at lowest temperature fixing everything and refining just thermal parameters by a carbox approach with same radius range as in A strategy. This should be allow to understand, depending on the Uiso values, if sufficient oxygen disorder has been included in the new model. In table 5.58 values calculated for the range 5.5-10 Å is presented and comparison is shown in figure 5.65.

Sample	Uiso Ba (Å^2)	Uiso Ti (Å^2)	Uiso Ce (Å^2)	Uiso O (Å^2)
BTC5 200K	0.003	0.006	0.051	0.011
BTC10 100K	0.003	0.014	0.000	0.030
BTC20 100K	0.004	0.008	0.005	0.027
BTC30 100K	0.007	0.006	0.008	0.035

Table 5.58: Parameters obtained in complex octahedra tilt refinements have been fixed and Uiso of different elements are now refined with a carbox approach. Only values calculated for lowest temperatures between 5.5-10 Å are here reported.

As evident Uiso for all the atoms are now decisively lower proving the goodness of the new model. This is then effectively able to describe the local disorder as statical and not dynamical. However, before show final fits,

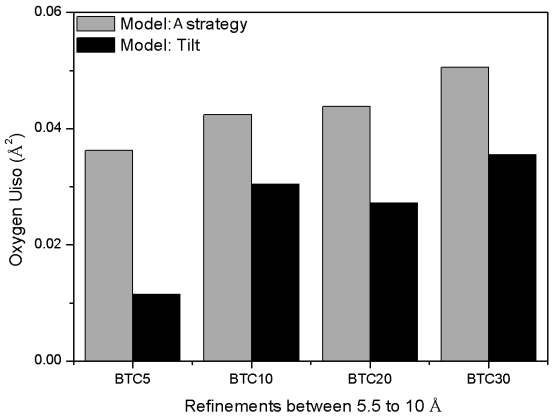

Figure 5.65: Comparison, only for lowest temperatures, between oxygen Uiso obtained in the radius range 5.5-10 Å for A strategy and complex octahedra tilt refinements.

some other parameters should be considered and refined: for example titanium displacements. Differently to this, cerium is to be considered fixed. Cerium octahedra have been indeed built as not distorted then it is not logical to impose a displacement especially for this kind of atomic size. Furthermore also the position of zirconium in BTZ is described as fixed (Laulhe et al. 2009). In order to determine Ti off-centering (table 5.59 and figure 5.66) other parameters, excluded Uiso, have been fixed to not weight on the refinements and to maintain results above reported.

	Temperature (K)	Ti displacement (Å)		Temperature (K)	Ti displacement (Å)
BTC5	200	0.049	BTC10	100	0.034
	300	0.062		200	0.052
	350	0.064		300	0.045
	380	0.065		400	0.057
	420	0.050			
	Temperature (K)	Ti displacement (Å)		Temperature (K)	Ti displacement (Å)
BTC20	100	0.008	BTC30	100	0.010
	200	0.005		200	0.008
	300	0.008		300	0.004
	400	0.007		400	0.009

Table 5.59: Ti displacements at different temperatures and doping amounts calculated using a model consisting in tilted octahedra.

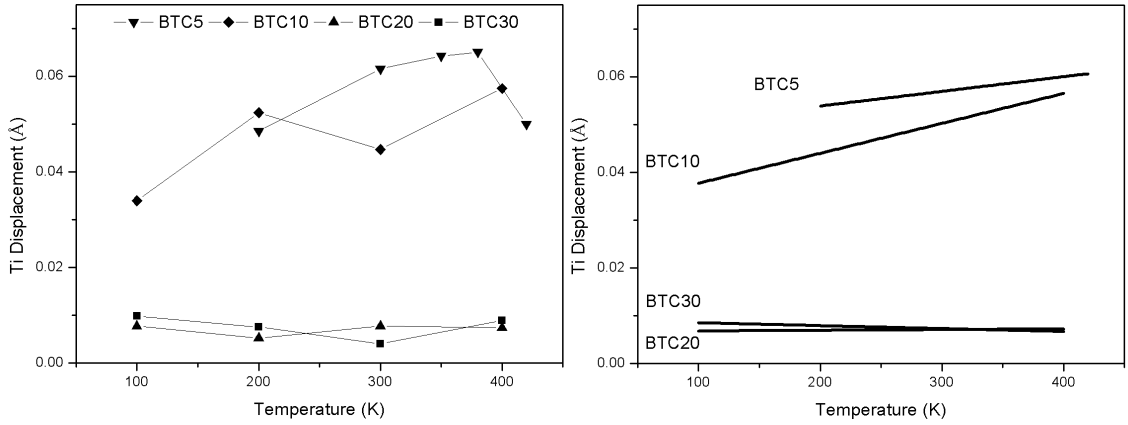

Figure 5.66: Comparison between different BTC in terms of Ti displacements. On the right part regression lines are reported as eye-guide.

Considering that Ti was constrained in xxx and the off-center displacement is recalculated from the cell center

and not from oxygen-octahedron center, these results must be read as indications and not as real movements. However samples with a higher doping level present very low Ti displacements whereas BTC5 and BTC10 show quite high values. Ti movements are then inhibited more the Ce atoms nearby, as reported in different works, already cited, about similar perovskite. Results are therefore congruent with dielectric measurements which indicate a relaxor behaviour for BTC20 and BTC30. Now it is important to remember that Ti octahedra volumes in different samples, previous reported, are very comparable, so these differences in titanium displacements are not related to the size of oxygens cage. Furthermore Ti movements have been calculated only for [111] direction. Then probably in BTC30 and BTC20 actually different titanium atoms moves in many different directions giving at the end a net value around zero. Differently to classical rhombohedric model where Ti off-center is along the cell body diagonal, here the many different distortions and rotations of the octahedra probably influence the displacement directions. At the end also Uiso values have been calculated and shown in tables 5.60, 5.61, 5.62, 5.63 and in figure 5.67.

BTC5	Uiso Ba (Å^2)	Uiso Ti (Å^2)	Uiso Ce (Å^2)	Uiso O (Å^2)
200 K	0.003	0.006	0.005	0.006
300 K	0.005	0.007	0.007	0.007
350 K	0.005	0.008	0.009	0.008
380 K	0.006	0.007	0.008	0.008
420 K	0.006	0.009	0.009	0.009

Table 5.60: Uiso of $BaTi_{0.95}Ce_{0.05}O_3$ at different temperatures. Tilted structure with Ti displacements has been used to perform refinements.

BTC10	Uiso Ba (Å^2)	Uiso Ti (Å^2)	Uiso Ce (Å^2)	Uiso O (Å^2)
100 K	0.003	0.005	0.009	0.014
200 K	0.004	0.006	0.008	0.015
300 K	0.005	0.008	0.009	0.015
400 K	0.006	0.008	0.009	0.015

Table 5.61: Uiso of $BaTi_{0.9}Ce_{0.1}O_3$ at different temperatures. Tilted structure with Ti displacements has been used to perform refinements.

BTC20	Uiso Ba (Å^2)	Uiso Ti (Å^2)	Uiso Ce (Å^2)	Uiso O (Å^2)
100 K	0.004	0.004	0.010	0.011
200 K	0.005	0.006	0.007	0.010
300 K	0.007	0.007	0.010	0.011
400 K	0.008	0.007	0.009	0.012

Table 5.62: Uiso of $BaTi_{0.8}Ce_{0.2}O_3$ at different temperatures. Tilted structure with Ti displacements has been used to perform refinements.

BTC30	Uiso Ba (Å^2)	Uiso Ti (Å^2)	Uiso Ce (Å^2)	Uiso O (Å^2)
100 K	0.005	0.004	0.009	0.016
200 K	0.007	0.004	0.012	0.017
300 K	0.008	0.007	0.010	0.018
400 K	0.009	0.007	0.010	0.016

Table 5.63: Uiso of $BaTi_{0.7}Ce_{0.3}O_3$ at different temperatures. Tilted structure with Ti displacements has been used to perform refinements.

In figure 5.67 particular trends are noticeable. Barium, which is the bigger atom, should present low Uiso, but in BTC30 titanium appears lower. Ce in all samples and temperatures has exaggerated values, which for sure are correlated to the fact that Ce atomic positions were kept fixed during the refinement. However in general

values for all atoms are rather acceptable. As reported in figure 5.68 (zoom in appendix), tilted structure used in this last subsection allows to achieve good fits and good results, as above demonstrated. Other refinements have been performed refining at the same time all the parameters taken into account in this analysis, unfortunately no good results have been obtained especially for unphysical calculated bond lengths. Used model indeed presents too many parameters, some of which strongly correlated, then, with available data, it is not possible to reach a perfect result. Obviously this solution is not the ideal one: some calculated peaks under 5 Å do not yet completely reproduce data, but, despite this, model proposed is for sure very good and could explain in most part the local disorder in $BaTi_{1-x}Ce_xO_3$.

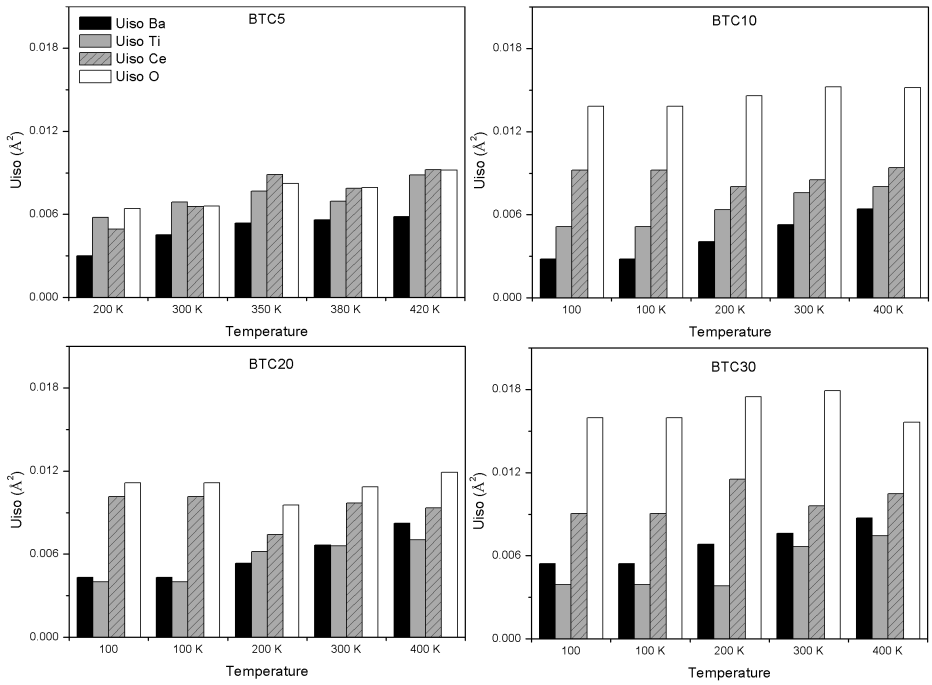

Figure 5.67: Uiso values of different BTCs and temperatures calculated using tilted structure model with Ti displacements.

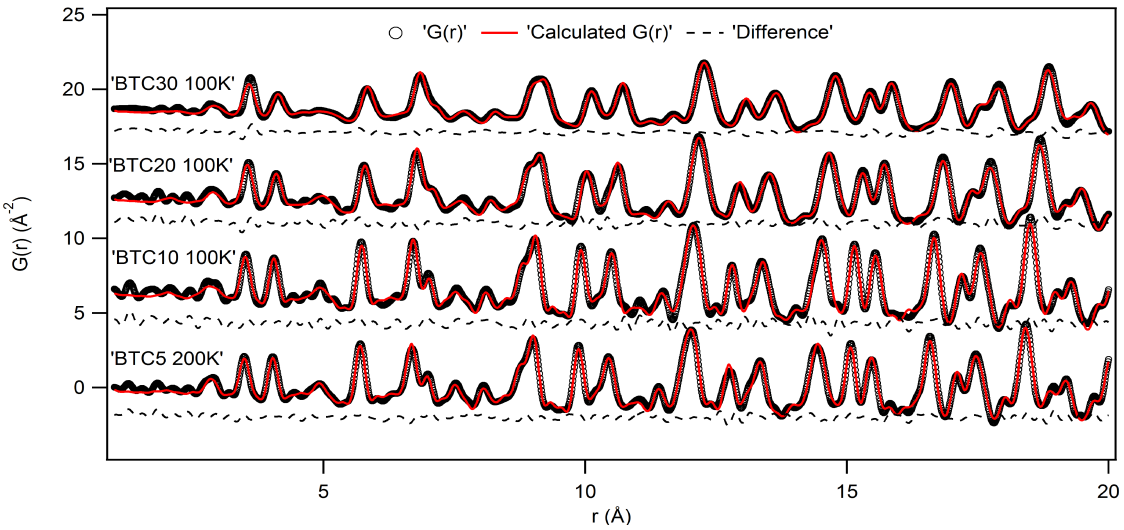

Figure 5.68: Fits of different BTCs at lowest temperatures obtained using final structural model (tilted structure with Ti displacements).

5.2.3 Reverse Monte Carlo

Reverse Monte Carlo (McGreevy & Pusztai 1988) approach has been used to explore local structure by the software RMCProfile (Tucker et al. 2007). Differently to other methods up to now presented, this does not include and exploit any crystallographic rule, a very big box is used in which every single atoms is treated as a single entity and moved independently from the others. The RMC method uses the Metropolis Monte Carlo algorithm to produce atomic configurations that are consistent with experimental data. Essentially a big configuration of atoms is modified by successive steps until function calculated from it is in best agreement with the observed data. An iterative approach is adopted and successive changes to the atomic configuration are proposed at random and then tested to see whether they improve or degrade the fit of the PDF (which is the function used in the present investigation). Then, instead of changing the potential energy of the configuration, the fit of the experimental data is used to determine if each move is accepted or rejected. If the proposed change improves the agreement with data, it is accepted, and the Monte Carlo algorithm moves forward one cycle in which a subsequent random change is proposed. The comparison between the calculated functions and experimental data is formalized by defining an agreement function (Tucker et al. 2007):

$$\chi^2_{g(r)} = \sum_j [g(r_j)_{calc} - g(r_j)_{expt}]^2 / \sigma_{g(r)^2}(r_j) \tag{5.1}$$

where in principle the σ parameters represent standard errors on individual data values. In order to guide the early stages of minimization and to produce more physically acceptable configurations it is often useful to use restraints and constraints as the most common examples of these values are bond lengths and bond angles. This approach should be useful to interpret local structure giving a precise picture of the disorder generated by a multitude of single cells neglecting their crystallographic relations in terms of translation also removing constrains between atoms. For this type of investigation only BTC5, 10 and 20 at lowest temperature have been treated.

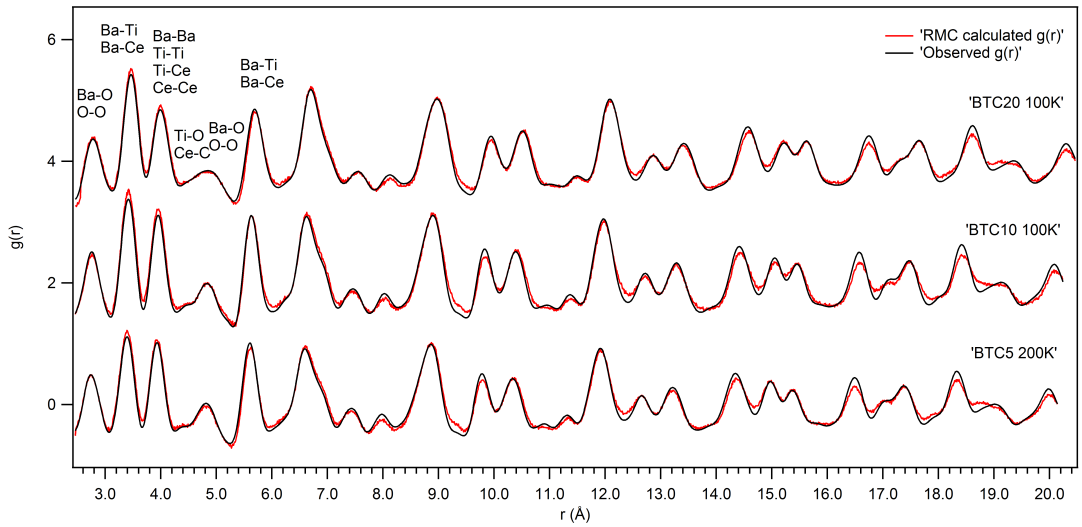

Figure 5.69: Fits between observed and calculated g(r) ($G(r) = 4\pi r \rho_0 (g(r) - 1)$) performed using RMCProfile software. Reached χ^2 values are: 18.36, 20.60, 13.47 respectively for BTC5, 10 and 20.

A box consisting of 5000 atoms (Ba=1000, Ti=1000-x, Ce=x and O=3000) has been used for each sample. Fits of PDFs have been performed between $\sim$ 2 and 20 Å. As many time highlighted, none of the functions considered presents a clear evidence of the first peak Ti-O/Ce-O, then refinements have been executed excluding the fit of the

lowest part of the PDFs. Constraints for all the bond distances have been deduced by Pair Distribution Functions, assigning as the allowed minimum and maximum values the starting and final point of the related peak. This method is obviously inapplicable for the first B-O bonds distances, then these constrains have been imposed using logic and physical acceptable values. Furthermore in order to evaluated B cation order the swap between titanium and cerium has been allowed. Each analysis has lasted up to reach the best fit, this is achieved when χ^2 value becomes constant (about 24 hours for each sample has been necessary). Resulting fit are reported in figure 5.69.

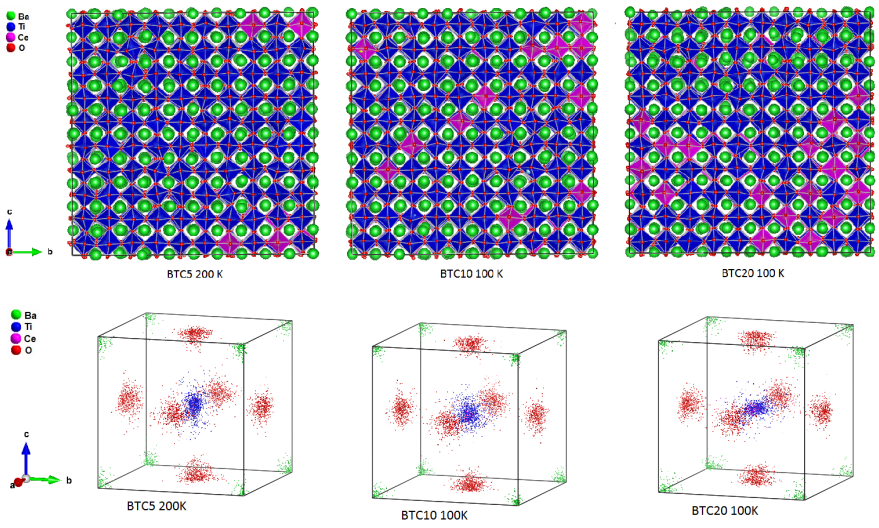

Figure 5.70: Obtained final configurations for the three samples. Supercells and supercells merged in one cells are shown.

Final refined structures are shown in the upper part of figure 5.70. As noticeable all octahedra, independently from the B cation, assume distorted configurations. Furthermore an almost homogeneous distribution of cerium has been predicted for all the BTCs. In order to better appraise results obtained by RMC analysis for each sample the configuration of the big box has been merged in a single unit cell, reported in the low part of figure 5.70. As demonstrated by this image, atoms are distributed less or more around classical positions, but they present very huge dispersions in all the samples. This demonstrates the effective disorder on the local structure which can be modeled only by a very complex configuration, even for lowest doping amount. Unfortunately by the investigation of the merged cells it is impossible to make more considerations. In order to explore more in detail local structure obtained partial PDFs for the lowest and higher cerium concentration are taken into account. No partials involving oxygen atoms is presented considering that constrains of Ti-O and Ce-O are just supposed and not proved by any peak in g(r). In figure 5.71 partials related to Ba-Ti and Ba-Ce bond lengths for BTC5 and BTC20 are reported. As shown, independently from cerium amount, distribution of Ba-Ce seems to be more sharp than that of Ba-Ti. On the other hand Ba-Ba lengths present a smaller distribution, as deducible by merged unit cell, which is moreover comparable in the two samples (figure5.71). Thus it is possible to suppose that differences in barium-titanium and barium-cerium distribution are due to the many titanium atomic positions rather than those of barium. An indicative distribution, around the merged cell center, of titanium and cerium atoms in BTC5 and BTC20 are reported in figure 5.72. By this, it seems to be clear that Ti atoms tend to be more distributed then cerium, which remain close to the center of the averaged cell. It is for now impossible to evaluate if titanium atoms are displaced or not within their oxygen cages, but for sure the disorder related to this atoms is more than that linked to cerium. However by this inspection no information about the nature of this disorder is deducible. It could be generated by different distortions of oxygen polyhedra, which change the center of the cages moving then the relative titanium, or the disorder could be caused by different effective Ti displacements or even by both.

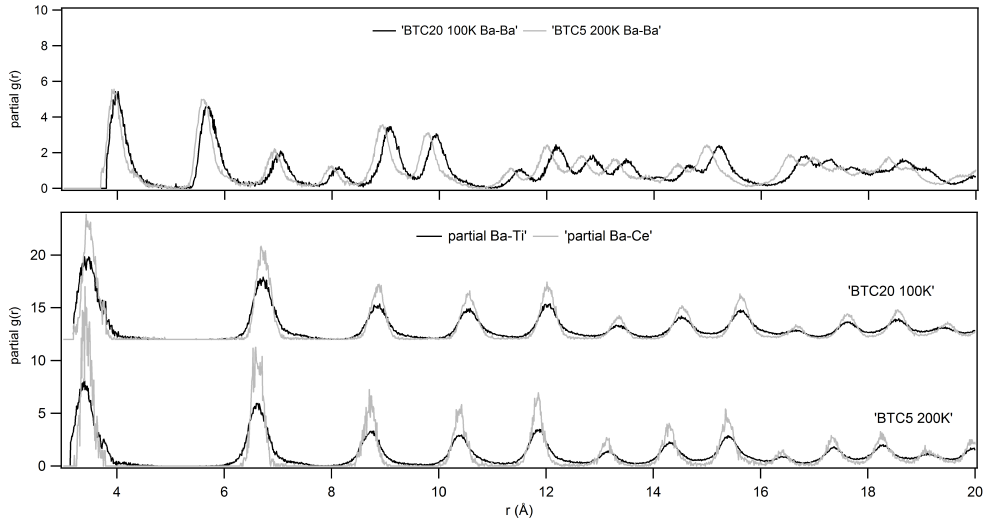

Figure 5.71: In the upper part: partial g(r) functions are reported for Ba-Ba in lowest and highest doped samples. In the lower part comparison between Ba-Ti and Ba-Ce partial g(r) are reported for BTC5 and BTC20.

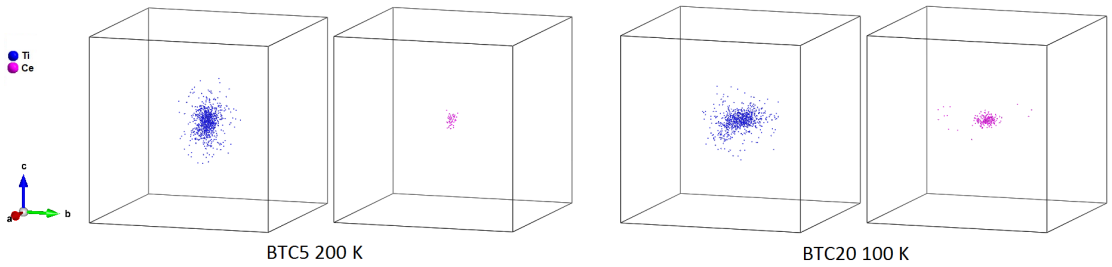

Figure 5.72: All the position of cerium and titanium atoms in the final supercell configurations are merged in a single cell. The case of BTC5 and BTC20 is presented.

Finally Ti-Ti bond lengths have been considered. As observable by figure 5.73, distribution of these distances are slight broader in BTC20 than those in BTC5. These effect seems to be more pronounced as radius increases. This could be a signal of the reduced correlation length of titanium displacements linked to cerium increment.

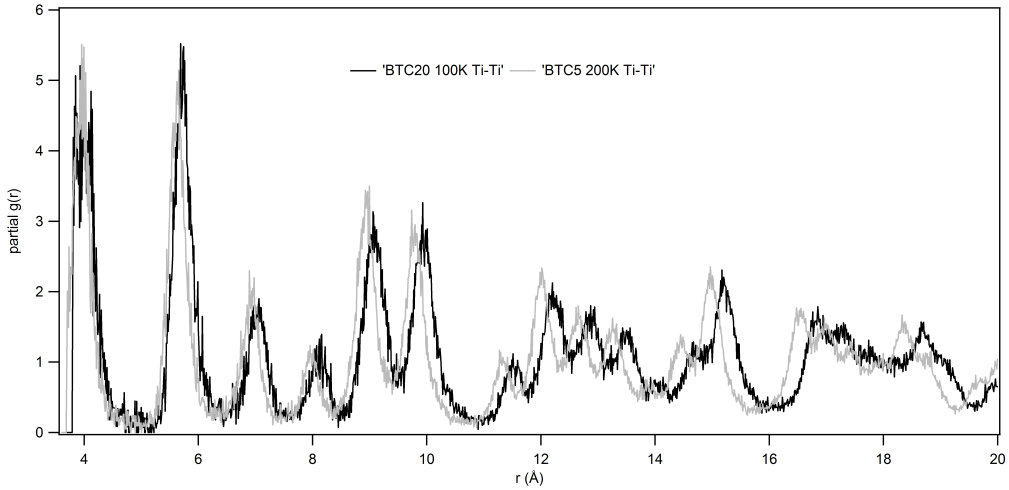

Figure 5.73: Partial g(r) for Ti-Ti are reported comparing BTC5 and BTC20.

5.3 Analysis of Raman scattering

Raman analysis and data interpretation have been performed thank to Dr. Marco DeLuca (Institut fur Struktur-und Funktionskeramik, Montanuniversitaet Leoben, Leoben, Austria). It is important to notice that these results have been obtained at the end of the present research path, then they are here reported for sake of completeness and for a term of comparison. Samples with x = 0.02, 0.05, 0.10 and 0.20 have been investigated at different temperatures between $\sim$ 78 and 438 K. Firstly depolarized Raman spectra of different BTCs at room temperature are reported in figure 5.74. BTC2 and BTC5 show great similarities, especially considering bands at 180, 250, 305, 520 and 715 cm^{-1}, with pure $BaTiO_3$ spectrum (DeLuca & Gajovic 2016). The silent mode at $\sim$305 cm^{-1}, together with the mode at 715 cm^{-1} and the dip at $\sim$180 cm^{-1}, indicates the existence of long-range ferroelectric order.

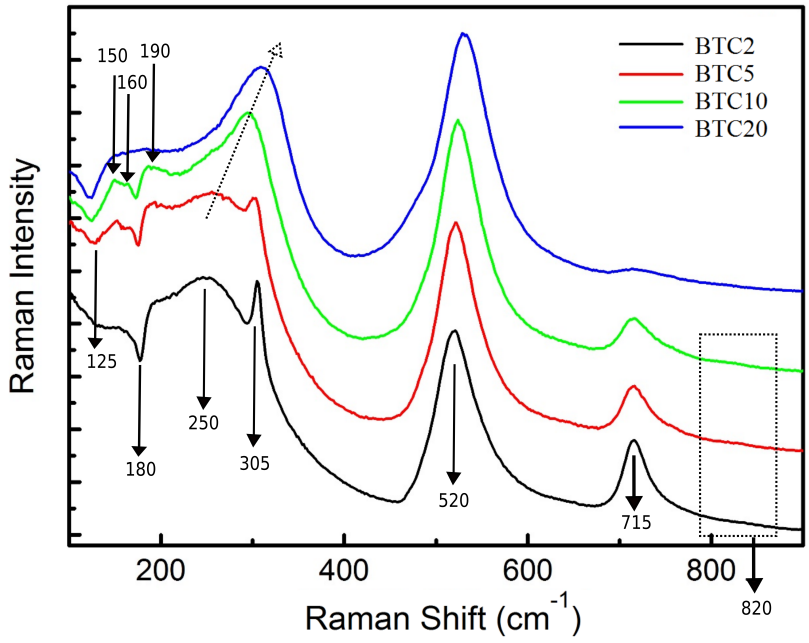

Figure 5.74: Raman spectra of $BaTi_{1-x}Ce_xO_3$ (x=0.02, 0.05, 0.1, 0.2) at room temperature shown in a waterfall-like diagram. Some discussed peaks are evidenced.

For BTC5, BTC10 and BTC20 the following additional features linked to Ce substitution at the B site can be also recognized:

- a pronounced interference feature at 125 cm^{-1}.
- the shift of the band at 250 cm^{-1} to higher wavenumbers ($\sim$310 cm^{-1} for x = 0.20).
- the progressive disappearance of the silent mode at 305 cm^{-1}.
- some weak additional bands at 150-190 cm^{-1} (x = 0.05, 0.10).

The interference feature seems to be attributed to a coupling between two A1(TO) modes belonging to two different types of oxygen octahedra (i.e., Ti based and Ce based) (Lu et al. 2007). The shift of the band at 250 cm^{-1} can be interpreted as a change of the bond length for the mode associated with the B-O bond. Considering that the ionic radius (VI-fold coordination) of Ce^{4+} is 0.82 Å whereas that of Ti^{4+} is 0.605 Å, an expansion of the BO_6 octahedron is likely. The disappearance of the silent mode for x = 0.1 and 0.2 indicates a significant reduction of the correlation length corresponding to the ferroelectric order in comparison to $BaTiO_3$. Spectrum

of $BaTi_{0.8}Ce_{0.2}O_3$ shows a lower number of features and lacks of both the silent mode and the dip at 180 cm^{-1}, which if present are typical of a ferroelectric long range order. Nevertheless, the persistence of the Raman activity indicates the existence of short range polar order despite the average cubic structure indicated by the XRD patterns. This is in agreement with the relaxor behaviour observed from permittivity measurements at different frequencies and the existence of polar nanoregions in a paraelectric matrix. The additional mode at 150 cm^{-1} might be an indication of a minor substitution of Ce^{3+} at the Ba site whereas the bands at 160 and 190^{-1} can belong to the rhombohedric modification, as will be discussed later. A very slight substitution of Ce^{3+} at the Ba site can be also inferred from the presence of a faint peak at ∼820 cm^{-1} for all compositions with x < 0.20, however this effect is so modest that it is undetectable by X ray diffraction data. Indeed this peak has been reported to be related to increased rare earth substitution on the A site of barium titanate (Lu et al. 2007) (Lu et al. 2013). Temperature dependent Raman spectra were collected between 78 and 438 K for all compositions, as shown in figure 5.75, and 5.76. As widely discussed in the literature, phase transitions in undoped $BaTiO_3$ can be clearly identified by the disappearance or frequency shift of some characteristic Raman modes with temperature. However, in the present case and especially for compositions x > 0.02, the bands progressively weakens with increasing temperature rather than disappear at a specific temperature, an indication that phase transitions in BTC are rather diffuse and occur on a broad temperature range.

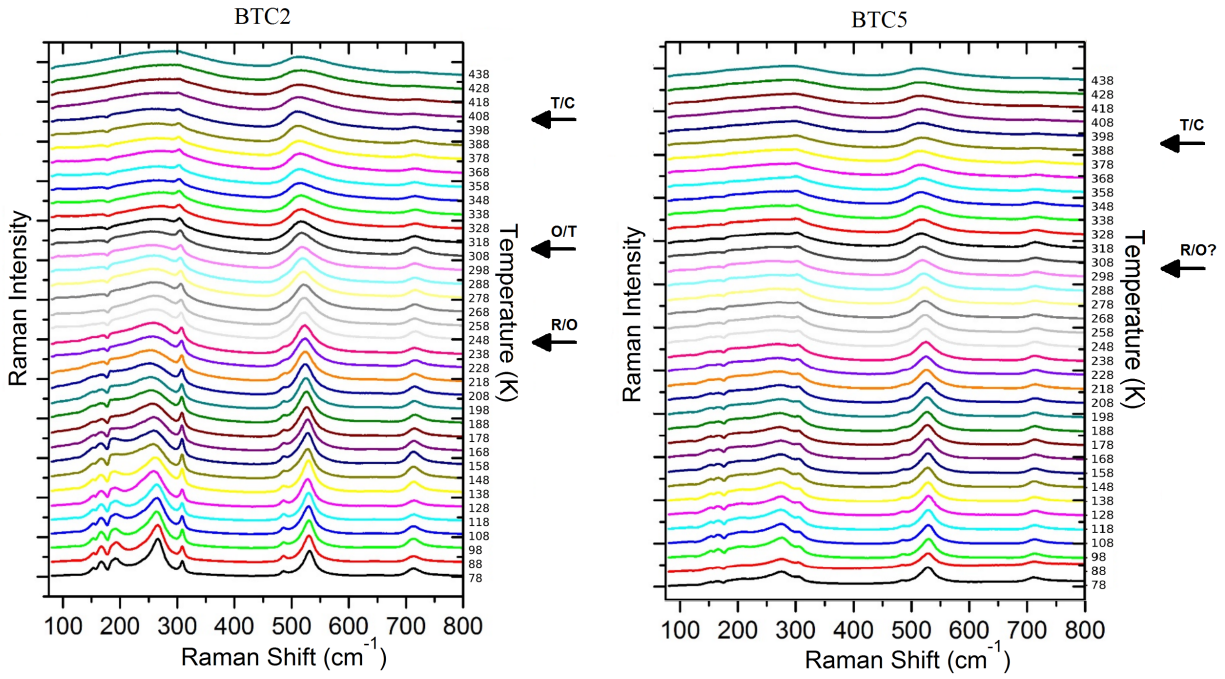

Figure 5.75: Temperature-dependent Raman spectra of the ceramic x = 0.02 and x = 0.05. Temperature values are reported next to each spectrum.

The temperature evolution of the spectra for the composition x = 0.02 resembles the typical behaviour of pure barium titanate. The peak observed at low temperature at ∼480 cm^{-1} is specific of the orthorhombic and rhombohedric phases of barium titanate (Buscaglia et al. 2006) (DeLuca & Gajovic 2016) (Buscaglia et al. 2014). This peak is exhibited by all compositions, including x = 0.20 and indicates that the phase stable at low temperature has a rhombohedric symmetry. Its intensity rapidly decreases between 248.15 and 238.15 K for x = 0.02, possibly indicating the rhombohedric to orthorhombic transition. At higher temperatures, only a shoulder remains which finally vanishes at around 273.15 K for all compositions. The two peaks at 165 and 190 cm^{-1}, observed at low temperature for all ceramics though more evident for x = 0.02, are characteristic of the rhombohedric phase

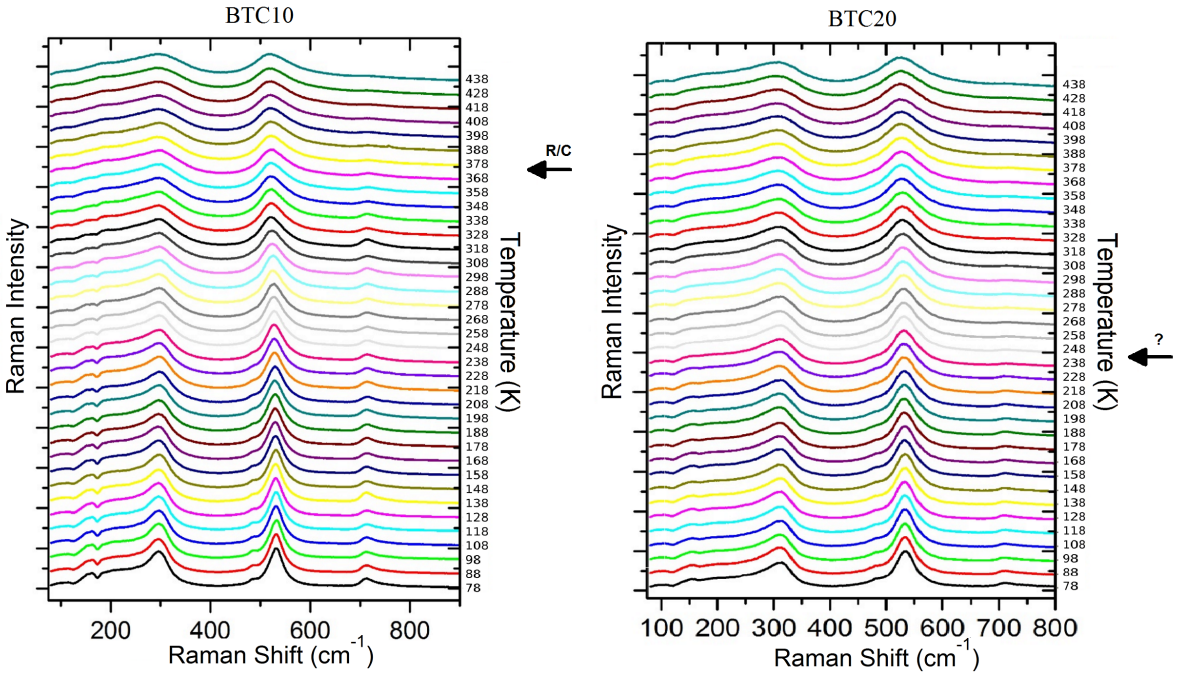

Figure 5.76: Temperature-dependent Raman spectra of the ceramic x = 0.1 and x = 0.2. Temperature values are reported next to each spectrum.

(Buscaglia et al. 2006) (Lu et al. 2013) (DeLuca & Gajovic 2016) (Buscaglia et al. 2014). These two features disappear between 248.15 and 258.15 K when x = 0.02 and between 298.15 and 308.15 K when x = 0.05 whereas they persist at higher temperature for x = 0.10. Opposite, when x = 0.20, the two bands disappear, together with the dip at 180 cm^{-1}, at lower temperature, between 238.15 and 248.15 K. The shift at high wavenumber of the band at 250 cm^{-1}. The shift of the band at 250 cm^{-1} at higher wavenumber between 308.15 and 318.15 K is an indication of the orthorhombic to tetragonal transition. This shift is not observed for x = 0.05. The transition from the ferroelectric long range order to a cubic paraelectric phase is indicated by the disappearance of the silent mode at 305 cm^{-1} and the dip at 180 cm^{-1} for x = 0.02 (398.15-408.15 K) and 0.05 (388.15-398.15 K) and only by the disappearance of the dip when x = 0.10 (368.15-378.15 K). The silent mode is not present in the ceramic x = 0.20 and the dip at 180 cm^{-1} is only observed below 238.15 K. The persistence of a Raman activity above this temperature again indicates the presence of small polar clusters in which the ions at the B site is displaced out of center. The interference feature at 122 cm^{-1} persist up to 438.15 K for compositions x = 0.10 and 0.20 whereas for x = 0.05 it vanishes above 373.15 K. In conclusions, the three transitions typical of $BaTiO_3$ (R/O, O/T and T/C) are also observed in the ceramic with x = 0.02. For x = 0.05 and 0.10 only the transition the ferroelectric to paraelectric transition can be clearly identified. For x = 0.05, only some clues of the rhombohedric to orthorhombic transition between 298.15 and 308.15 K exist. Despite the relaxor behaviour observed when x = 0.20, there is evidence for a phase transition or at least a change in the short range order between 248.15 and 238.15 K.

5.4 Implication of the average and local structure on BTC properties

This section is written in order to summarize all the results obtained by different techniques and to find a correlation between them and $BaTi_{1-x}Ce_xO_3$ ceramic properties. Cerium introduction in $BaTiO_3$ causes big differences in phase transitions and properties, in particular the big ionic radius generates a great strain, also demonstrated

by dislocation density, which leads a deep disorder in local structure. Starting from the average structure a good agreement between diffraction data analyses and Raman spectroscopy has been proved. As previously reported (Jing et al. 2003) and here also verified, a crossover from the ferroelectric to ferroelectric-relaxor behavior is observed with increasing Ce concentration. From the structural point of view Ce amount between 2 to 5% seems not to change the normal structural transition sequence of pure $BaTiO_3$. When doping increases, $BaTi_{1-x}Ce_xO_3$ (x is between 0.1) presents diffuse phase transition behaviour and then a direct transition from the paraelectric cubic to the ferroelectric rhombohedric structure. When x = 0.20, the ceramic shows a relaxor behaviour with a transition to long range polar order at temperatures below 200 K. This transition completely disappears in BTC30 which is indeed the sample presenting relaxor behaviour, here in fact cubic structure is stable at all the temperatures. In addition to the variations in polar behaviour, Ce doping also determines, as expected, an increase of the unit cell volume with increasing dopant concentration, at the same time, limiting the B cations off-center displacements. In order to elucidate this apparent contradiction and in order to understand the origin of polar behaviours, local structures have been deeply investigated. All local structures have been determined to be profoundly disordered. All the BTCs local structural characteristics are almost constant with temperature, as the type and amount of disorder is similar. This underlines a contrasting behaviour of the local and average structure as a function of temperature. This diversity could be interpreted applying the Ravel's (Ravel et al. 1998) theory (actually formulated for pure $BaTiO_3$): the sequence of phase transitions is explained by a disordering of domains wherein the local structural environment remains approximately rhombohedrally distorted at all temperatures around both metal sites. As the temperature is raised, the long range correlations between these local distortions change, resulting in the observed sequence of phase transitions. Taking into account the different amounts of doping, samples reveal great differences as cerium increases showing an increment of the local disorder.

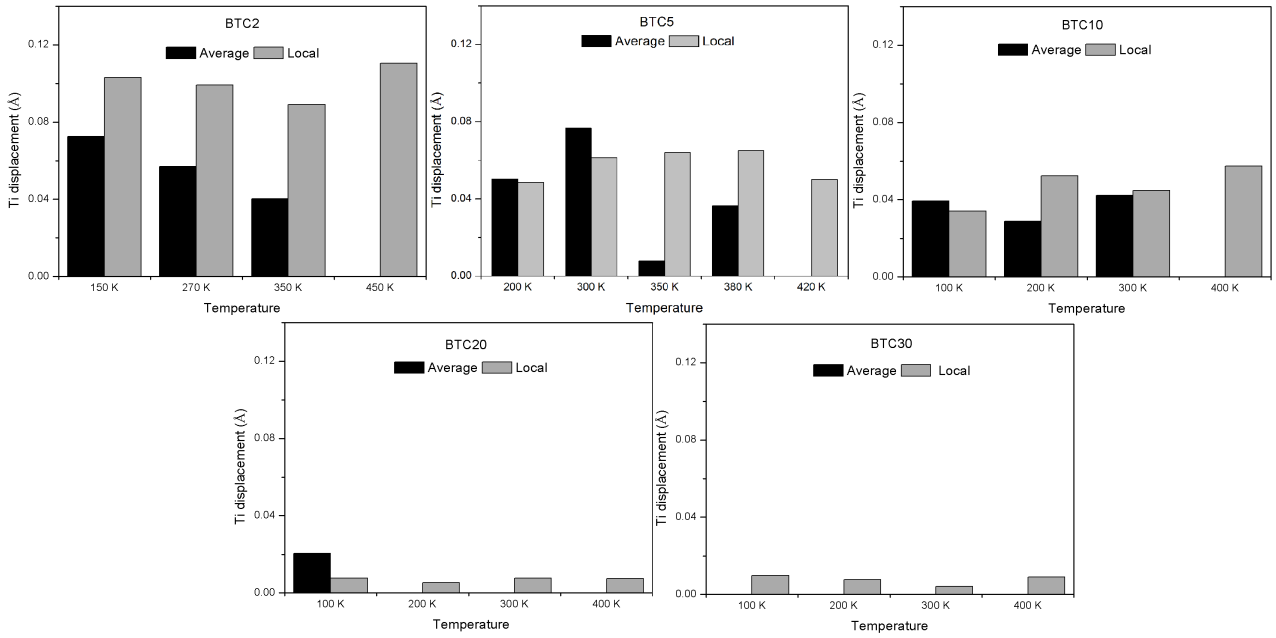

Figure 5.77: Titanium displacements obtained by average and local structure analyses. NB In the average structure Ti displacement is actually the B cations displacements, Ti and Ce have been indeed constrained in the same position.

This is generated by the size mismatch of titanium and cerium and obviously by their abundance. As demonstrated by Pair Distribution Function and Raman investigation Ti and Ce show differently deformed coordination polyhedra: strain induced by the different atomic sizes is accommodated by the creation of different oxygen bond lengths associated to the two different B cations. The distances Ce-O and Ti-O in the solid solutions tend to remain

close to those in the respective pure compounds. Furthermore the difference in size between barium and cerium causes a kind of octahedron tilting which consequently originates tilts and distortions in the Ti-centered octahedra which are close by. This mechanism seems to influence intensely Ti off-centering. In figure 5.77 Ti displacements obtained by local and average analysis are shown. In most of the cases Ti movements in local structure show higher values than on the average, but it is important to remember that this latter has been determined considering the contribution of both B cations. However in both the investigation scales titanium displacements are influenced and reduced as a function of cerium amount. According to bibliographic information (Ang et al. 2002a), Ce ions tend to make the distance between off-center Ti dipoles larger and thus weakens the correlation between these dipoles, which is supported by the experimental facts that the lattice parameter and volume of the cell increase with increasing Ce concentration. Ferroelectric/dielectric behaviour depends on the competition between the long range ferroelectric order owing to strong correlation of the off-center Ti dipoles and the random fields induced by the Ce doping. Then, as cerium amount increases, ferroelectric domains are destroyed and nanopolar regions are formed. It is very interesting to underline how this mechanism is involved in a complex sequence of cause-effect. The mismatch in size between Ti and Ce and Ba and Ce ions might cause substantial distortion of the oxygen octahedra. When cerium amount increases more titanium octahedra are involved then more disorder is generated. As demonstrated by RMC analysis, this kind of distortion seems to provoke titanium displacements in different directions giving at the end a reduced net value as a function of the doping in the local structure and also on the average. Moreover more disordered local structure seems to be related to higher symmetries on the average, as demonstrated in figure 5.78. Then on one hand more cerium, locally, generates more disorder and reduction of titanium displacements, and on the other hand these effects are averaged up to simulate an average structure presenting higher symmetries. Concluding different BTCs then present different polar behaviours and properties as a function of cerium amount and more important as a function of the degree of the local disorder.

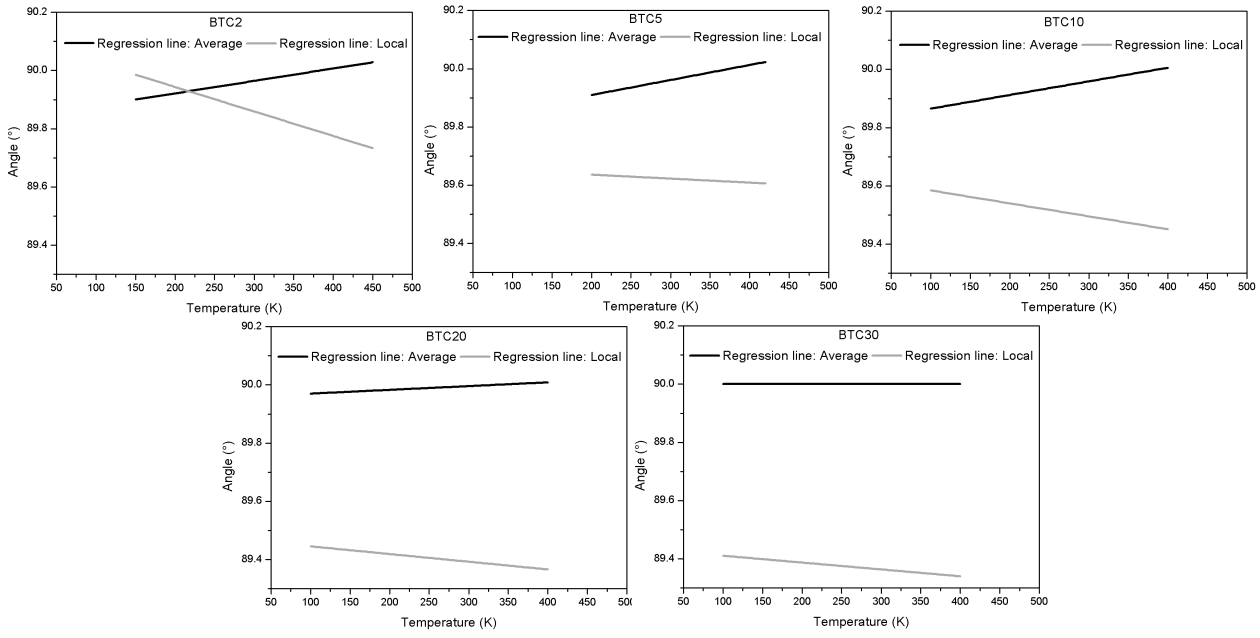

Figure 5.78: Comparison between cell angles on the average and local structure is shown. Only calculated regression lines are reported in order to better appraise trends. In this case cell angles is considered as a kind of distortion parameter, which determines the distortion from the parental cubic structure. BTC2 local structure results are reported for the simpler approach presented (consisting in a rhombohedric structure where Ti and Ce are distinct, but constrained by fractional occupancies), differently for other BTCs tilted structure are considered.

Chapter 6

Nano Powders: results and discussion

A deep study on ceramic BTCs has been reported in previous chapter, here a discussion on structural characterization of nano powders will be proposed. Exactly as for other samples, the research will be divided in two main parts: an average structural analysis and then a local structural investigation. In order to improve knowledge on these materials also a comparison between different grain sizes will be presented. Samples involved in this study are reported in section 3.1.

6.1 Average Structure: reciprocal space

Nano powders data have been collected in the second experiments then, as explained above, no high resolution data is available. On the other hand nano materials usually present very broad peaks due to the grain size, then in any case no subtle peak split or shoulder should be detectable. The resolution of collected diffractograms is then sufficient to explore briefly average structure of nano BTCs. The low crystallinity does not allow to distinguish different structures as a function of doping or temperature increase. The only information deducible by visual comparison is peak shifts as reported in figure 6.1 and 6.2.

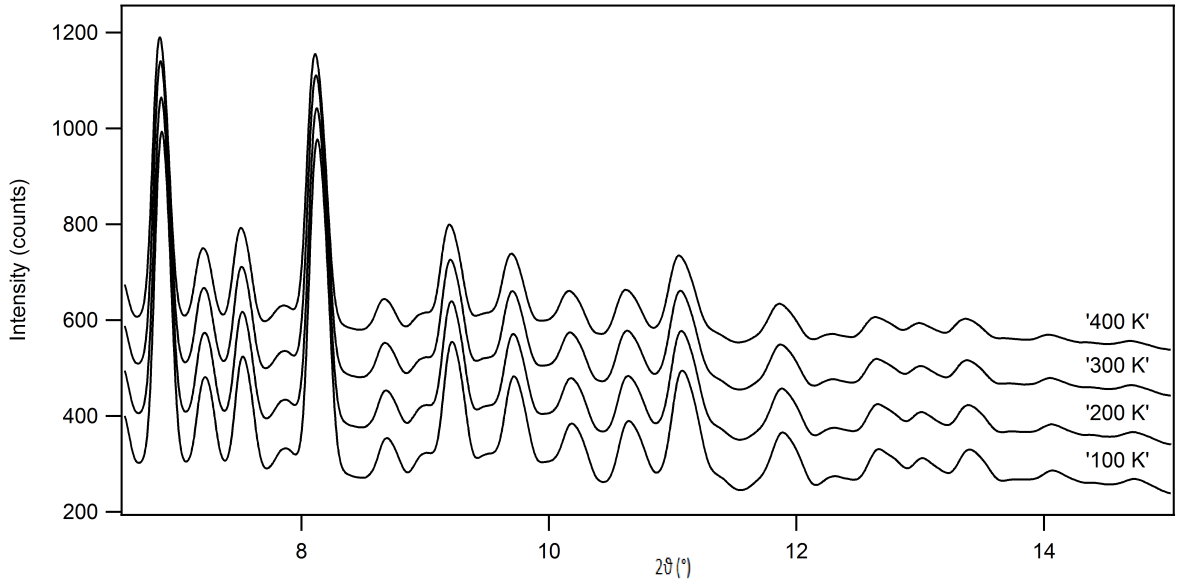

Figure 6.1: BTC20 Nano: comparison between diffractograms at different temperatures. Diffractograms are reported in a waterfall-like diagram.

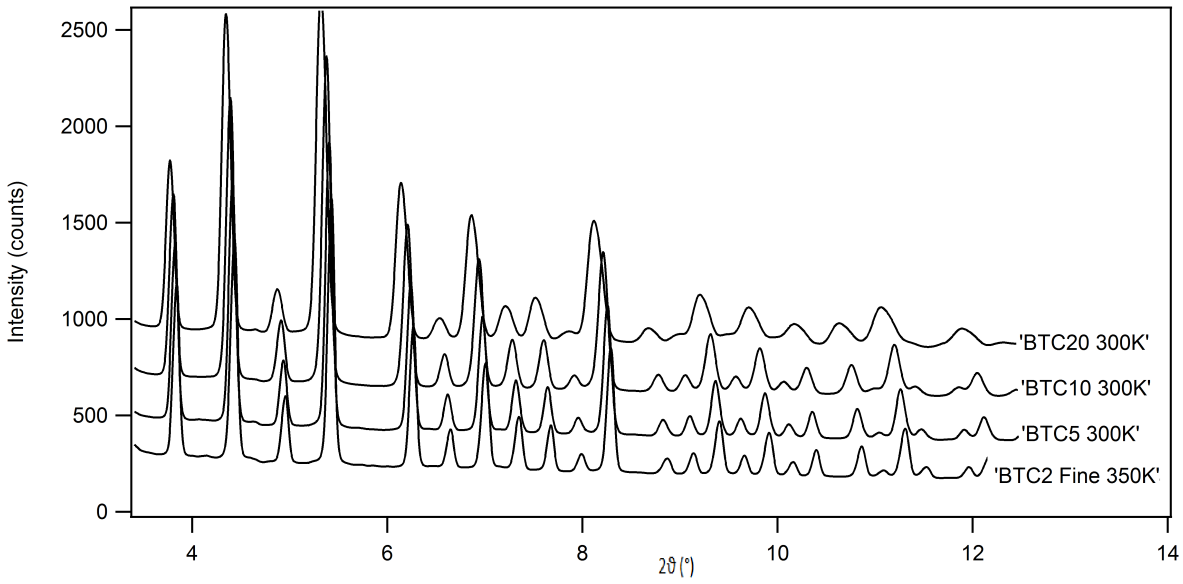

Figure 6.2: Comparison by waterfall-like diagram between diffractograms near 300 K of BTCs whit different cerium amount.

As noticed for ceramics, also here cerium introduction plays the most important role in cell evolution, whereas temperature increase does not seem to provoke great thermal expansions. In order to obtain objective results structural refinements have been performed by Maud software (Lutterotti & Wenk 1999). Only cubic structure belonging to Pm-3m has been used as the initial model for all samples and temperatures. Cell parameters, crystallite size and microstrain have been refined, while thermal parameters have been fixed to reasonable values for different temperatures. This is to keep the refined parameters number as small as possible, because low instrumental resolution coupled with very small grain size produces broad peaks which do not contain enough structural information. In tables 6.1 and 6.2 results for obtained cells and volumes are reported.

Nano Powders					
BTC2 Coarse	a (Å)	Volume (Å^3)	BTC2 Fine	a (Å)	Volume (Å^3)
150 K	4.0085(3)	64.408(8)	150 K	4.0123(3)	64.59(8)
270 K	4.0113(5)	64.55(1)	270 K	4.0150(3)	64.72(1)
350 K	4.0133(4)	64.64(1)	350 K	4.0165(3)	64.79(1)
450 K	4.0162(4)	64.78(1)	450 K	4.0193(3)	64.93(1)

Table 6.1: Cell parameters obtained from diffraction data analysis: $BaTi_{0.98}Ce_{0.02}O_3$ nano powders fine and coarse at different temperatures and grain sizes.

Nano Powders								
BTC5	a (Å)	Volume (Å^3)	BTC10	a (Å)	Volume (Å^3)	BTC20	a (Å)	Volume (Å^3)
200 K	4.0243(3)	65.174(8)	100 K	4.0468(4)	66.27(1)	100 K	4.0917(4)	68.50(1)
300 K	4.0269(4)	65.29(1)	200 K	4.0494(4)	66.40(1)	200 K	4.0942(4)	68.63(1)
350 K	4.0283(4)	65.37(1)	300 K	4.0524(4)	66.55(1)	300 K	4.0975(4)	68.79(1)
380 K	4.0290(4)	65.37(1)	400 K	4.0552(4)	66.69(1)	400 K	4.1010(4)	68.97(1)
420 K	4.0300(4)	65.37(1)						

Table 6.2: Cell parameters obtained from diffraction data analysis: $BaTi_{0.95}Ce_{0.05}O_3$, $BaTi_{0.9}Ce_{0.1}O_3$ and $BaTi_{0.8}Ce_{0.2}O_3$ nano powders at different temperatures.

As deducible by visual comparison, and now demonstrated by figure 6.3, cells do not show great dilatation as

temperature increase with an expansion ∼0.2 % (considering an average value calculated taking into account for each sample the highest and the lowest temperature); on the other hand, cerium amount has a higher effect with an increment of ∼2.08 % (obtained by values of BTC2 150 K and BTC30 100 K). However trends are linear for all the samples. No particular or surprising features are noticeable.

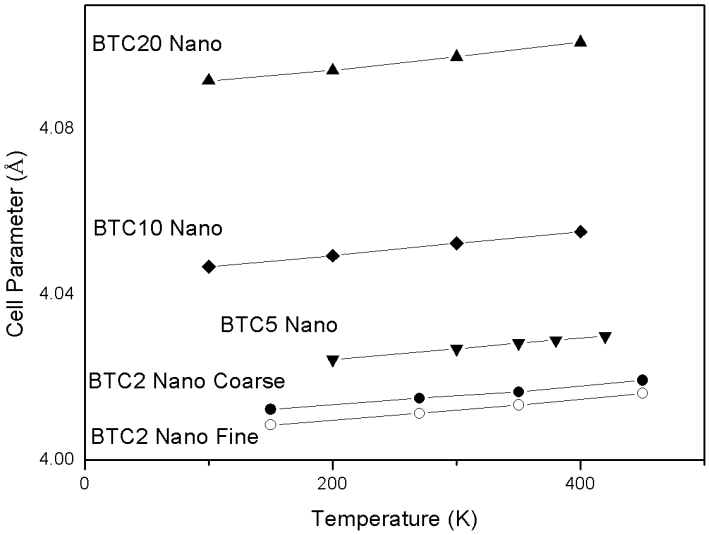

Figure 6.3: Average structure: comparison between different cell parameters as a function of temperature and doping.

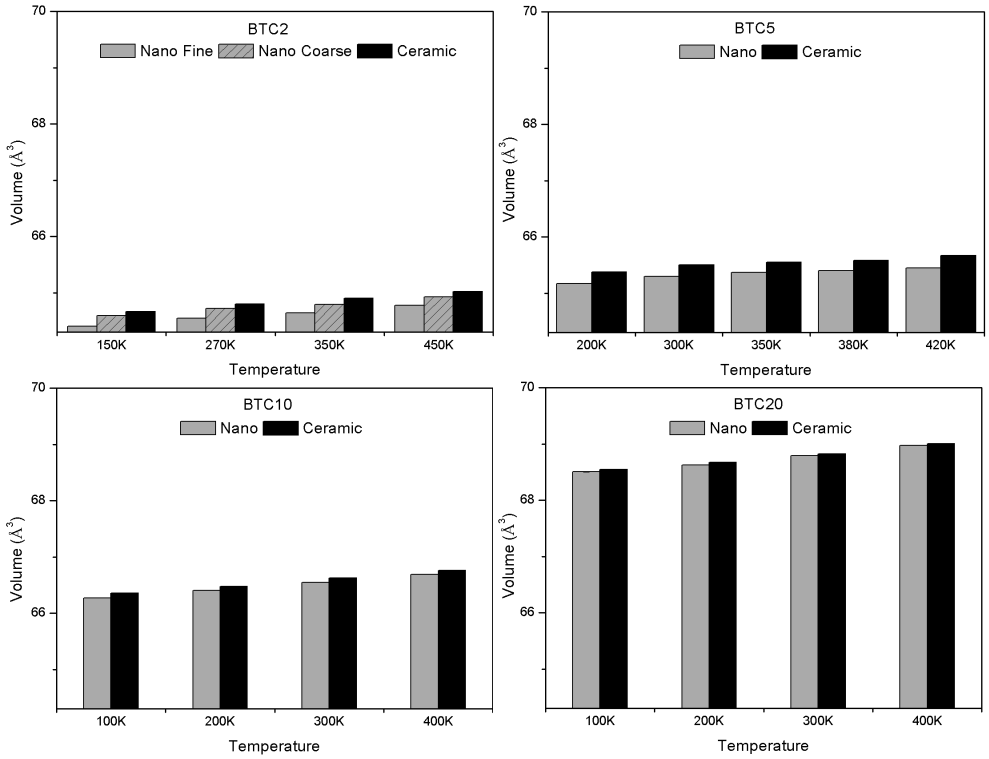

Figure 6.4: Comparison between average volumes of ceramic and nano powders BTCs.

In figure 6.4 results of cell volumes calculated for nano powders and ceramics are compared. All volumes are for sure conditioned by the grain size, in particular this is more evident in BTC2 where three different kinds of materials are available. In this case volume percentage variation between nano fine and ceramic sample is

$\sim$0.39%, whereas from coarse powders is $\sim$0.14 %. Other BTCs vary of $\sim$0.30 , 0.12 and 0.17 % for respectively BTC5, 10 and 20. Differences in volume between nano and ceramic samples are then little and this is also clear by comparison of diffraction data. In figure 6.5 data of BTC2 ceramic and nano fine are shown as example, obviously this direct comparison is possible only in this case, they are indeed the only samples, with different grain sizes, collected under the same conditions. By visual investigation peaks are not evidently shifted, but nano dimensions influence deeply the peak shapes showing a great broadening and intensity reduction.

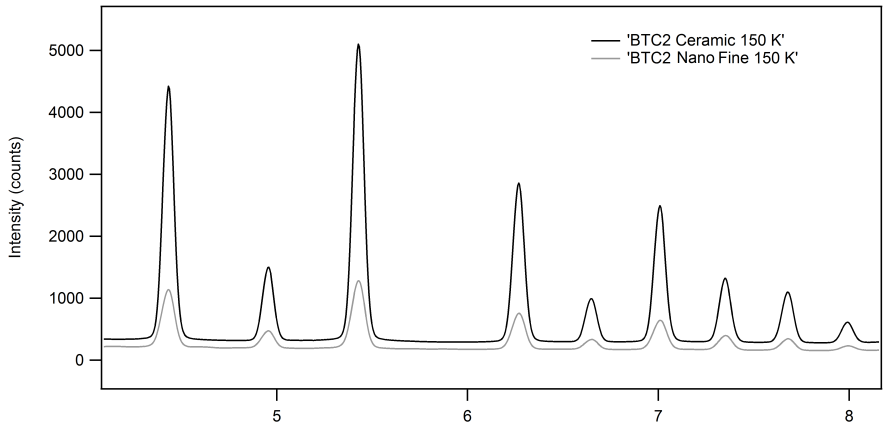

Figure 6.5: Visual comparison of diffractograms for $BaTi_{0.98}Ce_{0.02}O_3$ at 150 K presenting two different grain size. As noticeable nano particle dimensions influence peaks shape inducing a great broadening.

In order to evaluate domain coherence, crystallite size and microstrain have been refined. According to the Warren-Averbach method, microstrain is dependent to the harmonic order, while crystallite size contribution is constant and not subordinated to the order of reflections. Thus in order to discriminate between these two effects, a sufficient number of diffraction peaks should be analysed. Unfortunately, contrary to the ceramic data set, here analyses have been performed in a reduced 2θ range producing therefore a small number of Bragg effects. In this light, trying to separate the size from the strain effect may be meaningless. For this reason, a second kind of refinements has been executed fixing microstrain at low value (0.00005). This operation should allow to consider peak broadening as only caused by reduced domain sizes, then a better estimation of this parameter should be attainable, though attributing the whole of peak broadening to size. In tables 6.3, 6.4, 6.5, 6.6 and 6.7 results achieved in the two refinements are reported showing the evolution of values as a function of temperature and different doping.

BTC2 Nano Fine					
Crystallite Size and Microstrain free			Crystallite Size free and Microstrain fixed		
Temp.	Crystallite Size (Å)	r.m.s Microstrain	Temp.	Crystallite Size (Å)	r.m.s Microstrain
150 K	381(08)	0.00284(6)	150 K	275(03)	0.00005
270 K	388(08)	0.00321(6)	270 K	263(03)	0.00005
350 K	381(08)	0.00310(7)	350 K	266(03)	0.00005
450 K	373(03)	0.00262(5)	450 K	284(04)	0.00005

Table 6.3: $BaTi_{0.98}Ce_{0.02}O_3$ nano fine: comparison between two different refinements. In first microstrain and crystallite size have been refined together, in the second microstrain has been fixed at 0.00005.

Values presented in tables are also reported graphically in figure 6.6. Windows on the left show results obtained refining crystallite size and microstrain, on the right those obtained fixing microstrain are shown. Taking into account first analyses, domain size increases as a function of cerium amount as the microstrain. As already notice

BTC2 Nano Coarse					
Crystallite Size and Microstrain free			Crystallite Size free and Microstrain fixed		
Temp.	Crystallite Size (Å)	r.m.s Microstrain	Temp.	Crystallite Size (Å)	r.m.s Microstrain
150 K	585(14)	0.00229(5)	150 K	412(06)	0.00005
270 K	595(15)	0.00279(5)	270 K	375(02)	0.00005
350 K	578(15)	0.00275(6)	350 K	373(05)	0.00005
450 K	567(06)	0.00197(2)	450 K	437(06)	0.00005

Table 6.4: $BaTi_{0.98}Ce_{0.02}O_3$ nano coarse: comparison between two different refinements. In first microstrain and crystallite size have been refined together, in the second microstrain has been fixed at 0.00005.

BTC5 Nano					
Crystallite Size and Microstrain free			Crystallite Size free and Microstrain fixed		
Temp.	Crystallite Size (Å)	r.m.s Microstrain	Temp.	Crystallite Size (Å)	r.m.s Microstrain
200 K	406(02)	0.00344(5)	200 K	261(04)	0.00005
300 K	407(02)	0.00367(3)	300 K	253(03)	0.00005
350 K	400(04)	0.00367(3)	350 K	252(02)	0.00005
380 K	397(08)	0.00357(7)	380 K	255(03)	0.00005
420 K	400(04)	0.00338(3)	420 K	265(03)	0.00005

Table 6.5: $BaTi_{0.95}Ce_{0.05}O_3$ nano: comparison between two different refinements. In first microstrain and crystallite size have been refined together, in the second microstrain has been fixed at 0.00005.

BTC10 Nano					
Crystallite Size and Microstrain free			Crystallite Size free and Microstrain fixed		
Temp.	Crystallite Size (Å)	r.m.s Microstrain	Temp.	Crystallite Size (Å)	r.m.s Microstrain
100 K	413(05)	0.00473(3)	100 K	216(03)	0.00005
200 K	406(10)	0.00484(6)	200 K	213(01)	0.00005
300 K	405(06)	0.00497(4)	300 K	210(01)	0.00005
400 K	410(04)	0.00491(3)	400 K	214(03)	0.00005

Table 6.6: $BaTi_{0.9}Ce_{0.1}O_3$ nano: comparison between two different refinements. In first microstrain and crystallite size have been refined together, in the second microstrain has been fixed at 0.00005.

BTC20 Nano					
Crystallite Size and Microstrain free			Crystallite Size free and Microstrain fixed		
Temp.	Crystallite Size (Å)	r.m.s Microstrain	Temp.	Crystallite Size (Å)	r.m.s Microstrain
100 K	955(49)	0.00817(6)	100 K	163(03)	0.00005
200 K	959(61)	0.00820(6)	200 K	165(02)	0.00005
300 K	999(66)	0.00823(6)	300 K	167(03)	0.00005
400 K	1053(17)	0.00829(4)	400 K	173(03)	0.00005

Table 6.7: $BaTi_{0.8}Ce_{0.2}O_3$ nano: comparison between two different refinements. In first microstrain and crystallite size have been refined together, in the second microstrain has been fixed at 0.00005.

for ceramic, cerium introduction produces strain in $BaTi_{1-x}Ce_xO_3$ samples due to its big atomic size then it should be correct to notice an increment of this parameter from BTC2 to BTC20. In ceramics by increasing the substitution of Ce content a decrease of grains size takes place (Curecheriu et al. 2016), although grain size is usually related to the domain sizes, but these two are not exactly the same thing. The second is in fact a measure of domain coherence, whereas grain could be formed by a certain number of domains. Then if it is true that cerium in ceramics reduces grain size, it is not so obvious that the same effect occurs in nano BTCs and especially it is not sure which is the effect on the domain sizes. However from the first analysis BTC20 shows the higher crystallite

size value, which then decreases with cerium amount reduction.

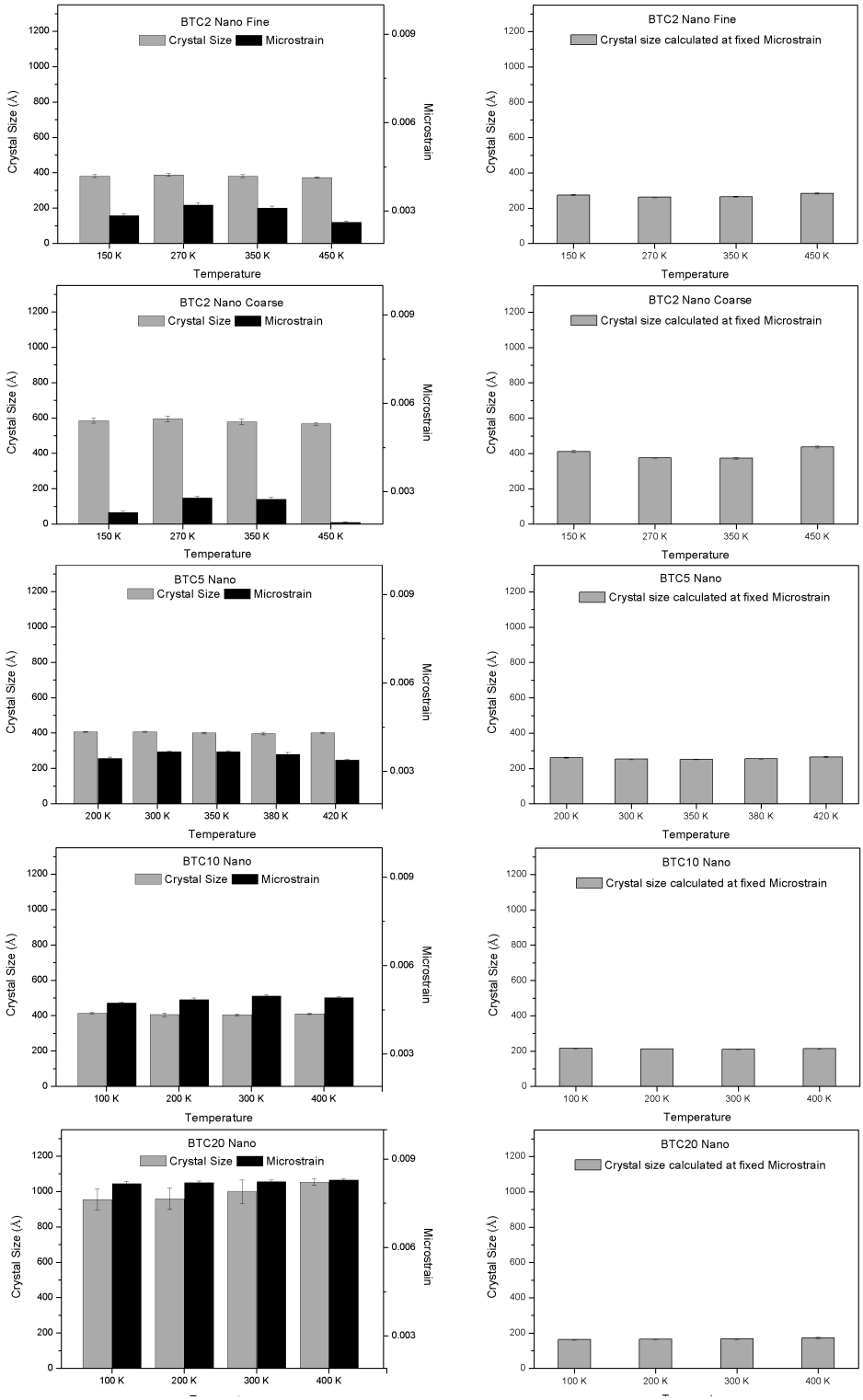

Figure 6.6: Comparison between two different refinements. In left windows results refining together microstrain are presented, on the right results of crystallite size obtained fixing microstrain at 0.00005 are shown.

This trends is subverted considering results of the second refinements. As a function of cerium increase, peaks are broader then, fixing microstrain, crystallite size value must be decreased to well fit data and this refined values show an increment with doping decrease. Despite all results are almost in trend, one or other depending on the type

of refinements, BTC2 nano coarse presents in both cases two high values for the crystallite size. No explanations are supplied for this behaviour. Concluding the two types of refinement strategies have shown evident diversities. It is not clear which refinement strategy (for the microstructural parameters) is best suited for this problem. However, taking into account the small number of peaks available (and their broadness), it seems more reasonable to trust the second approach. The level of detail of the Rietveld refinements of the nano powder is certainly not comparable to the one obtained for the ceramic materials, due also to the low resolution of the 2D detector geometry during the experiment. Despite this, it was possible to gain information about the influence of dopant content on cell volumes and to compare it with the one found for ceramics, and to produce a reasonable (though not certain) interpretation for the influence of Ce content on the microstructure. However broad peaks, cerium doping and nanometric size ensure a great probable disorder on the local structure. Analysis on this last is then necessary to characterized more these materials and understand the effects induced by chemical and size stress.

6.2 Local Structure

Pair Distribution Functions have been obtained using PDFgetX3 (Juhas et al. 2013) with these parameters: *qmax* and *qmaxinst* are fixed at 27, rpoly is 1.4 and *bgscale* is equal 1. In these extrapolations much attention has been paid on the background subtraction. Empty capillary has been collected at specific and different temperatures corresponding to those of the investigated sample, then each data has been treated subtracting the corresponding background. This last operation should guarantee a better PDF generation and a less noise. Before performing structural analysis, a visual investigation is essential to verify the PDFs goodness, but more important to briefly evaluate the local structures and the eventual disorder.

6.2.1 Local Structure: PDF visual comparison

In figure 6.7 a comparison between nano and ceramic BTC2 Pair Distribution Functions is reported to show the size effect on G(r). As already mention in chapter 2 nano dimensions cause an evident signal dampening, however grain sizes of nano BTCs are not so reduced and, despite a dampening, PDF is well resolved also at high radii.

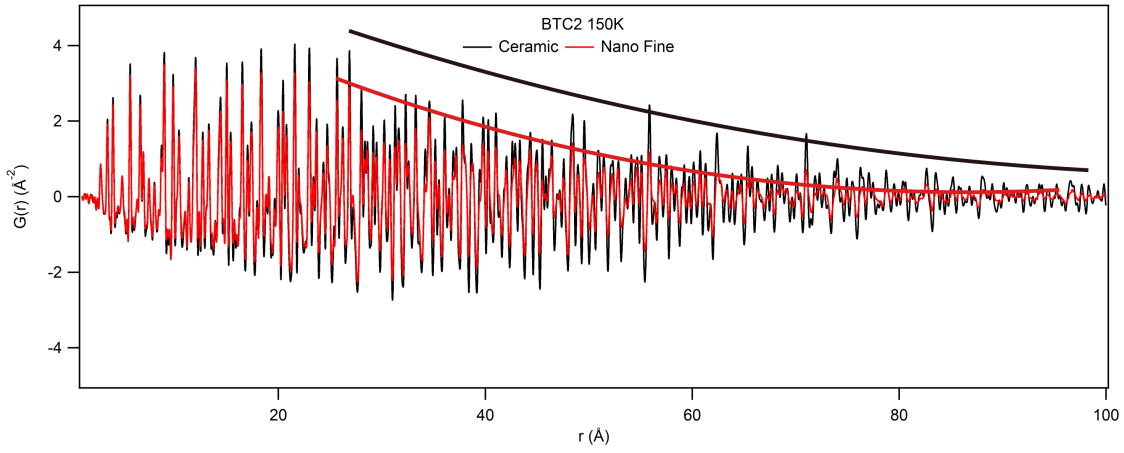

Figure 6.7: Comparison between PDFs of BTC2 ceramic and nano at 150 K. Signal dampening is evidenced for the two function.

In figures 6.8 and 6.9 all PDFs are reported between 1 and 10 Å in order to compare the evolution of each sample as a function of temperatures.

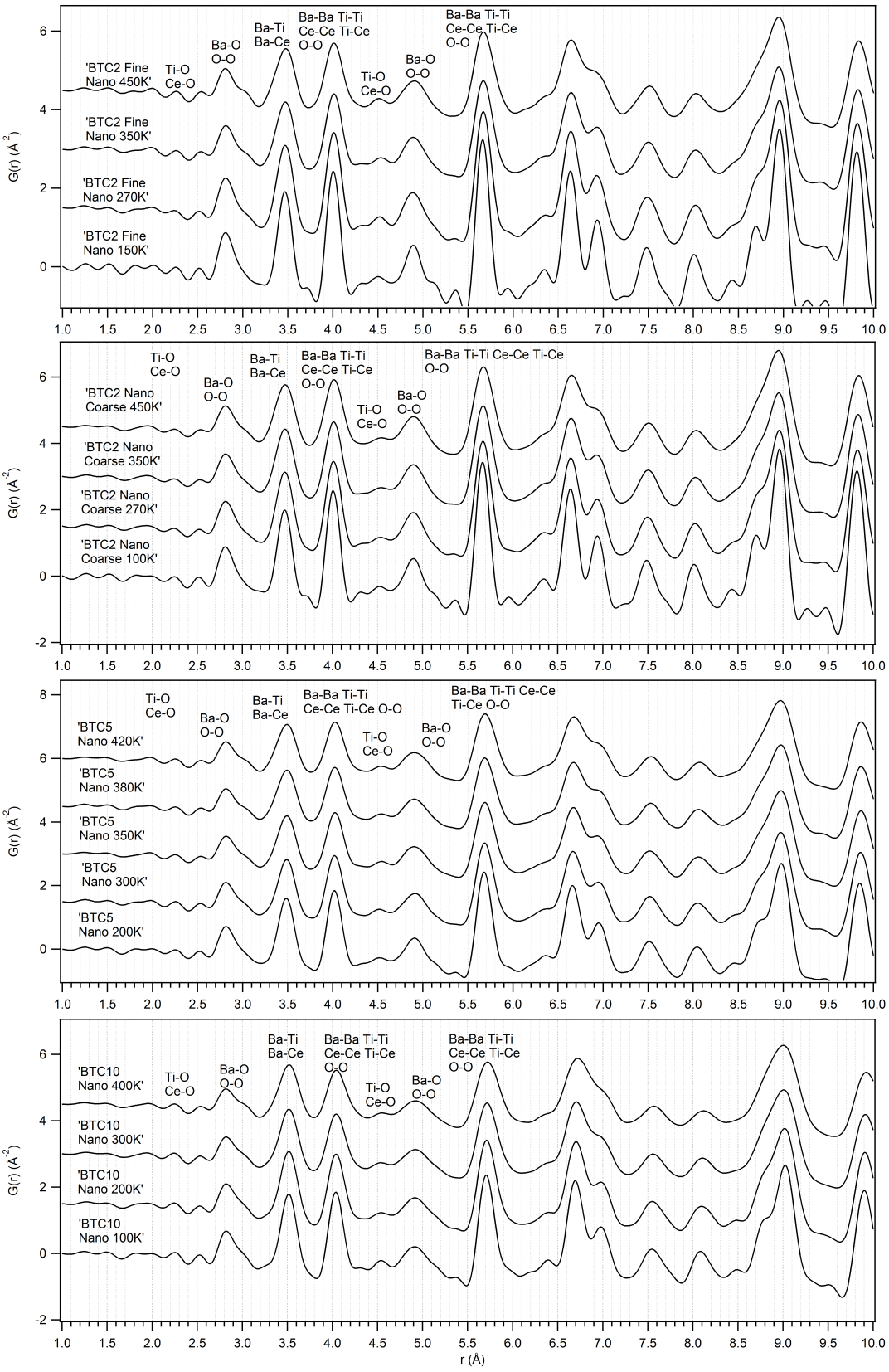

Figure 6.8: Nano BTCs: BTC2 fine, BTC2 coarse, BTC5 and BTC10. Pair Distribution Functions comparison as a function of temperature.

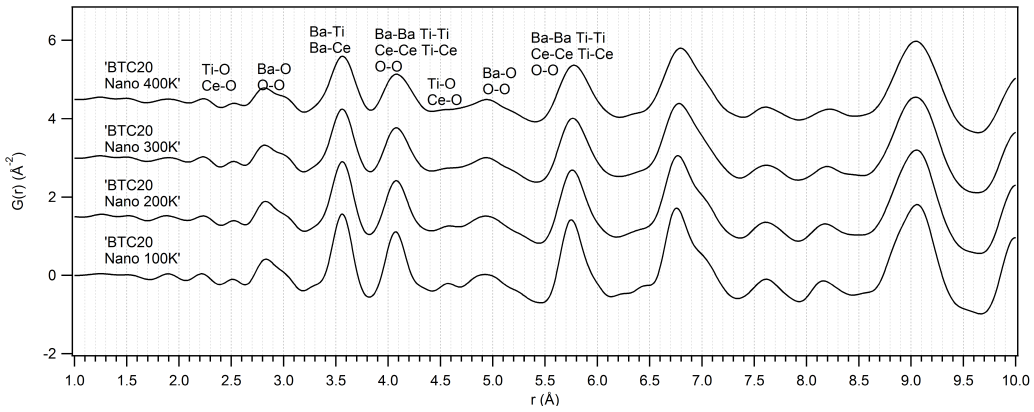

Figure 6.9: Nano BTCs: BTC20. Pair Distribution Functions comparison as a function of temperature.

The first interesting consideration is about the first peak Ti-O and Ce-O. Exactly as in ceramic samples, the first distance or distances between B cations and oxygens are not visible in each sample for any temperature. Termination ripples appear similar in position for all temperatures and low in intensity, but frequencies are not constant probably suggesting the presence of hidden B-O distances. Despite this, it is impossible to recognize or distinguish between noise and some indication of the first peak. Taking into account each sample in a radius range between 1 and 5 Å, peaks positions seem to be identical, indicating that the 'true' local structure should be similar at any temperature. Big differences are whereas noticeable in peaks intensity, obviously thermal vibrations influence deeply the peaks broadening and higher temperatures show more curvy shapes with less peak resolution and less evident features.

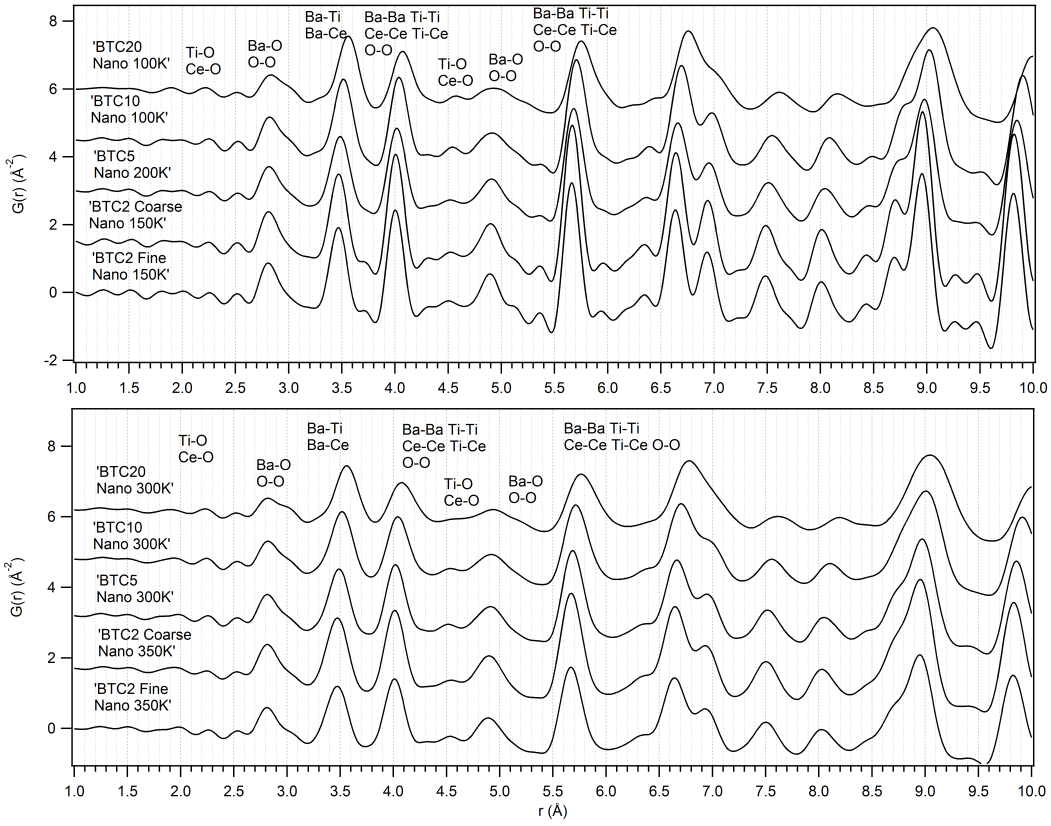

Figure 6.10: Pair Distribution Functions comparison at around 100 K and around 300 K as a function of doping amounts.

In figures 6.10 comparison between samples with different amount of cerium is presented for temperatures around 100 and 300 K. Differences are here well noticeable. First of all peaks are evidently shifted with cerium increase. This is more clear for peaks related to distance between heavier atoms as Ba-Ti and Ba-Ce at 3.5 Å or Ba-Ba, Ti-Ti, Ti-Ce and Ce-Ce at 4.0 Å. Furthermore peaks related to $BaTi_{0.9}Ce_{0.1}O_3$ and $BaTi_{0.8}Ce_{0.2}O_3$ show broader forms, especially if comparison at lowest temperatures is considered, demonstrating once again how cerium introduction creates disorder on the local structure.

6.2.2 Local Structure analysis

PDFgui (Farrow et al. 2007) software has been employed in local structure analyses, *Qdamp* have been fixed at 0.008. In order to understand the local symmetry different refinements have been performed using the four space groups which occur in pure $BaTiO_3$ phase transitions. This approach has been applied in three different radius ranges (1-10, 10-19 and 19-28 Å) to also evaluate the length of structural coherence. Investigations have been executed using a supercell 2x2x2 refining thermal parameters and every things allowed by the space group rules; Ti and Ce have been constrained by fractional occupancies, but positions have been considered independently. In tables 6.8, 6.9, 6.10, 6.11 and 6.12 different Rw values for each sample, temperature and radius range are reported.

BTC2 Nano Fine					
1-10 Å	Temperature	Cubic	Tetragonal	Orthorhombic	Rhombohedric
	150 K	0.1900	**0.1597**	0.1942	0.1804
	270 K	0.1788	**0.1714**	0.1787	0.1883
	350 K	0.1962	0.1657	**0.1638**	0.1860
	450 K	0.1975	0.1901	**0.1889**	0.1909
10-19 Å	Temperature	Cubic	Tetragonal	Orthorhombic	Rhombohedric
	150 K	0.2047	0.1285	**0.1235**	0.1459
	270 K	0.1307	**0.1050**	0.1080	0.1236
	350 K	0.1100	0.1055	**0.0909**	0.1368
	450 K	0.1150	**0.1084**	0.1086	0.1339
19-28 Å	Temperature	Cubic	Tetragonal	Orthorhombic	Rhombohedric
	150 K	0.1380	**0.1202**	0.1301	0.1321
	270 K	0.1562	**0.1149**	0.1324	0.1283
	350 K	0.1198	**0.1018**	0.1276	0.1419
	450 K	0.1170	**0.1055**	0.1250	0.1084

Table 6.8: Rw values obtained for local structural analyses of $BaTi_{0.98}Ce_{0.02}O_3$ fine nano powders. Refinements have been performed using four different symmetries in three different radius ranges. In bold style lowest Rw values are evidenced.

BTC2 Nano Coarse					
1-10 Å	Temperature	Cubic	Tetragonal	Orthorhombic	Rhombohedric
	150 K	0.1820	**0.1590**	0.1697	0.1671
	270 K	0.1881	**0.1680**	0.1745	0.1775
	350 K	0.1911	**0.1761**	0.1956	0.1812
	450 K	0.1921	0.1853	**0.1818**	0.1831
10-19 Å	Temperature	Cubic	Tetragonal	Orthorhombic	Rhombohedric
	150 K	0.115	**0.0975**	0.1059	0.1086
	270 K	0.1047	**0.0921**	0.0968	0.1209
	350 K	0.1043	**0.0985**	0.1540	0.1007
	450 K	0.1034	**0.0976**	0.1518	0.1387
19-28 Å	Temperature	Cubic	Tetragonal	Orthorhombic	Rhombohedric
	150 K	0.1150	**0.1070**	0.1534	0.1109
	270 K	0.1227	0.1185	**0.1069**	0.1209
	350 K	0.1249	**0.1220**	0.1398	0.1233
	450 K	0.1254	**0.1210**	0.1259	0.1222

Table 6.9: Rw values obtained for local structural analyses of $BaTi_{0.98}Ce_{0.02}O_3$ coarse nano powders. Refinements have been performed using four different symmetries in three different radius ranges. In bold style lowest Rw values are evidenced.

Taking into account comparison of different Rw values, tetragonal and orthorhombic structure usually show best fits. However considering the highest symmetry, tetragonal seems to be the best choice for each sample,

BTC5 Nano					
1-10 Å	Temperature	Cubic	Tetragonal	Orthorhombic	Rhombohedric
	200 K	0.1943	**0.1718**	0.2493	0.1813
	300 K	0.1971	**0.1786**	0.2115	0.1975
	350 K	0.1963	**0.1867**	0.2686	0.2040
	380 K	0.1976	**0.1842**	0.2274	0.1864
	420 K	0.1977	**0.1862**	0.2304	0.1868
10-19 Å	Temperature	Cubic	Tetragonal	Orthorhombic	Rhombohedric
	200 K	0.1185	**0.1060**	0.1909	0.1079
	300 K	0.1096	**0.1092**	0.1917	0.1975
	350 K	0.1082	0.1046	0.2089	**0.0995**
	380 K	0.1061	**0.0972**	0.1847	0.1283
	420 K	0.1035	**0.0952**	0.2101	0.1396
19-28 Å	Temperature	Cubic	Tetragonal	Orthorhombic	Rhombohedric
	200 K	0.1219	**0.1075**	0.1265	0.1092
	300 K	0.1170	**0.1082**	0.2862	0.1310
	350 K	0.1168	**0.1074**	0.1293	0.1110
	380 K	0.1166	0.1108	0.1836	**0.1089**
	420 K	0.1144	**0.1020**	0.1152	0.1075

Table 6.10: Rw values obtained for local structural analyses of $BaTi_{0.95}Ce_{0.05}O_3$ nano powders. Refinements have been performed using four different symmetries in three different radius ranges. In bold style lowest Rw values are evidenced.

BTC10 Nano					
1-10 Å	Temperature	Cubic	Tetragonal	Orthorhombic	Rhombohedric
	100 K	0.2083	0.1876	**0.1648**	0.1908
	200 K	0.1970	**0.1801**	0.1945	0.1975
	300 K	0.1930	**0.1829**	0.1857	0.1831
	400 K	0.1900	**0.1806**	0.2044	0.2080
10-19 Å	Temperature	Cubic	Tetragonal	Orthorhombic	Rhombohedric
	100 K	0.1319	**0.1213**	0.1461	0.1556
	200 K	0.1118	0.1021	0.1346	**0.0995**
	300 K	0.0980	**0.0896**	0.0980	0.0922
	400 K	0.0923	**0.0842**	0.1086	0.0860
19-28 Å	Temperature	Cubic	Tetragonal	Orthorhombic	Rhombohedric
	100 K	0.1265	0.1125	**0.1025**	0.1136
	200 K	0.1065	**0.0982**	0.1106	0.1337
	300 K	0.0924	**0.0872**	0.1203	0.1091
	400 K	0.0888	**0.0837**	0.0907	0.0853

Table 6.11: Rw values obtained for local structural analyses of $BaTi_{0.9}Ce_{0.1}O_3$ nano powders. Refinements have been performed using four different symmetries in three different radius ranges. In bold style lowest Rw values are evidenced.

BTC20 Nano					
1-10 Å	Temperature	Cubic	Tetragonal	Orthorhombic	Rhombohedric
	100 K	0.2211	**0.1213**	0.2758	0.2317
	200 K	0.2071	0.2000	**0.1929**	0.1958
	300 K	0.1981	0.1986	**0.1828**	0.1945
	400 K	0.1914	**0.1828**	0.1890	0.2288
10-19 Å	Temperature	Cubic	Tetragonal	Orthorhombic	Rhombohedric
	100 K	0.1382	**0.1213**	0.1257	0.1385
	200 K	0.1277	**0.1015**	0.1116	0.1089
	300 K	0.1174	**0.1044**	0.1145	0.1085
	400 K	0.1078	0.1362	**0.1030**	0.1149
19-28 Å	Temperature	Cubic	Tetragonal	Orthorhombic	Rhombohedric
	100 K	**0.1837**	0.2352	0.2707	0.2302
	200 K	**0.1666**	0.2828	0.1782	0.2828
	300 K	**0.1605**	0.2238	0.1744	0.1992
	400 K	**0.1649**	0.2923	0.2594	0.2079

Table 6.12: Rw values obtained for local structural analyses of $BaTi_{0.8}Ce_{0.2}O_3$ nano powders. Refinements have been performed using four different symmetries in three different radius ranges. In bold style lowest Rw values are evidenced.

temperature and radius range. Only in BTC20 cubic structure presents lowest Rw between 19 and 28 Å. All results reported confirm that, despite the unknown average atomic arrangement, BTC perovskites do not present paraelectric phase in the true local structure. In figure 6.11 an example of carbox fits is presented for BTC20

and BTC10 at 100 K. As expected refinements performed in lower part of PDFs show the worse agreement, for sure this is also linked to the missing information about the first unseen Ti-O/Ce-O peaks. However, despite little differences, fits, even in the first radius range, are very good especially if compared to those achieved for ceramic samples.

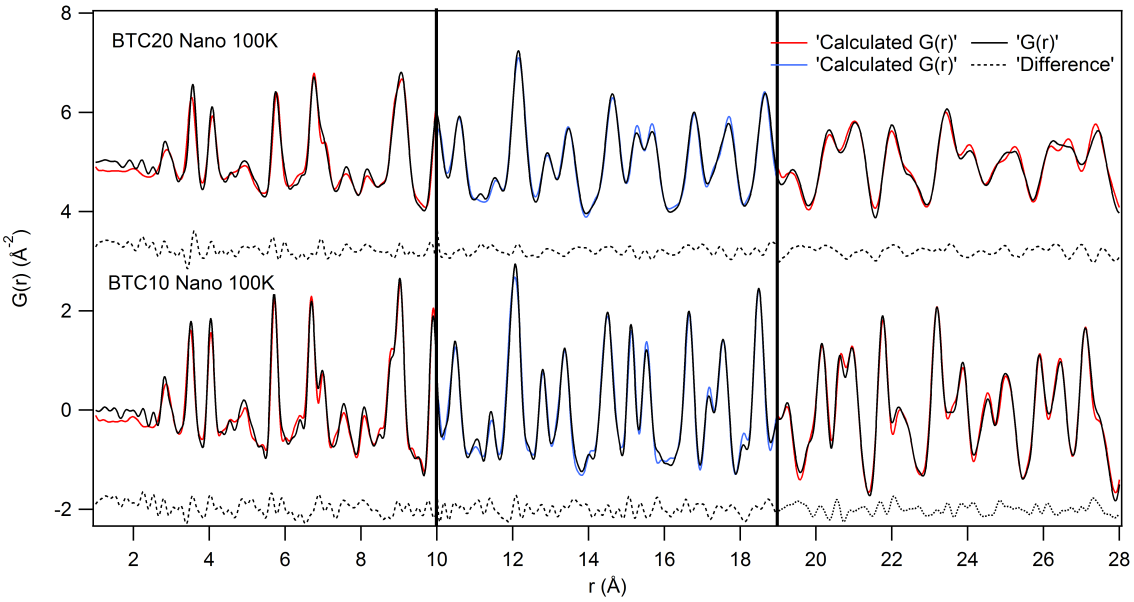

Figure 6.11: Example of carbox refinements. For BTC20 and BTC10 nano at 100K. Three different radius ranges have been considered and underlined by dashed lines.

BTC2 Nano Fine												
	1-10 (Å)				10-19 (Å)				19-28 (Å)			
	a (Å)	b (Å)	((c/a)-1)%	Vol. (Å^3)	a (Å)	b (Å)	((c/a)-1)%	Vol. (Å^3)	a (Å)	b (Å)	((c/a)-1)%	Vol. (Å^3)
150 K	3.995	4.029	0.855	64.29	3.998	4.026	0.677	64.36	4.001	4.021	0.508	64.37
270 K	3.995	4.040	1.140	64.48	4.002	4.031	0.716	64.55	4.003	4.028	0.632	64.55
350 K	4.003	4.029	0.641	64.56	4.003	4.030	0.675	64.59	4.004	4.026	0.546	64.57
450 K	3.999	4.042	1.062	64.65	4.006	4.033	0.681	64.72	4.009	4.026	0.434	64.69

Table 6.13: Local cell parameters and volumes calculated in different radius ranges for BTC2 nano fine.

BTC2 Nano Coarse												
	1-10 (Å)				10-19 (Å)				19-28 (Å)			
	a (Å)	b (Å)	((c/a)-1)%	Vol. (Å^3)	a (Å)	b (Å)	((c/a)-1)%	Vol. (Å^3)	a (Å)	b (Å)	((c/a)-1)%	Vol. (Å^3)
150 K	3.999	4.028	0.712	64.43	4.006	4.017	0.275	64.47	4.008	4.013	0.113	64.47
270 K	3.998	4.038	1.005	64.56	4.006	4.026	0.487	64.62	4.005	4.027	0.548	64.61
350 K	4.008	4.025	0.429	64.65	4.006	4.030	0.592	64.68	4.009	4.024	0.372	64.66
450 K	4.001	4.047	1.140	64.79	4.014	4.023	0.234	64.82	4.015	4.021	0.152	64.81

Table 6.14: Local cell parameters and volumes calculated in different radius ranges for BTC2 nano coarse.

BTC5 Nano												
	1-10 (Å)				10-19 (Å)				19-28 (Å)			
	a (Å)	b (Å)	((c/a)-1)%	Vol. (Å^3)	a (Å)	b (Å)	((c/a)-1)%	Vol. (Å^3)	a (Å)	b (Å)	((c/a)-1)%	Vol. (Å^3)
200 K	4.008	4.047	0.990	65.01	4.021	4.028	0.195	65.12	4.017	4.037	0.505	65.13
300 K	4.008	4.058	1.250	65.17	4.017	4.046	0.723	65.30	4.020	4.042	0.556	65.31
350 K	4.012	4.056	1.106	65.29	4.020	4.047	0.671	65.38	4.021	4.042	0.501	65.36
380 K	4.013	4.056	1.081	65.31	4.019	4.051	0.805	65.43	4.021	4.046	0.621	65.42
420 K	4.019	4.048	0.719	65.38	4.026	4.040	0.343	65.48	4.024	4.040	0.400	65.44

Table 6.15: Local cell parameters and volumes calculated in different radius ranges for BTC5 nano.

BTC10 Nano												
	1-10 (Å)				10-19 (Å)				19-28 (Å)			
	a (Å)	b (Å)	((c/a)-1)%	Vol. (Å^3)	a (Å)	b (Å)	((c/a)-1)%	Vol. (Å^3)	a (Å)	b (Å)	((c/a)-1)%	Vol. (Å^3)
100 K	4.026	4.075	1.217	66.07	4.042	4.057	0.376	66.27	4.037	4.068	0.757	66.30
200 K	4.028	4.082	1.340	66.25	4.036	4.077	1.037	66.40	4.040	4.067	0.668	66.37
300 K	4.034	4.076	1.038	66.35	4.041	4.070	0.711	66.46	4.045	4.060	0.381	66.42
400 K	4.033	4.092	1.467	66.55	4.041	4.080	0.961	66.63	4.046	4.066	0.509	66.56

Table 6.16: Local cell parameters and volumes calculated in different radius ranges for BTC10 nano.

BTC20 Nano												
	1-10 (Å)				10-19 (Å)				19-28 (Å)			
	a (Å)	b (Å)	((c/a)-1)%	Vol. (Å^3)	a (Å)	b (Å)	((c/a)-1)%	Vol. (Å^3)	a (Å)	b (Å)	((c/a)-1)%	Vol. (Å^3)
100 K	4.058	4.130	1.775	68.03	4.065	4.127	1.518	68.18	4.085		0.000	68.18
200 K	4.061	4.132	1.747	68.15	4.069	4.125	1.380	68.31	4.088		0.000	68.30
300 K	4.064	4.143	1.952	68.41	4.072	4.129	1.408	68.47	4.090		0.000	68.44
400 K	4.068	4.142	1.808	68.55	4.073	4.137	1.589	68.62	4.094		0.000	68.60

Table 6.17: Local cell parameters and volumes calculated in different radius ranges for BTC20 nano.

Results on cell parameters obtained by carbox approach are reported in tables 6.13, 6.14, 6.15, 6.16 and 6.17, furthermore a distortion parameter of tetragonal structure (Rabuffetti et al. 2014) is shown. Volumes correspondent to different samples, temperatures and radius ranges are shown in figure 6.12.

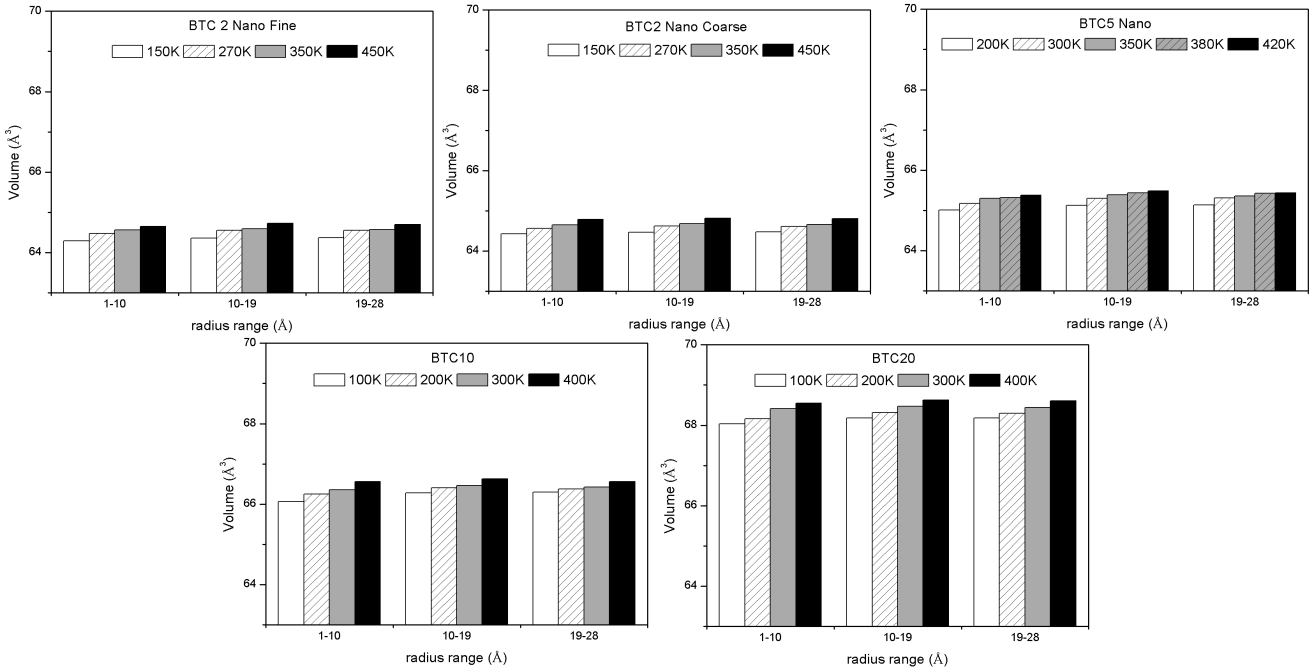

Figure 6.12: Volumes as a function of doping and temperature calculated in three different local ranges.

Focusing on one sample at time the first important consideration to make is a slight expansion of the cell as a function of temperature increase. As previously said for average and local ceramic structure and also for average nano powders, temperature seems to not generate great changes in volume. Looking the evolution in different radius ranges little increase is noticeable from the first to second range and then value remains almost constant in 10-19 and 19-28 Å. Comparing now samples with different cerium amount, again BTC20 shows the higher volumes which then decrease with doping reduction, the effect is very clear and significant. Taking into account only the grain size influence, which is possible only in BTC2 fine and coarse, little differences are noticeable. Indeed bigger powders dimensions determine bigger volumes. As previously reported, samples present tetragonal

structures independently for temperatures and analysis ranges (except for a cubic symmetry assigned for BTC20 19-28 Å). In light of this, it could be useful to define the grade of tetragonal cell distortion by the already used parameter 100*((c/a)-1) (Rabuffetti et al. 2014). In other words the idea is to evaluate how much a and c cell parameters are different and then how much tetragonal structure is actually different from the cubic one. In figure 6.13 results are shown and regression line calculated for each temperature (then between points belonging to same temperature, but different radial ranges) are also signaled.

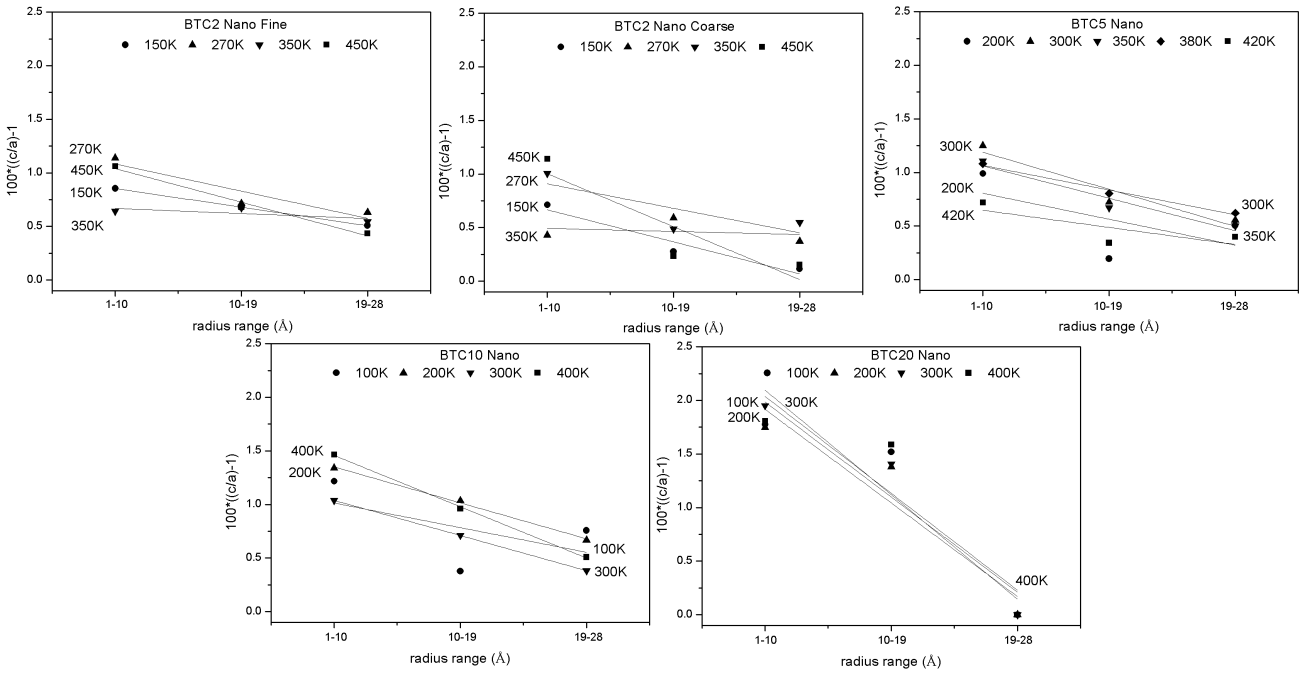

Figure 6.13: For each temperature of each sample tetragonal distortion parameters are reported for each radius range. Regression lines have been calculated to underline the structural evolution at increasing radius ranges.

Nano Powders									
BTC2 Fine	Slope	BTC2 Coarse	Slope	BTC5	Slope	BTC10	Slope	BTC20	Slope
150 K	-0.173	150 K	-0.300	200 K	-0.243	100 K	-0.230	100 K	-0.887
270 K	-0.254	270 K	-0.228	300 K	-0.347	200 K	-0.336	200 K	-0.874
350 K	-0.047	350 K	-0.029	350 K	-0.306	300 K	-0.328	300 K	-0.976
450 K	-0.314	450 K	-0.494	380 K	-0.230	400 K	-0.479	400 K	-0.904
				420 K	-0.160				

Table 6.18: Slope values of regression lines reported in figure 6.13 are shown.

In table 6.18 the slopes of each regression line are reported. Samples less doped show a higher dispersion of values, while BTC10 and BTC20 have, comparing different temperatures, more similar coefficients and on average higher values. This is especially evident in $BaTi_{0.8}Ce_{0.2}O_3$, but it is better to underline that this effect is so pronounced thank to the cubic structure chosen to fit the last radius range, where distortion parameter is obviously zero. Making some generic considerations cerium doping seems to provoke a faster transition between tetragonal to cubic structure. These variations should be linked to the material properties then also Ti displacements have been calculated. In order to reduce the effect of dynamic disorder only lowest temperatures (one for each sample) have been taken into account and results obtained by analyses in the first radius range will be presented. Titanium displacements have been calculated from the center of the octahedron then from the center of the parental cubic cell. Table 6.19 recaps titanium fractional coordinates, resulted by previously reported refinements, and related

displacements. In figure 6.14 a comparison between volumes, tetragonal distortion parameter and Ti displacements is shown.

Nano Powders					
	BT2 Fine 150K	BT2 Coarse 150K	BTC5 200K	BTC10 100K	BTC20 100K
Ti z coordinate	0.520	0.523	0.521	0.517	0.492
Ti displacement (Å)	0.020	0.023	0.021	0.017	0.008

Table 6.19: Titanium fractional coordinates and displacements calculated for BTCs nano at lowest temperatures. Only results obtained by analyses performed between 1 and 10 Å are considered.

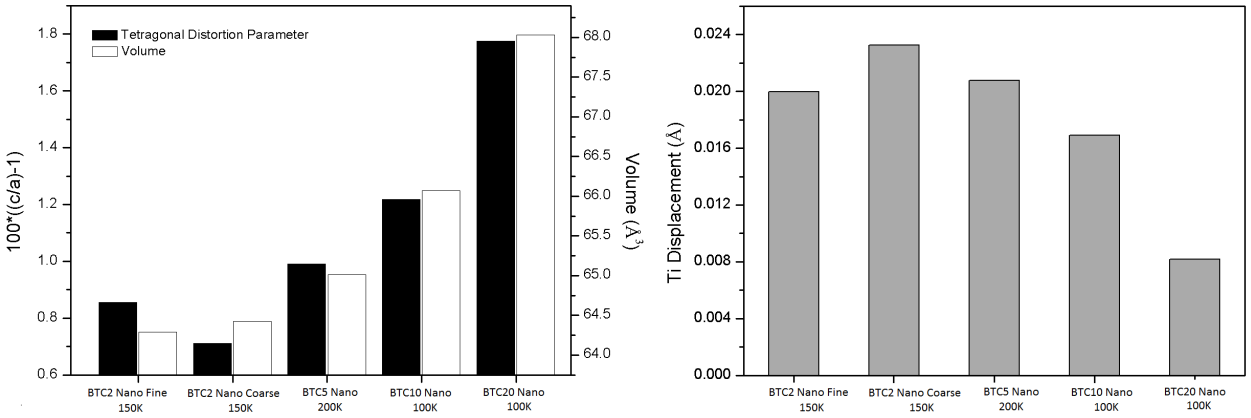

Figure 6.14: On the left tetragonal distortion parameters and volumes are presented, instead on the right titanium displacements are reported. Only results obtained calculated for BTCs nano at lowest temperatures and obtained by analyses performed between 1 and 10 Å are considered.

By figure 6.14 the focus of this discussion is passing from a study of the evolution of the local structures at different scales to a study on the true local structures, as so called in this dissertation. Embracing Ravel's theory (Ravel et al. 1998) average structural transitions in ceramic samples have been explained as a change in the long range correlations between local distortions. Probably these view could be applied also in nano BTC, then only lowest temperatures are now considered. As graphically shown, volumes increase as a function of the cerium amount, but also a correlation with tetragonal distortion is noticeable. Indeed cerium introduction seems to locally provoke an increase on cell parameters, but also a distortion more and more pronounced. At the same time Ti displacements decrease despite the increment of the volume (of the cell and obviously of BO_6 octahedron) and the distortion. Cerium doping then strongly inhibits titanium local off-center also in nano $BaTi_{1-x}Ce_xO_3$. Note that this effect is averaged, Ti probably could move in different directions, but the net values is clearly low demonstrating a short correlation between these movements. The well description of the local structure up to now reported is demonstrated also considered Uiso values calculated and shown in tables 6.20, 6.21, 6.22, 6.23 and 6.24.

BTC2 Nano Fine									
	Uiso refined over 1-10 Å			Uiso refined over 10-19 Å			Uiso refined over 19-28 Å		
Temperature	Ba (Å^2)	Ti-Ce (Å^2)	O (Å^2)	Ba (Å^2)	Ti-Ce (Å^2)	O (Å^2)	Ba (Å^2)	Ti-Ce (Å^2)	O (Å^2)
150 K	0.002	0.003	0.009	0.002	0.005	0.010	0.003	0.004	0.010
270 K	0.003	0.005	0.009	0.003	0.007	0.009	0.005	0.006	0.009
350 K	0.004	0.006	0.011	0.005	0.008	0.015	0.006	0.008	0.010
450 K	0.004	0.009	0.017	0.005	0.008	0.014	0.007	0.007	0.018

Table 6.20: BTC2 Nano fine: Uiso values calculated in three different radius ranges for each temperature.

BTC2 Nano Coarse									
	Uiso refined over 1-10 Å			Uiso refined over 10-19 Å			Uiso refined over 19-28 Å		
Temperature	Ba (Å^2)	Ti-Ce (Å^2)	O (Å^2)	Ba (Å^2)	Ti-Ce (Å^2)	O (Å^2)	Ba (Å^2)	Ti-Ce (Å^2)	O (Å^2)
150 K	0.002	0.003	0.012	0.002	0.005	0.009	0.003	0.002	0.008
270 K	0.003	0.005	0.009	0.004	0.007	0.010	0.004	0.007	0.014
350 K	0.004	0.005	0.010	0.005	0.007	0.018	0.005	0.011	0.010
450 K	0.005	0.008	0.014	0.007	0.006	0.016	0.007	0.007	0.014

Table 6.21: BTC2 nano coarse: Uiso values calculated in three different radius ranges for each temperature.

BTC5 Nano									
	Uiso refined over 1-10 Å			Uiso refined over 10-19 Å			Uiso refined over 19-28 Å		
Temperature	Ba (Å^2)	Ti-Ce (Å^2)	O (Å^2)	Ba (Å^2)	Ti-Ce (Å^2)	O (Å^2)	Ba (Å^2)	Ti-Ce (Å^2)	O (Å^2)
200 K	0.003	0.004	0.010	0.004	0.004	0.010	0.005	0.007	0.011
300 K	0.004	0.006	0.011	0.005	0.006	0.024	0.007	0.007	0.019
350 K	0.004	0.007	0.009	0.006	0.007	0.011	0.008	0.009	0.012
380 K	0.005	0.007	0.011	0.006	0.007	0.023	0.008	0.008	0.023
420 K	0.005	0.007	0.012	0.007	0.008	0.010	0.008	0.011	0.013

Table 6.22: BTC5 nano: Uiso values calculated in three different radius ranges for each temperature.

BTC10 Nano									
	Uiso refined over 1-10 Å			Uiso refined over 10-19 Å			Uiso refined over 19-28 Å		
Temperature	Ba (Å^2)	Ti-Ce (Å^2)	O (Å^2)	Ba (Å^2)	Ti-Ce (Å^2)	O (Å^2)	Ba (Å^2)	Ti-Ce (Å^2)	O (Å^2)
100 K	0.003	0.005	0.011	0.005	0.004	0.010	0.006	0.007	0.024
200 K	0.004	0.006	0.014	0.005	0.007	0.019	0.008	0.010	0.026
300 K	0.005	0.007	0.014	0.008	0.008	0.015	0.010	0.014	0.020
400 K	0.006	0.008	0.017	0.009	0.008	0.031	0.011	0.016	0.021

Table 6.23: BTC10 nano: Uiso values calculated in three different radius ranges for each temperature.

BTC20 Nano									
	Uiso refined over 1-10 Å			Uiso refined over 10-19 Å			Uiso refined over19-28 Å		
Temperature	Ba (Å^2)	Ti-Ce (Å^2)	O (Å^2)	Ba (Å^2)	Ti-Ce (Å^2)	O (Å^2)	Ba (Å^2)	Ti-Ce (Å^2)	O (Å^2)
100 K	0.005	0.007	0.017	0.009	0.009	0.029	0.020	0.025	0.065
200 K	0.005	0.008	0.016	0.011	0.011	0.035	0.021	0.026	0.067
300 K	0.007	0.007	0.020	0.012	0.012	0.033	0.023	0.027	0.069
400 K	0.008	0.008	0.022	0.012	0.013	0.029	0.024	0.028	0.071

Table 6.24: BTC20 nano: Uiso values calculated in three different radius ranges for each temperature.

In refinements Ti and Ce have been constrained to have equal Uiso parameters, because peaks in nano PDFs present broad shape then the independence of these two parameters had provoked meaningless values. However, looking tables, in most of the cases results are adequate for the investigated temperatures. Only parameters obtained for BTC20 between 19-28 Å, where refinements have been performed using cubic structure, show unusual high values. Comparison between these and those of BTC10 are reported in figure 6.15.

These unusual results for BTC20 are probably signal of a great disorder. Indeed, as previous mentioned, thermal vibration parameters are subjected to an increasing in their values in order to better fit broad peaks, whose width is actually due to the static rather than dynamic disorder. In this view results obtained are rather curious showing a contrast between the high symmetry used and the hidden disorder. Actually considered figure 6.16, where PDFs of different samples between 19 and 28 Å are reported, a good explanation is deducible. BTC20 presents very broad peaks, then recognize particulars is difficult and resolution is very low. Thus cubic structure, which presents less features than tetragonal, gives better fit, but, in order to improve it, Uiso values must be very

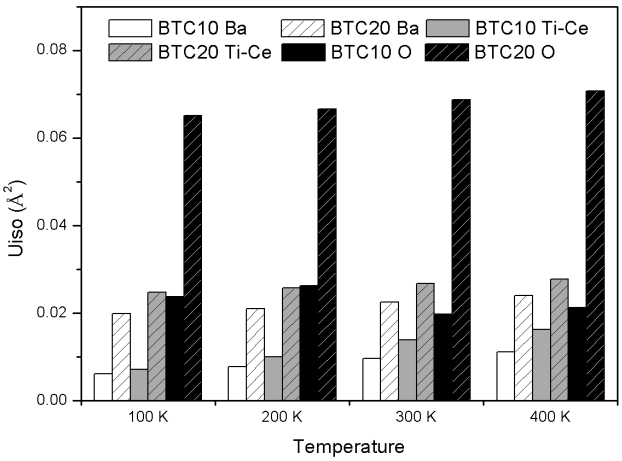

Figure 6.15: Uiso values obtained for nano samples of BTC10 and BTC20 calculated between 19 and 28 Å are shown.

high. Probably disorder in this sample is so deep that in a short range it is averaged giving a high symmetry, but where each peak is formed by a big bond lengths distribution. In next section this interpretation will be explained in more details giving a clearer description.

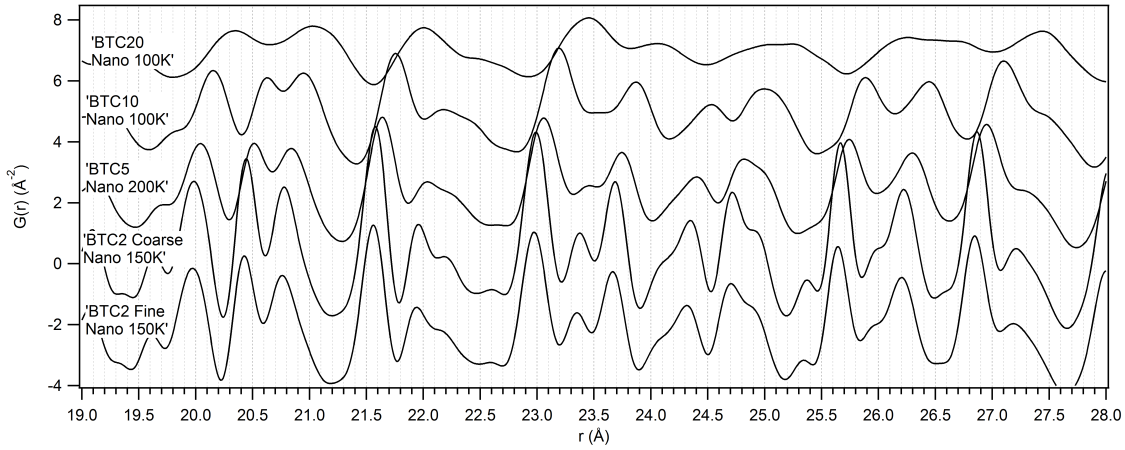

Figure 6.16: Comparison between PDFs of different samples at lowest temperature between 19 and 28 Å.

6.3 Nano powders vs. ceramic

As demonstrated before, reduction in particles size produces on the average structure a decrease in cell volumes in comparison to ceramics. Unfortunately no comparison between structural evolution is possible due to the large peak broadening for nano samples data. Despite the reduced information available on the average structure, a deeper discussion could be made on the local. In ceramic samples true local structures have been described as rhombohedric, whereas in nano size powders those have been defined as tetragonal.

In figure 6.17 comparison between PDFs of ceramic and nano materials is reported demonstrating a great similarity especially between 1 and 5 Å. Rhombohedric and tetragonal symmetries, chosen to model local structures, show actually little differences if calculated partials PDFs are considered, as reported in chapter 5. Thus one may wonder how these two so similar local arrangements could present two different structures, or how it is possible to distinguish correctly between two unit cells which present such a small difference. In this case the two different

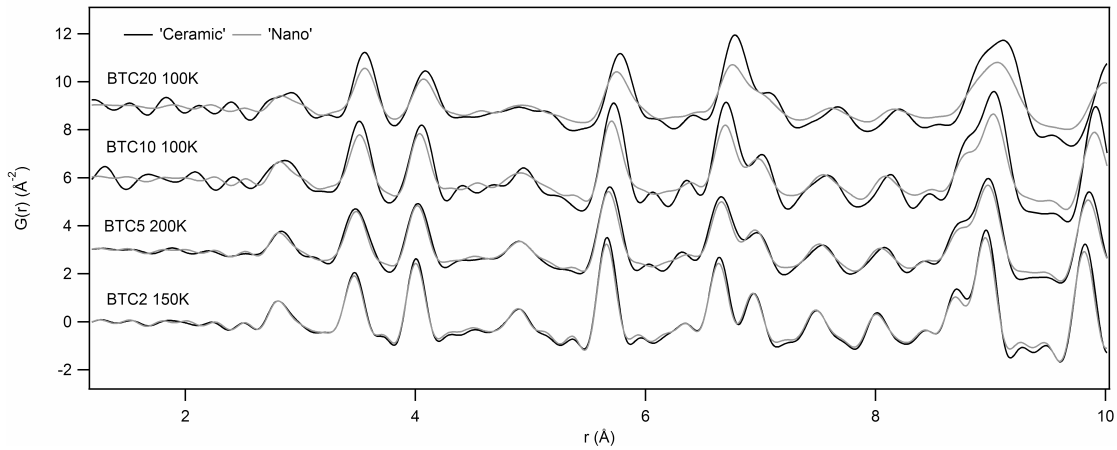

Figure 6.17: Comparison between nano and ceramic Pair Distribution Functions. Only PDFs at lowest temperatures are reported. Here BTC2 nano is used instead of BTC2 nano fine.

descriptions seem to be attributable to the following little detail. Peaks at $\sim$3.5 Å representing Ba-Ti and Ba-Ce are in the same position independently from the crystallite size, on the contrary peaks of Ba-Ba/Ti-Ti/Ti-Ce/Ce-Ce/O-O at $\sim$4 Å present a slight shift on the right hand side for all the ceramic samples, with respect to the correspondent nano ones. If this were to be attributed to a larger unit cell, both the cited peaks, in a tetragonal unit cell, should shift on the right hand side. Instead, in a rhombohedric symmetry, the peak at about 4 Å can be shifted on the right only by changing the angle of the rhombohedric unit cell. The two peaks in the nano samples are instead well described by a tetragonal unit cell. As noticeable by visual comparison samples with lowest cerium amount present a less disorder, presenting comparable nano and ceramic PDFs and similar to that of pure $BaTiO_3$ reported in bibliography (Yoneda et al. 2013) (and also in section 5.2). With doping increase peaks show broader shapes and this effect becomes more pronounced for nano materials. Then these two variables act as cooperative effects incrementing the local variations. Usually nano crystals are more disordered than their micro-sized equivalent then it is quite curious that, despite bigger broadening, BTCs nano present higher local symmetry than ceramics. This particularity could be explained if the coherent correlation length of structure is taken into account and considering that disorder in PDFs, even in the true local structure, represents an average of the correlations of all local variations of every single cell (Egami 2002). Probably in nano samples structural variations of each single cell are more conspicuous and more differentiated from each other than in ceramics. As consequence in the first case the true local structure will represent an average of many different deviations at cell level, the resulting signal (namely the PDF at low radius) will be then describable by a high symmetry, where however every peaks will be formed by a large distribution of bond distances. Differently in ceramics, cells are for sure distorted, but probably in similar way with each other. The average signal generated by so similar contributions will be then very representative of the disorder at cell level and then resulting structure will be present lower symmetry. Practically, despite the same radius range is considered, it is like to evaluate two different length scales. In figure 6.18 a graphical explanation of this concept is reported.

Projecting some knowledge acquired for ceramic samples to nano it becomes possible to make some final considerations. The two kinds of samples have local structures strongly affected by a disorder created by different bond lengths between Ti-O and Ce-O. The nonexistence of the first peaks suggests that the first coordination shell (for both cations) is disordered and formed by a broad distribution of lengths. However in case of nano materials the situation is more complicated due to the reduced grain size thus single cells should be more distorted with variations very different from each other. The true local structure, analysable by PDF, is then generated

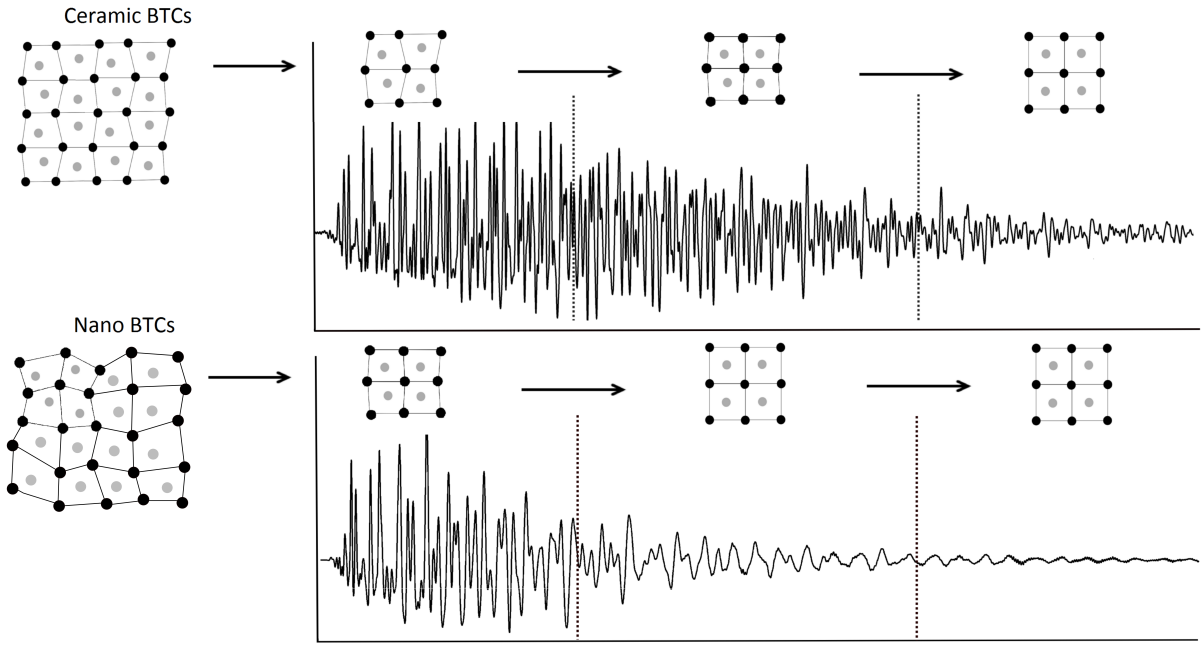

Figure 6.18: This sketch represents the evolution of local disorder in ceramic and nano BTCs. In nano materials structural variations in every single cells are more conspicuous then in ceramic then structure obtained by analysis of low radius range in G(r) results in a higher symmetry than in ceramics. This structure resulting actually by an average of each singles cells, which in nano materials are probably very different to one another. Taking into account increasing radius ranges structures determined are a version more and more averaged of the true local structure.

by an average of very different disorders which result in a higher symmetry than that in ceramic. This view is also applicable at different length scales, indeed in both types of BTC, samples with more local distortion (for ceramic this degree is evaluated by cell angles and for nano by tetragonal distortion parameters) present at the end less distorted average structure (which is the average structure for ceramic, whereas it is the structure calculated between 19-28 Å for the nano). Concluding cerium, as a function of its abundance, creates great distortions at single cells level limiting the titanium net displacements and resulting, on average, in a structure which approaches cubic symmetry. The size effect increase distortions reducing more local Ti movements, as demonstrating by figure 6.19 and at the same time accelerating, in terms of length scales, the appearance of an ordered structure. However, despite these indications, it is impossible to predict the correlations on a longer length scale of this displacements, so no sure previsions could be made on average structure and then on the polar behaviours of nano powders BTCs.

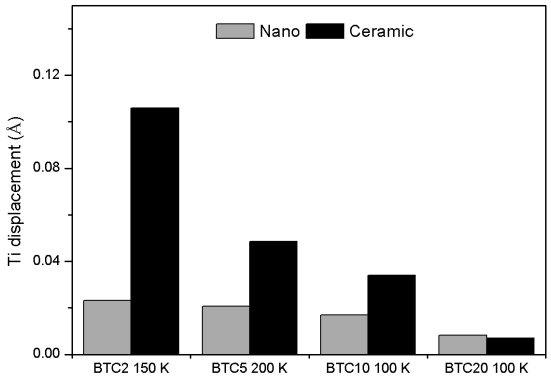

Figure 6.19: Ti displacements calculated for nano and ceramic samples, only results of lowest temperatures are reported. BTC2 nano is here used instead of BTC2 nano coarse. As noticeable Ti displacement in ceramic samples are more pronounced than in nano. Despite this comparison is useful, it is important to underlined that results for nano an BTC has been obtained in two different radius range: respectively 1-10 and 1-20 Å.

Chapter 7

Conclusions

In this chapter conclusions will be presented starting from the description of the effect of cerium introduction in ceramic $BaTiO_3$ as a function of the temperature and then they will proceed illustrating the consequences of the grain size reduction.

The suitability of BTC ceramic preparation has been proved by different investigations. The right stoichiometry has been verified by diffraction high resolution data which have demonstrated practically no impurities and by the refinements of Ti and Ce occupancies. Ceramic samples show a good agreement with the so called Vegard's law demonstrating to be near to ideal solid solutions, the chemical homogeneity has been also shown by microprobe and TEM investigations. Raman spectroscopy has verified the incorporation of Ce^{4+} at Ti site, despite very little amount of Ce^{3+} could be present in samples with lowest doping. On the average, solid solutions with lowest cerium amount, BTC doped by 2 and 5 %, present, as a function of the temperature, normal ferroelectric transitions. From the structural point of view this means a sequence, as temperature lowers, from paraelectric cubic structure to tetragonal, orthorhombic and rhombohedric. In samples with more cerium, such as BTC10, which are characterized by diffuse phase transition polar behaviour, a direct transition from cubic to rhombohedric structure has been determined. Ceramic BTC20 shows relaxor behaviour with transition to a phase with long range polar order below 200 K. The relaxor behaviour in sample BTC30 has been structurally confirmed by the maintenance of cubic average structure at all the temperatures. Some uncertainties in structural identifications by diffraction data, especially for BTC5, has been solved by Raman temperature dependent spectroscopy, indeed phase transitions in these materials do not occur at precise temperatures, but they are rather diffuse in broad temperature ranges. Phase stabilities determined during the present research show good agreement with those expected by dielectric measurements. Furthermore it has been confirmed that increasing cerium amount causes a lowering of the Curie temperature related to paraelectric-ferroelectric transition up to provoke its disappearance in relaxor type BTC. In addition the doping increase is linked to an increment on cell volumes, but, at the same time, to a decrease of B cations displacements. Moreover the big size of cerium atoms generates a great stress which is minimized with the creation of structural defects, as the high density dislocations detected by TEM investigations, residual strain and local disorder. Indeed it is in the local structure that cerium introduction powerfully shows its effect. In all samples Ti-O and Ce-O octahedra are locally so distorted, which such a large difference in B-O bond lengths that the first related PDF peaks are so weak and so broad that they are not distinguishable from the termination ripples. This missing information has strongly complicated the structural modeling. In general all the local structures present lower symmetries in comparison to the relative average structures. The degree of this local disorder is linked to the cerium amount. Indeed the local structure for BTC2, at all the temperatures, has been described by a simple rhombohedric structure, while other BTC with x > 0.02 have required more disordered an

complicate models, based anyway on a rhombohedric cell. In these samples local structural disorder is mainly ascribed to oxygen positions rather than to a particular B cation order, which has been defined and cerium has been verified to be homogeneously distributed. Taking into account these considerations a final model to describe local structure has been conceived. Cerium provokes a tilt of its oxygen cage, as occur in pure $BaCeO_3$, trying to maintain distances as long as possible. This creates contra rotations of the other octahedra, containing titanium atoms, close to it and distortions of Ti-O cages with distances approaching those in pure $BaTiO_3$. When the cerium content is larger, a larger number of TiO_6 octahedra are involved in this mechanism, and a larger degree of disorder is generated. This solution is able to represents adequately local disorders, especially from the second coordination shells, furnishing a new point of view on these materials. The strong point of this model is the introduction at local level of a kind of distortion, octahedra tilts, which is related only to $BaCeO_3$, but actually is not permitted in pure $BaTiO_3$. This allows to take into account the normal cerium atomic environment and insert it in a barium titanate matrix which must rearrange to minimized the induced strain. Despite very good results and the new approach, this model remain unsuitable to truly describe the first Ti-O Ce-O coordination shells. However, by results obtained, this distortion mechanism, caused by the difference size of the two B cations and of barium and cerium, seems to have important consequences also on local titanium displacements. Indeed their net value along the body diagonal of the rhombohedric cell diminish as doping increases. Probably titanium atoms, due to the distortions of their octahedra, are then forced to move not in just one direction, but can go off-center in different ways, as indicated by RMC analysis. This is possible because, despite different doping amounts, TiO_6 cages preserve more or less their volumes. If cerium is low the number of octahedra strongly distorted and tilted are less, then correlation of displacements is more probable. In more doped samples, instead, every single titanium probably moves differently and at the end their local net value is practically zero. Connecting these results on the local structure to those obtained on the average one, it seems that the larger the doping amount the more the local structure is distorted resulting in an average structure which will present higher symmetries. Then local disorder reduces the range of the structural coherent correlation length accelerating the perception of an average order. This last consideration is supported also by results obtained by nano size BTC. Here, in addition to cerium doping, also the contribution of size must be considered. On the average structure reduced size causes a decrease in cell volumes. However it has not been possible to calculate definitively the relative consequences on the domain sizes and microstrain. On the local structure once again first Ti-O and Ce-O bond distances are completely undetectable. All samples present a tetragonal local symmetry, but as cerium content increases, the degree of distortion of the local structure increases proportionally. The size effect seems to provoke a more pronounced diversification of each cell, probably due also to the larger number of surface atoms and bonds. This disorder is averaged giving the actual local structure observable in PDFs. Thank to this, the cumulative signal appears in one hand describable by higher symmetries than in ceramics, precisely by a tetragonal symmetry, and presenting more limited Ti displacements, but, on the other, this structure is originated by a broad distribution of bond lengths. Thus, in comparison to the only cerium introduction effect, the combination of this with the size reduction influences more the scale of the coherent structural correlation diminishing further the short range order which is averaged very faster giving rapidly the perception of an averaged ordered structure. However these considerations are proper for the local/medium structure, and remain true only at this investigation scale, it is indeed impossible to translate this last information on the average structure predicting the polar behaviour of the BTC nano powders.

Chapter 8

Appendix

In appendix supplementary results are reported:

- Ceramic: results of Rietveld refinements (subsection 5.1.1)
- Ceramic: results of Rietveld refinements where B cation occupancies are refined (subsection 5.1.1)
- Ceramic: results of PDF average refinements (subsection 5.1.2)
- Ceramic: results of PDF local refinements by simple approach (section 5.2)
- Ceramic: final tilted structure used to fit local structure (subsection 5.2.2)
- Nano Powders: carbox refinements (section 6.2)
- Ceramic: supplementary characterization technique (single crystal)

Ceramic: Rietveld refinements BTC2

BTC2	a (Å)	b (Å)	c (Å)	Angle (°)	Volume (Å^3)	Crystallite Size (Å)	Microstrain		
150 K	4.013852(2)			89.8667 (2)	64.67	3223(20)	0.0004883(2)		
270 K									
350 K	4.01067(2)		4.03505(3)	90	64.91	3349(1)	0.000469(2)		
450 K	4.02114(6)			90	65.02	5136(21)	0.000219(1)		
	Biso Ba (Å^2)	Biso Ti-Ce (Å^2)	Biso O (Å^2)	Ti x	Ti z	O1 x	O1 z	O2 x	O2 z
150 K	0.190(6)	0.22(2)	0.93(6)	0.4896(6)		0.515(2)	0.012(3)		
270 K									
350 K	0.352(9)	0.44(3)	1.11(8)		0.510(2)		-0.04(3)		0.480(4)
450 K	0.503(6)	0.83(1)	1.06(4)						

Table 8.1: Results of diffraction data analysis: $BaTi_{0.98}Ce_{0.02}O_3$ at different temperatures.

BTC2	a (Å)	b (Å)	c (Å)	Angle (°)	Crystallite Size (Å)	Microstrain	Biso Ba (Å^2)	Biso Ti-Ce (Å^2)	Biso O (Å^2)
150 K	4.013853(2)			89.8667 (2)	3220(4)	0.000488(2)	0.182(7)	0.31(2)	0.83(7)
270 K	4.0076(3)	5.68425(4)	5.69892(4)		2904(14)	0.0005200(4)	0.256(9)	0.50(3)	1.1(1)
350 K	4.01069(2)		4.03506(3)		3368(27)	0.0004725(3)	0.33(1)	0.68(4)	1.00(8)
450 K	4.02114(6)				5134(21)	0.000219(1)	0.508(6)	0.78(2)	1.08(4)
	Ti occupancy	Ti x	Ti z	O1 x	O1 z	O2 x	O2 z		
150 K	0.985(3)	0.4892(6)		0.519(2)	0.004(3)				
270 K	0.98(2)		0.510(1)		0.481(4)	0.264(4)	0.252(4)		
350 K	0.968(3)		0.511(2)		-0.035(3)		0.475(4)		
450 K	0.988(1)								

Table 8.2: Results of diffraction data analysis: $BaTi_{0.98}Ce_{0.02}O_3$ at different temperatures. B cation occupancy has been refined.

Ceramic: Rietveld refinements BTC5

BTC5	a (Å)	b (Å)	c (Å)	Angle (°)	Volume (Å^3)	Crystallite Size (Å)	Microstrain		
200 K	4.02849(1)			89.8858(2)	65.38	2801(12)	0.000640(2)		
300 K	4.03104(2)			89.999(8)	65.5	2981(20)	0.001066(3)		
350 K	4.02826(1)		4.03952(2)	90	65.55	3052.5(8)	0.000650(2)		
380 K	4.03123(1)		4.03544(2)	90	65.58	2989(10)	0.000373(2)		
420 K	4.034492(7)			90	65.67	3211(1)	0.000359(1)		
	Biso Ba (Å^2)	Biso Ti-Ce (Å^2)	Biso O (Å^2)	Ti x	Ti z	O1 x	O1 z	O2 x	O2 z
200 K	0.280(3)	0.48(1)	0.81(3)	0.4928(5)		0.516(1)	0.016(2)		
300 K	0.50(1)	0.19(5)	1.01(1)	0.489(2)		0.506(5)	0.031(2)		
350 K	0.547(4)	0.46(1)	1.23(4)		0.502(4)		-0.040(2)		0.50(1)
380 K	0.655(5)	0.53(2)	1.02(5)		0.509(2)		-0.047(2)		0.489(6)
420 K	0.668(4)	0.95(1)	1.31(1)						

Table 8.3: Results of diffraction data analysis: $BaTi_{0.95}Ce_{0.05}O_3$ at different temperatures.

BTC5	a (Å)	b (Å)	c (Å)	Angle (°)	Crystallite Size (Å)	Microstrain	Biso Ba (Å^2)	Biso Ti-Ce (Å^2)	Biso O (Å^2)
200 K	4.02849(1)			89.8858(2)	2801(12)	0.000640(2)	0.289(3)	0.43(1)	0.82(4)
300 K	4.03103(2)			89.995(5)	3050(19)	0.001064(2)	0.43(2)	0.5(1)	1.0(3)
350 K	4.02826(1)		4.03952(2)		3026(11)	0.000650(2)	0.508(4)	0.75(1)	1.16(4)
380 K	4.03123(1)		4.03544(2)		2977(11)	0.000375(2)	0.615(5)	0.80(2)	0.87(6)
420 K	4.034492(7)				3208(10)	0.000359(1)	0.668(4)	0.89(1)	1.33(3)
	Ti occupancy	Ti x	Ti z	O1 x	O1 z	O2 x	O2 z		
200 K	0.961(1)	0.4931(5)		0.514(1)	0.020(2)				
300 K	0.954(2)	0.489(4)		0.514(7)	-0.020(8)				
350 K	0.955(1)		0.502(4)		-0.032(2)		0.507(5)		
380 K			0.506(3)		-0.040(3)		0.522(3)		
420 K	0.960(1)								

Table 8.4: Results of diffraction data analysis: $BaTi_{0.95}Ce_{0.05}O_3$ at different temperatures. B cation occupancy has been refined.

Cermic: Rietveld refinements BTC10

BTC10	a (Å)	b (Å)	c (Å)	Angle (°)	Volume (Å^3)	Crystallite Size (Å)	Microstrain		
100 K	4.04856(1)			89.8740(2)	66.36	2567(10)	0.000753(1)		
200 K	4.05107(1)			89.8896(2)	66.48	2580(10)	0.000738(2)		
300 K	4.05397(1)			90.020(1)	66.63	2635(11)	0.0009066(4)		
400 K	4.05672(1)			66.76	2654(7)	0.0005483(2)			
	Biso Ba (Å^2)	Biso Ti-Ce (Å^2)	Biso O (Å^2)	Ti x	Ti z	O1 x	O1 z	O2 x	O2 z
100 K	0.261(3)	0.47(1)	0.80(4)	0.4944(5)		0.512(1)	0.025(1)		
200 K	0.433(4)	0.63(1)	0.98(1)	0.4959(8)		0.514(1)	0.025(1)		
300 K	0.579(6)	0.70(3)	0.7(1)	0.494(2)		0.484(2)	0.031(2)		
400 K	0.774(4)	0.99(1)	1.55(3)						

Table 8.5: Results of diffraction data analysis: $BaTi_{0.9}Ce_{0.1}O_3$ at different temperatures.

BTC10	a (Å)	b (Å)	c (Å)	Angle (°)	Crystallite Size (Å)	Microstrain	Biso Ba (Å^2)	Biso Ti-Ce (Å^2)	Biso O (Å^2)
100 K	4.04856(1)			89.8740(2)	2567(1)	0.000753(1)	0.273(3)	0.50(1)	0.80(4)
200 K	4.05107(1)			89.8896(2)	2577(10)	0.000737(2)	0.450(4)	0.55(1)	0.98(4)
300 K	4.05397(1)			90.020(1)	2622(11)	0.0009055(4)	0.588(8)	0.64(4)	1.1(1)
400 K	4.05672(1)				2651(10)	0.000548(2)	0.790(5)	0.90(1)	1.58(3)
	Ti occupancy	Ti x	Ti z	O1 x	O1 z	O2 x	O2 z		
100 K	0.914(1)	0.4948(6)		0.512(1)	0.027(1)				
200 K	0.916(1)	0.4960(8)		0.512(1)	0.028(1)				
300 K	0.909(1)	0.493(2)		0.492(3)	0.028(2)				
400 K	0.915(1)								

Table 8.6: Results of diffraction data analysis: $BaTi_{0.9}Ce_{0.1}O_3$ at different temperatures. B cation occupancy has been refined.

Ceramic: Rietveld refinements BTC20

BTC20	a (Å)	b (Å)	c (Å)	Angle (°)	Volume (Å^3)	Crystallite Size (Å)	Microstrain		
100 K	4.09255(1)			89.957(1)	68.55	2664(10)	0.001083(3)		
200 K	4.09513(1)			90	68.68	2501(10)	0.000947(2)		
300 K	4.09814(1)			90	68.83	2555(8)	0.000915(1)		
400 K	4.10164(1)			90	69	2580(10)	0.000907(2)		
	Biso Ba (Å^2)	Biso Ti-Ce (Å^2)	Biso O (Å^2)	Ti x	Ti z	O1 x	O1 z	O2 x	O2 z
100 K	0.443(4)	0.55(2)	0.57(8)	0.496(1)		0.487(1)	0.035(1)		
200 K	0.632(4)	0.761(7)	1.59(3)						
300 K	0.779(4)	0.862(7)	1.74(3)						
400 K	0.947(5)	0.987(9)	1.97(3)						

Table 8.7: Results of diffraction data analysis: $BaTi_{0.8}Ce_{0.2}O_3$ at different temperatures.

BTC20	a (Å)	b (Å)	c (Å)	Angle (°)	Crystallite Size (Å)	Microstrain	Biso Ba (Å^2)	Biso Ti-Ce (Å^2)	Biso O (Å^2)
100 K	4.09255(1)			89.957(1)	2664(3)	0.001080(3)	0.455(5)	0.50(1)	0.9(6)
200 K	4.09513(1)				2493(7)	0.0009474(6)	0.660(4)	0.67(1)	1.64(3)
300 K	4.09814(1)				2544(8)	0.00091(2)	0.807(5)	0.774(9)	1.80(3)
400 K	4.10164(5)				2574(10)	0.000906(2)	0.980(5)	0.88(1)	2.04(3)
	Ti occupancy	Ti x	Ti z	O1 x	O1 z	O2 x	O2 z		
100 K	0.800(2)	0.497(1)		0.498(2)	0.033(1)				
200 K	0.818(1)								
300 K	0.807(5)								
400 K	0.818(1)								

Table 8.8: Results of diffraction data analysis: $BaTi_{0.8}Ce_{0.2}O_3$ at different temperatures. B cation occupancy has been refined.

Ceramic: Rietveld refinements BTC30

BTC30	a (Å)	b (Å)	c (Å)	Angle (°)	Volume (Å^3)	Crystallite Size (Å)	Microstrain		
100 K	4.1346(2)				70.68	561(7)	0.00257(5)		
200 K	4.13711(6)			90	70.81	560(8)	0.00259(4)		
300 K	4.14035(6)			90	70.98	549(8)	0.00264(4)		
400 K	4.14385(6)			90	71.16	539(7)	0.00267(4)		
	Biso Ba (Å^2)	Biso Ti-Ce (Å^2)	Biso O (Å^2)	Ti x	Ti z	O1 x	O1 z	O2 x	O2 z
100 K	0.053(2)	0.83(3)	3.3(1)						
200 K	0.19(2)	0.91(3)	3.5(1)						
300 K	0.33(2)	1.00(3)	3.74(1)						
400 K	0.48(2)	1.1(3)	4.0(1)						

Table 8.9: Results of diffraction data analysis: $BaTi_{0.7}Ce_{0.3}O_3$ at different temperatures. Microstrain and crystallite size are not reliable results due to the problems during the data collection

Ceramic: PDF average analysis

BTC5	a (Å)	b (Å)	c (Å)	Angle (°)	Uiso Ba (^{2})	Uiso Ti-Ce (Å^2)	Uiso O (Å^2)
200 K	4.0288(5)			89.880(5)	0.006(5)	0.009(5)	0.022(5)
300 K	4.0311(5)			89.946(5)	0.010(5)	0.011(5)	0.027(5)
350 K	4.0283(5)		4.0395(5)	90	0.009(5)	0.014(5)	0.018(5)
380 K	4.0328(5)		4.0360(2)	90	0.010(5)	0.011(5)	0.015(5)
420 K	4.0346(5)			90	0.009(5)	0.014(5)	0.030(5)
	Ti x	Ti z	O1 x	O1 z	O2 x	O2 z	
200 K	0.488(5)		0.52(5)	0.03(5)			
300 K	0.486(5)		0.52(5)	0.03(5)			
350 K		0.511(5)		0.12(5)		0.50(5)	
380 K		0.525(5)		0.11(5)		0.52(5)	
420 K							

Table 8.10: Results of PDF average analysis: $BaTi_{0.95}Ce_{0.05}O_3$ at different temperatures.

BTC10	a (Å)	b (Å)	c (Å)	Angle (°)	Uiso Ba (Å^2)	Uiso Ti-Ce (Å^2)	Uiso O (Å^2)
100 K	4.0487(5)			89.866(5)	0.006(5)	0.009(5)	0.023(5)
200 K	4.0512(5)			89.892(5)	0.009(5)	0.011(5)	0.027(5)
300 K	4.0541(5)			89.974(5)	0.011(5)	0.011(5)	0.032(5)
400 K	4.0569(5)			90	0.011(5)	0.015(5)	0.035(5)
	Ti x	Ti z	O1 x	O1 z	O2 x	O2 z	
100 K	0.490(5)		0.52(5)	0.03(5)			
200 K	0.490(5)		0.52(5)	0.03(5)			
300 K	0.490(5)		0.51(5)	0.02(5)			
400 K							

Table 8.11: Results of PDF average analysis: $BaTi_{0.9}Ce_{0.1}O_3$ at different temperatures.

BTC20	a (Å)	b (Å)	c (Å)	Angle (°)	Uiso Ba (Å^2)	Uiso Ti-Ce (Å^2)	Uiso O (Å^2)
100 K	4.0925(5)			89.921(5)	0.009(5)	0.012(5)	0.029(5)
200 K	4.0950(5)			90	0.011(5)	0.015(5)	0.038(5)
300 K	4.0980(5)			90	0.013(5)	0.016(5)	0.040(5)
400 K	4.1015(5)			90	0.014(5)	0.017(5)	0.043(5)
	Ti x	Ti z	O1 x	O1 z	O2 x	O2 z	
100 K	0.497(5)		0.51(5)	0.03(5)			
200 K							
300 K							
400 K							

Table 8.12: Results of PDF average analysis: $BaTi_{0.8}Ce_{0.2}O_3$ at different temperatures.

Ceramic: PDF local analysis using simple approach: 10-20 Å

BTC2	a (Å)	Angle (°)	Ti x	Ce x	O1 x	O1 z
150 K	4.0090	89.959	0.515	0.507	0.48	0.03
270 K	4.0111	89.988	0.516	0.514	0.48	0.03
350 K	4.0129	89.842	0.515	0.505	0.47	-0.03
450 K	4.0173	89.773	0.514	0.517	0.47	-0.03

Table 8.13: Results of PDF local analysis: $BaTi_{0.98}Ce_{0.02}O_3$ at different temperatures (errors are not reported). Simplest approach has been used consisting in a classical rhombhoedric cell with Ti and Ce considered as independent, but constrained by fractional occupancies.

BTC5	a (Å)	Angle (°)	Ti x	Ce x	O1 x	O1 z
200 K	4.0297	89.734	0.514	0.496	0.48	-0.03
300 K	4.0322	89.762	0.514	0.500	0.48	-0.03
350 K	4.0338	89.621	0.514	0.495	0.47	-0.01
380 K	4.0338	89.721	0.514	0.496	0.47	-0.02
420 K	4.0362	89.597	0.514	0.494	0.47	0.00

Table 8.14: Results of PDF local analysis: $BaTi_{0.95}Ce_{0.05}O_3$ at different temperatures (errors are not reported). Simplest approach has been used consisting in a classical rhombhoedric cell with Ti and Ce considered as independent, but constrained by fractional occupancies.

BTC10	a (Å)	Angle (°)	Ti x	Ce x	O1 x	O1 z
100 K	4.0496	89.722	0.493	0.472	0.52	0.03
200 K	4.0522	89.682	0.492	0.475	0.53	0.02
300 K	4.0555	89.561	0.493	0.477	0.53	0.01
400 K	4.0584	89.505	0.494	0.474	0.53	0.01

Table 8.15: Results of PDF local analysis: $BaTi_{0.9}Ce_{0.1}O_3$ at different temperatures (errors are not reported). Simplest approach has been used consisting in a classical rhombhoedric cell with Ti and Ce considered as independent, but constrained by fractional occupancies.

BTC20	a (Å)	Angle (°)	Ti x	Ce x	O1 x	O1 z
100 K	4.0903	90.529	0.504	0.475	0.47	0.00
200 K	4.0931	90.571	0.503	0.472	0.47	-0.01
300 K	4.0960	90.591	0.496	0.462	0.47	0.00
400 K	4.1000	90.598	0.500	0.471	0.47	0.00

Table 8.16: Results of PDF local analysis: $BaTi_{0.8}Ce_{0.2}O_3$ at different temperatures (errors are not reported). Simplest approach has been used consisting in a classical rhombhoedric cell with Ti and Ce considered as independent, but constrained by fractional occupancies.

BTC30	a (Å)	Angle (°)	Ti x	Ce x	O1 x	O1 z
100 K	4.1271	90.612	0.494	0.516	0.53	0.00
200 K	4.1300	90.640	0.493	0.514	0.53	0.00
300 K	4.1334	90.667	0.491	0.514	0.53	0.00
400 K	4.1370	90.692	0.491	0.515	0.53	0.00

Table 8.17: Results of PDF local analysis: $BaTi_{0.7}Ce_{0.3}O_3$ at different temperatures (errors are not reported). Simplest approach has been used consisting in a classical rhombhoedric cell with Ti and Ce considered as independent, but constrained by fractional occupancies.

Ceramic: final tilted structure used to fit local structure

BTC5	a (Å)	Angle (°)	Ce x	Ti x	O1 x	O1 z	O2 x	O2 z
200 K	4.0299	89.602	0.5	0.507	0.441	-0.063	0.498	-0.032
300 K	4.0322	89.691	0.5	0.509	0.434	-0.074	0.496	-0.034
350 K	4.0333	89.607	0.5	0.507	0.438	-0.060	0.487	-0.031
380 K	4.0340	89.608	0.5	0.507	0.439	-0.062	0.483	-0.033
420 K	4.0355	89.583	0.5	0.507	0.439	-0.054	0.477	-0.031
	O3x	O3z	Uiso Ba ($Å^2$)	Uiso Ti ($Å^2$)	Uiso Ce ($Å^2$)	Uiso O ($Å^2$)		
200 K	0.517	0.234671	0.003	0.006	0.005	0.006		
300 K	0.515	0.233229	0.005	0.007	0.007	0.007		
350 K	0.492	0.242969	0.005	0.008	0.009	0.008		
380 K	0.500	0.210217	0.006	0.007	0.008	0.008		
420 K	0.500	0.199841	0.006	0.009	0.009	0.009		

Table 8.18: Tilted local structure for BTC5. Three groups of oxygens have been used.

BTC10	a (Å)	Angle (°)	Ce x	Ti x	O1 x	O1 z	O2 x	O2 z
100 K	4.0494	89.587	0.5	0.505	0.538	0.000	0.498	-0.028
200 K	4.0522	89.543	0.5	0.507	0.537	0.000	0.497	-0.035
300 K	4.0551	89.502	0.5	0.506	0.538	0.000	0.498	-0.034
400 K	4.0580	89.450	0.5	0.508	0.535	0.000	0.485	-0.039
	Uiso Ba ($Å^2$)	Uiso Ti ($Å^2$)	Uiso Ce ($Å^2$)	Uiso O ($Å^2$)				
100 K	0.003	0.005	0.009	0.014				
200 K	0.004	0.006	0.008	0.015				
300 K	0.005	0.008	0.009	0.015				
400 K	0.006	0.008	0.009	0.015				

Table 8.19: Tilted local structure for BTC10. Two groups of oxygens have been used.

BTC20	a (Å)	Angle (°)	Ce x	Ti x	O1 x	O1 z	O2 x	O2 z
100 K	4.0945	89.450	0.5	0.499	0.559	0.000	0.506	-0.025
200 K	4.0970	89.413	0.5	0.499	0.554	0.000	0.501	-0.026
300 K	4.1002	89.392	0.5	0.501	0.550	0.000	0.499	-0.028
400 K	4.1037	89.369	0.5	0.501	0.549	0.000	0.499	-0.030
	Uiso Ba ($Å^2$)	Uiso Ti ($Å^2$)	Uiso Ce ($Å^2$)	Uiso O ($Å^2$)				
100 K	0.004	0.004	0.010	0.011				
200 K	0.005	0.006	0.007	0.010				
300 K	0.007	0.007	0.010	0.011				
400 K	0.008	0.007	0.009	0.012				

Table 8.20: Tilted local structure for BTC20. Two groups of oxygens have been used.

BTC30	a (Å)	Angle (°)	Ce x	Ti x	O1 x	O1 z
100 K	4.132	89.403	0.5	0.501	0.486	-0.041
200 K	4.134	89.393	0.5	0.501	0.479	-0.036
300 K	4.137	89.375	0.5	0.499	0.475	-0.028
400 K	4.141	89.331	0.5	0.501	0.467	-0.009
	Uiso Ba ($Å^2$)	Uiso Ti ($Å^2$)	Uiso Ce ($Å^2$)	Uiso O ($Å^2$)		
100 K	0.005	0.004	0.009	0.016		
200 K	0.007	0.004	0.012	0.017		
300 K	0.008	0.007	0.010	0.018		
400 K	0.009	0.007	0.010	0.016		

Table 8.21: Tilted local structure for BTC30.

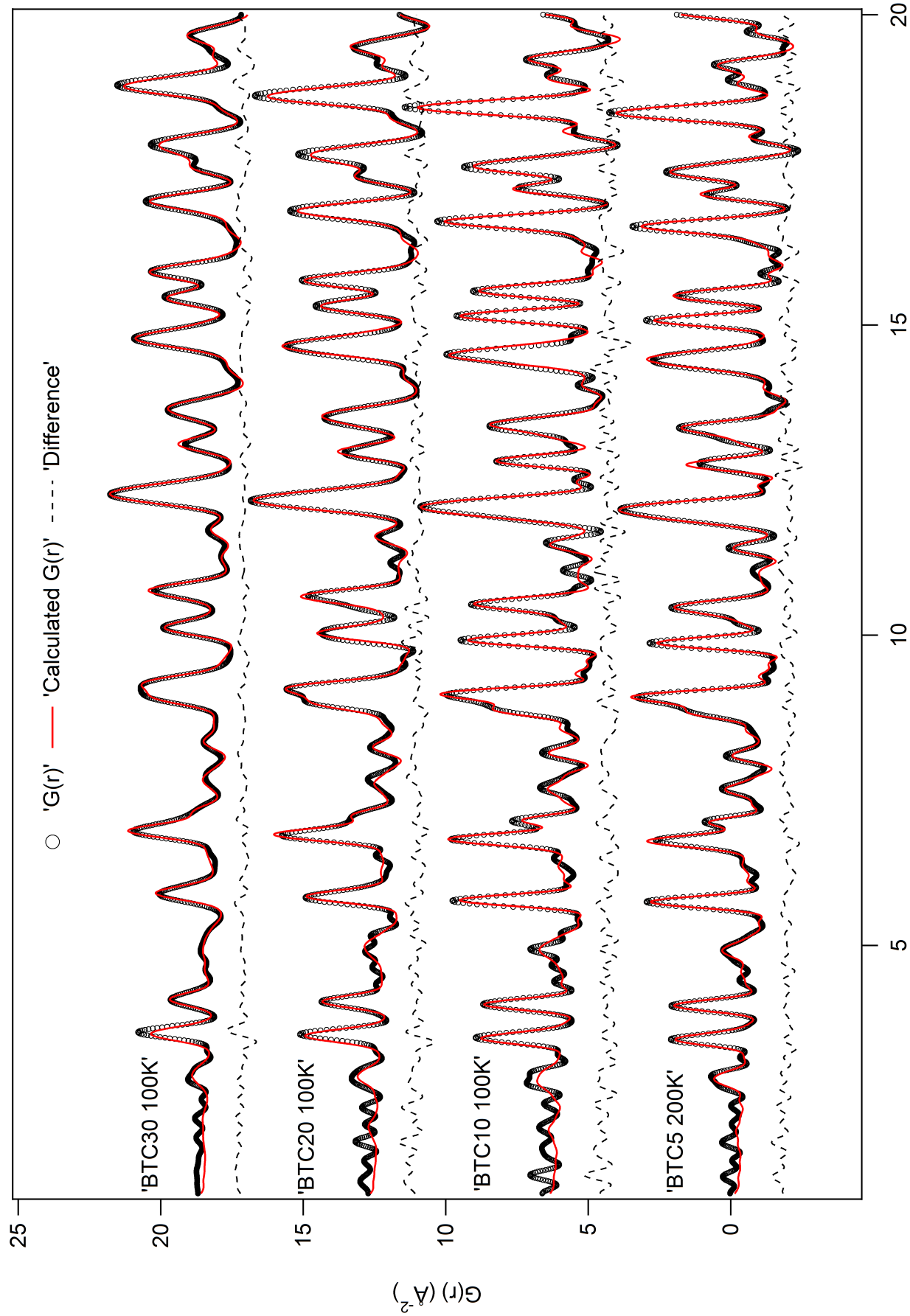

Figure 8.1: Fits of different BTCs at lowest temperatures obtained using final structural model (tilted structure with Ti displacements).

Nano Powders: carbox refinements

BTC2 Nano Fine										
	Range (Å)	a (Å)	c (Å)	Ti z	Ce z	O1 z	O2 z	Uiso Ba (Å^2)	Uiso Ti-Ce (Å^2)	Uiso O (Å^2)
150 K	1-10	3.995	4.029	0.520	0.576	0.114	0.493	0.002	0.003	0.009
150 K	10-19	3.998	4.026	0.516	0.530	0.116	0.491	0.002	0.005	0.010
150 K	19-28	4.001	4.021	0.521	0.532	0.138	0.491	0.003	0.004	0.010
270 K	1-10	3.995	4.040	0.482	0.483	-0.115	0.514	0.003	0.005	0.009
270 K	10-19	4.002	4.031	0.486	0.501	-0.123	0.520	0.003	0.007	0.009
270 K	19-28	4.003	4.028	0.519	0.512	0.120	0.485	0.005	0.006	0.009
350 K	1-10	4.003	4.029	0.478	0.504	-0.074	0.529	0.004	0.006	0.011
350 K	10-19	4.003	4.030	0.487	0.508	-0.079	0.501	0.005	0.008	0.015
350 K	19-28	4.004	4.026	0.484	0.529	-0.131	0.516	0.006	0.008	0.010
450 K	1-10	3.999	4.042	0.489	0.538	0.079	0.513	0.004	0.009	0.017
450 K	10-19	4.006	4.033	0.484	0.544	0.060	0.493	0.005	0.008	0.014
450 K	19-28	4.009	4.026	0.475	0.541	-0.006	0.529	0.007	0.007	0.018

Table 8.22: BTC2 Nano Fine: local structural refinements by carbox approach.

BTC2 Nano Coarse										
	Range (Å)	a (Å)	c (Å)	Ti z	Ce z	O1 z	O2 z	Uiso Ba (Å^2)	Uiso Ti-Ce (Å^2)	Uiso O (Å^2)
150 K	1-10	3.999	4.028	0.523	0.521	0.112	0.490	0.002	0.003	0.012
150 K	10-19	4.006	4.017	0.514	0.510	0.127	0.481	0.002	0.005	0.009
150 K	19-28	4.008	4.013	0.527	0.523	0.144	0.488	0.003	0.002	0.008
270 K	1-10	3.998	4.038	0.517	0.504	0.112	0.482	0.003	0.005	0.009
270 K	10-19	4.006	4.026	0.515	0.509	0.122	0.480	0.004	0.007	0.010
270 K	19-28	4.005	4.027	0.520	0.501	0.031	0.480	0.004	0.007	0.014
350 K	1-10	4.008	4.025	0.520	0.498	0.109	0.480	0.004	0.005	0.010
350 K	10-19	4.006	4.030	0.520	0.496	0.033	0.471	0.005	0.007	0.018
350 K	19-28	4.009	4.024	0.492	0.544	0.139	0.513	0.005	0.011	0.010
450 K	1-10	4.001	4.047	0.513	0.492	0.080	0.470	0.005	0.008	0.014
450 K	10-19	4.014	4.023	0.529	0.502	0.016	0.459	0.007	0.006	0.016
450 K	19-28	4.015	4.021	0.477	0.443	-0.014	0.534	0.007	0.007	0.014

Table 8.23: BTC2 Nano Coarse: local structural refinements by carbox approach.

BTC5 Nano										
	Range (Å)	a (Å)	c (Å)	Ti z	Ce z	O1 z	O2 z	Uiso Ba ($Å^2$)	Uiso Ti-Ce ($Å^2$)	Uiso O ($Å^2$)
200 K	1-10	4.008	4.047	0.521	0.508	0.110	0.490	0.003	0.004	0.010
200 K	10-19	4.021	4.028	0.523	0.554	0.121	0.479	0.004	0.004	0.010
200 K	19-28	4.017	4.037	0.522	0.491	-0.124	0.488	0.005	0.007	0.011
300 K	1-10	4.008	4.058	0.516	0.507	0.111	0.482	0.004	0.006	0.011
300 K	10-19	4.017	4.046	0.481	0.466	0.035	0.534	0.005	0.006	0.024
300 K	19-28	4.020	4.042	0.479	0.440	0.007	0.544	0.007	0.007	0.019
350 K	1-10	4.012	4.056	0.512	0.479	0.117	0.478	0.004	0.007	0.009
350 K	10-19	4.020	4.047	0.508	0.578	0.128	0.482	0.006	0.007	0.011
350 K	19-28	4.021	4.042	0.521	0.552	0.115	0.481	0.008	0.009	0.012
380 K	1-10	4.013	4.056	0.514	0.510	0.110	0.479	0.005	0.007	0.011
380 K	10-19	4.019	4.051	0.475	0.508	0.006	0.530	0.006	0.007	0.023
380 K	19-28	4.021	4.046	0.520	0.555	-0.025	0.530	0.008	0.008	0.023
420 K	1-10	4.019	4.048	0.514	0.510	0.112	0.480	0.005	0.007	0.012
420 K	10-19	4.026	4.040	0.525	0.493	0.123	0.480	0.007	0.008	0.010
420 K	19-28	4.024	4.040	0.515	0.535	-0.118	0.500	0.008	0.011	0.013

Table 8.24: BTC5 Nano: local structural refinements by carbox approach.

BTC10 Nano										
	Range (Å)	a (Å)	c (Å)	Ti z	Ce z	O1 z	O2 z	Uiso Ba ($Å^2$)	Uiso Ti-Ce ($Å^2$)	Uiso O ($Å^2$)
100 K	1-10	4.026	4.075	0.517	0.518	0.103	0.482	0.003	0.005	0.011
100 K	10-19	4.042	4.057	0.518	0.546	0.117	0.469	0.005	0.004	0.010
100 K	19-28	4.037	4.068	0.474	0.509	0.054	0.529	0.006	0.007	0.024
200 K	1-10	4.028	4.082	0.484	0.491	0.109	0.510	0.004	0.006	0.014
200 K	10-19	4.036	4.077	0.497	0.541	0.103	0.503	0.005	0.007	0.019
200 K	19-28	4.040	4.067	0.477	0.503	0.074	0.486	0.008	0.010	0.026
300 K	1-10	4.034	4.076	0.484	0.501	0.111	0.521	0.005	0.007	0.014
300 K	10-19	4.041	4.070	0.517	0.519	0.123	0.483	0.008	0.008	0.015
300 K	19-28	4.045	4.060	0.522	0.499	0.105	0.471	0.010	0.014	0.020
400 K	1-10	4.033	4.092	0.485	0.493	0.106	0.520	0.006	0.008	0.017
400 K	10-19	4.041	4.080	0.473	0.500	0.032	0.491	0.009	0.008	0.031
400 K	19-28	4.046	4.066	0.496	0.497	0.082	0.457	0.011	0.016	0.021

Table 8.25: BTC10 Nano: local structural refinements by carbox approach.

BTC20 Nano										
	Range (Å)	a (Å)	c (Å)	Ti z	Ce z	O1 z	O2 z	Uiso Ba (Å^2)	Uiso Ti-Ce (Å^2)	Uiso O (Å^2)
100 K	1-10	4.058	4.130	0.492	0.494	0.102	0.525	0.005	0.007	0.017
100 K	10-19	4.065	4.127	0.489	0.496	0.068	0.530	0.009	0.009	0.029
100 K	19-28	4.085						0.020	0.025	0.065
200 K	1-10	4.061	4.132	0.489	0.499	0.118	0.521	0.005	0.008	0.016
200 K	10-19	4.069	4.125	0.485	0.488	0.067	0.515	0.011	0.011	0.035
200 K	19-28	4.088						0.021	0.026	0.067
300 K	1-10	4.064	4.143	0.489	0.495	0.102	0.527	0.007	0.007	0.020
300 K	10-19	4.072	4.129	0.511	0.515	0.071	0.481	0.012	0.012	0.033
300 K	19-28	4.090						0.023	0.027	0.069
400 K	1-10	4.068	4.142	0.489	0.494	0.100	0.528	0.008	0.008	0.022
400 K	10-19	4.073	4.137	0.497	0.449	0.080	0.473	0.012	0.013	0.029
400 K	19-28	4.094						0.024	0.028	0.071

Table 8.26: BTC20 Nano: local structural refinements by carbox approach.

Ceramic: supplementary characterization technique (single crystal)

In order to better characterize BTC samples also single crystal analysis has been proposed. Ceramic BTC20 have been grained and thank to the experienced of Dr. Nicola Rotiroti (Department of Earth Sciences, University of Milan, Italy) possible single crystals have been chosen. Data collection, investigating these crystals, has been performed at Department of Earth Sciences, University of Milan, Italy. A 4-circle kappa diffractometer Xcalibur-Oxford Diffraction, equipped with both point and CCD detector, has been employed with a Mo X ray tube operating at 50 keV and 40 mA. As reported in figure 8.2 also most promising single crystals have been proved to be actually polycrystalline showing typical diffraction rings. This confirms the good preparation of ceramic sample which not present micro single crystals.

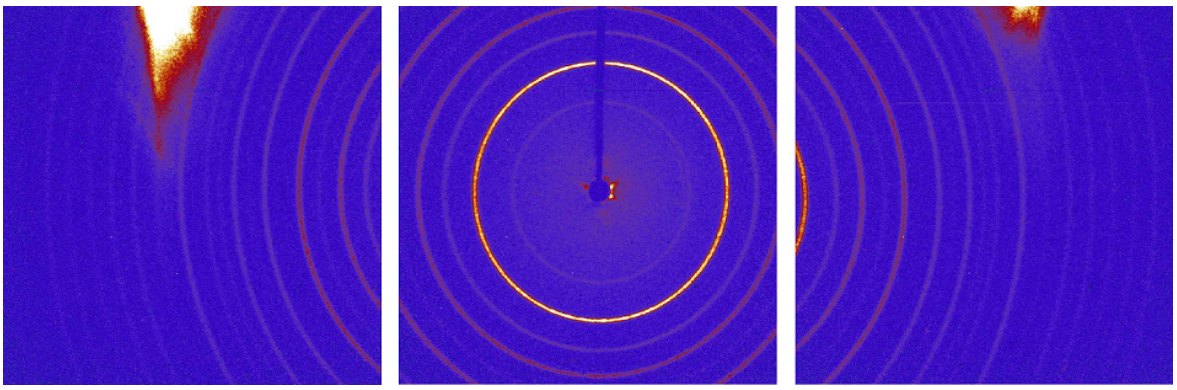

Figure 8.2: Some grains of ceramic samples, investigated as single crystals, have shown typical powders diffractograms.

Bibliography

2002/95/EC, E. D. (2003), 'Restriction of the Use of Certain Hazardous Substances in Electrical and Electronic Equipment (RoHS)', *Official Journal of the European Union* **43**.

Alguero, M., Gregg, J. & Mitoseriu, L. (2016), *Nanoscale Ferroelectrics and Multiferroics Key Processing and Characterization Issues, and Multifferroics Jey Processing and Characterization Issues and Nanoscale Effects*, John Wiley and Sons, chapter Preface.

Amr-Mineral-Metal-Inc (2016), 'Enablers of High Tech Applications and Green Energy Technologies', *www.amrmineralmetal.com* .

Ang, C., Jing, Z. & Yu, Z. (2002a), 'Ferroelectric relaxor $Ba(TiCe)O_3$', *Journal of Physics Condensed Matter* **14**(38), 8901–8912.

Ang, C., Yu, Z., Jing, Z., Guo, R., Bhalla, A. & Cross, L. (2002b), 'Piezoelectric and electrostrictive strain behavior of Ce-doped $BaTiO_3$ ceramics', *Applied Physics Letters* **8**(18), 3424–3426.

Anwar, S., Sagdeo, P. & Lalla, N. (2006), 'Ferroelectric relaxor behavior in hafnium doped barium-titanate ceramic', *Solid State Communications* **138**(7), 331–336.

Balzar, D. (2000), *Defect and microstructure analysis by diffractio*, Oxford Science Publication, chapter Voigt-function model in diffraction line-broadening analysis.

Baxter, P., Hellicar, N. & Lewis, B. (1959), 'Effect of Additives of Limited Solid Solubility on Ferroelectric Properties of Barium Titanate Ceramics', *Journal of the American Ceramic Society* **42**(10), 465–470.

Belushkin, A. V., Kozlenko, D. P., Golosova, N. O., Zetterstrom, P. & Savenko, B. N. (2006), 'A study of disorder effects at ferroelectric phase transition in $BaTiO_3$', *Physica B-Condensed Matter* **385**(1, SI), 85–87. 8th International Conference (ICNS 2005), Sydney, Australia, Nov 27-Dec 02, 2005.

Billinge, S. (2004), 'The Atomic Pair Distribution function: past and present', *Zeitschrift für Kristallographie* **219**(3).

Billinge, S. (2008), *Powder Diffraction. Theory and Practice*, RSCPublishing, chapter Local structure from Total Scattering and Atomic Pair Distribution Function (PDF) analysis.

Billinge, S. (2012), 'Pair distribution function technique: principles and methods', *NATO Science for Peace and Security Series B: Physics and Biophysics* .

Billinge, S. & Kanatzidis, M. (2004), 'Beyond crystallography: the study of disorder, nanocrystallinity and crystallographically challenged materials with pair distribution functions', *Chemical Communications* pp. 749–760.

Bokov, A. & Ye, Z. (2006), 'Recent progress in relaxor ferroelectrics with perovskite structure', *Journal Of Materials Science* **41**(1), 31–52.

Bozin, E. (2003), 'Charge stripes and local structural inhomogeneities in $La_{2-x}(Sr, Ba)_xCuO_4$ high temperature superconductors', *PhD Thesis* .

Buscaglia, V., Buscaglia, M. T., Viviani, M., Mitoseriu, L., Nanni, P., Trefiletti, V., Piaggio, P., Gregora, I., Ostapchuk, T., Pokorny, J. & Petzelt, J. (2006), 'Grain size and grain boundary-related effects on the properties of nanocrystalline barium titanate ceramics', *Journal of the European Ceramic Society* **26**(14), 2889–2898. COST 525 Meeting on Grain Boundary Engineering of Electronic Ceramics, Portoroz, Slovenia, Jun, 2005.

Buscaglia, V., Tripathi, S., Petkov, V., Dapiaggi, M., Deluca, M., Gajovic, A. & Ren, Y. (2014), 'Average and local atomic-scale structure in $BaZr_xTi_{1-x}O_3$ (x=0.10, 0.20, 0.40) ceramics by high-energy x-ray diffraction and Raman spectroscopy', *Journal of Physics Condensed Matter* **26**(6).

Camilo de Souza, E. C. & Muccillo, R. (2010), 'Properties and Applications of Perovskite Proton Conductors', *Materials Research-Ibero-American Journal Of Materials* **13**(3), 385–394.

Caviglia, A. D., Gariglio, S., Reyren, N., Jaccard, D., Schneider, T., Gabay, M., Thiel, S., Hammerl, G., Mannhart, J. & Triscone, J. M. (2008), 'Electric field control of the $LaAlO_3/SrTiO_3$ interface ground state', *Nature* **456**(7222), 624–627.

Chakhmouradian, A. & Mitchell, R. (1998), 'Compositional variation of perovskite-group minerals from the Khibina complex, Kola Peninsula, Russia', *Canadian Mineralogist* **36**(4), 953–969.

Chandra, P. & Littlewood, P. (2007), *Physics of Ferroelectrics: A Modern Perspective*, Springer, chapter A Landau Primer for Ferroelectrics.

Chaves, A., Barreto, F., Nogueira, R. & Zeks, B. (1977), Thermodynamics of an eight-site order-disorder model for ferroelectrics, *in* 'Ferroelectrics', Vol. 16, Univ. Puerto Rico; Nat. Sci. Found; et al, p. 93. .

Chen, M., Shen, Z., Tang, S., Shi, W., Cui, D. & Chen, Z. (2000), 'Stress effect on Raman spectra of Ce-doped $BaTiO_3$ films', *Journal Of Physics-Condensed Matter* **12**(31), 7013–7023.

Chen, X. Y., Ma, C., Zhang, Z. & Wang, B. N. (2008), 'Ultrafine gahnite $(ZnAl_2O_4)$ nanocrystals: Hydrothermal synthesis and photoluminescent properties', *Materials Science And Engineering B-Advanced Functional Solid-State Materials* **151**(3), 224–230.

Ciomaga, C., Viviani, M., Buscaglia, M. T., Buscaglia, V., Mitoseriu, L., Stancu, A. & Nanni, P. (2007), 'Preparation and characterisation of the $Ba(Zr, Ti)O_3$ ceramics with relaxor properties', *Journal of the European Ceramic Society* **27**(13-15), 4061–4064. International Conference on Electroceramics, Toledo, Spain, Jun 18-22, 2006.

Cochran, W. (1986), 'Crystal Stability and the Theroy of Ferroelectricity', *Advances in Physics* **9**, 387–423.

Coduri, M., Brunelli, M., Allieta, M., Masala, P., Capogna, L., Fischer, H. & Ferrero, C. (2012a), 'Rare earth doped ceria: a combined X ray and neutron Pair Distribution Function study', *Zeitshrift fur Kristallographie* **304**, 272–279.

Coduri, M., Scavini, M., Allieta, M., Brunelli, M. & Ferrero, C. (2012b), 'Local disorder in yttrium doped ceria $Ce_{1-x}Y_xO_{2-x/2}$ probed by joint X-ray and Neutron Powder Diffraction', *Journal of Physics Conference Series* **5**, 272–279.

Cohen, R. (1992), 'Origin of ferroelectricity in perovskite oxides)', *Nature* **358**.

Comes, R., Lambert, M. & Guinier, A. (1970), 'Desordre Lineaire dans les Cristaux (cas du Silicium, du Quartz, et des Perovskites Ferroelectriques)', *Acta Crystallographica Section A* **26**, 244.

Confalonieri, G., Dapiaggi, M., Sommariva, M., Gateshki, M., Fitch, A. N. & Bernasconi, A. (2015), 'Comparison of total scattering data from various sources: the case of a nanometric spinel', *Powder Diffraction* **30**(1), S65–S69. 14th European Powder Diffraction Conference (EPDIC), Aarhus, DENMARK, JUN 15-18, 2014.

Cowley, R. A., Gvasaliya, S. N., Lushnikov, S. G., Roessli, B. & Rotaru, G. M. (2011), 'Relaxing with relaxors: a review of relaxor ferroelectrics', *Advances In Physics* **60**(2), 229–327.

Cross (1993), *Ferroelectric Ceramics. Tutorial reviews, theory, processing, and applications*, Birkhauser Basel, chapter Ferroelectric Ceramics: Tailoring Properties for Specific Applications.

Curecheriu, L. P., Ciomaga, C. E., Musteata, V., Canu, G., Buscaglia, V. & Mitoseriu, L. (2016), 'Diffuse phase transition and high electric field properties of $BaCe_yTi_{1-y}O_3$ relaxor ferroelectric ceramics', *Ceramics International* **42**(9), 11085–11092.

Curecheriu, L. P., Deluca, M., Mocanu, Z. V., Pop, M. V., Nica, V., Horchidan, N., Buscaglia, M. T., Buscaglia, V., van Bael, M., Hardy, A. & Mitoseriu, L. (2013), 'Investigation of the ferroelectric-relaxor crossover in Ce-doped $BaTiO_3$ ceramics by impedance spectroscopy and Raman study', *Phase Transitions* **86**(7, SI), 703–714.

Damjanovic, D. (1998), 'Ferroelectric, dielectric and piezoelectric properties of ferroelectric thin films and ceramics', *Reports on Progress in Physics* **61**, 1267–1324.

Dapiaggi, M., Kim, H., Bozin, E., Billinge, S. & Artioli, G. (2008), 'Study of the negative thermal expansion of cuprite-type structures by means of temperature dependent pair distribution function analysis: Preliminary results', *Journal of Physics and Chemistry of Solids* **69**, 2182–2186.

Davies, P. K., Wu, H., Borisevich, A. Y., Molodetsky, I. E. & Farber, L. (2008), 'Crystal chemistry of complex perovskites: New cation-ordered dielectric oxides', *Annual Review of Materials Research* **38**, 369–401.

DeLuca, M. & Gajovic, A. (2016), *Nanoscale Ferroelectrics and Multiferroics Key processing and Characterization Issues and Nanoscale Effects*, John Wiley and Sons, chapter Raman Spectroscopy of Nanostructured Ferroelectric Materials.

Dmowski, W., Akbas, M., Egami, T. & Davies, P. (2002), 'Structure refinement of large domain relaxors in the $Pb(Mg_{1/3}Ta_{2/3})O_3 - PbZrO_3$ system', *Journal Of Physics And Chemistry Of Solids* **63**(1), 15–22.

Dughaish, Z. & Issa, M. (2008), 'Dielectric Properties of $BaTiO_3$ Doped CeO_2 Ceramics', *Journal of Natural Sciences and Mathematics* **2**(1), 63–72.

Egami, T. (2002), *Local Structure from Diffraction*, Klumer Academic Publishers, chapter PDF Analysis Applied to Crystalline Materials.

Egami, T. Billinge, S. (2003), *Underneath the Bragg Peaks: Structural Analysis of Complex Materials*, Pergamon Press, Elsevier, Oxford.

Farhi, R., El Marssi, M., Simon, A. & Ravez, J. (1999), 'A Raman and dielectric study of ferroelectric $Ba(Ti_{1-x}Zr_x)O_3$ ceramics', *European Physical Journal B* **9**(4), 599–604.

Farrow, C. & Billinge, S. (2009), 'Relationship between the atomic pair distribution function and small-angle scattering: implications for modeling of nanoparticles', *Acta Crystallographica Section A* **65**, 232–239.

Farrow, C. L., Juhas, P., Liu, J. W., Bryndin, D., Bozin, E. S., Bloch, J., Proffen, T. & Billinge, S. J. L. (2007), 'PDFfit2 and PDFgui: computer programs for studying nanostructure in crystals', *Journal of Physics Condensed Matter* **19**(33). 3rd Workshop on Reverse Monte Carlo Methods, Budapest, Hungary, Sep 28-30, 2006.

Feng, D., Shivaramaiah, R. & Navrotsky, A. (2016), 'Rare-earth perovskites along the $CaTiO_3-Na_{0.5}La_{0.5}TiO_3$ join: Phase transitions, formation enthalpies, and implications for loparite minerals', *American Mineralogist* **101**(9-10), 2051–2056.

Fernandez Martinez, A., Cuello, G., Daniels, J. & Charlet, L. (2008), 'X-ray Pair Distribution Function studies of nanosize minerals', *Revista de la Sociedad Espanola de Mineralogia* **8**.

Fitch, A. (2004), 'The high resolution powder diffraction beam line at ESRF', *Journal of research of the National Institute of Standards and Technology* **109**(1), 133–142. 3rd Conference on Accuracy in Powder Diffraction, NIST, Gaithersburg, MD, Apr 22-25, 2001.

Fitch, A. (2012), 'ID22: conceptual design report', *Personal Document* .

Fitch, A. (2013), 'Transfer of ID31 to ID22, technical design report', *Personal Document* .

Freeman, C. L., Dawson, J. A., Chen, H.-R., Harding, J. H., Ben, L.-B. & Sinclair, D. C. (2011), 'A new potential model for barium titanate and its implications for rare-earth doping', *Journal of Materials Chemistry* **21**(13), 4861–4868.

Frenkel, A., Frey, M. & Payne, D. (1999), 'XAFS analysis of particle size effect on local structure in $BaTiO_3$', *Journal Of Synchrotron Radiation* **6**(3), 515–517. 10th International Conference on XAFS (XAFS X), Illinois Inst Technol, Chicago, Illinois, Aug 10-14, 1998.

Fu, D. & Itoh, M. (2015), *Ferroelectric Materials - Synthesis and Characterization*, InTech, chapter Role of Ca off-Centering in Tuning Ferroelectric Phase Transitions in $Ba(Zr, Ti)O_3$ System.

Galasso, F. (1969), *Structure properties and preparation of perovskite-type compounds*, Pergamon Press.

Gale, J. (1996), 'Empirical potential derivation for ionic materials', *Philosophical Magazine B Physics of Condensed Matter Statistical Mechanics Electronic Optical and Magnetic Properties* **73**(1), 3–19. Meeting on Interatomic Potentials, Mansfield Coll, Oxford, England, Jul 04-05, 1994.

Gale, J. (1997), 'GULP: A computer program for the symmetry-adapted simulation of solids', *Journal of the Chemical Society Faraday Transactions* **93**(4), 629–637.

Gale, J. & Rohl, A. (2003), 'The General Utility Lattice Program (GULP)', *Molecular Simulation* **29**(5), 291–341.

Gerra, G., Tagantsev, A., Setter, N. & Parlinski, K. (2006), 'Ionic polarizability of conductive metal oxides and critical thickness for ferroelectricity in $BaTiO_3$', *Physical Review Letters* **96**(10).

Girshberg, Y. & Yacoby, Y. (2001), 'Off-centre displacements and ferroelectric phase transition in dilute $KTa_{1-x}Nb_xO_3$', *Journal of Physics Condensed Matter* **13**(39), 8817–8830.

Glasser, L. & Jenkins, H. (2000), 'Lattice energies and unit cell volumes of complex ionic solids', *Journal of the American Chemical Society* **122**(4), 632–638.

Glazer, A. M. (1972), 'The Classification of Tilted Octahedra in Perovskites', *Journal of Physics and Chemistry of Solids* **B**(28), 3384–3392.

Gupta, C. & Krishnamurthy, N. (1992), 'Extractive metallurgy of rare-earths', *International Materials Reviews* **37**(5), 197–248.

Hagemann, H. & Hennings, D. (1981), 'Reversible Weight Change of Acceptor-Doped $BaTiO_3$', *Journal of the American Ceramic Society* **64**(10), 590–594.

Hennings, D., Schnell, A. & Simon, G. (1982), 'Diffuse ferroelectric phase transitions in $Ba(Ti_{1-y}Zr-y)O_3$ ceramics', *Journal of the American Ceramic Society* **65**, 539–44.

Heywang, W., Lubitz, K. & Wersing, W. (2008), *Piezoelectricity Evolution and Future of a Technology*, Springer.

Honda, A., Higai, S., Motoyoshi, Y., Wada, N. & Takagi, H. (2011), 'Theoretical Study on Interactions between Oxygen Vacancy and Doped Rare Earth Elements in Barium Titanate', *Japanese Journal of Applied Physics* **50**(9).

Hong, C., Kim, H., Choi, B., Han, H., Son, J., Ahn, C. & Jo, W. (2016), 'Lead free piezoceramics e Where to move on?', *Journal of Materiomics* **2**, 1–24.

Howard, C. & Stokes, H. (1998), 'Group-theoretical analysis of octahedral tilting in perovskites', *Acta Crystallographica Section B Structural Science* **54**(6), 782–789.

Howell, R., Proffen, T. & Conradson, S. (2006), 'Pair distribution function and structure factor of spherical particles', *Physical Review B* **73**(9).

Hwang, J. & Han, Y. (2000), 'Dielectric properties of $(Ba_{1-x}Ce_x)TiO_3$', *Japanese Journal of Applied Physics* **39**(5A), 2701–2704.

Hwang, J. & Han, Y. (2001), 'Electrical properties of cerium-doped $BaTiO_3$', *Journal of the American Ceramic Society* **84**(8), 1750–1754.

Ianculescu, A., Berger, D., Vasilescu, C., Olariu, M., Vasile, B., Curecheriu LP, Gajovic, A. & Trusca, R. (2016), *Nanoscale ferroelectrics and multiferroics key processing and characterization issues, and nanoscale effects*, John Wiley and Sons, chapter Incorporation Mechanism and Functional Properties of Ce-Doped BaTiO3 Ceramics Derived from Nanopowders Prepared by the Modified Pechini Method.

Ihlefeld, J., Harris, D., Keech, R., Jones, J., Maria, J. & Troiler-McKinstry, S. (2016), 'Scaling effects in perovskite ferroelectrics: fundamental limits and process-structure-property relations', *Journal of the American Ceramic Society* **99**(8), 2573–2557.

Irifune, T. (1994), 'Absence of an aluminous phase in the upper part of the earths lower mantle', *Nature* **370**(6485), 131–133.

Issa, M., Molokhia, M. & Dughaish, Z. (1983), 'Effect of cerium oxide CeO_2 additives on the dielectric properties of $BaTiO_3$ ceramics', *Journal of Physics D: Applied Physics* **16**(6), 1109–1115.

Jacob, K., Ray, S. & Rannesh, L. (2007), 'Vegard's law: a fundamental relation or an approximation?', *International Journal of Material Research* **98**, 776–779.

Jaffe, F. & Cook, WR anf Jaffe, H. (1971), *Non Metallic Solids: Piezoelectric Ceramics*, Academic Press.

Jeon, J. (2004), 'Effect of $SrTiO_3$ concentration and sintering temperature on microstructure and dielectric constant of $Ba_{1-x}Sr_xTiO_3$', *Journal of the European Ceramic Society* **24**(6), 1045–1048. 8th International Conference on Electronic Ceramics and Their Applications (Electroceramics VIII), Pontificia Univ Lateranensis, Rome, Italy, Aug 25-28, 2002.

Jing, Z., Ang, C., Yu, P., Vilarinho, P. & Baptista, J. (1998), 'Dielectric properties of $Ba(Ti_{1-y}Y_y)O_3$ ceramics', *Journal of applied physics* **84**, 983–986.

Jing, Z., Yu, Z. & Ang, C. (2003), 'Crystalline structure and dielectric properties of $Ba(Ti_{1-y}Ce_y)O_3$', *Journal of Materials Science* **38**(5), 1057–1061.

Jonker, J. (1964), 'Some aspects of semiconducting barium titanate', *Solid-State Electronics* **6**(12), 895–903.

Juhas, P., Davis, T., Farrow, C. L. & Billinge, S. J. L. (2013), 'PDFgetX3: a rapid and highly automatable program for processing powder diffraction data into total scattering pair distribution functions', *Journal of Applied Crystallography* **46**(2), 560–566.

Juhas, P., Farrow, C. L., Yang, X., Knox, K. R. & Billinge, S. J. L. (2015), 'Complex modeling: a strategy and software program for combining multiple information sources to solve ill posed structure and nanostructure inverse problems', *Acta Crystallographica A Foundation and Advances* **71**(6), 562–568.

Keen, D. (2001), 'A comparison of various commonly used correla- tion functions for describing total scattering', *Journal of Applied Crystallography* **34**, 172–177.

Kim, H. (2007), 'The role of the local structure in electronic properties of various materials', *PhD Thesis* .

Kingery, W., Bowen, H. & Uhlmann, D. (1960), *Introduction to Ceramics*, John Wiley and Sons.

Kishi, H., Kohzu, N., Sugino, J., Ohsato, H., Iguchi, Y. & Okuda, T. (1999), 'The effect of rare-earth (La, Sm, Dy, Ho and Er) and Mg on the microstructure in $BaTiO_3$', *Journal of European Ceramic Society* **19**(6-7), 1043–1046. Electroceramics VI 98, Montreux, Switzerland, Aug 24-27, 1998.

Koito, S., Akaogi, M., Kubota, O. & Suzuki, T. (2000), 'Calorimetric measurements of perovskites in the system $CaTiO_3-CaSiO_3$ and experimental and calculated phase equilibria for high-pressure dissociation of diopside', *Physics Of The Earth And Planetary Interiors* **120**(1-2), 1–10.

Krayzman, V. & Levin, I. (2008), 'Determination of B-cation chemical short-range order in perovskites from the total pair-distribution function', *Journal Of Applied Crystallography* **41**(2), 386–392.

Kumari, P., Raia, R., Sharmab, S., Shandilyaa, M. & Tiwari, A. (2015), 'State of the art of lead free ferroelectrics: A critical review', *Advanced Materials Letters* **6**(6), 453–484.

Kwei, G., Lawson, A., Billinge, S. & Cheong, S. (1993), 'Structures of the ferroelectric phases of barium-titanate', *Journal Of Physical Chemistry* **97**(10), 2368–2377.

Labiche, J.-C., Mathon, O., Pascarelli, S., Newton, M. A., Ferre, G. G., Curfs, C., Vaughan, G., Homs, A. & Fernandez Carreiras, D. (2007), 'Invited article: The fast readout low noise camera as a versatile x-ray detector for time resolved dispersive extended x-ray absorption fine structure and diffraction studies of dynamic problems in materials science, chemistry, and catalysis', *Review Of Scientific Instruments* **78**(9).

Laulhe, C., Hippert, F., Bellissent, R., Simon, A. & Cuello, G. J. (2009), 'Local structure in $BaTi_{1-x}Zr_xO_3$ relaxors from neutron pair distribution function analysis', *Physical Review B* **79**(6).

Laulhe, C., Hippert, F., Kreisel, J., Maglione, M., Simon, A., Hazemann, J. L. & Nassif, V. (2006), 'EXAFS study of lead-free relaxor ferroelectric $BaTi_{1-x}Zr_xO_3$ at the Zr K edge', *Physical Review B* **74**(1).

Laulhe, C., Pasturel, A., Hippert, F. & Kreisel, J. (2010), 'Random local strain effects in homovalent-substituted relaxor ferroelectrics: A first-principles study of $BaTi_{0.74}Zr_{0.26}O_3$', *Physical Review B* **82**(13).

Levin, I., Cockayne, E., Krayzman, V., Woicik, J. C., Lee, S. & Randall, C. A. (2011), 'Local structure of $Ba(Ti, Zr)O_3$ perovskite-like solid solutions and its relation to the band-gap behavior', *Physical Review B* **83**(9).

Levin, I., Cockayne, E., Lufaso, M., Woicik, J. & Maslar, J. (2006), 'Local structures and Raman spectra in the $Ca(Zr, Ti)O_3$ perovskite solid solutions', *Chemistry Of Materials* **18**(3), 854–860.

Li, C., Lu, X., Ding, W., Feng, L., Gao, Y. & Guo, Z. (2008), 'Formability of ABX(3) (X = F, Cl, Br, I) halide perovskites', *Acta Crystallographica Section B-Structural Science* **64**(6), 702–707.

Li, G., Alberta, E., Yu, Z., Guo, R. & Bhalla, A. (2005), $Ba(Zr_xT_{1-x})O_3$: MgO composites for field and frequency tunable applications, *in* WongNg, W and Goyal, A and Guo, R and Bhalla, AS, ed., 'Synthesis, Properties, And Crystal Chemistry Of Perovskite-Based Materials', Vol. 169 of *Ceramic Transactions*, pp. 67–75. 106th Annual Meeting of the American-Ceramic-Society, Indianapolis, IN, Apr 18-21, 2004.

Lin, S., Lu, T., Jin, C. & Wang, X. (2006), 'Size effect on the dielectric properties of $BaTiO_3$ nanoceramics in a modified Ginsburg-Landau-Devonshire thermodynamic theory', *Physical Review B* **74**(13).

Liu, L. (1975), 'Post-oxide phases of olivine and pyroxene and mineralogy of the mantle', *Nature* **258**, 510–512.

Liu, L. (1976), 'Orthorhombic perovskite phases observed in olivine, pyroxene and garnet at high pressures and temperatures', *Physics of The Earth and Planetary Interiors* **11**(4), 289–298.

Liu, L. (1989), 'Silicate perovskites - a review', *Surveys In Geophysics* **10**(1), 63–81.

Lu, D., Han, D. & Sun, X. (2012), 'Mutual solid solubility and phase equilibrium in the system $BaTiO_3$Ű$BaCeO_3$', *Japanese Journal of Applied Physics* **51**.

Lu, D.-Y., Han, D.-D., Sun, X.-Y., Zhuang, X.-L. & Zhang, Y.-F. (2013), 'Raman Evidence for Ba-Site Ce^{3+} in $BaTiO_3$', *Japanese Journal Of Applied Physics* **52**(11).

Lu, D.-Y., Sun, X.-Y. & Toda, M. (2007), 'A novel high-k 'Y5V' barium titanate ceramics co-doped with lanthanum and cerium', *Journal Of Physics And Chemistry Of Solids* **68**(4), 650–664.

Lucchesi, S., Della Giusta, A. & Russo, U. (1998), 'Cation distribution in natural Zn-aluminate spinels', *Mineralogical Magazine* **62**(1), 41–54.

Lutterotti, L. Matthies, S. & Wenk, H. (1999), 'MAUD: a friendly Java program for material analysis using diffraction', *IUCr: Newsletter of the CPD* **21**, 14–15.

Maiti, T., Guo, R. & Bhalla, A. S. (2008), 'Structure-property phase diagram of $BaZr_xTi_{1-x}O_3$ system', *Journal Of The American Ceramic Society* **91**(6), 1769–1780.

Makovec, D., Samardzija, Z. & Kolar, D. (1996), 'Solid solubility of cerium in $BaTiO_3$', *Journal Of Solid State Chemistry* **123**(1), 30–38.

Malavasi, L., Kim, H. & Proffen, T. (2009), 'Local and average structures of the proton conducting Y-doped $BaCeO_3$ from neutron diffraction and neutron pair distribution function analysis', *Journal Of Applied Physics* **105**(12).

Masadeh, A. S., Bozin, E. S., Farrow, C. L., Paglia, G., Juhas, P., Billinge, S. J. L., Karkamkar, A. & Kanatzidis, M. G. (2007), 'Quantitative size-dependent structure and strain determination of CdSe nanoparticles using atomic pair distribution function analysis', *Physical Review B* **76**(11).

McGreevy, R. & Pusztai, L. (1988), 'Reverse Monte Carlo Simulation: a new technique for the determination of disordered structures', *Journal of Molecular Simulation* **1**(6), 359–367.

Metzmacher, C. & Albertsen, K. (2001), 'Microstructural investigations of barium titanate-based material for base metal electrode ceramic multilayer capacitor', *Journal Of The American Ceramic Society* **84**(4), 821–826.

Miura, K., Azuma, M. & Funakubo, H. (2011), 'Electronic and Structural Properties of ABO3: Role of the B-O Coulomb Repulsions for Ferroelectricity)', *Materials* **4**, 260–273.

Moulson, A. & Herbert, J. (2003), *Electroceramics: Materials, Properties, Applications, Second Edition*, John Wiley and Sons.

Moure, C. & Pena, O. (2015), 'Recent advances in perovskites: Processing and properties', *Progress In Solid State Chemistry* **43**(4), 123–148.

Muller, K. & Berlinger, W. (1986), 'Microscopic probing of order-disorder versus displacive behavior in $BaTi0_3$ by Fe^{3+} electron-paramagnetic-res', *Physical Review B* **34**(9), 6130–6136.

Muller, K., Berlinger, W. & Blazey, K. (1987), 'Electron paramagnetic resonance of Mn^{4+} in $BaTiO_3$', *Solid State Communications* **61**(1), 21–25.

Murakami, M., Hirose, K., Kawamura, K., Sata, N. & Ohishi, Y. (2004), 'Post-perovskite phase transition in $MgSiO_3$)', *Science* **304**, 855–858.

Nandi, R., Kuo, W., Schlosberg, W., Wissler, G., Cohen, J. & Crist, B. (1984), 'Single-peak methods for Fourier analysis of peak shapes', *Journal of Apllied Crystallography* .

Neirman, S. (1988), 'The curie-point temperature of $BaTi_{1-x}Zr_xO_3$ solid-solutions', *Journal Of Materials Science* **23**(11), 3973–3980.

Nijenhuis, J. T., Gateshki, M. & Fransen, M. J. (2009), 'Possibilities and limitations of X-ray diffraction using high-energy X-rays on a laboratory system', *Zeitschrift Fur Kristallographie* **30**, 163–169.

Nuraje, N. & Su, K. (2013), 'Perovskite ferroelectric nanomaterials', *Nanoscale* **5**(19), 8752–8780.

Oganov, A. & Ono, S. (2000), 'Theoretical and experimental evidence for post-perovskite ohase of $MgSiO_3$ in Earth's D" layer ', *Nature* **430**, 445–448.

Ohta, H., Kim, S., Mune, Y., Mizoguchi, T., Nomura, K., Ohta, S., Nomura, T., Nakanishi, Y., Ikuhara, Y., Hirano, M., Hosono, H. & Koumoto, K. (2007), 'Giant thermoelectric Seebeck coefficient of two-dimensional electron gas in $SrTiO_3$', *Nature Materials* **6**(2), 129–134.

Ono, S. & Oganov, A. (2005), 'In situ observations of phase transition between perovskite and $CaIrO_3$-type phase in $MgSiO_3$ and pyrolitic mantle composition', *Earth And Planetary Science Letters* **236**(3-4), 914–932.

Ortega SanMartin, L., Chapman, J., Hernandez-Bocanegra, E., Insausti, M., Arriortua, M. & Rojo, T. (2004), 'Structural phase transitions in the ordered double perovskite Sr_2MnTeO_6', *Journal Of Physics: Condensed Matter* **16**, 3879–38881.

Page, K., Proffen, T., Niederberger, M. & Seshadri, R. (2010), 'Probing Local Dipoles and Ligand Structure in $BaTiO_3$ Nanoparticles', *Chemistry Of Materials* **22**(15), 4386–4391.

Park, Y. & Kim, H. (1997), 'The microstructure analysis of cerium-modified barium titanate having core-shell structured grains', *Ceramics International* **23**(4), 329–336.

Park, Y. & Kim, Y. (1995), 'The dielectric temperature characteristic of additives modified barium-titanate having core-shell structured ceramics', *Journal Of Materials Research* **10**(11), 2770–2776.

Pasciak, M., Wolcyrz, M. & Pietraszko, A. (2007), 'Interpretation of the diffuse scattering in Pb-based relaxor ferroelectrics in terms of three-dimensional nanodomains of the <110> directed relative interdomain atomic shifts', *Physical Review B* **76**(1).

Payne, W. & Tennery, V. (1965), 'Dielectric and Structural Investigations of the System $BaTiO_3 - BaHfO_3$', *Journal of the American Ceramic Society* **48**(8), 413–417.

Petkov, V., Buscaglia, V., Buscaglia, M. T., Zhao, Z. & Ren, Y. (2008), 'Structural coherence and ferroelectricity decay in submicron- and nano-sized perovskites', *Physical Review B* **78**(5).

Price, G. (2009), *Mineral Physic. Volume 2*, Elsevier.

Proffen, T. (2006), 'Analysis of disordered materials using Total Scattering and the Atomic Pair Distribution Function', *Reviews in Mineralogy and Geochemistry* **63**, 255–274.

Proffen, T. (2007), 'Characterization of Materials using the PDF', *Canadian Powder Diffraction Workshop* .

Proffen, T. & Kim, H. (2009), 'Advances in total scattering analysis', *Journal of Materials Chemistry* **19**, 5078–5088.

Proffen, T. & Neder, R. (1999), 'DISCUS, a program for diffuse scattering and defect structure simulations - update', *Journal of Applied Crystallography* **32**, 838–839.

Rabuffetti, F. A., Culver, S. P., Lee, J. S. & Brutchey, R. L. (2014), 'Local structural investigation of Eu^3+ doped $BaTiO_3$ nanocrystals', *Nanoscale* **6**(5), 2909–2914.

Ravel, B., Stern, E., Vedrinskii, R. & Kraizman, V. (1998), 'Local structure and the phase transitions of $BaTiO_3$', *Ferroelectrics* **206**(1-4), 407–430. 1997 Williamsburg Workshop on Ferroelectrics, Williamsburg, Virginia, Feb 02-05, 1997.

Ravel, R. (1957), 'Classification of Perovskite and Other $AB0_3$-Type Compounds', *Journal of Research of the National Bureau of Standards* **52**(2).

Ravez, J. & Simon, A. (1997a), 'Raman spectroscopy and soft modes in the model ferroelastics', *The European Physical Journal Applied Physics* **11**, 9–13.

Ravez, J. & Simon, A. (1997b), 'The crystal chemistry of the higher tungsten oxides', *Journal of Solid State Chemistry* **34**(1).

Reiss, C. A., Kharchenko, A. & Gateshki, M. (2012), 'On the use of laboratory X-ray diffraction equipment for Pair Distribution Function (PDF) studies', *Zeitschrift Fur Kristallographie* **227**(5), 257–261.

Ringwood, A. (1962), 'A model for the upper mantle', *Journal Of Geophysical Research* **67**(2).

Samara, G. (2003), 'The relaxational properties of compositionally disordered ABO_3 perovskites', *Journal Of Physics-Condensed Matter* **15**(9), R367–R411.

Santos, I. & Eiras, J. (2001), 'Phenomenological description of the diffuse phase transition in ferroelectrics', *Journal Of Physics-Condensed Matter* **13**(50), 11733–11740.

Scavini, M., Coduri, M., Allieta, M., Brune, M. & Ferrero, C. (2012), 'Probing Complex Disorder in $Ce_{1-x}Gd_xO_{2-x/2}$ Using the Pair Distribution Function Analysis', *Chemistry Of Materials* **24**(7), 1338–1345.

Sen, S. & Choudhary, R. (2005), 'Structural, dielectric and electrical properties of Ca modified $BaSn_{0.15}Ti_{0.85}O_3$ Ceramics', *Journal Of Materials Science* **40**(20), 5457–5462.

Shannon, R. (1967), 'Synthesis of Some New Perovskites Containing Indium and Thallium', *Inovganzc Chemistry* **6**(8).

Shrout, T. & Zhang, S. (2007), 'Lead-free piezoelectric ceramics: Alternatives for PZT?', *Journal of Electroceramics* **19**, 111–24.

Shvartsman, V. V. & Lupascu, D. C. (2012), 'Lead-Free Relaxor Ferroelectrics', *Journal Of The American Ceramic Society* **95**(1), 1–26.

Sidorkin, A. (2006), *Domain structure in ferroelectrics and related materials*, Cambridge International Science Publishing.

Sinogeikin, S., Bass, J. & Katsura, T. (2003), 'Single-crystal elasticity of ringwoodite to high pressures and high temperatures: implications for 520 km seismic discontinuity', *Physics Of The Earth And Planetary Interiors* **136**(1-2), 41–66. Workshop on Phase Transitions and Mantle Discontinuities, Potsdam, Germany, 2001.

Smith, M. B., Page, K., Siegrist, T., Redmond, P. L., Walter, E. C., Seshadri, R., Brus, L. E. & Steigerwald, M. L. (2008), 'Crystal structure and the paraelectric-to-ferroelectric phase transition of nanoscale $BaTiO_3$', *Journal Of The American Chemical Society* **130**(22), 6955–6963.

Sommariva, M. (2013), Multi-Technique Approach for Nanoparticles Characterization on a Laboratory X-Ray Diffractometer, *in* Stroz, D and Dercz, G, ed., 'Applied Crystallography XXII', Vol. 203-204 of *Solid State Phenomena*, pp. 17–20. 22nd Conference on Applied Crystallography, Targanice, Poland, Sep 02-06, 2012.

Sommariva, M., Gateshki, M., Bolze, J., Reiss, C. & Dapiaggi, M. (2013), 'How multipurpose in-house XRD systems can contribute to an efficient use of synchrotron beamlines: from small angle to total scattering experiments', *Oral presentation at SILS Conf., 13 September 2013, Politecnico di Milano, Milano, Italy* .

Soni, R., Petraru, A., Meuffels, P., Vavra, O., Ziegler, M., Kim, S., Jeong, D., Pertsev, N. & Kohlstedt, H. (2014), 'Giant electrode effect on tunnelling electroresistance in ferroelectric tunnel junctions', *Nature Communications* **5**, 5414.

Soper, A. (2011), 'GudrunN and GudrunX: programs for correcting raw neutron and X-ray diffraction data to differential scattering cross section', *Science and Technology Facilities Council, Great Britain, Didcot* .

Stern, E. (2004), 'Character of order-disorder and displacive components in barium titanate', *Physical Review Letters* **93**(3).

Suntivich, J., Gasteiger, H. A., Yabuuchi, N., Nakanishi, H., Goodenough, J. B. & Shao-Horn, Y. (2011), 'Design principles for oxygen-reduction activity on perovskite oxide catalysts for fuel cells and metal-air batteries', *Nature Chemistry* **3**(7), 546–550.

Suntivich, J., May, K. J., Gasteiger, H. A., Goodenough, J. B. & Shao-Horn, Y. (2011), 'A Perovskite Oxide Optimized for Oxygen Evolution Catalysis from Molecular Orbital Principles', *Science* **334**(6061), 1383–1385.

Tenne, D., Turner, P., Schmidt, J., Biegalski, M., Li, Y., Chen, L., Soukiassian, A., Trolier-McKinstry, S., Schlom, D., Xi, X., Fong, D., Fuoss, P., Eastman, J., Stephenson, G., Thompson, C. & Streiffer, S. (2009), 'Ferroelectricity in ultrathin $BaTiO_3$ films: probing the size effect by ultraviolet raman spectroscopy', *Physical Review Letters* **103**(17).

Thomas, N. (1996), 'The compositional dependence of octahedral tilting in orthorhombic and tetragonal perovskites', *Acta Crystallographica Section B-Structural Science* **52**(1), 16–31.

Thomas, N. & Beitoliahi, A. (1994), 'Interrelationship of octahedral geometry, polyhedral volume ratio and ferroelectric properties in thombohedral perovskites', *Acta Crystallographica Section B-Structural Science* **50**(5), 549–560.

Tidrow, S. (2014), 'Mapping Comparison of Goldschmidt's Tolerance Factor with Perovskite Structural Conditions', *Ferroelectrics* **470**, 13–27.

Toby, B. & Egami, T. (1992), 'Accuracy of Pair Distribution Function Analysis Applied to Crystalline and Non-Crystalline Materials', *Acta Crystallographica Section A* **48**, 336–346.

Tucker, M., Keen, D., Dove, M., Goodwin, A. & Hui, Q. (2007), 'RMCProfile: reverse Monte Carlo for polycrystalline materials', *Journal of Physics of Condensed Matter* **19**.

Uchino, K. (1994), 'Relaxor Ferroelectrics Devices', *Ferroelectrics* **151**, 321–330.

Uchino, K. (2010), *Ferroelectric Devices, 2th edition*, CRC Press.

Uchino, K., Sadanaga, E. & Hirose, T. (1989), 'Dependence of the crystal-structure on particle-size in barium-titanate', *Journal Of The American Ceramic Society* **72**(8), 1555–1558.

Upadhyay, S., Shrivastava, J., Solanki, A., Choudhary, S., Sharma, V., Kumar, P., Singh, N., Satsangi, V. R., Shrivastav, R., Waghmare, U. V. & Dass, S. (2011), 'Enhanced Photoelectrochemical Response of $BaTiO_3$ with Fe Doping: Experiments and First-Principles Analysis', *Journal Of Physical Chemistry C* **115**(49), 24373–24380.

Veksler, L. & Teptelev, M. (1990), 'Conditions for crystallization and concentration of perovskitetype minerals in alkaline magmas', *Lithos* **26**, 177–189.

Verma, A. & Jindal, V. (2010), *Perovskites: structure, properties and uses*, Nova Science Publishers, chapter ABX3 type oxides and halides: their structure and physical properties.

Veselinovic, L., Mitric, M., Mancic, L., Vukomanovic, M., Hadzic, B., Markovic, S. & Uskokovic, D. (2014), 'The effect of Sn for Ti substitution on the average and local crystal structure of $BaTi_{1-x}Sn_xO_3$ (0 <= x <= 0.20)', *Journal Of Applied Crystallography* **47**(3), 999–1007.

Wainer, E. & Salomon, A. (1942), 'Electrical Reports of the Titanium Alloy Manufacturing Division, Report 10', *National Lead Co., Winchester(USA)* .

Wen, Z., Li, C., Wu, D., Li, A. & Ming, N. (2013), 'Ferroelectric-field-effect-enhanced electroresistance in metal/ferroelectric/semiconductor tunnel junctions', *Nature Materials* **12**(7), 617–621.

Westphal, V., Kleemann, W. & Glinchuk, M. (1992), 'Diffuse phase-transitions and random-field-induced domain states of the relaxor ferroelectric $PbMg_{1/3}Nb_{2/3}O_3$', *Physical Review Letters* **68**(6), 847–850.

Woodley, S., Battle, P., Gale, J. & Catlow, C. (1999), 'The prediction of inorganic crystal structures using a genetic algorithm and energy minimisation', *Physical Chemistry Chemical Physics* **1**(10), 2535–2542.

Woodward, P. (1997), 'Octahedral tilting in perovskites .1. Geometrical considerations', *Acta Crystallographica Section B-Structural Science* **53**(1), 32–43.

Wul, B. & Goldman, J. (1945), 'Dielectric Constants of Titanates of Metals of Second Group', *Comptes Rendus (Doklady) de l'Académie des Sciences de l'URSS* **46**, 139.

Xi, Y., Zhili, C. & Cross, L. (1983), 'Polarization and depolarization behavior of hot pressed lead lanthanum zirconate titanate ceramics', *Journal of Applied Physics* **54**, 3399.

Xu, Y. (1991), *Ferroelectric Materials and Their Applications*, North-Holland, Elsevier Science Publishers B.V.

Ya-min, Z., Xiu-yun, S. & Da-yong, L. (2006), 'Effects of cerium doping at Ti sites and europium doping at Ba sites on dielectric properties of $BaTiO_3$ ceramics', *Chemical Research In Chinese Universities* **22**(4), 515–519.

Yang, J. (2005), *An introduction to the theory of piezoelectricity*, Springer.

Yashima, M. & Ali, R. (2009), 'Structural phase transition and octahedral tilting in the calcium titanate perovskite CaTiO3', *Solid State Ionics* **180**(2-3), 120–126.

Yasmin, S., Choudhury, S., Hakim, M. A., Bhuiyan, A. H. & Rahman, M. J. (2011), 'Effect of Cerium Doping on Microstructure and Dielectric Properties of $BaTiO_3$ Ceramics', *Journal Of Materials Science And Technology* **27**(8), 759–763.

Ye, Z. (2008), *Handbook of advanced dielectric,piezoelectric and ferroelectric materials*, CRC Press.

Yoneda, Y., Kohara, S. & Kato, K. (2013), 'Local Structure Analysis of $BaTiO_3$ Nanoparticles', *Japanese Journal Of Applied Physics* **52**(9, 2, SI).

Yu, Z., Ang, C., Guo, R. & Bhalla, A. (2007), 'Dielectric properties of $Ba(Ti_{1-x}Zr_x)O_3$ solid solutions', *Materials Letters* **61**, 326–329.

Zaghete, M., Moura, F., Simoes, A., Varela, J. & Longo, E. (2011), *Advances in Ceramics Electric and Magnetic Ceramics, Bioceramics, Ceramics and Environment*, InTech, chapter Influence of Dopants, Temperature and Atmosphere of Sintered on the Microstructure and Behavior of Lead Free Ceramics.

Zheludev, I. (1971), *Physics of crystalline dielectrics Volume 1: Crystallography and Spontaneous Polarization*, Plenum Press.

Zheludev, I. (1988), *Modem Crystallography IV Physical Properties of Crystals*, Springer Verlag Berlin Heidelberg, chapter Electrical Properties of Crystals.

Zheng, S. J., Du, K., Sang, X. H. & Ma, X. L. (2007), 'TEM and STEM investigation of grain boundaries and second phases in barium titanate', *Philosophical Magazine* **87**(34), 5447–5459.

Zhu, X. & Liu, Z. (2011), 'Size effects in perovskite ferroelectric nanostructures: current progress and future perspectives', *Journal of Advanced Dielectrics* **1**(3), 289–301.

Zou, J.-P., Zhang, L.-Z., Luo, S.-L., Leng, L.-H., Luo, X.-B., Zhang, M.-J., Luo, Y. & Guo, G.-C. (2012), 'Preparation and photocatalytic activities of two new Zn-doped $SrTiO_3$ and $BaTiO_3$ photocatalysts for hydrogen production from water without cocatalysts loading', *International Journal Of Hydrogen Energy* **37**(22), 17068–17077.

Acknowledgments

Finally this hard work has come to an end, but its conclusion would not have been possible without the support and guidance that I have received from many people.

Firstly I would like to thank Prof. Monica Dapiaggi for the continuous encouragement. Your guidance helped me in all the time.

Special thanks to Andrea Bernasconi, Matteo Galimberti, Nicola Rotiroti, Nicoletta Marinoni, Pietro Vignola, your help has been indispensable; moreover I thank also Alessandro Pavese, Vincenzo Buscaglia, Mauro Coduri, all of the Botticelli's PhD students, technicians (Elena, Andrea, Franco), colleagues and all of those who have contributed to this thesis.

Last, but not least I would like to express my endless gratitude to my family, to Federico and all my friends for providing me with unfailing support. This thesis is for you.

I am very grateful to all of those with whom I have had the pleasure to work and share this adventure.
To all of you: thank you so much.